

Parameter tuning and cooperative control for automated guided vehicles

Citation for published version (APA):

Stouten, B. (2005). *Parameter tuning and cooperative control for automated guided vehicles*. [Phd Thesis 1 (Research TU/e / Graduation TU/e), Electrical Engineering]. Technische Universiteit Eindhoven.
<https://doi.org/10.6100/IR590723>

DOI:

[10.6100/IR590723](https://doi.org/10.6100/IR590723)

Document status and date:

Published: 01/01/2005

Document Version:

Publisher's PDF, also known as Version of Record (includes final page, issue and volume numbers)

Please check the document version of this publication:

- A submitted manuscript is the version of the article upon submission and before peer-review. There can be important differences between the submitted version and the official published version of record. People interested in the research are advised to contact the author for the final version of the publication, or visit the DOI to the publisher's website.
- The final author version and the galley proof are versions of the publication after peer review.
- The final published version features the final layout of the paper including the volume, issue and page numbers.

[Link to publication](#)

General rights

Copyright and moral rights for the publications made accessible in the public portal are retained by the authors and/or other copyright owners and it is a condition of accessing publications that users recognise and abide by the legal requirements associated with these rights.

- Users may download and print one copy of any publication from the public portal for the purpose of private study or research.
- You may not further distribute the material or use it for any profit-making activity or commercial gain
- You may freely distribute the URL identifying the publication in the public portal.

If the publication is distributed under the terms of Article 25fa of the Dutch Copyright Act, indicated by the "Taverne" license above, please follow below link for the End User Agreement:

www.tue.nl/taverne

Take down policy

If you believe that this document breaches copyright please contact us at:

openaccess@tue.nl

providing details and we will investigate your claim.

**Parameter Tuning and Cooperative Control
for
Automated Guided Vehicles**



This Ph.D. project was carried out in cooperation with FROG Navigation Systems B.V. (Utrecht, The Netherlands).



This dissertation has been completed in partial fulfillment of the requirements of the Dutch Institute of Systems and Control DISC for graduate study.



This research is supported by the Technology Foundation STW, applied science division of NWO and the technology programme of the Ministry of Economic Affairs.

CIP-DATA LIBRARY TECHNISCHE UNIVERSITEIT EINDHOVEN

Stouten, Bart

Parameter tuning and cooperative control for automated guided vehicles / by Bart Stouten. – Eindhoven : Technische Universiteit Eindhoven, 2005.

Proefschrift. – ISBN 90–386–1703–8

NUR 977

Trefw.: geautomatiseerde transportmiddelen / nietlineaire regelsystemen ; parameterschatting / gedistribueerde regelsystemen / mobiele robots / parameteridentificatie.

Subject headings: automatic guided vehicles / parameter estimation / distributed control / mobile robots / multi-robot systems.

Copyright ©2005 by Bart Stouten

Printed by Universiteitsdrukkerij TU Eindhoven, Eindhoven, The Netherlands.

Parameter Tuning and Cooperative Control for Automated Guided Vehicles

PROEFSCHRIFT

ter verkrijging van de graad van doctor aan de
Technische Universiteit Eindhoven, op gezag van de
Rector Magnificus, prof.dr.ir. C.J. van Duijn, voor een
commissie aangewezen door het College voor
Promoties in het openbaar te verdedigen
op donderdag 26 mei 2005 om 16.00 uur

door

Bart Stouten

geboren te Uden

Dit proefschrift is goedgekeurd door de promotor:

prof.dr.ir. P.P.J. van den Bosch

Copromotoren:

dr.ir. A.J. de Graaf

en

dr.ir. A.A.H. Damen

Abstract

For several practical control engineering applications it is desirable that multiple systems can operate independently as well as in cooperation with each other. Especially when the transition between individual and cooperative behavior and vice versa can be carried out easily, this results in flexible and scalable systems. A subclass is formed by systems that are physically separated during individual operation, and very tightly coupled during cooperative operation.

One particular application of multiple systems that can operate independently as well as in concert with each other is the cooperative transportation of a large object by multiple Automated Guided Vehicles (AGVs). AGVs are used in industry to transport all kinds of goods, ranging from small trays of compact and video discs to pallets and 40-tonne coils of steel. Current applications typically comprise a fleet of AGVs, and the vehicles transport products on an individual basis. Recently there has been an increasing demand to transport very large objects such as sewer pipes, rotor blades of wind turbines and pieces of scenery for theaters, which may reach lengths of over thirty meters. A realistic option is to let several AGVs operate together to handle these types of loads.

This Ph.D. thesis describes the development, implementation, and testing of distributed control algorithms for transporting a load by two or more Automated Guided Vehicles in industrial environments. We focused on the situations where the load is connected to the AGVs by means of (semi-)rigid interconnections. Attention was restricted to control on the velocity level, which we regard as an intermediate step for achieving fully automatic operation. In our setup the motion setpoint is provided by an external host. The load is assumed to be already present on the vehicles. Docking and grasping procedures are not considered. The project is a collaboration between the company FROG Navigation Systems (Utrecht, The Netherlands) and the Control Systems group of the Technische Universiteit Eindhoven. FROG provided testing facilities including two omni-directional AGVs.

Industrial AGVs are custom made for the transportation tasks at hand and come in a variety of forms. To reduce development times it is desirable to follow a model-based control design approach as this allows generalization to a broad class of vehicles. We have adopted rigid body modeling techniques from the field of robotic manipulators to derive the equations of motion for the AGVs and load in a systematic way. These models are based on physical considerations such as Newton's second law and the positions and dimensions of the wheels, sensors, and actuators. Special emphasis is put on the modeling of the wheel-floor interaction, for which we have adopted tire models that stem from the field of vehicle dynamics. The resulting models have a clear physical interpretation and capture a large class of vehicles with arbitrary wheel configurations. This ensures us that the controllers, which are based on these models, are applicable to a broad class of vehicles.

An important prerequisite for achieving smooth cooperative behavior is that the individual AGVs operate at the required accuracy. The performance of an individual AGV is directly related to the precision of the estimates for the odometric parameters, i.e. the effective wheel diameters and the offsets of the encoders that measure the steering angles of the wheels.

Cooperative transportation applications will typically require AGVs that are highly maneuverable, which means that all the wheels of an individual AGV should be able to steer. Since there will be more than one steering angle encoder, the identification of the odometric parameters is substantially more difficult for these omni-directional AGVs than for the mobile wheeled robots that are commonly seen in literature and laboratory settings. In this thesis we present a novel procedure for simultaneously estimating effective wheel diameters and steering angle encoder offsets by driving several pure circle segments. The validity of the tuning procedure is confirmed by experiments with the two omni-directional test vehicles with varying loads. An interesting result is that the effective wheel diameters of the rubber wheels of our AGVs increase with increasing load.

A crucial aspect in all control designs is the reconstruction of the to-be-controlled variables from measurement data. Our to-be-controlled variables are the planar motion of the load and the motions of the AGVs with respect to the load, which have to be reconstructed from the odometric sensor information. The odometric sensor information consists of the drive encoder and steering encoder readings. We analyzed the observability of an individual AGV and proved that it is theoretically possible to reconstruct its complete motion from the odometric measurements. Due to practical considerations, we pursued a more pragmatic least-squares based observer design. We show that the least-squares based motion estimate is independent of the coordinate system that is being used. The motion estimator was subsequently analyzed in a stochastic setting. The relation between the motion estimator and the estimated velocity of an arbitrary point on the vehicle was explored. We derived how the covariance of the velocity estimate of an arbitrary point on the vehicle is related to the covariance of the motion estimate. We proved that there is one unique point on the vehicle for which the covariance of the estimated velocity is minimal. Next, we investigated how the local motion estimates of the individual AGVs can be combined to yield one global estimate. When the load and AGVs are rigidly interconnected, it suffices that each AGV broadcasts its local motion estimate and receives the estimates of the other AGVs. When the load is semi-rigidly interconnected to the AGVs, e.g. by means of revolute or prismatic joints, then generally each AGV needs to broadcast the corresponding information matrix as well. We showed that the information matrix remains constant when the load is connected to the AGV with a revolute joint that is mounted at the aforementioned unique point with the smallest velocity estimate covariance. This means that the corresponding AGV does not have to broadcast its information matrix for this special situation.

The key issue in the control design for cooperative transportation tasks is that the various AGVs must not counteract each others' actions. The decentralized controller that we derived makes the AGVs track an externally provided planar motion setpoint while minimizing the interconnection forces between the load and the vehicles. Although the control design is applicable to cooperative transportation by multiple AGVs with arbitrary semi-rigid AGV-load interconnections, it is noteworthy that a particularly elegant solution arises when all interconnections are completely rigid. Then the derived local controllers have the same structure as the controllers that are normally used for individual operation. As a result, changing a few parameter settings and providing the AGVs with identical setpoints is all that is required to achieve cooperative behavior on the velocity level for this situation.

The observer and controller designs for the case that the AGVs are completely rigidly interconnected to the load were successfully implemented on the two test vehicles. Experi-

ments were carried out with and without a load that consisted of a pallet with 300 kg pave stones. The results were reproducible and illustrated the practical validity of the observer and controller designs. There were no substantial drawbacks when the local observers used only their local sensor information, which means that our setup can also operate satisfactory when the velocity estimates are not shared with the other vehicles.

Contents

Abstract	5
1 Introduction	13
1.1 Cooperating systems	13
1.2 Project description	14
1.2.1 Partners	15
1.2.2 Problem statement	15
1.3 Related work	15
1.3.1 Traditional robotics and industry	16
1.3.2 Artificial Intelligence and mobile robotic agents	17
1.3.3 Cooperative transportation by multiple robots	17
1.3.4 Issues in cooperative transportation studies	19
1.3.5 Positioning of this work	20
1.4 Methods	21
1.4.1 Design methodology	22
1.4.2 Centralized versus decentralized control	23
1.4.3 AGV-load interaction	23
1.4.4 Setpoint	23
1.4.5 Communication media	23
1.4.6 Number of AGVs	23
1.5 Scope	24
1.6 Outline	24
2 Experimental setup	27
2.1 Background	27
2.2 Description of the setup	28
2.2.1 Hardware	28
2.2.2 Software	30
2.3 Summary	32
3 Model	35
3.1 Introduction	35
3.2 Related work	35
3.2.1 Wheeled mobile robots	36
3.2.2 Vehicle dynamics	36
3.2.3 Tire models	37
3.3 Kinematics	38
3.3.1 Relative position	38
3.3.2 Relative velocity	40
3.3.3 Steering pole	44

3.3.4	Signed radius, side slip angle and tangential velocity	44
3.3.5	Numerical integration of twists	46
3.4	Dynamics	50
3.4.1	Acceleration	50
3.4.2	Acceleration and gravity	51
3.4.3	Equations of motion	52
3.5	Wheel model	55
3.5.1	Kinematics	55
3.5.2	Constitutive equations	56
3.5.3	Additional assumptions for OLS vehicles	58
3.6	Model of a single AGV that is affine in the inputs	60
3.6.1	Traditional methods	61
3.6.2	Kinematic steering angle	61
3.6.3	Approximation based on the momentary twist	62
3.7	Model of the interconnected system	65
3.7.1	Equation of motion for the load	65
3.7.2	Interconnections	65
3.7.3	Equations of motion for the interconnected system	67
4	Tuning	71
4.1	Introduction	71
4.2	Related work	72
4.2.1	Wheeled mobile robots	72
4.2.2	Positioning of our work	74
4.3	Procedure	75
4.4	Estimation of the circular trajectory	77
4.4.1	Radial residuals	78
4.4.2	Tangential residuals	81
4.4.3	Nonlinear least-squares estimator	83
4.5	Calculation of steering angle encoder offset and effective wheel radius	83
4.5.1	Kinematic steering angle and signed radius of the wheel center	84
4.5.2	Steering encoder offsets and effective wheel radius	85
4.6	Experimental results	86
4.6.1	General issues and a priori parameter settings	86
4.6.2	Low speed experiments	88
4.6.3	Medium speed experiments with various loads	95
4.7	Concluding remarks and discussion	101
5	Observer	103
5.1	Introduction	103
5.2	Related work	103
5.2.1	Vehicle dynamics	104
5.2.2	Positioning of our work	106
5.3	Observability	107
5.3.1	Local observability	109

5.3.2	Practical considerations	111
5.4	Least-squares observer for a single AGV	112
5.4.1	Description of the observer	112
5.4.2	Stochastic interpretation	115
5.4.3	Velocity estimate for an arbitrary point on the AGV	118
5.4.4	Example	122
5.5	Least-squares observer for multiple AGVs transporting a common load	126
5.5.1	Centralized observer design	126
5.5.2	Distributed implementation	130
5.5.3	Examples where the amount of information sharing can be reduced	132
5.6	Concluding remarks and discussion	134
6	Control	137
6.1	Introduction	137
6.2	Related work	137
6.2.1	Automated Guided Vehicle control	138
6.2.2	Vehicle dynamics control	138
6.2.3	Cooperative transportation	140
6.2.4	Positioning of our work	141
6.3	Velocity controller for a single AGV	142
6.3.1	Desired behavior	143
6.3.2	Velocity controller	144
6.3.3	Force distribution	145
6.4	Control for the cooperative system	146
6.4.1	Desired behavior	147
6.4.2	Velocity controller	149
6.4.3	Special case: completely rigid interconnections	153
6.5	Distributed central vehicle controller	154
6.6	Concluding remarks and discussion	156
7	Results	159
7.1	Introduction	159
7.2	Experimental setup	160
7.2.1	Hardware	160
7.2.2	Architecture	161
7.3	Parameter settings	164
7.3.1	Wheel parameters	164
7.3.2	Desired behavior	165
7.3.3	Observer	165
7.3.4	Controller	166
7.4	Experimental results	168
7.4.1	Setpoints	168
7.4.2	Realized trajectories	169
7.4.3	Integrated twist estimates	170
7.4.4	Twist tracking errors	171

7.5	Concluding remarks and discussion	173
8	Conclusion and recommendations	177
8.1	Concluding remarks	177
8.2	Recommendations	179
A	Minimization of the nonlinear least-squares tuning criterion	181
A.1	Introduction	181
A.2	Iterative procedure	182
A.2.1	Establish initial estimates for θ_r and β_v	182
A.2.2	Gauss-Newton method to estimate θ_r for given β_v	183
A.2.3	Establish initial estimates for θ_t	184
A.2.4	Gauss-Newton method to estimate θ_t for given θ_r	185
B	Additional figures for the medium speed tuning experiments with various loads	187
C	Nomenclature	189
C.1	Abbreviations	189
C.2	Greek symbols	189
C.3	Latin symbols	191
	Bibliography	195
	Acknowledgments	203
	Samenvatting	205
	Curriculum vitae	209

1

Introduction

1.1 Cooperating systems

For several practical control engineering applications it is desirable that multiple systems can operate independently as well as in cooperation with each other. Especially when the transition between individual and cooperative behavior and vice versa can be carried out easily, this results in flexible and scalable systems. A subclass is formed by systems that are physically separated during individual operation, and very tightly coupled during cooperative operation. One example is the use of multiple electrical generators to produce the power that is required by an electrical network. Each generator can work standalone, but they can also be connected to the same network to achieve output powers that they cannot achieve by themselves. Since the line frequency is the same for all generators, this introduces strong physical interconnections. In this example, the main argument for combining systems that can also operate independently is *scalability*.

Cooperating devices that are able to act independently are also found in systems where redundancy is essential to guarantee safe operation even in the presence of malfunctioning devices. Examples are complex processes such as aircraft control and the operation of chemical plants. A closer examination of such systems learns that redundancy is often already built-in at the device level. An example of a local device that is constructed with built-in redundancy is the front wheels' steering system of the Phileas. Phileas is a light-weight (multi-)articulated vehicle with all wheel steering that forms the heart of a new type of public transport that has been operational in and around the city of Eindhoven, The Netherlands, since the summer of 2004. By detecting magnetic markers that are buried in the road, the Phileas docks at bus stations very precisely and without any human intervention. Since the front wheel steering system is critical for safe operation, the front steering axle is equipped with two identical electrical motors. During normal operation the motors operate together. In case that one fails, the motor that is still working is able to carry out the steering task by itself. The main argument for using multiple motors in this example is to increase *reliability*. Note that there is a strong physical interaction between the devices, and that the capacity of the system during normal operation is larger than required.

Intuitively, a necessary condition for achieving cooperative behavior in physically interconnected systems is that all systems share a common goal. Two people that are riding a tandem bicycle should have similar desired speeds in mind to achieve coherent operation. Carrying a large table with several people does only make sense when all intend to move it to the same spot. Although the global intention should be the same, there is still room for some flexibility in the behavior of the individual members. In the tandem bicycle example it is often desirable that the pedaling force is distributed evenly according to the cyclists' capacities.

From a pure individualistic point of view it may be beneficial to let the other person do all the work. However, when fulfilling the common task takes precedence over satisfying individual objectives, then it is only natural that a fair distribution of the required effort among the members will result in a much better performance.

In a few situations it can be an advantage when multiple connected systems exert opposing efforts on the object by which they are interconnected. Although there will be no net movement if one person pushes and the other one pulls the table, they can exploit the forces they feel to infer information about the intentions of the other individual. People who are carrying a table together often share messages like ‘I prefer to proceed a little bit slower’ by using the table as an implicit communication channel. Since opposing efforts such as internal forces result in power dissipation that does not contribute to executing the cooperative task, it is generally desirable to restrict those to a minimum.

Another aspect that deserves attention is the influence of measurement errors on the execution of the cooperative task. Modern control systems rely on measurements to reconstruct the variables that represent the processes they aim to control. Measurement errors, which are always present, result in a biased observation of the truth. Even for systems that were designed to be identical, measurements will vary from one system to another due to production tolerances and random measurement noises. Hence, when several interconnected systems individually reconstruct a common process from their local measurements only, then each system will have its own version of reality. Since the local versions will always differ due to the measurement errors, it is impossible to make them all identical to the desired situation. Therefore, the local systems should not try to realize the desired situation exactly to avoid opposing goals that result in large control actions.

1.2 Project description

This thesis focuses on the control of one particular application of multiple systems that can operate independently as well as in cooperation with each other, namely the cooperative transportation of a large object by multiple Automated Guided Vehicles (AGVs). AGVs are used in industry to transport all kinds of goods, ranging from small trays of compact and video discs to pallets and 40-tonne coils of steel. Current applications typically comprise a fleet of AGVs, and the vehicles transport products on an individual basis. Recently there has been an increasing demand to transport very large objects such as sewer pipes, rotor blades of wind turbines and pieces of scenery for theaters, which may reach lengths of over thirty meters. A realistic option is to let several AGVs operate together to handle these types of loads, instead of one unique, complex and cost inefficient vehicle with long and unpredictable development times.

Combining several AGVs makes it possible to transport larger loads than that each individual vehicle is capable of, thus the main reasons for using multiple vehicles are scalability and flexibility rather than improved robustness. The common goal for the cooperative task is typically provided by an external reference, for example the plant manager who wants to transport a load to a certain point in the factory according to a prescribed path. The AGVs’ motions are reconstructed from encoder data of the wheel and steering encoders. Since the encoder readings are affected by the slip between the wheels and the ground, it is important

to gain insight in these phenomena for understanding the accuracy of the motion estimates. Although the main focus of this thesis is cooperative transportation by multiple AGVs, some of the ideas can be applied to other mechanical systems that are rigidly interconnected.

1.2.1 Partners

The project is a cooperation between FROG Navigation Systems B.V. (Utrecht, The Netherlands) and the Control Systems group of the Department of Electrical Engineering of the Eindhoven University of Technology (Eindhoven, The Netherlands). FROG Navigation Systems is a company that develops and markets Automated Guided Vehicle Systems and navigation hard- and software. Applications range from industrial AGVs to automated people movers. The aim of the Control Systems group is to control dynamic physical systems. The group is actively co-developing the fundamentals of control engineering, namely system and control theory. This research is supported by the Technology Foundation STW, applied science division of NWO and the technology programme of the Ministry of Economic Affairs.

1.2.2 Problem statement

There exists a lot of knowledge on the control of (fleets of) individually operating AGVs. In this thesis we investigate what extensions are required to let multiple AGVs transport a single load in cooperation with each other. The strong physical interactions between the AGVs and the common load make this problem harder than the control of a fleet of physically separated AGVs, because in the latter case the individual AGVs do not influence each other's motions. We are particularly interested in developing distributed control solutions for the cooperative transportation task, where the local controllers for achieving cooperative behavior are extensions of the controllers that are normally used for individual AGV operation.

We focus on the situation that the motion setpoint for the load and the AGVs is provided by an external host, which can be a computer or a human operator. The load is assumed to be already present on the vehicles, and therefore docking and grasping procedures are not considered. Furthermore, the load is assumed to be (semi-)rigidly connected to the AGVs, e.g. by means of revolute joints, slider joints, or fully rigid interconnections.

1.3 Related work

Studies on multiple AGVs that transport a load in coordination can be classified as research on *mobile multi-robot systems*. Research on mobile multi-robot systems is a relatively new area. Coordination and interactions of multiple intelligent software agents have been studied in the field of Distributed Artificial Intelligence (DAI) since the early 1970s [24]. Early work on multiple industrial manipulators handling a single object in coordination started around the same time (e.g. [88]). With the availability of affordable robotic components and fast hardware, the field of multiple mobile robot systems exhibiting cooperative behavior suddenly became very active in the mid 1980s. Whereas the first research concerned small groups of mobile robots, currently the field is moving toward miniaturization, distributed control, and larger groups of robots [11].

Furthermore, research on mobile multi-robot systems is a very broad field and covers all aspects of robotics. An extensive survey of the cooperative mobile robotics literature up to the mid 1990s was published by Cao *et al.* [24]. Other reviews and taxonomies (collection of axes) to classify multi-robot systems research include the studies by Dudek *et al.* [34], Stone *et al.* [111], Iochi *et al.* [58], Parker *et al.* [95], and the book by Liu and Wu [73]. Some prefer to classify research by characteristics of the domain, whereas others favor categorization according to the properties of the individual robots [58], or the principal topic areas that have generated significant levels of study [95]. Key issues in multi-robot systems research are homogenous versus heterogeneous robot teams, centralized versus distributed approaches, loosely coupled versus tightly coupled tasks, ensemble versus individual performance, known versus unknown environments, and no communication versus extensive information sharing [11, 111]. Prototypical tasks for multi-robot systems are foraging (e.g. retrieval, i.e. searching and returning certain lost objects), consuming (e.g. mine-clearing), grazing (e.g. reconnaissance of a certain terrain), formations/flocking, and object transport [11].

The design of a mobile multi-robot system for commercial applications requires cooperation of scientists of various disciplines. It is characteristic for scientific research to focus on one particular aspect of multi-robot cooperation, for example path planning, self localization and mapping (SLAM), hardware development, etc. When studying the literature, it appears that the techniques used to resolve these issues either stem from the field of traditional robotics or the field of Artificial Intelligence (AI).

1.3.1 Traditional robotics and industry

The first industrial robots became available in the 1960s, marking a new era in the history of industrial automation [10, 44, 79, 87]. The most important form of the industrial robot is the mechanical manipulator. They are especially known from their welding, spray painting and assembly tasks in the highly automated assembly lines of the automotive industries. To increase the speed and accuracy while at the same time reducing costs, a vast amount of research has been carried out to model, control and design these devices. The models used for control typically consist of a set of differential equations based on Newton's second law. These models describe the dynamical behavior of the manipulator in response to external forces. The field of industrial manipulators is one of the most prominent fields where advanced, model based nonlinear control algorithms are generally accepted and implemented in practice. A key feature of industrial manipulators is that they perform relatively simple, repetitive tasks in a manufacturing-oriented environment.

Traditional industrial manipulators are rigidly attached to the ground. Some have suggested to mount the manipulators and other parts of factories on mobile wheeled bases to increase the reconfigurability of assembly lines. When the mobile bases can be clustered in various configurations automatically, this makes it possible to realize specific work stations for the task at hand. One example of a study that analyzed the technical feasibility of such a concept is the MART-project [32].

Another technique to improve the reconfigurability of factories is by introducing AGVs to transport goods. The first AGVs were developed in the early 1950s by Barrett Electronics in the USA. The first system was installed in 1954 at Mercury Motor Freight in Columbia, South

Caroline [52]. Originally the movement of the AGVs was restricted to paths that were defined by white lines on the floor or electrical wires in the ground. In the end of the 1980s, FROG Navigation Systems introduced AGV navigation based on two dimensional grids defined by e.g. colored tiles on the floor, allowing for more flexibility in the definition of paths [120]. Nowadays a popular method to define the grid is by placing magnetic markers at regular intervals in the ground. In modern applications, AGVs run day and night, transport loads up to 40,000 kg, and some can even use elevators to switch floors.

1.3.2 Artificial Intelligence and mobile robotic agents

An aspect often associated with robotics but that has been less relevant for industrial robots is intelligence. The study and development of intelligent systems finds its roots in Artificial Intelligence (AI), which deals amongst others with perception of dynamically changing environments, reasoning about intentions and goals, learning new behaviors, understanding natural languages, decision making, and deliberate interaction with the environment. Systems that exhibit one or more of these properties are often referred to as intelligent agents. Intelligent software agents consist of software only, whereas robotic agents are part of the physical world and can really interact with it and move around. Robotic agents come in a variety of forms, including snake-like designs, legged versions, humanoids and wheeled systems.

The birth of Artificial Intelligence as a distinct field is generally associated with the Dartmouth Summer Research Conference the summer conference held in August 1955 [10]. Originally, AI focused on using symbolic reasoning to achieve intelligence behavior. When several decades of research had not yielded satisfactory results in the mid 1980s, some scientists started to criticize the symbolic AI paradigm and started exploring alternative ways to realize intelligent behavior. One of the most important critics was Rodney Brooks. He proposed that intelligent behavior can be generated without the explicit representations and abstract reasoning of symbolic AI, and that intelligence is an emergent property of certain complex systems. Brooks illustrated his ideas by building systems based on his so-called subsumption architecture [22]. A subsumption architecture determines the behavior of the agent by weighing several –possibly competing– simple low level rules such as ‘turn left when detecting an obstacle’ and ‘turn right when you see the light to your right.’ The movement that was started by Rodney Brooks is referred to as behavior-based robotics. Due to the many similarities with the control mechanisms that are seen in small organisms such as ants and bugs, behavior-based roboticists are often inspired by biological systems.

1.3.3 Cooperative transportation by multiple robots

Cooperative transportation of objects by multiple mobile robots has been extensively described in literature since the 1990s. One of the earliest studies is the work by Hashimoto *et al.* [47, 48]. In that study, the authors introduce a hierarchical coordinative control scheme to cooperatively transport a common object. They illustrated their approach with simulation results and equipped a robot with a mechanically compliant coupler to demonstrate that it is capable to deliver the desired force for transporting the load. It is interesting to note that these authors propose to use commercially available industrial mobile robots, which they refer to as AGVs, for their transportation task.

Another early study that is often cited is the work by Stilwell *et al.* [109, 110]. They propose to use multiple mobile robots to collectively transport a single palletized load. Each robot is equipped with a local controller and a force sensor to distill information about the intentions of one specific robot that is designated to act as the leader. Stilwell *et al.* pointed out that albeit distributed load-bearing problems had been studied before in other areas such as multi-legged vehicles and multi-fingered grasping, all those approaches assume a centralized control structure to optimize applied forces. Stilwell *et al.* used the analogy with the transport of materials by ants to motivate that a decentralized scheme allows the transport system to reconfigure itself to handle loads of varying size and shape, and to replace malfunctioning robots.

Whereas Stilwell *et al.*'s work was a simulation study and Hashimoto *et al.* used only one AGV to demonstrate the force generation capabilities of their setup, around the same time various research groups started examining cooperative transportation with physical robot teams that handled real objects.

Box-pushing

An interesting transportation task that has received a fair amount of attention in literature is the so-called box-pushing problem. Parker used this prototypical task to illustrate the validity of her behavior-based ALLIANCE architecture for heterogeneous robots. She demonstrated that a team consisting of two wheeled robots as well as a team consisting of one wheeled robot plus a six-legged robot were able to cooperatively push a box in a certain direction [94]. Rus *et al.* describe how coordinated pushing robots can be used to reorient a couch [104]. Mataric *et al.* successfully managed to let two six-legged walking robots push an elongated box towards a goal [76]. The reader is referred to the articles by Cao *et al.* [24] and Mataric *et al.* [76] for a more complete description of the earlier work on physical experiments related to the box-pushing problem.

Transport of objects without floor contact

To reduce friction and consequently avoiding damage to the floor and the object, for some transportation tasks it is preferred that the object is not in contact with the ground during transportation. In other words, it is carried instead of pushed. The literature overview presented below illustrates the diversity in multiple mobile robot transportation studies.

Ahmadabadi *et al.* propose to divide a multi-robot team in two groups. One group constrains the object in the directions in which it should not move, and the other group moves the object in the unconstrained direction [2]. Their ideas were illustrated with a group of four wheeled robots that were each equipped with a lifting mechanism. Lacroix *et al.* experimented with two car-like robots with servomotor-actuated forklifts to transport a long beam [68] to a goal. The position and orientation of the beam with respect to the vehicles is derived from the images of the CCD cameras that are present on the vehicles. Asahiro *et al.* present a distributed control algorithm for transporting a ladder by two omni-directional mobile robots through a corridor [13, 12]. Due to oscillations originating from force sensor information in combination with a rigid attachment of the ladder to the robots, the authors decided to introduce additional flexibility in the interconnection of the ladder to the robots.

Kosuge *et al.* proposed a *leader-follower* based scheme where the leader generates the main effort to move a load along a prescribed trajectory, and the follower robots act like virtual caster wheels [66]. Their decentralized control algorithm was implemented on a team of two tracked mobile robots that were equipped with a force sensor and held the object through a free joint. Hirata *et al.* extended the algorithm to handle objects in 3D, and implemented it on two robots with omni-directional wheels and two arm-like manipulators to transport a plate [51]. Miyata *et al.* performed experiments with four car-like wheeled robots that grasped an object using their compliant grasping mechanisms [81]. By deactivating their electro-magnetic placeholders, the robots are able to change their relative positions during transport. This is also known as regrasping the object. Trebi-Ollennu *et al.* describe a pair of wheeled MARS rovers that transport a long payload such as parts of a photovoltaic tent array [56, 119]. At the heart of the rovers is a distributed control architecture based on a multi-agent behavior-based methodology, and the robots are equipped with compliant grippers that are controlled by local PD controllers. Tang *et al.* examined a decentralized kinematic control scheme for multiple differentially driven wheeled mobile robots [118]. Their robots use relatively large end effectors that can rotate around a revolute joint. Sugar *et al.* carried out experiments with two mobile platforms that were each equipped with a dedicated forklift manipulator [116]. They used a leader-follower based scheme, where the leader plans a desired trajectory and the followers retain a desired formation with respect to the leader. The object is not rigidly grasped, but instead clamped between the manipulators of the two robots. As a last example, Bicho *et al.* describe experiments with two mobile robots that carry a long beam using an algorithm that is based on so-called attractor dynamics [17, 18, 107]. The robots, which had no force/torque sensors and were equipped solely with low-level ultrasonic sensors and sensors to measure the position of the load with respect to the vehicles, were able to carry the object indoors while avoiding obstacles in a relatively cluttered environment.

1.3.4 Issues in cooperative transportation studies

Although the literature survey above is far from complete, it does illustrate the variety of studies on the multiple mobile robot transportation task. All studies above make use of real physical robots. Some teams consist of identical robots, whereas other teams are a collection of heterogeneous members. Mobility of the robots is achieved by legs, differentially driven tracks, differentially driven wheels, omni-directional wheels, and wheels in a car-like configuration. Mechanisms for holding the to-be-transported objects range from dedicated arms that resemble industrial manipulators to electro-magnetic placeholders and configurations where the object is ‘squeezed’ between two robots. The to-be-transported objects themselves include boxes, furniture, ladders, beams, pallets, and even space mission related objects. The trend is to study situations where the communication is fairly limited, and to focus on decentralized/distributed control approaches. All experimental studies above consider teams of maximal four robots. Therefore, most studied transportation tasks are tightly coupled tasks because they cannot be accomplished when one of the team members fails. The box-pushing problem forms an exception. Parker showed in her experiments that the wheeled robot was still able to successfully move the box after its team member had been deactivated deliberately.

Industrial versus human-oriented environments

Although all transportation studies have in common that the objective is to transfer a load from some initial position to a designated goal, the path that is followed depends on the particular application that the researchers have in mind. For transportation in a relatively static, well known environment such as an industrial setting, the load and robots must typically follow a pre-specified trajectory. Since it is important that products arrive at the designated location at the specified time, the mobile robots must strictly adhere to their pre-planned routes. In human-oriented and less structured environments on the other hand, the main objective is to bring the load to the goal despite obstacles, possibly moving, that are encountered underway. Adequately reacting to dynamically changing situations is more important than fast transportation for this scenario. The differences between the industrial and the human-oriented settings are reflected in the techniques that are used to deal with these two scenarios. Industrial applications are more likely to borrow ideas from the field of traditional robotic manipulators, whereas robots that are deployed in human-oriented environments will typically employ behavior-based robotics strategies.

1.3.5 Positioning of this work

The work that is described in this thesis focuses on cooperative transportation in industrial environments. As the environment in such applications is rather static and well known, this work is more related to the field of traditional mechanical manipulators than to the field of Artificial Intelligence and behavior-based robotics. The path for the load is prescribed in the applications we consider. Attention is restricted to following a generalized velocity profile rather than a path. Later on it will become clear that this is in correspondence with the control architecture that is used by FROG, where achieving operation on the velocity level is seen as an intermediate step for realizing fully automatic operation. As was stated in the problem statement, the load is assumed to be present on the vehicles, and therefore docking and grasping procedures are not considered.

In correspondence with the literature that has been discussed so far, we believe it is important to perform real experiments. Two AGVs that were designed to be identical in hardware were available for experimentation. They will be introduced in more detail in Chapter 2. Compared to the mobile robots described in the literature, the AGVs we used are quite heavy (200 kg each) and can move reasonably fast (the maximum speed was limited to 1 m/s for safety reasons). The load we used was not large in size, but it was heavy (300 kg) compared to the other studies. We will focus on a decentralized/distributed control strategy approach. Furthermore, we focus on (semi-)rigid AGV-load interconnections. This is in contrast with most cooperative transportation literature, where the load is typically held by some compliant mechanism. We will not use force/torque sensors. In order to position very large objects accurately, it is natural that the AGVs are designed such that they are omni-directional, i.e. can move in any direction. Thus constraints introduced by car-like vehicles are not an issue in this study. Finally, we will incorporate tire models that describe the relation between wheel slip and tire forces. So our AGV models are more related to what is seen in the automotive literature than in kinematic mobile robot studies. An extended motivation of these choices is presented in the next section.

1.4 Methods

There is a noticeable difference between the aims of research in industry and research that is performed at academic institutions. The focus of industrial research is to develop techniques that can be used directly to design new or to improve existing products. In contrast, academic research targets to produce general theory that covers a large class of problems and systems. Even when the knowledge that arises from academic research is implemented on a real test setup to prove the validity of the developed concepts, then the step to a commercial application is generally quite large. For fundamental academic research this is of course no problem as the main issue is to unveil the mysteries of nature rather than to generate commercial products. However, nowadays academic research in the applied sciences is often sponsored by companies directly, or by governmental bodies that aim to stimulate the transfer of knowledge from universities to industry. For such research it is desirable that newly developed techniques can find their way to practical applications quite easily.

The discrepancy between scientific literature and commercial applications is particularly present in the field of (multiple) mobile robots. Despite an impressive amount of scientific literature on for example Artificial Intelligence and mobile robots, commercially successful robot systems remain few [65]. Perhaps the most commercially successful robotic AI application is the SONY Aibo entertainment robot dog. An important example where academic research did result in nice demonstrations but not in practical, commercially available products is the PATH project on Automated Highway Systems (AHS) in the USA. PATH is a collaboration between the California Department of Transportation (Caltrans), the University of California, other public and private academic institutions, and private industry. Although the demonstrations showed satisfactory results, practical issues relating to the robustness, safety and acceptability of such a large system prohibit it from being implemented in the near future. The lack of practical applications recently resulted in reduction in funding, and as a result, the focus of the research performed at the involved academic institutions had to shift away from the full scale AHS application (Tomizuka, personal communication, Eindhoven, April 8, 2003).

Another illustrative example is the 320-kilometer Grand DARPA Challenge that was organized recently by the US Defense Advanced Research Projects Agency (DARPA). It received a considerable amount of attention in the popular media [67, 77, 99]. In this contest, mobile robots had to navigate and drive autonomously through the Mojave Desert. Goal was to pass the finish line within ten hours. None of the competitors came even close to reaching the finish. The robot that travelled the farthest was the modified Humvee from Carnegie Mellon University. It travelled a distance of 12 kilometers at an average speed of 36 kilometers before it got stuck on a rock. Although the contest was held in an extremely rough environment, one would expect that a team that spent 3 million dollars on equipment and which consists of more than 25 students as well as volunteers and experts from 30 corporations and organizations would do better than to travel for 20 minutes only. The DARPA challenge clearly showed that the individual robots developed by academic institutions are far from reliable and there is a long way to go to produce real-life applications. This makes one wonder about the reliability of systems that consist of multiple cooperating robots instead of single robots. It is often argued that using multiple robots introduces redundancy in the system, and that a task can still be performed even when one or more robots fail. However, when we are in the

situation that *none* of the robots is reliable enough to complete the task at hand, as was e.g. seen in the DARPA Challenge, then adding more unreliable robots will not solve this.

Although it is not the aim or responsibility for universities to develop commercial products, interesting industry and helping them to benefit from the developed techniques would certainly help to secure future funding. In turn, industry can help academic research to retain a down to earth view on the applicability of their research.

1.4.1 Design methodology

This project is carried out in close cooperation with FROG Navigation Systems. Therefore, additional requirements and limitations have been defined to increase the probability that this research will indeed result in commercially meaningful applications. The most important requirement is that the designed control algorithms can actually run on the computers and architectures used in FROG's industrial AGVs. The control design procedure that has been very popular at academic institutions can be summarized as

1. make mathematical models of the system;
2. use the models to design a control law;
3. test the controller in a simulation and/or hardware-in-the-loop environment;
4. if time and resources are available, try the controller on the real system.

Some caveats appear when this procedure is used to develop an industrial application. Usually a lot of time is spent on steps one to three before the controller is tested in reality. We have experienced more than once that controllers which performed satisfactory in simulation did not work on the real system because of modeling imperfections. Furthermore, as the goal of step four is to test the control algorithm, it is common to develop a small piece of real-time software for some dedicated digital signal processor (DSP) to implement the control law. The DSP typically executes the small test program and logs some data, but performs no other tasks. In contrast, industrial applications require a lot of overhead related to safety issues and communication with other hosts. Often it is far from trivial how the new control algorithm can be incorporated in an existing architecture. It takes a lot of effort to start with a small test program and evolve it into a robust industrial application.

To overcome these problems, we decided to use the current industrial AGV architecture and controller used by FROG as a starting point. Because we start with a working application, we can perform experiments and detect modeling errors at an early stage. The original architecture and control algorithm are extended and modified as needed to realize the desired cooperative behavior. Control algorithms are still designed using the four step methodology described before, but with the important restriction that the models and controllers fit into the current AGV architecture. Furthermore, new control algorithms are always incorporated in the full architecture required to constitute an industrial application and are never tested as standalone applications. Of course, for a final application additional safety loops and communication with operators need to be introduced, but this is a relatively small step compared to building an application from scratch. Drawback of this approach is that, since attention is restricted to controllers that fit into the existing AGV framework, more effective controllers may result if complete design freedom is allowed.

1.4.2 Centralized versus decentralized control

In the scenario we consider, the AGVs perform some tasks individually and other tasks in cooperation with each other. To prevent software restarts when switching from individual to cooperative mode, we aim at developing decentralized controllers for the cooperative tasks. We expect that with a decentralized solution it is easier to form new couples, for example if one AGV is under repair. Ideally, it suffices to change a few parameter settings in the control algorithm to go from individual to cooperative mode and vice versa.

1.4.3 AGV-load interaction

Current AGV controllers have been developed for individual operation. They do not take the external forces that result from the interconnection of several vehicles by a load into account. The inability to cope with interconnection forces is the main reason that the original controllers are extended. We decided to focus on the case that the load is (semi-)rigidly attached to the vehicles, e.g. by means of revolute joints, slider joints, or fully rigid interconnections. It seems realistic to assume (semi-)rigid connections for the transportation of large objects.

1.4.4 Setpoint

FROG uses a layered architecture for controlling their industrial AGVs. Such a layered approach makes it easy to define various operation modes. The control architecture will be discussed in more detail in Chapter 2. As mentioned before, operation on the velocity level is seen as an intermediate step for achieving fully automatic operation, and is for example used in manual operation mode where a human operator provides a setpoint with a joystick. Therefore, we will focus on tracking of a generalized velocity profile rather than a path. Automatic guidance can be achieved by adding an outer loop that translates position errors into velocity setpoints, that are subsequently realized by the velocity controller. Extensions to fully automatic operation are of later concern and beyond the scope of this thesis.

1.4.5 Communication media

Typical industrial AGVs can be connected to a wireless local area network (WLAN) and a controller area network (CAN). CAN is a serial broadcast type of network that is often used to facilitate the communication between sensors and electronic control units in passenger cars and trucks [57]. Attention is restricted to these two communication media.

1.4.6 Number of AGVs

From a theoretical point of view, we aim at control algorithms that can be generalized to an arbitrary number of AGVs. More AGVs will generally lead to more communication, and problems with the available bandwidth are expected when the number of AGVs increases beyond a certain point. Since most cooperative transportation tasks we consider can be performed by two to four AGVs, we do not explicitly take communication bandwidth problems arising from very large numbers of AGVs into account.

1.5 Scope

As we indicated in the problem statement that was presented in subsection 1.2.2, in this thesis we investigate what extensions are required to let multiple AGVs cooperatively transport a common load. We aim to develop *distributed control* solutions. Cooperative transportation applications require highly maneuverable AGVs that can move in every direction, otherwise it is not possible to move a long load through places where space is limited. We therefore focus on *omni-directional* AGVs. AGVs come in a variety of forms as they are tailored to the transportation task at hand. To be able to deal with a large class of AGVs in a systematic way, we follow a *model-based observer and control design* approach. In Chapter 3 we will see that we use *planar rigid body descriptions* to model the AGVs and the load, and the interaction between the wheels and the floor is described by *static, linear tire models*.

An important prerequisite for achieving smooth cooperative behavior is that the individual AGVs operate at the required accuracy. The accuracy at which the AGVs can operate is largely determined by the precision at which their odometric parameters are known, i.e. the accuracy of the effective wheel diameters and the offsets of the encoders that measure the wheels' steering angles. *Identification of the odometric parameters* is more complicated for our AGVs than for the simpler laboratory robots that are found in literature, since all the wheels of our AGVs are steerable to achieve omni-directionality. Therefore, we discuss a new experimental procedure to systematically identify the odometric parameters. Since the nominal parameter values are used as a starting value, we refer to this procedure as *tuning*.

For the control and observer design for the cooperative transportation task, we focus on cases where the *load is (semi-)rigidly attached to the AGVs*. This approach differs from mainstream literature, where the interconnections typically exhibit some compliant behavior. We feel that (semi-)rigid interconnections are more realistic than compliant mechanisms for transporting very large objects. Furthermore, in this thesis we focus on control at the velocity level, i.e. *the goal of the controller is to realize a certain planar velocity setpoint that is provided by an external host*. Control at the velocity level is an important intermediate step towards achieving fully automated operation. To achieve smooth cooperative behavior, the various AGVs *must not counteract each others actions*. Finally, we require that the AGVs are able to operate cooperatively as well as individually, and switching between these modes should be easy.

This project is carried out in close cooperation with the company FROG Navigation Systems. We are eager to develop control algorithms that will eventually result in industrially meaningful applications. Therefore, the *developed algorithms are implemented and evaluated on real industrial AGVs*. Two AGVs that were designed to be identical in hardware were provided by FROG. Although the experiments and parameter settings were adjusted to match these two specific test vehicles, the model-based design approach guarantees us that the ideas are generalizable to other load-AGV combinations.

1.6 Outline

The outline of this thesis is as follows. Chapter 2 introduces the vehicles that have been used for the experiments that are described in this thesis. It is intended to give a flavor of the

components that are used in industrial AGVs. Chapter 3 deals with the modeling of AGVs in general, and to the modeling of a system that consists of multiple AGVs that are semi-rigidly connected to a load in particular. Good operation requires accurate identification of the effective wheel diameters and the offsets of the steering angle encoders. The fine tuning of these parameters is handled in Chapter 4. Chapter 5 discusses a decentralized observer design for estimating the velocities of the load and the AGVs with respect to the floor. The relation between the accuracy of the identified parameters and the velocity estimate from the observer is analyzed. A distributed controller design for achieving cooperative behavior is presented in Chapter 6. Experiments with our two test vehicles that are cooperatively transporting a load are discussed in Chapter 7. Finally, Chapter 8 contains the conclusions and recommendations for future work.

Experimental setup

Testing facilities including two AGVs for performing experiments were provided by FROG Navigation Systems. Industrial AGVs are always part of a larger system. This chapter starts with some background on the various aspects of the AGV applications that are installed in factories. Subsequently, the AGVs that were available for experimentation are introduced and the peculiarities of these specific AGVs are highlighted. Because the observers and controllers that are developed in Chapters 5 and 6 will be tested on the software and control architecture that is used by FROG, a brief description of these is given towards the end of this chapter. The discussion of the required hardware adjustments for achieving cooperative transportation is postponed until Chapter 7, where the cooperative transportation experiments are presented. The two test vehicles that were used for the experiments are merely examples of industrial AGVs that could be used for a cooperative transportation task. It is remarked that the models, the tuning procedure, the observers, and the controllers that will be discussed in the subsequent chapters are also applicable to other industrial AGVs with different sensor and actuator configurations.

2.1 Background

From a plant manager's perspective, AGVs are nothing more than a mean to transport goods from one place in a factory to another. A plant operator is not really interested in the exact behavior of the vehicles, as long as they pick-up and deliver the products at the right times and at the right places. The route planning of the AGVs and the allocation of a specific AGV to a certain product transportation task are typically carried out by a dedicated supervisory system that is designed to control the entire fleet of AGVs. This supervisory system interacts with the plant manager and the control system of the factory, and translates their demands to routes and commands for the individual AGVs. Modern supervisory controllers communicate with the AGVs over wireless networks.

Each AGV has its own local computer to follow the routes that are received from the supervisory control system. It is the AGVs responsibility to keep track of its position. To this end, they are equipped with encoders that measure the angles of the steering systems and the rotation of the wheels. Since this so-called odometric data provides only position information relative to the previous measurement, the AGVs are also equipped with a system that provides absolute position information. These absolute measurement systems rely on the detection of for example colored tiles, transponders in the floor, reflectors on the walls, magnets that are placed at known positions, etc. Furthermore, the vehicles have sensors such as flexible bumpers with contact switches and SICK laser range finders to avoid running into obstacles that may have inadvertently blocked the pre-planned routes. The devices for

loading and unloading the goods depend on the types of products, and include for example roller conveyer belts and electric lifting mechanisms. Other important components that are present on all industrial AGVs are the batteries and mechanisms for recharging them, controls for manual operation, and emergency buttons.

For more background information on Automated Guided Vehicle Systems, the reader is referred to the books by Müller [86], Hammond [45], and Hollier [53], and the proceedings of the International Conferences on Automated Guided Vehicle Systems.

2.2 Description of the setup

In the previous section we have seen how the AGV is part of a larger transportation system. In this section we will focus on the hardware and the software of the test vehicles. The necessary adjustments for achieving cooperative operation are discussed to Chapter 7, where the experiments are presented.

2.2.1 Hardware

A photograph of the two AGVs that were used for the experiments is depicted in Figure 2.1. They are part of a set of four identical AGVs that were designed for the so-called OLS project. Goal of the OLS project was to investigate the feasibility of an underground logistic system between Schiphol Airport, Aalsmeer flower auction and a railterminal at Hoofddorp for transporting flowers and time critical cargo. The four AGVs were in fact 1:5 scale models of vehicles that would be used in a final application. Due to these origins, the AGVs are also referred to as the OLS 1:5 vehicles. After the project had been concluded with a successful demonstration several years ago, two of the vehicles went to the Delft University of Technology and the other two to FROG Navigation Systems. The left AGV in Figure 2.1 is the OLS 1, and the vehicle on the right is the OLS 2. The OLS 2 has been extensively used to develop and test the latest major revision of FROG's control software.



Figure 2.1: The two OLS 1:5 AGVs in the hall of FROG Navigation Systems. The left vehicle is the OLS 1, and the right vehicle is the OLS 2.

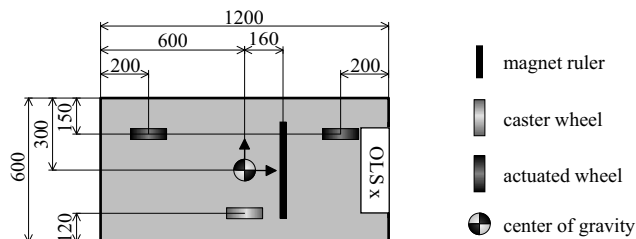


Figure 2.2: Schematic representation of a single OLS 1:5 AGV (dimensions in mm). The wheels are depicted in their neutral steering positions.

Figure 2.2 sketches a schematic representation of a single OLS 1:5 AGV. The vehicle weighs about 200 kg and has a moment of inertia of approximately $50 \text{ kg}\cdot\text{m}^2$. The AGV has three wheels. The wheel on the middle right is a swivel caster wheel that can rotate freely. The other two wheels are part of standard Schabmuller units that have been installed on the front left and rear left of the AGV. Each Schabmuller unit features a wheel, an electric drive system, an electric steering system, an on/off type of brake, and optical encoders to measure the wheel's rotational velocity and steering angle. The resolution of the steering encoder is 17.46 counts per degree steering angle, and the resolution of the drive encoder equals 11.00 per degree rotation of the wheel. The drive system can exert forces up to $\pm 375 \text{ N}$ on the floor. The steering angle range is approximately $\pm 85 \text{ deg}$, and is determined by means of limit switches. The large steering angles make the AGV highly maneuverable, such that it can for example move sideways. Figure 2.2 depicts the neutral steering positions of the wheels. The AGV is powered by two 12 V batteries.

The configuration of the wheels is rather unusual. Ordinary AGVs for transporting light products typically have a car-like configuration with an un-actuated fixed axis at the rear, and a single actuated wheel unit for steering and propulsion at the front. AGVs for transporting larger and heavier loads in narrow spaces may feature all wheel steering to improve maneuverability, but even for those more exotic AGVs are usually symmetrical with respect to the longitudinal vehicle axis. The actuated wheels of the OLS AGV have been deliberately placed asymmetrical with respect to the center of gravity to make the vehicle more difficult to control when accelerating and decelerating. This was done to test all aspects of AGV control. When the steering angles are fixed to 90 deg, then the AGV is similar to the differentially driven vehicles often seen in mobile robots literature. When the rear steering angle is fixed to the neutral steering position, than a car-like vehicle can be emulated. Because for positioning large objects it is only natural that the AGVs are omni-directional, in this project the full range of the steering system will be used.

Absolute position information for this AGV is provided by a magnet ruler can detect magnets that are buried in the floor. The magnets form staggered grid with a width of 80 cm, see Figure 2.3. The length of the magnet ruler is 40 cm, and its height above the floor is a few centimeters. The magnet ruler uses the measured magnetic field to determine when it is exactly above a magnet. At that time instance, the position of the detected magnet along the ruler is returned. From this information and the relative position of the magnet ruler with respect to the vehicle it is possible to determine the position of the vehicle with respect to the

detected magnet. Because the AGV has only a single magnet ruler that is also quite short, it is difficult to reconstruct the sideways movement for these two test AGVs. It is common to equip AGVs with multiple magnet rulers that are mounted perpendicular to each other to deal with sideways motions.

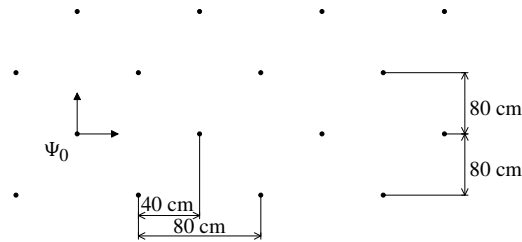


Figure 2.3: Layout of the magnet grid in the hall of FROG Navigation Systems (top view). The magnet which origin coincides with the floor coordinate system Ψ_0 defines the $(0, 0)$ coordinate on the floor.

A control panel is mounted on the rear of the AGV. The control panel contains a joystick, a key switch for selecting manual or automatic operation mode, a serial port for communicating with the computer, a light that indicates that the AGV is on, and a button that can be configured for various purposes in the software. For safety, the AGV features two emergency stops and bumpers with contact switches.

Each AGV is equipped with its own Frogbox (a robust industrial PC with local I/O for AGV applications) with a Pentium I 166 MHz processor, 64 MB ram, and 92 MB flash disk. The operating system is Linux. A wireless local area network connection, serial ports, and a controller area network (CAN) interface [57] are available for communication. For additional analysis purposes, an Toshiba Satellite Pro 4300 series Windows 2000 laptop with Vector CANalyzer or I+ME PCMCIA Key is available to monitor CAN communication.

2.2.2 Software

In the main introduction we discussed that we aim to develop distributed control laws that can be seen as an extension of the controllers that are currently used for individual AGV operation. A block scheme of the control architecture that is present in FROG's current AGV controllers is depicted in Figure 2.4. We recognize a layered control structure with an inner velocity layer to control the velocity, and an outer control loop that controls the position.

The task of the *velocity layer* is to realize a certain planar velocity setpoint. As we will see in Chapter 3 about modeling, the planar velocity of the AGV with respect to the floor is also known as the *twist* of the AGV with respect to the floor. The planar velocity setpoint consists of the rotational, longitudinal and lateral velocity setpoints for a coordinate system Ψ_v that is attached to a special point P on the AGV. The velocity setpoint is compared to the velocity estimate that is derived from the odometric measurements of the AGV, i.e. its steer and wheel encoders readings. A velocity controller computes the generalized force, which consists of a torque, a longitudinal force, and lateral force, that should be exerted on the AGV to realize the desired behavior. The generalized force on the vehicle is also known as the *wrench* on

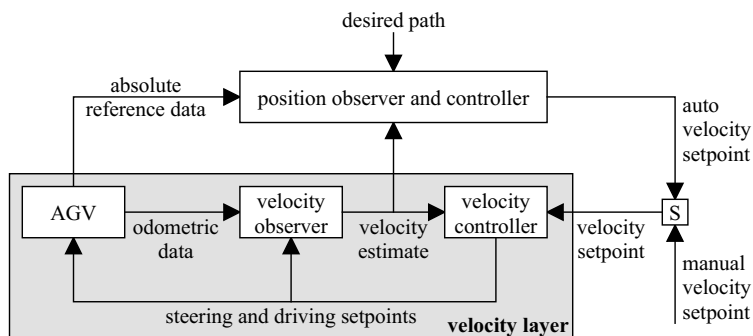


Figure 2.4: Block scheme of a standard AGV controller. The velocity controller forms the heart of the controller. The switch ‘S’ is used to select the operation mode of the AGV, which can be either manual or automatic. In manual mode, the velocity layer aims to realize the manual velocity setpoint that is provided by a human operator. In automatic mode, the velocity setpoint for the velocity layer is computed by the outer position control loop from the position error.

the vehicle. The desired generalized force that was computed by the velocity controller is distributed among the actuators. Since our AGVs have two steering actuators and two drive servo’s, they are *overactuated*. Thus there are multiple possibilities to select the setpoints for the steering and driving systems that will all result in the same net generalized force. To overcome this ambiguity, the steering and driving setpoints are chosen such that some norm of the tire forces is minimized. In subsection 6.2.2 of Chapter 6 on control, we will see that the control strategies that are applied in the velocity layer of the AGV controller are very similar to the strategies that are found in generic controllers that are used in modern vehicle dynamics control systems. In Chapter 5 that deals with observer design, it will become clear that the steering and driving setpoints are also passed to the observer to enhance the velocity estimate.

For industrial AGVs it is important to have a manual operation mode as well as an automatic operation mode. During manual operation, the setpoint for the velocity layer is provided by joystick that is controlled by a human operator. During fully automatic operation, the velocity layer is controlled by an outer *position control loop*. The position control loop estimates the current AGV position by integrating the twist estimates from the velocity observer and by using information from an absolute reference system. In our case, the absolute reference system is the magnet ruler that detects magnets in the floor. The estimated AGV position is compared to the desired path. The position error is translated to a velocity setpoint. To close the loop, the velocity setpoint is feed to the velocity layer. A switch that is present on the AGVs allows the user to select between manual and operation mode.

As we will see later, the adjustments for dealing with the interaction forces of the load and the other AGVs are made in the velocity observer and the velocity controller. These are most easily tested in manual mode. Because AGVs are always equipped with a manual mode and because we expect that some cooperative transportation applications do not require an automatic mode, in the sequel we will focus on the velocity layer and manual operation only.

Although position information is not required for manual operation, the position observer remains active during the experiments that will be described in Chapters 4 and 7. It turns out to be useful to analyze the position observer's data as a step towards fully automatic control. To improve the reproducibility for the cooperative transportation experiments, we will also use velocity setpoints that are generated by a computer instead of a human operator.

The implementation of the control cycle in manual mode is sketched in Figure 2.5. The execution of the control cycle is triggered by a timer event every 100 ms. At the beginning of each cycle, the AGV starts reading its sensors. After the sensor information has been retrieved, a delayed timer event instructs the velocity observer to estimate the AGV's twist with respect to the floor. Next, the joystick setpoint is translated into the twist setpoint. Finally, the velocity layer computes the outputs for the steering and driving actuators, and these are subsequently send to the actuators.

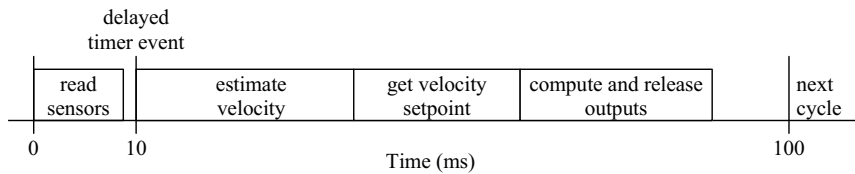


Figure 2.5: Implementation of the control cycle for a single AGV in manual mode.

2.3 Summary

In this section we presented the two industrial AGVs that we used for the experiments that will be discussed in Chapters 4 and 7. We saw that both AGVs are highly maneuverable, and can move sideways at 85 degree angles. They have rather peculiar asymmetric wheel configurations, viz. a single caster wheel on one side and two actuated wheel units on the other side. The fact that the center of gravity is not in between the two actuated wheels makes these AGVs more difficult to control than standard AGVs.

We saw that the available measurements for each AGV are two optical steering encoders to measure the steering angles of the actuated wheels, and two optical drive encoders to measure the driven distance of the actuated wheels. These four sensor readings together constitute the so-called *odometric measurements*. Each vehicle is furthermore equipped with a magnet ruler to detect magnets that are buried in the floor of the hall of FROG Navigation Systems, where the experiments are carried out. Whereas the optical encoders provide information about the relative velocity of the AGV with respect to the floor, the magnet ruler provides information about the relative position of the AGV with respect to the floor.

The wheels of the actuated wheel units are both steered and driven. Each AGV has two actuated wheel units. So there are four actuator inputs per AGV, namely two steering angle setpoints for the local steering systems, and two torque setpoints for the local drive servos of the actuated wheel units. A CAN bus is available for realtime communication. In the experiments of Chapter 7 we will use the CAN bus to send the setpoints to the AGVs and to exchange the local velocity estimates.

A layered control approach is used to control the AGVs. The inner loop deals with control on the velocity level. In that layer, the difference between the estimated and the desired *twist* is translated into a desired *wrench* on the AGV. The desired wrench is distributed among the wheels by computing local wheel forces. The local wheel forces are subsequently translated into setpoints for the AGV's steering and drive systems. The outer loop consists of position control, which translates position errors into setpoints for the velocity layer. Only the velocity control layer is considered in this thesis.

Finally, we would like to remark that the two OLS test vehicles are fully operational industrial AGVs, with all relevant software, hardware, and safety measures installed. We believe that implementing and testing new control algorithms directly on a real industrial system in an early phase will reduce the step towards the development of real, commercially available applications.

3

Model

3.1 Introduction

The model based tuning, observer and control design procedures we will apply in the subsequent chapters rely on models of the AGVs. This chapter introduces dynamical models for a single AGV and for multiple AGVs that are (semi-)rigidly interconnected to a common load. First we will start with a brief overview of related work on models for wheeled vehicles that are used in the mobile robotics and vehicle dynamics literature, and give a brief overview of tire modeling literature. Subsequently, the AGV is modelled as a planar rigid body with tires. We will use a so-called linear tire model to describe the behavior of the tires, which means that the force that is exerted by the wheel on the vehicle depends linearly on the wheel slip. The floor is assumed to be an inertial reference space. Such models proved to be sufficient to operate individual AGVs at the required accuracy in numerous applications that were realized by FROG. As we will see, the derived model is not affine in the inputs. Input affinity is a useful property when studying controllability and observability for nonlinear systems. Therefore, we introduce some additional simplifications to achieve input affinity of the initial model. The chapter ends with a discussion of a dynamical model for multiple AGVs that are (semi-)rigidly interconnected to a common, rigid load.

The dynamic models that will be presented in the next sections essentially relate the mass properties and the external wrenches that are acting on the AGVs and load to the systems acceleration with respect to the inertial floor. It is possible to describe the dynamical behavior of a rigid body in a coordinate free way using *differential geometry*. The advantage of differential geometric formulations is that they use very thorough definitions of concepts as ‘relative position’ and ‘relative velocity,’ which are in addition independent of a particular choice of coordinates. Drawback is that the notation becomes very abstract and a lot of preliminary knowledge is required to interpret the models. Therefore, we will try to avoid abstract differential geometric notations and quickly jump to suitable coordinate representations. Thus the coordinate descriptions that are used throughout this thesis are in fact parameterizations of more abstract geometric concepts.

3.2 Related work

There is an abundance of literature dealing with the modeling of wheeled vehicles. Two important research areas where such models are used for observer and control purposes are the field of mobile robotics and the field of vehicle dynamics. Furthermore, an essential part for modeling vehicle dynamics is the modeling of tires. Each of these three research fields is now discussed in more detail.

3.2.1 Wheeled mobile robots

Since laboratory robots typically operate at low speeds, the wheeled mobile robot (WMR) community often uses so-called *kinematic models*. Kinematic models are stated in terms of positions and velocities. Accelerations resulting from external forces do not play a role. It is furthermore assumed that there is no wheel slip at the tire-ground interface, i.e. the wheels are modelled as so-called *nonholonomic* constraints.

There are a lot of works focusing on control strategies for vehicles with these nonholonomic wheels. This implies that, according to these models, such robots cannot move perpendicular to the wheel plane. A robot with nonholonomic wheels can still move in any direction when all the nonholonomic wheels are steerable. Robots with the ability to move in any direction are said to be *omni-directional*. It is remarked that omni-directionality can also be achieved without steering by equipping the robot with special *omni-directional wheels*. These wheels are equipped with rollers that are mounted at an angle of 45° at the wheel circumference, see e.g. the robots that are described by Hirata *et al.* [51].

When the robots are not omni-directional, e.g. robots with regular wheels that are positioned in a car-like configuration (e.g. [68, 81]) or in a parallel fashion as with differentially steered robots (e.g. [17, 60]), then it is not trivial how to produce a net sideways movement. Several studies focus on control strategies to tackle this problem. Especially control of sideways parking a car-like robot has become a prototypical test case for evaluating nonlinear control laws, since by Brockett's Theorem [21] it is not possible to stabilize such a robot to a certain pose with a (nonlinear) static state feedback that is continuously differentiable with respect to the state. Other more difficult tasks that use nonholonomic wheel models include for example the control of a backwards driving truck with multiple trailers that do not have rear wheel steering, see e.g. [5, 6]. Also studies on wheeled mobile robots where the control problem is not the primary interest are likely to adopt kinematic models. Examples include studies on object avoidance, multi-object tracking, path planning, etc.

FROG's experience with dozens of vehicles is that kinematic models that assume zero wheel slip often do not yield the required accuracy for estimating an AGV's velocity. Additional problems arise when the center of gravity is positioned towards one side of the vehicle. Then it is not possible to accelerate in a straight line using a kinematic controller due to inevitable wheel slip. Therefore, we will use modeling approaches that are typically seen in the field of vehicle dynamics. It is remarked that not all mobile robot studies model the wheels as nonholonomic constraints. An interesting work with this respect is the study by Motte [85], which relates the control design for mobile robots that do satisfy the ideal wheel constraints to control design for mobile robots that do not satisfy these ideal constraints.

3.2.2 Vehicle dynamics

The use of dynamical vehicle models for the design, analysis and control of modern passenger cars and trucks has grown over the years. There are models for crash test analyses, durability analyses and evaluating the comfort of possibly active suspension systems. Our interest is restricted to models that describe the planar behavior of the vehicles. The study of vehicle responses to steering, often in combination with braking and acceleration, is also referred to as handling analysis. An important yet difficult aspect of handling analysis is to relate

subjective driver feelings to physical quantities. Measuring lateral and yaw rate responses to standardized steering wheel inputs are commonly used methods. Whereas the translation of physical quantities to subjective driver feelings is fairly complicated, models that relate steering inputs to physical vehicle behavior are quite accurate.

In literature we find, in increasing order of complexity (number of degrees of freedoms, number of parameters, simulation time), single track or bicycle models with static linear tire models, bicycle models with nonlinear tire characteristics with load transfer during cornering, four track models that include vehicle roll motion, models where the suspension system and compliance of the steering system are taken into account, up to finite element (FEM) models with well over one hundred degrees of freedom. Except for the FEM models, all models have real-time capabilities. Models for articulated vehicles, i.e. the Phileas [30, 31], truck-semitrailers [27, 35], dogloggers [36, 37], etc., are typically more complex than passenger car models due to the articulation point(s) and the larger number of wheels. Allen *et al.* [4] describe the role that tire characteristics play in vehicle handling. A comparison of various models for a truck with trailer is discussed by El-Gindy *et al.* [35] and later also by Dahlberg *et al.* [27]. They compared lateral acceleration, yaw rate and articulation angle as obtained by computer simulations to measurement results from field experiments. Noticeably, both articles concluded that a more sophisticated model is not necessarily better than a simpler model. When a simple non-linear MATLAB model with linear tire characteristics and a more detailed model in the multi-body package ADAMS were subjected to the same sine wave steering inputs, this resulted in similar frequency responses for the Phileas in its nominal range [64].

Because the three-wheel AGVs we consider lack a suspension system, we will model them as planar rigid bodies with wheels. These models have led to satisfactory results for the development and analysis of AGV guidance systems in the past. The next subsection discusses the various tire models that exist in the literature in more detail.

3.2.3 Tire models

Tire models describe the relation between the deformation of a tire and the forces and moments that are related to this deformation. These models are used, amongst others, for control purposes, handling analysis, and tire design. Depending on the application, the models range in complexity from simple algebraic relations between deformation and induced wrenches to very complex finite element models. There are static models as well as dynamical models that describe tire behavior for frequencies up to over 50 Hz. Models range from analytical models, which are open to theoretical analysis, to fully empirical models that are just intended to represent experimental data as accurately as possible. Another important distinction is that between models that describe the vertical tire behavior, i.e. perpendicular to the road, and the horizontal tire behavior. The vertical behavior is important for the evaluation of suspension systems and ride comfort. Vertical deformation is often characterized by the tire deflection, which depends on the loaded and unloaded tire radius. The horizontal behavior is closely related to the “handling characteristics.” For horizontal tire behavior, models for lateral behavior (“cornering”), longitudinal behavior (e.g. “braking”), and lateral plus longitudinal behavior (e.g. “combined steering and braking”) exist. The horizontal behavior will change with varying vertical loads. Horizontal deformation is typically quantified by two slip quanti-

ties, namely the so-called longitudinal slip and the slip angle. For different applications, e.g. motorcycles, off-road vehicles, race-cars, commercial vehicles, aircraft landing gears, etc., different tires with their corresponding models have been developed.

Since this project is about AGVs, we will focus on tire models that have been developed for vehicle dynamic studies and we disregard the nonholonomic models that are often used by the wheeled mobile robots community. A very popular model for the simulation of vehicle dynamics is the so-called Magic Formula model, which is based on the ideas that were first introduced by Bakker *et al.* [14]. Since then, it has been modified and extended several times. A recent version with transient properties is described by Pacejka *et al.* [92]. The Magic Formula describes the relation between combined horizontal slip and the longitudinal forces, lateral forces as well as the aligning moment of the tire. It also takes into account that the tire properties change under different vertical loads. The Magic Formula model is also valid for extreme maneuvers such as emergency braking and drifting through corners. The model was designed for pneumatic tires, and in particular, for passenger car tires. Since a typical Magic Formula tire model contains over hundred parameters, by selecting the appropriate values it can describe other tire types, such as truck tires, to a certain extent as well. Another vehicle simulation tire model is STIREMOD. STIREMOD can handle both paved as well as off-road surfaces such as loose soil [3]. An example of a tire model for truck tires is the one by Fancher *et al.* [38]. All three models contain simple relaxation effects. Recently the dynamic range of tire models has been extended to over 50 Hz. The reader is referred to several Ph.D. theses [105, 130, 78, 96] by the Delft University of Technology and the Proceedings of the International Colloquia on Tyre Models for Vehicle Dynamic Analysis for more information about tire modeling.

The AGVs we consider have a low center of gravity and in addition the trajectories are often chosen such that the lateral accelerations remain small. Therefore, for our applications tire models that describe only the horizontal behavior will suffice. Since the maneuvers of AGVs are smooth and relatively slow, we use tire model where the relation between the wheel slip and the exerted forces is static. Furthermore, load transfer from the inner to the outer wheels when cornering is not taken into account.

3.3 Kinematics

This section introduces the notation for the relative position and the relative velocity of an AGV with respect to the floor. Different parameterizations for both concepts are discussed. Finally, the advantages and disadvantages of two methods for integrating relative velocities are discussed. The two main approaches to describe rigid body motions are *screw theory* and *Lie group theory*. See [114] for a description of both methods and their one-to-one and onto relationship. The approach we follow is most closely related to Lie group theory.

3.3.1 Relative position

To describe the relative position of an AGV with respect to the floor, we attach a coordinate system Ψ_v to the vehicle and a coordinate system Ψ_0 to the floor. The relative position H_v^0 of

the vehicle with respect to the floor is described by the matrix

$$H_v^0 = \begin{pmatrix} c\varphi_v & -s\varphi_v & x_v \\ s\varphi_v & c\varphi_v & y_v \\ 0 & 0 & 1 \end{pmatrix} \in SE(2) \quad (3.1)$$

and the relative position of the floor with respect to the vehicle by

$$H_0^v = (H_v^0)^{-1} = \begin{pmatrix} c\varphi_v & s\varphi_v & -x_v c\varphi_v - y_v s\varphi_v \\ -s\varphi_v & c\varphi_v & x_v s\varphi_v - y_v c\varphi_v \\ 0 & 0 & 1 \end{pmatrix} \in SE(2). \quad (3.2)$$

Here (x_v, y_v) are the coordinates of the origin of Ψ_v expressed in floor coordinates Ψ_0 , and φ_v is the orientation of Ψ_v with respect to Ψ_0 . See Figure 3.1 for an illustration. The relative position H_v^0 of the vehicle with respect to the world is also known as the *pose* of the vehicle. The set of all homogenous matrices H_v^0 forms the matrix Lie group $SE(2)$. Every element corresponds to a unique relative position of the vehicle with respect to the floor. Vice versa, every relative position of the vehicle with respect to the floor corresponds to a unique element of $SE(2)$. This one-to-one relation (bijection) between elements of $SE(2)$ and relative positions partly explain the popularity of this method.

From equation (3.1) we see that we can also use the triplet $q_v = (\varphi_v, x_v, y_v) \in \mathbb{R}^3$ to describe the relative position of the vehicle with respect to the floor. Advantage of the latter description is that we only need three numbers instead of the nine numbers for H_v^0 . The disadvantage is that the one-to-one relationship between the physical pose of the vehicle and the parametrization is lost. To illustrate this, the relation between the (φ_v, x_v, y_v) parametrization and the physical relative positions of the vehicle is sketched in Figure 3.2. The x_v and y_v coordinates are on the horizontal axes, and the φ_v coordinate along the vertical axis. Thus each horizontal plane corresponds to a particular orientation of the vehicle. As we move from a given point in the vertical direction, every 2π we arrive at a point that represents exactly the same situation as the one we have started from. To indicate this, we *identify* all points that represent the same situation.

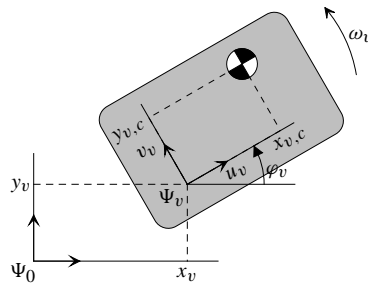


Figure 3.1: Notation for the AGV's rigid body model. Here ω_v is the rotational, u_v the longitudinal, and v_v the lateral velocity of the vehicle fixed coordinate system Ψ_v with respect to the floor.

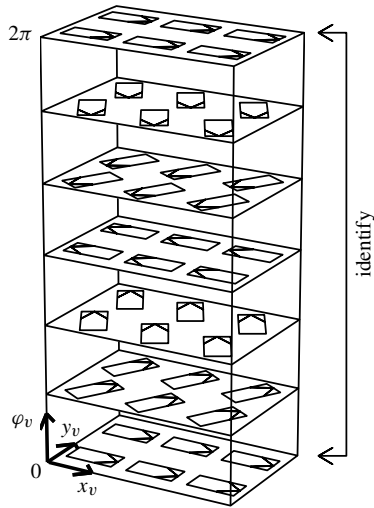


Figure 3.2: Sketch of the relation between the (φ_v, x_v, y_v) parametrization and the physical vehicle pose.

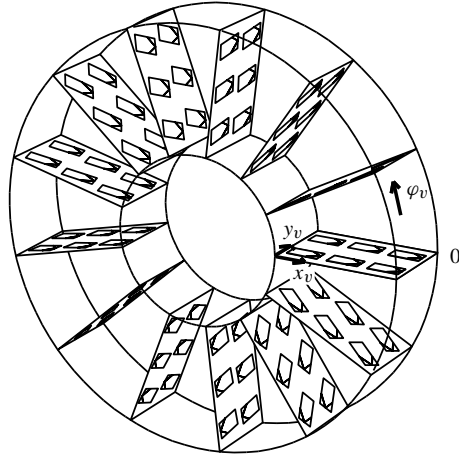


Figure 3.3: Alternative representation of the relation between the (φ_v, x_v, y_v) parametrization and the physical vehicle pose.

To illustrate the concept of identifying objects, consider the standard textbook example of a straight line with identified end points, see Figure 3.4. Since the end points are identified, we can go from point A to point C without passing through point B . To do this, we move from point A to the left end point, subsequently ‘jump’ to the right end point (actually we are already there because the two end points are identified), and finally move towards the left until we reach point C . Just think of the famous computer game PacMan, where the yellow character leaves the maze on the left to subsequently pop up on the right. From a topological point of view, the straight line with identified end points is identical to a circle, see Figure 3.4. Indeed, for the circle we can also go from point A to point C without going through point B .

Similarly as we rolled up the line to a circle, we can roll up the vertical column from Figure 3.2 to obtain a ring that is topologically identical. The result is sketched in Figure 3.3. We see that the relative vehicle position with respect to the floor is a three dimensional manifold. It is topologically the same as the manifold $S \times \mathbb{R}^2$, and also as the three dimensional manifold $SE(2)$. It is remarked that this is no longer true when we go to a higher dimension, e.g. the topology of the manifold $SE(3)$ differs from the topology of the manifold $S^3 \times \mathbb{R}^3$.

3.3.2 Relative velocity

The relative velocity of body B_i with respect to another body B_j is also known as the *twist* of B_i with respect to B_j [114]. To parameterize the twist, we only need a single coordinate

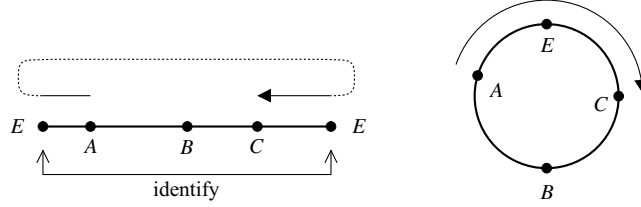


Figure 3.4: From a topological point of view, the straight line (left) with identified end points E is identical to the circle on the right. For both, it is possible to go from point A to C without passing through point B .

system. We call $T_i^{k,j}$ the twist of B_i with respect to B_j expressed in coordinate system Ψ_k . It is important to remark that the subscript i and the superscript j indicate *bodies*, whereas the superscript k refers to a *coordinate system*. Before we show how to express $T_i^{k,j}$ in any other coordinate system Ψ_l , we will first focus on the special case that Ψ_k is equal to Ψ_i . The twist of the AVG with respect to the floor expressed in the AGV's coordinate system Ψ_v reads

$$T_v^{v,0} = \begin{pmatrix} \dot{\varphi}_v \\ \dot{x}_v \cos \varphi_v + \dot{y}_v \sin \varphi_v \\ -\dot{x}_v \sin \varphi_v + \dot{y}_v \cos \varphi_v \end{pmatrix} = \begin{pmatrix} \omega_v \\ u_v \\ v_v \end{pmatrix} \quad (3.3)$$

Here the first component ω_v is interpreted as the rotational velocity of the AGV with respect to the floor. The second component u_v represents the longitudinal velocity and the last component v_v the lateral velocity of the origin of Ψ_v with respect to the floor, respectively. This is illustrated by Figure 3.1. To describe the relation between H_v^0 and $T_v^{v,0}$, it is convenient to write the components of $T_v^{v,0}$ in a matrix using the *tilde operator*:

$$T_v^{v,0} = \begin{pmatrix} \omega_v \\ u_v \\ v_v \end{pmatrix} \Leftrightarrow \tilde{T}_v^{v,0} = \begin{pmatrix} 0 & -\omega_v & u_v \\ \omega_v & 0 & v_v \\ 0 & 0 & 0 \end{pmatrix} \quad (3.4)$$

This (bijective) mapping is more general, and can also be applied to a twist of one body B_i to another body B_j expressed in any coordinate system k , i.e. $T_i^{k,j} \Leftrightarrow \tilde{T}_i^{k,j}$. The relation between $T_v^{v,0}$, H_v^0 , and its time derivative \dot{H}_v^0 satisfies

$$\tilde{T}_v^{v,0} = (H_v^0)^{-1} \dot{H}_v^0 = H_v^0 \dot{H}_v^0 = \begin{pmatrix} 0 & -\omega_v & u_v \\ \omega_v & 0 & v_v \\ 0 & 0 & 0 \end{pmatrix} \in se(2). \quad (3.5)$$

Note $\tilde{T}_v^{v,0}$ has a special form. Here $se(2)$ denotes the Lie algebra corresponding to $SE(2)$. To illustrate the interpretation of $H_v^0 \dot{H}_v^0$, a curve $H_v^0(t)$ has been drawn in Figure 3.5. For convenience the manifold $SE(2)$ is schematically represented as a two dimensional surface, but in fact it has the topology that was discussed in the previous section and is sketched in Figures 3.2 and 3.3. What basically happens is that $H_v^0(t)$ transports the velocity $\dot{H}_v^0(t)$,

which lives in the tangent space $T_{H_v^0(t)}SE(2)$ of point $H_v^0(t)$, to the tangent space $T_I SE(2)$ that corresponds to the identity element I of the matrix Lie group. The identity element I is simply the 3×3 identity matrix. The tangent space $T_I SE(2)$ corresponds to the vector space of the unique Lie algebra $se(2)$ that comes with the Lie group $SE(2)$. Thus $T_v^{v,0}$ is interpreted as a parametrization of \dot{H}_v^0 after it has been transported to the tangent space at the identity of $SE(2)$.

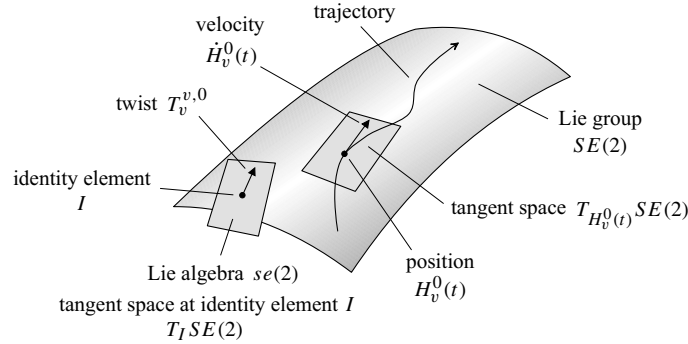


Figure 3.5: Interpretation of $\tilde{T}_v^{v,0} = H_0^v \dot{H}_v^0$.

Another way to interpret $T_v^{v,0}$ is by considering the $q_v = (\varphi_v, x_v, y_v)$ parametrization of the manifold $Q = S \times \mathbb{R}^2$ that is sketched in Figure 3.6. At each point q on the manifold we have a tangent space $T_q Q$. The relative velocities corresponding to position q are elements of the tangent space $T_q Q$. One possibility to parameterize the elements of $T_q Q$ is by using the vectors e_φ , e_x and e_y that point into the directions of their corresponding coordinate axes. Thus for every point q on the manifold we have three vectors (e_φ, e_x, e_y) to span the tangent space at that point. All e_φ vectors together constitute a vector field on the manifold. The same is true for all vectors e_x and e_y . These three vector fields (e_φ, e_x, e_y) together define a *frame* of vector fields. For a curve $q(t) = (\varphi_v(t), x_v(t), y_v(t))$, the velocity at point $q(t)$ is simply $\dot{\varphi}_v(t)e_\varphi + \dot{x}_v(t)e_x + \dot{y}_v(t)e_y$. Furthermore, we note that the frame of vector fields (e_φ, e_x, e_y) is a *coordinate frame* since the Lie brackets¹ of all combinations of the vector fields are zero, see p. 243 of [39]. Indeed, $[e_\varphi, e_x] = [e_\varphi, e_y] = [e_x, e_y] = 0$. An alternative for (e_φ, e_x, e_y) is to use the frame of vector fields (e_φ, e_u, e_v) , where

$$e_u = e_x c\varphi_v + e_y s\varphi_v \quad (3.6)$$

$$e_v = -e_x s\varphi_v + e_y c\varphi_v. \quad (3.7)$$

The latter parametrization is illustrated in Figure 3.7. Thus we see that e_u coincides with the x_v -axis of Ψ_v , and e_v coincides with the y_v -axis of Ψ_v . The velocity of the curve above expressed in this base satisfies $\omega_v(t)e_\varphi + u_v(t)e_u + v_v(t)e_v$, where u_v and v_v are defined according to equation (3.3). Thus we see that the components of $T_v^{v,0}$ can also be interpreted

¹The Lie bracket $[f(x), g(x)]$ of the vectorfields $f(x)$ and $g(x)$ is a third vectorfield. It is computed as $[f(x), g(x)] = \frac{dg(x)}{dx} f(x) - \frac{df(x)}{dx} g(x)$.

as the relative velocity expressed in the (e_φ, e_u, e_v) base. Finally, note that

$$[e_\varphi, e_u] = \left[\begin{pmatrix} 1 \\ 0 \\ 0 \end{pmatrix}, \begin{pmatrix} 0 \\ c\varphi_v \\ s\varphi_v \end{pmatrix} \right] = \begin{pmatrix} 0 \\ -s\varphi_v \\ c\varphi_v \end{pmatrix} \neq 0. \quad (3.8)$$

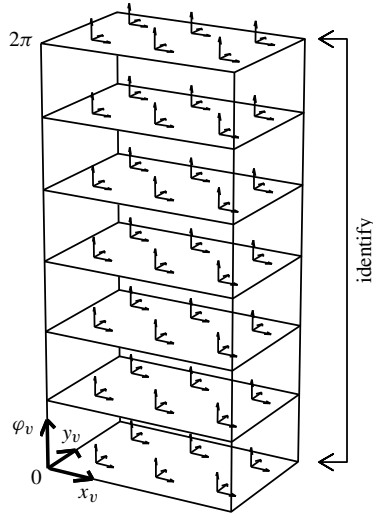


Figure 3.6: The coordinate frame of vector fields (e_φ, e_x, e_y) .

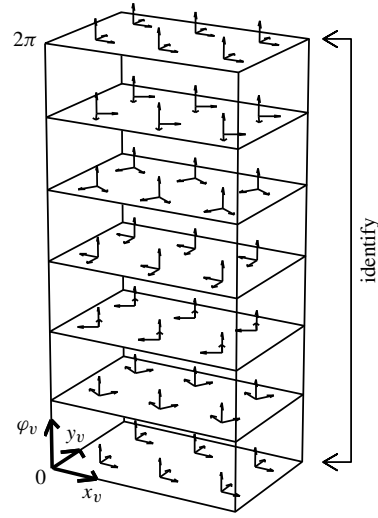


Figure 3.7: The frame of vector fields (e_φ, e_u, e_v) .

Now that we have seen various interpretations of the components of the twist $T_v^{v,0}$, we briefly summarize how to transform a twist that is expressed in one coordinate system Ψ_k to another coordinate system Ψ_l . A twist that is expressed in ‘tilde’ representation $\tilde{T}_v^{k,0}$ transforms corresponding to

$$\tilde{T}_v^{l,0} = H_k^l \tilde{T}_v^{k,0} H_l^k, \quad (3.9)$$

and a twist in column notation $T_v^{k,0}$ according to

$$T_v^{l,0} = Ad_{H_k^l} T_v^{k,0}, \quad (3.10)$$

with

$$Ad_{H_k^l} = \begin{pmatrix} 1 & 0 & 0 \\ p_2 & R_{11} & R_{12} \\ -p_1 & R_{21} & R_{22} \end{pmatrix}, \quad H_k^l = \begin{pmatrix} R_{11} & R_{12} & p_1 \\ R_{21} & R_{22} & p_2 \\ 0 & 0 & 1 \end{pmatrix}. \quad (3.11)$$

From equations (3.9)-(3.10) we see that both transformations are *linear*. We can use this notation to investigate the relation between the twist $T_v^{v,0}$ and $\dot{q} = (\dot{\varphi}_v, \dot{x}_v, \dot{y}_v)$. To this end, define a new coordinate system $\Psi_{\bar{v}}$ such that its origin coincides with the origin of Ψ_v , and

its orientation corresponds to the orientation of Ψ_0 . In other words, $\Psi_{\bar{v}}$ moves along with Ψ_v while keeping its rotation with respect to the floor equal to zero. From equations (3.11) and (3.3) it follows that the components of the twist $T_v^{v,0}$ are related to $(\dot{\varphi}_v, \dot{x}_v, \dot{y}_v)$ by

$$T_v^{v,0} = \begin{pmatrix} \omega_v \\ u_v \\ v_v \end{pmatrix} = \underbrace{\begin{pmatrix} 1 & 0 & 0 \\ 0 & c\varphi_v & s\varphi_v \\ 0 & -s\varphi_v & c\varphi_v \end{pmatrix}}_{Ad_{H_v^v}} \underbrace{\begin{pmatrix} \dot{\varphi}_v \\ \dot{x}_v \\ \dot{y}_v \end{pmatrix}}_{T_v^{\bar{v},0}} = Ad_{H_v^v} T_v^{\bar{v},0}. \quad (3.12)$$

Thus we see that we can interpret $\dot{q}_v = T_v^{\bar{v},0}$ as the twist of the vehicle with respect to the floor expressed in the coordinate system $\Psi_{\bar{v}}$.

3.3.3 Steering pole

Every planar rigid body motion has an *instantaneous center of rotation*, which is also known as the *steering pole*. For a given twist $T_v^{v,0}$ expressed in Ψ_v , the coordinates of the steering pole C expressed in Ψ_v are given by

$$C^v = \begin{pmatrix} C_x^v \\ C_y^v \\ 1 \end{pmatrix} = \begin{pmatrix} -v_v/\omega_v \\ u_v/\omega_v \\ 1 \end{pmatrix} \quad (3.13)$$

see Figure 3.8. The coordinates above are also known as *homogenous coordinates*, which basically means that the 2D space of points on a rigid body is extended with an additional dimension (the last element “1” corresponds to this additional dimension). The additional dimension makes it for instance possible to use a linear instead of an affine operation to transform coordinates. Furthermore, homogenous coordinates allows us to deal with points at infinity. For example, the steering pole is at infinity for pure translational motions ($\omega_v = 0$). The homogeneous coordinates for that case are

$$C^v = \begin{pmatrix} -v_v \\ u_v \\ 0 \end{pmatrix}. \quad (3.14)$$

The last element “0” indicates that the steering pole is at infinity. We can express C^v , which may either be finite or infinite, in any other coordinate system Ψ_k using

$$C^k = H_v^k C^v. \quad (3.15)$$

Note that the steering pole is undefined for $T_v^{v,0} = 0$. Furthermore, note that the coordinate transformation above is a linear transportation.

3.3.4 Signed radius, side slip angle and tangential velocity

In Chapter 4 we will drive circle segments with the AGVs for tuning the wheel diameters and the offsets for the steering encoders. We will see that the algorithm for estimating the

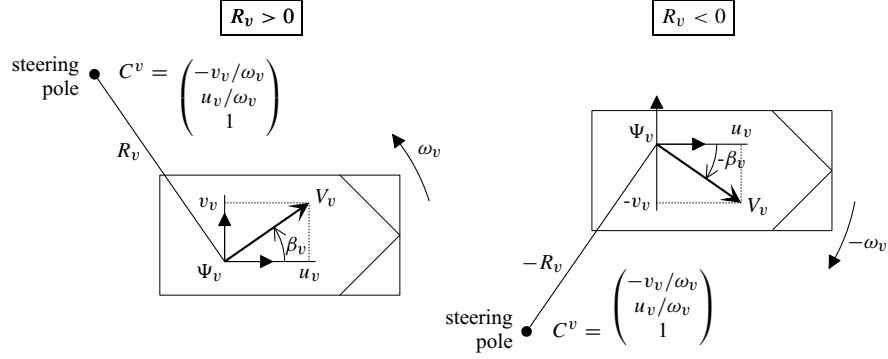


Figure 3.8: Definitions of the steering pole C , signed radius R_v , side slip angle β_v , and tangential velocity V_v .

parameters does not depend on the vehicle speed, but only on the shape of the realized circle segment. For that reason it is useful to have a parametrization that decomposes the twist in a part that is related to the steering pole and a part that represents the velocity of the AGV.

First we discuss the *signed radius* R_v . The squared distance $\|C - o_v\|^2$ of the origin o_v of the AGV's coordinate system Ψ_v to C is denoted by R_v^2 , i.e. R_v^2 is the squared radius of the circle segment corresponding to the instantaneous motion of o_v . We define that R_v is of the same sign as the y -coordinate of the center of orientation C expressed in Ψ_v , that is

$$\text{sign}(R_v) = \text{sign}(C_y^v). \quad (3.16)$$

In other words, R_v is positive for a left hand turn and negative for a right hand turn. It is assumed that the center of the vehicle coordinate system does not coincide with the center of orientation, hence $R_v \neq 0$. See Figure 3.8 for a sketch of the situations $R_v > 0$ and $R_v < 0$. For dealing with large radii R_v , the *signed curvature* ρ_v is defined as

$$\rho_v = R_v^{-1}. \quad (3.17)$$

Next, the *side slip angle* $\beta_v \in (-\frac{\pi}{2}, \frac{\pi}{2}]$ is defined as the angle between the tangent to the instantaneous motion of o_v and the x_v -axis of Ψ_v , see Figure 3.8. From the figure it is easily seen that the signed radius and side slip angle are related to the vehicle coordinates of the steering pole C according to

$$C^v = \begin{pmatrix} C_x^v \\ C_y^v \\ 1 \end{pmatrix} = \begin{pmatrix} -R_v s\beta_v \\ R_v c\beta_v \\ 1 \end{pmatrix}. \quad (3.18)$$

The inverse relation satisfies

$$R_v = \text{sign}(C_y^v) \sqrt{(C_x^v)^2 + (C_y^v)^2}, \quad \beta_v = \arctan \left(-\frac{C_x^v}{C_y^v} \right) \quad (3.19)$$

The equations above show that both the signed curvature R_v and the side slip angle β_v depend on the pose of the vehicle coordinate system Ψ_v . They can be transformed to other coordinate systems, for example a coordinate system that is attached to the wheels. This will turn out to be useful for the estimation of the steering encoder offsets in Chapter 4. To transform R_v and β_v from coordinate system Ψ_v to coordinate system Ψ_k , first compute C^v with equation (3.18), subsequently transform this to Ψ_k by $C^k = H_v^k C^v$, and finally compute R_k and β_k with equation (3.19). Note that whereas changing coordinates for a twist $T_v^{v,0}$ was a linear operation, changing coordinates for the signed radius R_v and side slip angle β_v is a nonlinear operation.

The alternative parametrization of the twist $T_v^{v,0}$ is completed by adding the *tangential velocity* V_v that is defined as the absolute velocity of the origin o_v of Ψ_v with respect to the floor:

$$\boxed{V_v = u_v c\beta_v + v_v s\beta_v} \quad (3.20)$$

The components of the twist $T_v^{v,0}$ are related to (R_v, β_v, V_v) according to

$$T_v^{v,0} = \begin{pmatrix} \omega_v \\ u_v \\ v_v \end{pmatrix} = \begin{pmatrix} V_v/R_v \\ \omega_v C_y^v \\ -\omega_v C_x^v \end{pmatrix} = V_v \begin{pmatrix} R_v^{-1} \\ c\beta_v \\ s\beta_v \end{pmatrix} = V_v \begin{pmatrix} \rho_v \\ c\beta_v \\ s\beta_v \end{pmatrix}. \quad (3.21)$$

The careful reader must have noted that there are a few situations where the (R_v, β_v, V_v) parametrization is not well defined. First, for pure translational motions R_v is infinite. We can change R_v for ρ_v and use the (ρ_v, β_v, V_v) parametrization to overcome this. Second, equation (3.19) leads to problems when $C_y^v = 0$. This is resolved by letting $R_v = -C_x^v$ and $\beta_v = \frac{\pi}{2}$ for that case. Finally, the situation that the steering pole coincides with the origin of Ψ_v is more serious. Then $C_x^v = C_y^v = 0$ and β_v is undefined. Since V_v will be zero, the translational velocity components u_v and v_v can still be reconstructed correctly from equation (3.21). The information for the rotational velocity, however, is lost as $\omega_v = V_v/R_v = 0/0$ for this case.

In conclusion, we saw that a change of coordinates for the (R_v, β_v, V_v) parametrization is a nonlinear transformation. Furthermore, the coordinates are not well defined when the steering pole coincides with the origin of the coordinate system. The advantage of this parametrization, however, is that the position of the steering pole is separated from the velocity information of the motion. We will use the (R_v, β_v, V_v) parametrization only in the next chapter, where the tuning of the AGVs' wheel diameters and steering angle encoder offsets is discussed. The AGVs perform circular trajectories with a large radius and a small side slip angle in those experiments. Therefore, R_v will always be finite and unequal to zero. Thus we can safely use the (R_v, β_v, V_v) parametrization for those experiments without having to worry about the problem cases described above.

3.3.5 Numerical integration of twists

Although this thesis mainly focuses on control on the velocity level, it is illustrative to study integrated twist estimates. In Chapter 7 where the experiments are analyzed, these are for example compared to integrated twist setpoints and to positions estimates from the AGVs'

ranging modules. The relation between the time derivative of the relative vehicle position H_v^0 and the twist $T_v^{v,0}$ equals [114, 115]:

$$\dot{H}_v^0 = H_v^0 \tilde{T}_v^{v,0}. \quad (3.22)$$

Because the control software is implemented on a digital computer, the twist estimate $\hat{T}_v^{v,0}$ is only available at distinct time instances. If the relative position H_v^0 of the AGV with respect to the floor is known at some time instant t , then some assumptions on behavior of the twist have to be made to compute the relative position of the AGV at time instant $t + \Delta t$.

Euler integration scheme

One possibility is to assume that the time derivatives of (φ_v, x_v, y_v) , i.e.

$$\begin{pmatrix} \dot{\varphi}_v \\ \dot{x}_v \\ \dot{y}_v \end{pmatrix} = \begin{pmatrix} \omega_v \\ u_v c \varphi_v - v_v s \varphi_v \\ u_v s \varphi_v + v_v c \varphi_v \end{pmatrix}, \quad (3.23)$$

remain constant during $[t, t + \Delta t)$. Applying a standard forward Euler integration scheme leads to

$$\varphi_v(t + \Delta t) = \varphi_v(t) + \dot{\varphi}_v(t) \Delta t \quad (3.24)$$

$$x_v(t + \Delta t) = x_v(t) + \dot{x}_v(t) \Delta t \quad (3.25)$$

$$y_v(t + \Delta t) = y_v(t) + \dot{y}_v(t) \Delta t. \quad (3.26)$$

Twist exponential integration scheme

Another possibility is to assume that the twist is constant. Then it can be shown that (see e.g. [115])

$$\boxed{H_v^0(t + \Delta t) = H_v^0(t) e^{\tilde{T}_v^{v,0}(t) \Delta t}} \quad (3.27)$$

A constant twist implies that the position of steering pole with respect to the floor as well as with respect to the AGV is constant during the motion, i.e. C^0 and C^v are constant. For 3D rigid body motions there is an explicit expression for the exponential of a 3D twist, see e.g. [115]. A motion of a planar rigid body can be interpreted as a special case of a 3D rigid body motion. Thus there also exists an explicit expression for the exponential of $\tilde{T}_v^{v,0} \Delta t \in se(2)$:

$$e^{\tilde{T}_v^{v,0} \Delta t} = \begin{pmatrix} \cos(\omega_v \Delta t) & -\sin(\omega_v \Delta t) & \sin(\omega_v \Delta t) \frac{u_v}{\omega_v} - (1 - \cos(\omega_v \Delta t)) \frac{v_v}{\omega_v} \\ \sin(\omega_v \Delta t) & \cos(\omega_v \Delta t) & (1 - \cos(\omega_v \Delta t)) \frac{u_v}{\omega_v} + \sin(\omega_v \Delta t) \frac{v_v}{\omega_v} \\ 0 & 0 & 1 \end{pmatrix} \in SE(2). \quad (3.28)$$

Here we used $\omega_v = \omega_v(t)$, $u_v = u_v(t)$ and $v_v = v_v(t)$ for notational convenience. For a pure translational motion $\omega_v = 0$ the expression above reduces to

$$e^{\tilde{T}_v^{v,0} \Delta t} = \begin{pmatrix} 1 & 0 & u_v \Delta t \\ 0 & 1 & v_v \Delta t \\ 0 & 0 & 1 \end{pmatrix} \in SE(2). \quad (3.29)$$

Although analytical expressions exist, in practice it is more convenient to use standard software for numerical matrix manipulations to compute the exponential of a matrix. We will use MATLAB's 'expm' routine, which uses the Padé approximation with scaling and squaring (see e.g. pp42–43 of the article by Moler and Van Loan for more information [84] on this routine).

Comparison of the Euler and the twist exponential integration schemes

Since the Euler integration scheme and the twist exponential integration scheme make different assumptions on the behavior of the twist during the time interval $[t, t + \Delta t)$, they will generally produce different results. To illustrate this, consider a vehicle with a coordinate system Ψ_v that is fixed to the middle of the vehicle, see Figure 3.9. At time t the position of the vehicle is such that Ψ_v coincides with Ψ_0 . Suppose that the rotational velocity is 1 rad/s, the longitudinal velocity 4 m/s, and the lateral velocity is zero at time t : $T_v^{v,0}(t) = (1, 4, 0)^T$. Furthermore, we attach an additional coordinate system Ψ_k to the front left corner of the vehicle. Since the vehicle in this example has a length of 1 m and a width of 0.5 m, this results in $T_v^{k,0}(t) = (1, 3.75, 0.5)^T$. Let us take $\Delta t = 1$ s.

The vehicle positions as computed with the Euler scheme (3.24)-(3.26) applied to Ψ_v and Ψ_k , and the positions as computed with the twist exponential integration scheme (3.27) applied to Ψ_v and Ψ_k are drawn in Figure 3.9. The Figure shows that for the Euler scheme it obviously matters which coordinate system is chosen to carry out the integration. Since choosing a different coordinate system implicitly means assuming a different behavior for the twist, the results depend on the particular choice of coordinates for the Euler integration scheme. For the twist integration scheme, however, the results are *independent* of the selected coordinate system. No matter what coordinate system is chosen, the twist exponential integration scheme will always assume that the vehicle performs a pure circular motion around the steering pole. Since a different choice of coordinates gives the same results, the twist exponential integration scheme is said to be *geometrically well defined*.

That the twist exponential integration scheme is geometrically well defined can be verified as follows. Consider a finite point P that is fixed to the vehicle. Its homogenous coordinates expressed in Ψ_v are denoted as P^v :

$$P^v = \begin{pmatrix} P_x^v \\ P_y^v \\ 1 \end{pmatrix}, \quad (3.30)$$

where (P_x^v, P_y^v) are the x - and y -coordinates of P expressed in Ψ_v . The last component of P^v is equal to zero for a point at infinity, and it is usually taken equal to one for a finite point. At time $t + \Delta t$, the coordinates of P as computed with the exponential integration scheme and expressed in Ψ_0 are

$$P^0(t + \Delta t) = H_v^0(t + \Delta t)P^v = H_v^0(t)e^{\tilde{T}_v^{v,0}(t)\Delta t}P^v. \quad (3.31)$$

Next, consider the coordinate system Ψ_k that is also attached to the vehicle. The relation between Ψ_v and Ψ_k is described by H_v^k . Since both Ψ_v and Ψ_k are fixed with respect to each other, the matrix H_v^k is constant. Furthermore, The coordinates of P expressed in Ψ_k are

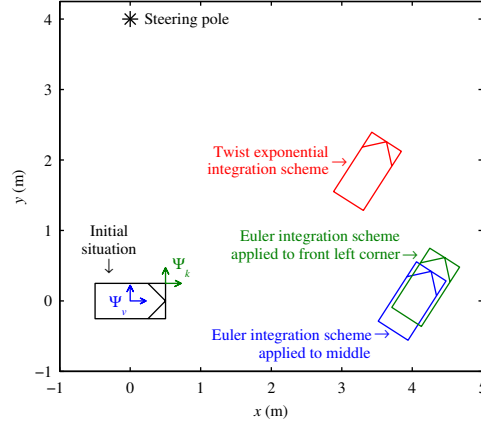


Figure 3.9: For the Euler integration scheme, the final position of the vehicle depends on the choice of coordinates. For the twist exponential integration scheme, the final position of the vehicle is independent of the chosen coordinate system.

$P^k = H_v^k P^v$. Applying the exponential integration scheme using this alternative coordinate system Ψ_k results in

$$\begin{aligned} P^0(t + \Delta t) &= H_k^0(t + \Delta t) P^k = H_k^0(t) e^{\tilde{T}_v^{k,0}(t)\Delta t} P^k = H_k^0(t) e^{H_v^k \tilde{T}_v^{v,0}(t) H_k^v \Delta t} P^k \\ &= H_k^0(t) H_v^k e^{\tilde{T}_v^{v,0}(t)\Delta t} H_k^v P^k = H_v^0(t) e^{\tilde{T}_v^{v,0}(t)\Delta t} P^v. \end{aligned} \quad (3.32)$$

Here we used that $H_k^v = (H_v^k)^{-1}$ to write H_k^k and H_k^v outside the exponent. Note that the two equations (3.31) and (3.32) produced identical coordinates for $P^0(t + \Delta t)$. So it does indeed not matter for the final result what coordinate system is used to perform the twist exponential integration scheme.

Because the twist integration scheme is geometrically well defined whilst the Euler integration scheme is not, we prefer to use the former for our numerical integrations. Since every integration scheme makes certain assumptions on the behavior of the twist, all integration schemes produce slightly incorrect results when the assumptions are violated. The twist exponential integration scheme produces exact results when the steering pole is constant, i.e. for motions that are purely circular and have constant speed during the integration period. The Euler integration scheme has a worse performance for these circular motions. There are, of course, also situations where the Euler scheme performs better. One example is the reconstruction of the trajectory of a rock that is tumbling through free space in the absence of gravity. Then the steering pole is not constant but moving at a constant velocity that is identical to the velocity of the object's center of gravity. Whereas the Euler scheme applied to the center of gravity produces the exact results, the twist exponential integration scheme will result in unrealistic trajectories with very large loops for this situation. Interestingly, there are also special cases where the two schemes produce identical results. For example when the twist equals zero or when pure translational motions are considered. A less trivial

situation is when the origin of the coordinate system used to carry out the Euler integration scheme coincides exactly with the steering pole. Although there are situations where the Euler integration scheme performs better, in the sequel we will solely use the twist exponential integration scheme (3.27) as the latter is geometrically well defined.

3.4 Dynamics

This section discusses a model for the dynamics of an AGV. The dynamical model describes the relation between the acceleration, inertial properties, and generalized forces that act on the body. First we will zoom in on the concept of acceleration. Subsequently the Lagrangian approach is used to derive the equations of motion. The relation between the steering angles of the wheels, the torques exerted by the drive systems, and the net wrench on the AGV are discussed in section 3.5 that deals with the model of the wheels.

3.4.1 Acceleration

At first it may seem counterintuitive that the discussion of the concept of ‘acceleration’ is found here in the dynamics section and not in the kinematics section. The rationale behind this decision will become clear in a minute. When the relative velocity of a body at time t is denoted as $v(t)$, then intuitively the definition for the acceleration $a(t)$ of that body would look something like

$$a(t) = \lim_{\Delta t \rightarrow 0} \frac{v(t + \Delta t) - v(t)}{\Delta t}. \quad (3.33)$$

From a differential geometrical perspective, however, a serious problem occurs when interpreting this expression. In section 3.3.2 we have seen that relative velocities live in tangent spaces. Let us consider a trajectory $q : \mathbb{R} \rightarrow Q$. At time t the relative position of the body is $q(t)$ and its relative velocity equals $v(t) = \dot{q}(t) \in T_{q(t)}Q$. At time $t + \Delta t$ the relative position is $q(t + \Delta t)$ and its relative velocity is $v(t + \Delta t) = \dot{q}(t + \Delta t) \in T_{q(t + \Delta t)}Q$. This is sketched in Figure 3.10. Generally speaking $q(t) \neq q(t + \Delta t)$. Thus we see that the velocities $v(t)$ and $v(t + \Delta t)$ are elements of *different* tangent spaces: $v(t)$ lives in the tangent space $T_{q(t)}Q$ that corresponds to $q(t)$, and $v(t + \Delta t)$ lives in the tangent space $T_{q(t + \Delta t)}Q$ that corresponds to $q(t + \Delta t)$. Recall that a tangent space is a vector space. As the ‘-’ operator is only defined for elements that live in the *same* vector space, the expression ‘ $v(t + \Delta t) - v(t)$ ’ in equation (3.33) is undefined as $v(t + \Delta t)$ and $v(t)$ are elements of *different* vector spaces.

This problem of computing the ‘difference’ between elements of two different tangent spaces is resolved by transporting one element to the tangent space of the other element, e.g. transporting $v(t + \Delta t)$ to the tangent space $T_{q(t)}Q$ of $v(t)$. Since the ‘-’ operator is well defined for two elements in the same tangent space, $v(t)$ can easily be subtracted from the transported version of $v(t + \Delta t)$ that also is in $T_{q(t)}Q$.

Obviously we need a recipe that describes how to transport elements from one tangent space to another. To this end we use a so-called *connection*. For an n -dimensional manifold, a connection is expressed in coordinates using n^3 *connection coefficients* Γ_{ij}^k .² The connection

²Usually the symbols ω_{ij}^k are used to express a connection. Since ω was already used for the rotational velocity, here we will use Γ_{ij}^k instead.

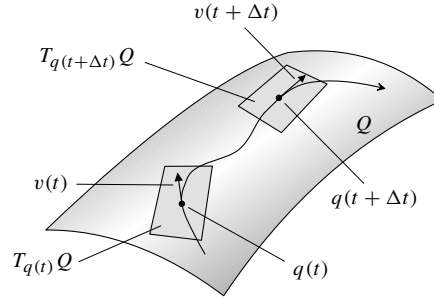


Figure 3.10: The velocities $v(t)$ and $v(t + \Delta t)$ live in different tangent spaces.

allows us to compute the *geometrical acceleration* of a curve. Since the connection gives an expression for the acceleration, we can now consider the situation that the geometrical acceleration is zero. This corresponds to the situation that no external forces are acting on a body. A curve with zero acceleration is called a *geodesic*. The geodesic $q(t)$ passing through a point $q(t_0) = q_0$ with relative velocity $v(t_0) = \dot{q}(t_0) = v_0$ is found by solving the set of n differential equations

$$\ddot{q}^k + \Gamma_{ij}^k \dot{q}^i \dot{q}^j = 0 \quad (3.34)$$

with initial conditions $q(t_0) = q_0$ and $\dot{q}(t_0) = v_0$. The complete left hand side, i.e. ' $\ddot{q}^k + \Gamma_{ij}^k \dot{q}^i \dot{q}^j$,' is the k^{th} component of the geometrical acceleration expressed in coordinates. In differential geometry it is the convention to sum over indices that appear in subscripts as well as in superscripts, i.e. $\Gamma_{ij}^k \dot{q}^i \dot{q}^j$ means $\sum_{i=1}^n \sum_{j=1}^n \Gamma_{ij}^k \dot{q}^i \dot{q}^j$. This is called the *Einstein summation convention*. Later on we will see that most of the connection coefficients for a rigid body are zero, and that we can write the geometrical acceleration in matrix notation instead of the ' k^{th} component' notation (3.34). It is important to note that the k^{th} component of the geometrical acceleration of a curve expressed in coordinates, i.e. $\ddot{q}^k + \Gamma_{ij}^k \dot{q}^i \dot{q}^j$, is generally *not* identical to the second time derivative of the k^{th} coordinate of that curve, which is given by \ddot{q}^k . In the sequel we will see that, once the inertial properties of the vehicle are known, it is straightforward to calculate the connection coefficients and the equations of motion. Furthermore, we will see how the connection coefficients transform when they are expressed in another coordinate system.

3.4.2 Acceleration and gravity

As the concept of acceleration is the key ingredient for interpreting the equations of motion, we will now shortly illustrate that there are several ways to define acceleration even for the same problem. Consider an apple that is hanging in a tree. As the apple is not moving, person A says its acceleration is zero. He furthermore notes that the force resulting from gravity, i.e. $f_{grav} = -mg$, is exactly cancelled out by the force $f_{stalk} = mg$ that is exerted by the tree on the apple stalk. Thus the net force on the apple is zero, resulting in zero acceleration. Person

A writes the apple's equation of motion as

$$\ddot{h} = m^{-1}(f_{grav} + f_{stalk}), \quad (3.35)$$

with h the height of the apple above the ground and m its mass. The term ' \ddot{h} ' represents the geometrical acceleration of the apple. It is in fact equal to $\ddot{h} + \Gamma_{hh}^h \dot{h}\dot{h}$, but the Christoffel symbol $\Gamma_{hh}^h = 0$ for this case. When the stalk breaks ($f_{stalk} = 0$), then it follows that $\ddot{h} = m^{-1}f_{grav} = -g$, and the apple falls from the tree with a nonzero, negative geometric acceleration.

Person B, on the other hand, looks at the apple from a general relativistic point of view. He does not model the effect of gravity as an explicit force on the apple. Instead, in his view of the universe gravity curves the space-time continuum, and time t is part of the space-time coordinates used to describe the behavior of the apple. Information about the effects of gravity, i.e. the curvature of the space-time continuum, is encapsulated in the Christoffel symbols that are related to the metric for the space-time continuum. His equation of motion for the height of the apple reads³

$$\ddot{h} + g = m^{-1}f_{stalk} \quad (3.36)$$

Hence, for person B the geometrical acceleration of the apple is represented by the term ' $\ddot{h} + g$,' where g comes from the term $\Gamma_{tt}^h \frac{dt}{dt} \frac{dt}{dt} = g$. Thus for person A the acceleration of the apple is zero ($\ddot{h} = 0$) when it is hanging in the tree, whereas for person B the acceleration of the apple is zero ($\ddot{h} + g = 0$) when the apple is in free fall. Since person A models gravity as a force and person B does not, in both cases it is true that zero acceleration of the apple corresponds to zero net force on the apple. The physical motion of the apple is of course different for the two situations. Conversely, for a particular physical motion there can be different definitions of the geometrical acceleration depending on the view of the universe that is used. The definitions have in common that zero acceleration corresponds to zero net force on the object.

3.4.3 Equations of motion

The Lagrangian approach and the Hamiltonian approach are the two most popular methods to derive the equations of motions for mechanical systems. The Lagrangian approach uses the relative velocity $v = \dot{q}$ as state. The Hamiltonian approach uses momentum $p = mv$ as state. A manual operator can directly infer the velocity of a vehicle from its movement. Since a human operator usually has only a very rough idea about the inertial properties of the vehicle, it is much more difficult to spot the momentum of a vehicle. Furthermore, in

³Schwarzschild derived in 1916 that the gravity around a spherical body of mass M is described by $ds^2 = (1 - \frac{2GM}{c^2 r})c^2 dt^2 - (1 - \frac{2GM}{c^2 r})^{-1} c^2 dr^2 - r^2(d^2\theta + \sin^2\theta d\varphi^2)$, which is known as the *Schwarzschild solution* or *Schwarzschild metric*. Here (t, r, θ, φ) are the (spherical) coordinates for the space time-continuum, G is the gravitational constant, and c is the speed of light. The motion $\gamma \rightarrow (t, r, \theta, \varphi)$ for an object that is falling towards the center of the earth is found by computing the Christoffel symbols corresponding to the Schwarzschild metric, noting that $\frac{d\theta}{d\gamma} = \frac{d\varphi}{d\gamma} = 0$, letting $\gamma = t$ since $\frac{d^2\theta}{d\gamma^2} \approx 0$, and finally substituting $\gamma = t$ and the properties of the earth in the equation for $\frac{d^2r}{d\gamma^2}$. Since Γ_{rr}^r is very small, this yields $\frac{d^2r}{dt^2} + \Gamma_{tt}^r \frac{dt}{dt} \frac{dt}{dt} + \Gamma_{rr}^r \frac{dr}{dt} \frac{dr}{dt} \approx \ddot{r} + \frac{(c^2 r - 2GM)GM}{c^2 r^3} = \ddot{r} + g = 0$.

our problem statement the setpoints are provided in terms of velocities and not in terms of momentum. Therefore, we use the Lagrangian approach to derive the AGV's equations of motion. The floor is assumed to be an inertial reference frame. As we consider planar motions only, the influence of the earth's gravitational field is not considered.

The inertial properties of the AGV are described by the *inertia tensor*. The inertia tensor corresponding to a certain position q expressed in the coordinate frame of vector fields (e_φ, e_x, e_y) (see section 3.3.2) is a symmetric matrix:⁴

$$M_{\bar{v},v}(q_v) = \begin{pmatrix} I_v + m_v(x_{v,c}^2 + y_{v,c}^2) & & \text{sym.} \\ -m_v(x_{v,c}s\varphi_v + y_{v,c}c\varphi_v) & m_v & \\ m_v(x_{v,c}c\varphi_v - y_{v,c}s\varphi_v) & 0 & m_v \end{pmatrix}. \quad (3.37)$$

Here m_v is the mass of the AGV, $(x_{v,c}, y_{v,c})$ the coordinates of its center of gravity expressed in Ψ_v , and I_v the moment of inertia corresponding to the center of gravity. The subscript \bar{v} in $M_{\bar{v},v}$ indicates that the inertia tensor is expressed using the coordinate frame of vector fields (e_φ, e_x, e_y) . Later on we will express the inertia tensor in the frame of vector fields (e_φ, e_u, e_v) , and denote this as $M_{v,v} = M_v$. The inertia tensor defines a so-called *Riemannian metric* on the manifold, which is a norm for the magnitude of velocity vectors. We can for example use the metric to compute the *kinetic co-energy* E_k of the rigid body for a given velocity \dot{q}_v :

$$E_k = \frac{1}{2} \dot{q}_v^T M_{\bar{v},v}(q_v) \dot{q}_v. \quad (3.38)$$

For a given metric M , there is one particular unique connection that has some special properties. This special connection is called the Levi-Civita connection. Its connection coefficients are computed from the metric M as

$$\Gamma_{ij}^k = \frac{1}{2} M^{lk} \left(\frac{\partial M_{lj}}{\partial q^i} + \frac{\partial M_{li}}{\partial q^j} - \frac{\partial M_{ij}}{\partial q^l} \right). \quad (3.39)$$

Here M_{ij} denotes the $(i, j)^{th}$ component of M , and M^{ij} denotes the $(i, j)^{th}$ component of M^{-1} . When the connection coefficients of the Levi-Civita connection are expressed in a coordinate frame of vector fields, as we did here, they are also known as the *Christoffel symbols of the second kind*. For the AGV there are only two Christoffel symbols of the second kind that are nonzero:

$$(\Gamma^{\bar{v},v})_{\varphi\varphi}^x = -x_{v,c}c\varphi_v + y_{v,c}s\varphi_v \quad (3.40)$$

$$(\Gamma^{\bar{v},v})_{\varphi\varphi}^y = -x_{v,c}s\varphi_v - y_{v,c}c\varphi_v \quad (3.41)$$

Again we added the superscript \bar{v} to indicate that the connection coefficients are expressed in the coordinate frame of vector fields (e_φ, e_x, e_y) . Note that the connection coefficients depend on φ_v , but not on x_v and y_v . Now that we have the connection coefficients and, hence, the acceleration of the vehicle, we are ready to introduce the equations of motion for the AGV:

$$(\ddot{q}_v)^k + (\Gamma^{\bar{v},v})_{pr}^k (\dot{q}_v)^p (\dot{q}_v)^r = (M_{\bar{v},v})^{ks} (W^{\bar{v}})_s. \quad (3.42)$$

⁴To be precise, the inertia tensor is a 2-covariant tensor. Here we used the basis $(e_\varphi^*, e_x^*, e_y^*) \otimes (e_\varphi^*, e_x^*, e_y^*)$, with $(e_\varphi^*, e_x^*, e_y^*)$ the unique frame of co-vector fields that corresponds to the frame of vector fields (e_φ, e_x, e_y) .

The left-hand side represents the geometrical acceleration of the AGV, and $W^{\bar{v}}$ is the generalized force acting on the AGV. Generalized forces acting on rigid bodies are also called *wrenches* [114]. Although we will simplify the notation for the equations of motion in the next section, in equation (3.42) we can readily recognize the formula $a = m^{-1}f$ that we already saw in the dynamical equations (3.35)-(3.36) for the apple in section 3.4.2.

Body fixed coordinates

It is more convenient to express the equations of motion (3.42) in ‘body fixed’ coordinates. In other words, in terms of the components of the twist $T_v^{v,0}$, or, equivalently, in terms of the coordinates that correspond to the frame of vector fields (e_φ, e_u, e_v) . The matrix representation of the inertia tensor expressed in body fixed coordinates equals

$$M_v = Ad_{H_v^{\bar{v}}}^T M_{\bar{v},v} Ad_{H_v^{\bar{v}}} = \begin{pmatrix} I_v + m_v(x_{v,c}^2 + y_{v,c}^2) & -m_v y_{v,c} & m_v x_{v,c} \\ -m_v y_{v,c} & m_v & 0 \\ m_v x_{v,c} & 0 & m_v \end{pmatrix} \quad (3.43)$$

$M_{\bar{v},v}$ was abbreviated to M_v for notational convenience. The connection coefficients that represent the Levi-Civita connection are expressed in this alternative frame of vector fields (e_φ, e_u, e_v) as well, which yields four nonzero components ($\Gamma^{v,u}$ is abbreviated to Γ^v):

$$(\Gamma^v)_{\varphi\varphi}^u = -x_{v,c} \quad (3.44)$$

$$(\Gamma^v)_{\varphi v}^u = -1 \quad (3.45)$$

$$(\Gamma^v)_{\varphi\varphi}^v = -y_{v,c} \quad (3.46)$$

$$(\Gamma^v)_{\varphi u}^v = +1. \quad (3.47)$$

To express the equations of motion in a more convenient matrix notation, define the matrix $\Gamma_{v,v} = \Gamma_v$ as

$$\Gamma_v = \begin{pmatrix} (\Gamma^v)_{\varphi\varphi}^{\varphi} & (\Gamma^v)_{\varphi u}^{\varphi} & (\Gamma^v)_{\varphi v}^{\varphi} \\ (\Gamma^v)_{\varphi\varphi}^u & (\Gamma^v)_{\varphi u}^u & (\Gamma^v)_{\varphi v}^u \\ (\Gamma^v)_{\varphi\varphi}^v & (\Gamma^v)_{\varphi u}^v & (\Gamma^v)_{\varphi v}^v \end{pmatrix} = \begin{pmatrix} 0 & 0 & 0 \\ -x_{v,c} & 0 & -1 \\ -y_{v,c} & 1 & 0 \end{pmatrix} \quad (3.48)$$

Note that Γ_v is *constant*. The equations of motion in body fixed coordinates in matrix notation are

$$\dot{T}_v^{v,0} + \omega_v \Gamma_v T_v^{v,0} = M_v^{-1} (W^v)^T \quad (3.49)$$

The left-hand side again represents the geometric acceleration. Furthermore, W^v is a row vector with the components of the wrench that is exerted on the AGV expressed in Ψ_v . The row representation highlights that wrenches are of a covariant nature. The relation between the twist and the relative position of the AGV with respect to the floor was given by equation (3.22), which we will reiterate here to complete the AGV’s equations of motion:

$$\dot{H}_v^0 = H_v^0 \tilde{T}_v^{v,0} \quad (3.50)$$

For a single AGV, the net wrench acting on the AGV is equal to the wrench that is exerted by the wheels on the AGV. Hence, the equation of motion for a single AGV satisfies

$$\dot{T}_v^{v,0} + \omega_v \Gamma_v T_v^{v,0} = M_v^{-1} (W_w^v)^T, \quad (3.51)$$

where W_w^v is the wrench that is exerted by the wheels on the vehicle. The model for the wheels is discussed in the next section.

3.5 Wheel model

The wrench W_w^v that is exerted by the wheels on the AGV depends on the longitudinal and lateral forces that are acting on each wheel. The model for a single wheel consists of two parts. The kinematic part describes how the twist of wheel w_i with respect to the floor is related to the twist of the AGV with respect to the floor and the steering angles. The second part is formed by the constitutive equations that describe the relation between the wrench that is exerted by the wheel on the vehicle and the twist of the wheel with respect to the floor.

For the OLS vehicles, the longitudinal wheel forces are prescribed by electric drive systems, and the lateral wheel forces depend on the twist of the vehicle with respect to the floor and the steering angles of the wheels. The steering angles are realized by electric servo systems.

3.5.1 Kinematics

Consider wheel w_i of an arbitrary AGV. We attach a coordinate system Ψ_{w_i} to the wheel such that the x_{w_i} -axis is aligned with the wheel plane, the y_{w_i} -axis is perpendicular to the wheel plane, and the origin is at the center of the contact patch of the wheel. This is illustrated in Figure 3.11. Furthermore, the steering angle δ_{w_i} for wheel w_i is defined as the relative angle of Ψ_{w_i} with respect to Ψ_v , see also Figure 3.11. Thus the steering angle is zero when the x_{w_i} -axes of Ψ_{w_i} is aligned with the x_v -axis of Ψ_v . The relative position of the wheel with

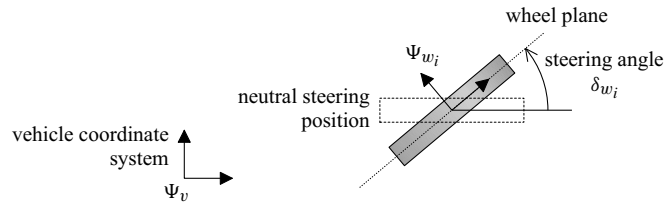


Figure 3.11: Definitions of the coordinate system Ψ_{w_i} and the steering angle δ_{w_i} for wheel w_i of an arbitrary AGV.

respect to the vehicle is parameterized by a homogeneous matrix $H_{w_i}^v$ that depends on the steering angle δ_{w_i} of wheel w_i , i.e. $H_{w_i}^v = H_{w_i}^v(\delta_{w_i})$. The twist of the wheel with respect to the vehicle can be expressed in the Ψ_{w_i} coordinate system and satisfies

$$\tilde{T}_{w_i}^{w_i,v} = H_v^{w_i} \dot{H}_{w_i}^v = H_v^{w_i} \left. \frac{\partial H_{w_i}^v}{\partial \delta_{w_i}} \right|_{\delta_{w_i}} \dot{\delta}_{w_i}. \quad (3.52)$$

The twist of the wheel with respect to the floor expressed in Ψ_{w_i} reads

$$\begin{aligned}\tilde{T}_{w_i}^{w_i,0} &= H_0^{w_i} \dot{H}_{w_i}^0 = H_v^{w_i} H_0^v \frac{dH_v^0 H_{w_i}^v}{dt} = H_v^{w_i} \underbrace{H_0^v \dot{H}_v^0}_{\tilde{T}_v^{v,0}} H_{w_i}^v + \underbrace{H_v^{w_i} \overbrace{H_0^v H_v^0}^I}_{\tilde{T}_{w_i}^{v,v}} \dot{H}_{w_i}^v \\ &= H_v^{w_i} \tilde{T}_v^{v,0} H_{w_i}^v + \tilde{T}_{w_i}^{w_i,v},\end{aligned}\quad (3.53)$$

which can also be written as

$$\boxed{T_{w_i}^{w_i,0} = Ad_{H_v^{w_i}} T_v^{v,0} + T_{w_i}^{w_i,v} = T_v^{w_i,0} + T_{w_i}^{w_i,v}} \quad (3.54)$$

Here $Ad_{H_v^{w_i}}$ depends on δ_{w_i} , and $T_{w_i}^{w_i,v}$ generally depends on both δ_{w_i} and $\dot{\delta}_{w_i}$. Thus we see that the twist of the wheel with respect to the floor is equal to the twist of the vehicle with respect to the floor plus the twist of the wheel with respect to the vehicle.

3.5.2 Constitutive equations

In section 3.2.3 it was discussed that there exist numerous tire models in the literature. All models have in common that the relation between the quantities that represent the tire deformation and the induced wrench is approximately linear for normal operation. For more extreme maneuvers, i.e. when a vehicle is subjected to high accelerations, the tire deformation becomes larger and nonlinearities start to appear. In the most extreme cases, e.g. during braking with full wheel lock, the tire simply behaves as a piece of rubber that is dragged over the ground. Since AGVs are operated such that extreme accelerations are avoided, the tire deformation remains relatively small and the tire operates in its linear region. Therefore, we will restrict ourselves to *linear tire models*. This means that the relation between the slip and the induced force is linear. Additionally, attention is restricted to *static tire models*, i.e. models where the relation between the slip and the induced wrench is static.

First we introduce the tire model that is used by FROG in its applications. Subsequently we show that when some small terms are neglected, the FROG model is identical to the linear tire models that are commonly found in literature.

FROG tire model

According to the FROG tire model, the wrench that is exerted by wheel w_i on the vehicle expressed in Ψ_{w_i} reads

$$W_{w_i}^{w_i,v} = \begin{pmatrix} 0 & C_{\text{long}}^{w_i} \frac{\dot{\theta}_{w_i} r_{w_i} - (T_{w_i}^{w_i,0})_u}{|\dot{\theta}_{w_i}| r_{w_i}} & -C_{\text{lat}}^{w_i} \frac{(T_{w_i}^{w_i,0})_v}{|\dot{\theta}_{w_i}| r_{w_i}} \end{pmatrix}, \quad (3.55)$$

with $C_{\text{long}}^{w_i}$ the *longitudinal stiffness*, $C_{\text{lat}}^{w_i}$ the *lateral cornering stiffness*, r_{w_i} the wheel radius of wheel w_i . $\dot{\theta}_{w_i}$ is the wheel's *spin velocity*, i.e. the rotational velocity of the wheel about its shaft. Furthermore, $(T_{w_i}^{w_i,0})_u$ denotes the second component and $(T_{w_i}^{w_i,0})_v$ the third component of $T_{w_i}^{w_i,0}$, respectively. The “0” in the equation above means that the aligning moment

of the wheel is neglected. For the OLS vehicles, the longitudinal wheel force $(W_{w_i}^{w_i,v})_u$ is prescribed by a drive system. Solving the longitudinal wheel velocity $(T_{w_i}^{w_i,0})_u$ for a given longitudinal wheel force $(W_{w_i}^{w_i,v})_u$ from the second component of equation (3.55) yields

$$\boxed{(T_{w_i}^{w_i,0})_u = \dot{\theta}_{w_i} r_{w_i} - \frac{|\dot{\theta}_{w_i}| r_{w_i} (W_{w_i}^{w_i,v})_u}{C_{\text{long}}^{w_i}} = \dot{\theta}_{w_i} r_{w_i} \left(1 - \frac{(W_{w_i}^{w_i,v})_u}{C_{\text{long}}^{w_i}} \text{sign}(\dot{\theta}_{w_i}) \right)} \quad (3.56)$$

This equation can for example be used to estimate the longitudinal velocity of the wheel for a given measured spin velocity $\dot{\theta}_{w_i}$ and drive setpoint $(W_{w_i}^{w_i,v})_u$. Because during normal operation $|(W_{w_i}^{w_i,v})_u|/C_{\text{long}}^{w_i} < 0.1$ [-], the last term in the equation above is always larger than zero. The wheel radius r_{w_i} is also larger than zero. Therefore, it follows that, according to the FROG wheel model, the spin velocity $\dot{\theta}_{w_i}$ must have the same sign as the longitudinal wheel velocity during normal operation:

$$\text{sign}(\dot{\theta}_{w_i}) = \text{sign}(T_{w_i}^{w_i,0})_u. \quad (3.57)$$

After substituting this equality in equation (3.56), solving for $\frac{1}{\dot{\theta}_{w_i} r_{w_i}}$ and subsequently for $\frac{1}{|\dot{\theta}_{w_i}| r_{w_i}}$ results in

$$\frac{1}{\dot{\theta}_{w_i} r_{w_i}} = \frac{1 - \frac{(W_{w_i}^{w_i,v})_u}{C_{\text{long}}^{w_i}} \text{sign}(T_{w_i}^{w_i,0})_u}{(T_{w_i}^{w_i,0})_u} \Rightarrow \frac{1}{|\dot{\theta}_{w_i}| r_{w_i}} = \frac{1 - \frac{(W_{w_i}^{w_i,v})_u}{C_{\text{long}}^{w_i}} \text{sign}(T_{w_i}^{w_i,0})_u}{|(T_{w_i}^{w_i,0})_u|}. \quad (3.58)$$

By substituting the last expression in the third component of equation (3.55), we find that the lateral wheel force $(W_{w_i}^{w_i,v})_v$ satisfies

$$(W_{w_i}^{w_i,v})_v = -C_{\text{lat}}^{w_i} \frac{(T_{w_i}^{w_i,0})_v}{|(T_{w_i}^{w_i,0})_u|} \left(1 - \overbrace{\frac{(W_{w_i}^{w_i,v})_u}{C_{\text{long}}^{w_i}} \text{sign}(T_{w_i}^{w_i,0})_u}^{\text{small}} \right). \quad (3.59)$$

In the sequel we will neglect the contribution of the coupling term $\frac{(W_{w_i}^{w_i,v})_u}{C_{\text{long}}^{w_i}} \text{sign}(T_{w_i}^{w_i,0})_u$ to the lateral wheel force. Thus for a given drive force $(W_{w_i}^{w_i,v})_u$, the wrench that is exerted by wheel w_i on the vehicle satisfies

$$\boxed{W_{w_i}^{w_i,v} = \left(0 \quad (W_{w_i}^{w_i,v})_u \quad -C_{\text{lat}}^{w_i} \frac{(T_{w_i}^{w_i,0})_v}{|(T_{w_i}^{w_i,0})_u|} \right)} \quad (3.60)$$

Relation to other wheel models described in literature

The slip quantities that are typically encountered in the tire models found in literature are the *slip angle* α for the lateral tire behavior and the *longitudinal slip* κ for the longitudinal

behavior. The slip angle α_{w_i} for wheel w_i is usually defined as

$$\alpha_{w_i} = \arctan \left(\frac{(T_{w_i}^{w_i,0})_v}{|(T_{w_i}^{w_i,0})_u|} \right) \approx \frac{(T_{w_i}^{w_i,0})_v}{|(T_{w_i}^{w_i,0})_u|} \quad (3.61)$$

For our applications α_{w_i} is small, typically less than 5 deg. Then α_{w_i} is approximately equal to the ratio of the lateral and longitudinal wheel velocities as indicated above. The longitudinal slip κ_{w_i} for wheel w_i is typically defined as

$$\kappa_{w_i} = \frac{\dot{\theta}_{w_i} r_{w_i} - (T_{w_i}^{w_i,0})_u}{|(T_{w_i}^{w_i,0})_u|}, \quad (3.62)$$

where r_{w_i} is the *effective rolling radius* of wheel w_i . The absolute signs in the denominator are often left out when only forward driving is considered. Comparing the slip quantities α_{w_i} and κ_{w_i} with the quantities that are used in the FROG tire model, i.e. respectively $\frac{(T_{w_i}^{w_i,0})_v}{|\dot{\theta}_{w_i} r_{w_i}|}$ and $\frac{\dot{\theta}_{w_i} r_{w_i} - (T_{w_i}^{w_i,0})_u}{|\dot{\theta}_{w_i} r_{w_i}|}$ (see equation (3.55)), then we see that they are very similar. In particular, the slopes of the slip-force relation is identical for the zero slip situation. With the aid of side slip angle α_{w_i} , the wrench that is exerted by wheel w_i on the vehicle can be written as

$$W_{w_i}^{w_i,v} = (0 \quad (W_{w_i}^{w_i,v})_u \quad -C_{\text{lat}}^{w_i} \alpha_{w_i}) \quad (3.63)$$

Note the linear relation between the lateral wheel force $(W_{w_i}^{w_i,v})_v$ and the slip angle α_{w_i} . The slope is determined by the cornering stiffness $C_{\text{lat}}^{w_i}$. This is in correspondence with the linear, static tire models that are found in literature.

Netto wrench exerted by the wheels on the vehicle

The netto wrench $W_w^{v,v} \stackrel{\text{def}}{=} W_w^v$ that is produced by the n wheels together on the vehicle is equal to the sum of the individual wrenches:

$$W_w^v = \sum_{i=1}^n W_{w_i}^v = \sum_{i=1}^n W_{w_i}^{w_i,v} Ad_{H_v^{w_i}} \quad (3.64)$$

Note that $Ad_{H_v^{w_i}}$ depends on δ_{w_i} as $H_v^{w_i}$ depends on δ_{w_i} . For the OLS vehicles we have $n = 2$ as the caster wheel is assumed to produce no forces. This completes the model of the wheels.

3.5.3 Additional assumptions for OLS vehicles

The wheel units of the OLS vehicles were designed such that the center of the contact patch of the wheels remains at the same place with respect to the vehicle when the wheels are steered. This makes it possible to steer when the vehicle stands still without moving the

vehicle. Therefore, for the OLS vehicles it is assumed that the origin of Ψ_{w_i} is fixed with respect to Ψ_v . Then it is easily seen that the twist of wheel w_i with respect to the vehicle satisfies

$$T_{w_i}^{w_i,v} = \begin{pmatrix} \dot{\delta}_{w_i} \\ 0 \\ 0 \end{pmatrix}. \quad (3.65)$$

Since $T_{w_i}^{w_i,0} = T_v^{w_i,0} + T_{w_i}^{w_i,v}$ (see equation (3.54)) and the u - and v -components of $T_{w_i}^{w_i,v}$ are zero for the OLS vehicles (see above), this implies that

$$(T_{w_i}^{w_i,0})_u = (T_v^{w_i,0})_u \quad (3.66)$$

$$(T_{w_i}^{w_i,0})_v = (T_v^{w_i,0})_v. \quad (3.67)$$

These equations (3.66)-(3.67) can be used to rewrite the wrench that is exerted by wheel w_i on the AGV (3.60) as

$$W_{w_i}^{w_i,v} = \begin{pmatrix} 0 & (W_{w_i}^{w_i,v})_u & -C_{\text{lat}}^{w_i} \frac{(T_v^{w_i,0})_v}{|(T_v^{w_i,0})_u|} \end{pmatrix}. \quad (3.68)$$

Thus the wrench that is exerted by a certain wheel on the OLS vehicle depends on the twist $T_v^{w_i,0}$ of the AGV with respect to the floor, but *not* on the twist $T_{w_i}^{w_i,v}$ of the wheel with respect to the AGV.

Alternative notation for wrenches exerted by wheels

To ease notation, define the longitudinal velocity u_{w_i} , the lateral velocity v_{w_i} , the longitudinal force $F_{w_i,u}$ and the lateral force $F_{w_i,v}$ for wheel w_i as

$$\begin{array}{l} u_{w_i} = (T_{w_i}^{w_i,0})_u = (T_v^{w_i,0})_u \\ v_{w_i} = (T_{w_i}^{w_i,0})_v = (T_v^{w_i,0})_v \\ F_{w_i,u} = (W_{w_i}^{w_i,v})_u \\ F_{w_i,v} = (W_{w_i}^{w_i,v})_v \end{array} \quad (3.69)$$

The assumption that the actuated wheels of the OLS AGV steer about the center of their contact patch (3.66)-(3.67) was used in the first two equations. As the caster wheel is assumed to exert no horizontal forces on the OLS AGVs, we consider the situation that $i \in \{1, 2\}$ for now. To express the wrench W_w^v that is exerted by the wheels on the OLS vehicle in a more convenient form, define matrix B as

$$B = B(\delta_{w_1}, \delta_{w_2}) = \begin{pmatrix} B_{w_1,u} \\ B_{w_2,u} \\ B_{w_1,v} \\ B_{w_2,v} \end{pmatrix} = \begin{pmatrix} x_{w_1}^v s\delta_{w_1} - y_{w_1}^v c\delta_{w_1} & c\delta_{w_1} & s\delta_{w_1} \\ x_{w_2}^v s\delta_{w_2} - y_{w_2}^v c\delta_{w_2} & c\delta_{w_2} & s\delta_{w_2} \\ x_{w_1}^v c\delta_{w_1} + y_{w_1}^v s\delta_{w_1} & -s\delta_{w_1} & c\delta_{w_1} \\ x_{w_2}^v c\delta_{w_2} + y_{w_2}^v s\delta_{w_2} & -s\delta_{w_2} & c\delta_{w_2} \end{pmatrix} \quad (3.70)$$

Here $(x_{w_i}^v, y_{w_i}^v)$ are the coordinates of the center of wheel w_i expressed in Ψ_v . It can be shown that

$$u_{w_i} = B_{w_i,u} T_v^{v,0} \quad (3.71)$$

$$v_{w_i} = B_{w_i,v} T_v^{v,0}. \quad (3.72)$$

Now the wrench W_w^v that is exerted by the wheels on the vehicle can be written as

$$\begin{aligned}
 (W_w^v)^T &= \sum_{i=1}^n Ad_{H_v}^{T w_i} (W_{w_i}^{w_i, v})^T = B^T \begin{pmatrix} F_{w_1, u} \\ F_{w_2, u} \\ -C_{\text{lat}}^{w_1} \frac{v_{w_1}}{|u_{w_1}|} \\ -C_{\text{lat}}^{w_2} \frac{v_{w_2}}{|u_{w_2}|} \end{pmatrix} \\
 &= \begin{pmatrix} B_{w_1, u} \\ B_{w_2, u} \end{pmatrix}^T \begin{pmatrix} F_{w_1, u} \\ F_{w_2, u} \end{pmatrix} - \begin{pmatrix} C_{\text{lat}}^{w_1} B_{w_1, v}^T \\ C_{\text{lat}}^{w_2} B_{w_2, v}^T \end{pmatrix}^T \begin{pmatrix} \frac{B_{w_1, v}}{|B_{w_1, u} T_v^{v, 0}|} \\ \frac{B_{w_2, v}}{|B_{w_2, u} T_v^{v, 0}|} \end{pmatrix} T_v^{v, 0}
 \end{aligned} \tag{3.73}$$

Although the expression above is tailored for the OLS vehicles with $n = 2$ actuated wheels, it can easily be generalized to an AGV with n actuated wheels as long as they all steer about the centers of their corresponding contact patches and the wheel slip remains small.

3.6 Model of a single AGV that is affine in the inputs

The equations of motion for the AGV that were derived in the previous sections consist of two parts. One part describes the relation between the geometrical acceleration and the wrench that is acting on the AGV (3.49). The other part relates the derivative of the AGV's relative position to the instantaneous relative twist of the AGV (3.50). As this thesis mainly focuses on control at the velocity level of the AGV, we are mainly interested in the former. Recall that acceleration of a single OLS AGV is described by (3.49)

$$\dot{T}_v^{v, 0} + \omega_v \Gamma_v T_v^{v, 0} = M_v^{-1} (W_w^v)^T, \tag{3.74}$$

with W_w^v the wrench that is exerted by the wheels on the vehicle (3.73):

$$(W_w^v)^T = B^T \begin{pmatrix} F_{w_1, u} \\ F_{w_2, u} \\ -C_{\text{lat}}^{w_1} \frac{v_{w_1}}{|u_{w_1}|} \\ -C_{\text{lat}}^{w_2} \frac{v_{w_2}}{|u_{w_2}|} \end{pmatrix}. \tag{3.75}$$

Here B depends on $(\delta_{w_1}, \delta_{w_2})$. If we consider the inputs to be $(F_{w_1, u}, F_{w_2, u}, \delta_{w_1}, \delta_{w_2})$ and take the twist $T_v^{v, 0}$ as the state x , then we see that equation (3.74) combined with equation (3.75) is of the form

$$\dot{x} = f(x, F_{w_1, u}, F_{w_2, u}, \delta_{w_1}, \delta_{w_2}). \tag{3.76}$$

This model is obviously not affine in the inputs $(F_{w_1, u}, F_{w_2, u}, \delta_{w_1}, \delta_{w_2})$. This makes it for example difficult to find the inputs corresponding to the equilibrium $\dot{x} = \dot{T}_v^{v, 0} = 0$. In addition, several analysis tools for nonlinear systems require that the nonlinear system is affine in the inputs. It is therefore desirable to adjust the model such that it does become affine in the inputs.

First it is briefly discussed why two traditional methods to achieve input affinity are not so appropriate for the AGV model. Subsequently, the model is approximated using the momentary twist $T_v^{v,0}$ of the vehicle with respect to the floor and the corresponding ‘kinematic steering angles’ as a starting point. The simplified model will be used in Chapter 5 to show that a single AGV is locally observable, and in Chapter 6 to show that the state is locally strongly accessible.

3.6.1 Traditional methods

In handling dynamics studies of passenger cars and trucks, the steering angles δ_{w_i} remain typically small: $\delta_{w_i} \approx 0$. So in those studies the vehicle models are often linearized about the nominal steering angle(s) $\delta_{w_i} = 0$. In the OLS vehicles we consider, however, the steering angles can become as large as 85 [deg]. Thus in our applications it is not justifiable to linearize about $\delta_{w_i} = 0$ to produce a system that is affine in the inputs.

Another method to achieve input affinity is by defining new inputs $v_{1\dots 2n}$ that are equal to the derivatives of the original inputs (see e.g. p. 190 in [89]). Then the system becomes

$$\dot{T}_v^{v,0} = f(T_v^{v,0}, F_{w_1,u}, F_{w_2,u}, \delta_{w_1}, \delta_{w_2}) \quad (3.77)$$

$$\dot{F}_{w_i,u} = v_i \quad (3.78)$$

$$\dot{\delta}_{w_i} = v_{n+i}, \quad (3.79)$$

with $x = (T_v^{v,0}, F_{w_1,u}, F_{w_2,u}, \delta_{w_1}, \delta_{w_2})^T$ the new state. Although the above model is indeed affine in the new inputs $v_{1\dots 2n}$, the new state has dimension seven and the model is as complex as the original model. Therefore, we will follow a different approach to achieve affine inputs. Before we discuss the approximation, we will first introduce the concept of the kinematic steering angle.

3.6.2 Kinematic steering angle

Suppose that the twist $T_v^{v,0}$ of the vehicle with respect to the floor is given. If wheel w_i is modelled as a nonholonomic constraint, i.e. such that wheel slip cannot occur, then the wheel plane must be aligned with the velocity vector of the wheel. Otherwise motion is not possible. The steering angle $\bar{\delta}_{w_i}$ corresponding to this theoretical, nonholonomic situation is called the *kinematic steering angle* for wheel w_i . When there is no lateral wheel slip, this implies that $T_{w_i}^{w_i,0}$ is of the form

$$T_{w_i}^{w_i,0} = Ad_{H_{w_i}^v} T_v^{v,0} + T_{w_i}^{w_i,v} = \begin{pmatrix} * \\ * \\ 0 \end{pmatrix}. \quad (3.80)$$

We already saw with equation (3.65) that the last component of $T_{w_i}^{w_i,0}$ is zero for the OLS vehicles. Furthermore, the relative position of wheel w_i with respect to the vehicle is given by

$$H_{w_i}^v = \begin{pmatrix} c\delta_{w_i} & -s\delta_{w_i} & x_{w_i}^v \\ s\delta_{w_i} & c\delta_{w_i} & y_{w_i}^v \\ 0 & 0 & 1 \end{pmatrix}, \quad (3.81)$$

and the relative position of the vehicle with respect to the wheel w_i satisfies

$$H_v^{w_i} = (H_{w_i}^v)^{-1} = \begin{pmatrix} c\delta_{w_i} & s\delta_{w_i} & -x_{w_i}^v c\delta_{w_i} - y_{w_i}^v s\delta_{w_i} \\ -s\delta_{w_i} & c\delta_{w_i} & x_{w_i}^v s\delta_{w_i} - y_{w_i}^v c\delta_{w_i} \\ 0 & 0 & 1 \end{pmatrix}, \quad (3.82)$$

with $(x_{w_i}^v, y_{w_i}^v)$ the coordinates of the wheel center expressed in Ψ_v , and $(x_v^{w_i}, y_v^{w_i})$ the coordinates of the origin of Ψ_v expressed in Ψ_{w_i} . Hence,

$$Ad_{H_v^{w_i}} = \begin{pmatrix} 1 & 0 & 0 \\ y_v^{w_i} & c\delta_{w_i} & s\delta_{w_i} \\ -x_v^{w_i} & -s\delta_{w_i} & c\delta_{w_i} \end{pmatrix} = \begin{pmatrix} 1 & 0 & 0 \\ x_{w_i}^v s\delta_{w_i} - y_{w_i}^v c\delta_{w_i} & c\delta_{w_i} & s\delta_{w_i} \\ x_{w_i}^v c\delta_{w_i} + y_{w_i}^v s\delta_{w_i} & -s\delta_{w_i} & c\delta_{w_i} \end{pmatrix}. \quad (3.83)$$

Use this expression to rewrite the bottom row of equation (3.80) as

$$\begin{aligned} 0 &= (x_{w_i}^v c\delta_{w_i} + y_{w_i}^v s\delta_{w_i})(T_v^{v,0})_\varphi - s\delta_{w_i}(T_v^{v,0})_u + c\delta_{w_i}(T_v^{v,0})_v \\ &= \left(x_{w_i}^v (T_v^{v,0})_\varphi + (T_v^{v,0})_v\right) c\delta_{w_i} + \left(y_{w_i}^v (T_v^{v,0})_\varphi - (T_v^{v,0})_u\right) s\delta_{w_i} \\ &= (x_{w_i}^v \omega_v + v_v) c\delta_{w_i} + (y_{w_i}^v \omega_v - u_v) s\delta_{w_i}. \end{aligned} \quad (3.84)$$

All solutions to this transcendental equation are [44]

$$\delta_{w_i} = \arctan\left(\frac{x_{w_i}^v \omega_v + v_v}{-y_{w_i}^v \omega_v + u_v}\right) + k\pi, \quad k \in \mathbb{N}. \quad (3.85)$$

In theory, each solution corresponds to a kinematic steering angle $\bar{\delta}_{w_i}$. By physical considerations, we select the one with the smallest absolute value. This yields the relation between the kinematic steering angle $\bar{\delta}_{w_i}$ and the twist of the vehicle $T_v^{v,0}$ that we were looking for:

$$\boxed{\bar{\delta}_{w_i} = \arctan\left(\frac{x_{w_i}^v \omega_v + v_v}{-y_{w_i}^v \omega_v + u_v}\right)} \quad (3.86)$$

Finally, we define a new coordinate system $\Psi_{\bar{w}_i}$ such that its origin coincides with the origin of Ψ_{w_i} and that its relative rotation with respect to Ψ_v equals $\bar{\delta}_{w_i}$. This is illustrated in Figure 3.12.

3.6.3 Approximation based on the momentary twist

We will use these kinematic steering angles that correspond to the momentary twist $T_v^{v,0}$ as the basis for our approximation. Since the slip angle α_{w_i} for wheel w_i is in fact defined as the difference between the kinematic steering angle $\bar{\delta}_{w_i}$ and the true steering angle δ_{w_i} , see also equation (3.61), the latter can be written as

$$\boxed{\delta_{w_i} = \bar{\delta}_{w_i} - \alpha_{w_i} \text{sign}(u_{w_i}) = \bar{\delta}_{w_i} - \alpha_{w_i} \text{sign}(u_{\bar{w}_i})} \quad (3.87)$$

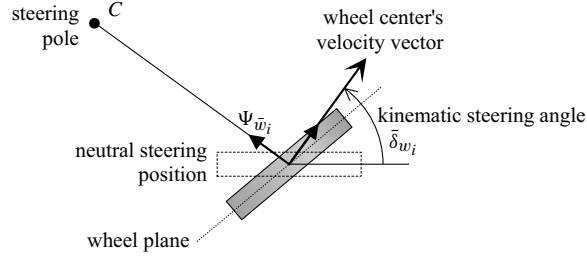


Figure 3.12: Definition of the kinematic steering angle $\bar{\delta}_{w_i}$ and coordinate system $\Psi_{\bar{w}_i}$ for wheel w_i .

The sign is added to account for backwards driving. Here u_{w_i} is the longitudinal velocity of the wheel center with respect to the floor expressed in Ψ_{w_i} . Analogously, $u_{\bar{w}_i}$ is the longitudinal velocity of the wheel center with respect to the floor expressed in $\Psi_{\bar{w}_i}$. For $|\delta_{w_i}| < \frac{\pi}{2}$ it holds that

$$\text{sign}(u_{w_i}) = \text{sign}(u_{\bar{w}_i}). \quad (3.88)$$

Matrix B will be approximated using first order Taylor expansion around the kinematic steering angles $\bar{\delta}_{w_i}$. The derivatives of the rows of B with respect to the steering angles satisfy

$$\begin{aligned} \frac{\partial B_{w_i,u}}{\partial \delta_{w_i}} &= \frac{\partial}{\partial \delta_{w_i}} (x_{w_i}^v s\delta_{w_i} - y_{w_i}^v c\delta_{w_i} \quad c\delta_{w_i} \quad s\delta_{w_i}) \\ &= (x_{w_i}^v c\delta_{w_i} + y_{w_i}^v s\delta_{w_i} \quad -s\delta_{w_i} \quad c\delta_{w_i}) = B_{w_i,v} \end{aligned} \quad (3.89)$$

$$\begin{aligned} \frac{\partial B_{w_i,v}}{\partial \delta_{w_i}} &= \frac{\partial}{\partial \delta_{w_i}} (x_{w_i}^v c\delta_{w_i} + y_{w_i}^v s\delta_{w_i} \quad -s\delta_{w_i} \quad c\delta_{w_i}) \\ &= (-x_{w_i}^v s\delta_{w_i} + y_{w_i}^v c\delta_{w_i} \quad -c\delta_{w_i} \quad -s\delta_{w_i}) = -B_{w_i,u} \end{aligned} \quad (3.90)$$

and

$$\frac{\partial B_{w_i,u}}{\partial \delta_{w_j}} = \frac{\partial B_{w_i,v}}{\partial \delta_{w_j}} = 0, \quad i \neq j. \quad (3.91)$$

Hence, the first order Taylor approximation for B around the kinematic steering angles $\bar{\delta}_{w_i}$ is

$$B = \begin{pmatrix} B_{w_1,u} \\ B_{w_2,u} \\ B_{w_1,v} \\ B_{w_2,v} \end{pmatrix} \approx \begin{pmatrix} \bar{B}_{w_1,u} - \frac{\partial B_{w_1,u}}{\partial \delta_{w_1}} \Big|_{\bar{\delta}_{w_1}} \alpha_{w_1} \text{sign}(u_{\bar{w}_1}) \\ \bar{B}_{w_2,u} - \frac{\partial B_{w_2,u}}{\partial \delta_{w_2}} \Big|_{\bar{\delta}_{w_2}} \alpha_{w_2} \text{sign}(u_{\bar{w}_2}) \\ \bar{B}_{w_1,v} - \frac{\partial B_{w_1,v}}{\partial \delta_{w_1}} \Big|_{\bar{\delta}_{w_1}} \alpha_{w_1} \text{sign}(u_{\bar{w}_1}) \\ \bar{B}_{w_2,v} - \frac{\partial B_{w_2,v}}{\partial \delta_{w_2}} \Big|_{\bar{\delta}_{w_2}} \alpha_{w_2} \text{sign}(u_{\bar{w}_2}) \end{pmatrix} = \begin{pmatrix} \bar{B}_{w_1,u} - \bar{B}_{w_1,v} \alpha_{w_1} \text{sign}(u_{\bar{w}_1}) \\ \bar{B}_{w_2,u} - \bar{B}_{w_2,v} \alpha_{w_2} \text{sign}(u_{\bar{w}_2}) \\ \bar{B}_{w_1,v} + \bar{B}_{w_1,u} \alpha_{w_1} \text{sign}(u_{\bar{w}_1}) \\ \bar{B}_{w_2,v} + \bar{B}_{w_2,u} \alpha_{w_2} \text{sign}(u_{\bar{w}_2}) \end{pmatrix}, \quad (3.92)$$

where

$$\begin{pmatrix} \bar{B}_{w_1,u} \\ \bar{B}_{w_2,u} \\ \bar{B}_{w_1,v} \\ \bar{B}_{w_2,v} \end{pmatrix} = \begin{pmatrix} B_{w_1,u}(\bar{\delta}_{w_1}) \\ B_{w_2,u}(\bar{\delta}_{w_2}) \\ B_{w_2,v}(\bar{\delta}_{w_2}) \\ B_{w_2,v}(\bar{\delta}_{w_2}) \end{pmatrix} = \bar{B} \quad (3.93)$$

Substitute this in (3.75), neglect the slip angles for the longitudinal forces $F_{w_i,u}$, neglect the higher order terms with $\alpha_{w_i}^2$, and use $\bar{B}_{w_i,v}T_v^{v,0} = 0$ to arrive at

$$\begin{aligned} (W_w^v)^T &\approx \begin{pmatrix} \bar{B}_{w_1,u}^T & \bar{B}_{w_2,u}^T \end{pmatrix} \begin{pmatrix} F_{w_1,u} \\ F_{w_2,u} \end{pmatrix} - \begin{pmatrix} \frac{C_{\text{lat}}^{w_1} \bar{B}_{w_1,v}^T \bar{B}_{w_1,u} \alpha_{w_1} \text{sign}(u_{\bar{w}_1})}{|\bar{B}_{w_1,u} T_v^{v,0}|} \\ \frac{C_{\text{lat}}^{w_2} \bar{B}_{w_2,v}^T \bar{B}_{w_2,u} \alpha_{w_2} \text{sign}(u_{\bar{w}_2})}{|\bar{B}_{w_2,u} T_v^{v,0}|} \end{pmatrix} T_v^{v,0} \\ &= \begin{pmatrix} \bar{B}_{w_1,u}^T & \bar{B}_{w_2,u}^T & -C_{\text{lat}}^{w_1} \bar{B}_{w_1,v}^T & -C_{\text{lat}}^{w_2} \bar{B}_{w_2,v}^T \end{pmatrix} \begin{pmatrix} F_{w_1,u} \\ F_{w_2,u} \\ \alpha_{w_1} \\ \alpha_{w_2} \end{pmatrix} \end{aligned} \quad (3.94)$$

Here we used that $\bar{B}_{w_i,u} T_v^{v,0} \text{sign}(u_{\bar{w}_i}) = |\bar{B}_{w_i,u} T_v^{v,0}|$. The physical interpretation of the above approximation is that the longitudinal drive forces $F_{w_i,u}$ are tangent to the instantaneous motion of the corresponding wheel centers. The lateral tire forces $-C_{\text{lat}}^{w_i} \alpha_{w_i}$ act perpendicular to the instantaneous motion of the corresponding wheel centers, i.e. in the direction of the steering pole. This is illustrated in Figure 3.13. Next, define the inputs u as

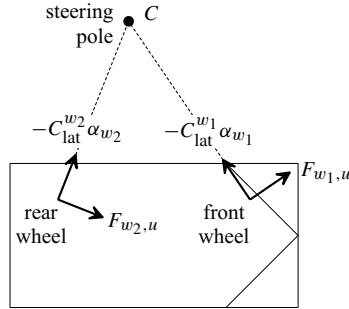


Figure 3.13: Physical interpretation of the approximated wheel forces in the simplified AGV model.

$$u = \begin{pmatrix} F_{w_1,u} \\ F_{w_2,u} \\ \alpha_{w_1} \\ \alpha_{w_2} \end{pmatrix} \quad (3.95)$$

From equation (3.94) we see that there is a linear relation between the wrench W_w^v and the above inputs u . Take $x = T_v^{v,0}$ as the vehicle state. Since the mass matrix M_v^{-1} of the vehicle

is constant, we see that with the approximations above the vehicle model is now of the form

$$\dot{x} = f(x) + g(x)u, \quad (3.96)$$

with

$$f(x) = -\omega_v \Gamma_v T_v^{v,0} \quad (3.97)$$

and

$$g(x) = M_v^{-1} \begin{pmatrix} \bar{B}_{w_1,u}^T & \bar{B}_{w_2,u}^T & -C_{\text{lat}}^{w_1} \bar{B}_{w_1,v}^T & -C_{\text{lat}}^{w_2} \bar{B}_{w_2,v}^T \end{pmatrix}. \quad (3.98)$$

As desired, the simplified model is affine in the inputs u .

3.7 Model of the interconnected system

In the cooperative transportation applications we consider, multiple AGVs operate together to transport a load. Whereas the previous sections deal with modeling of the dynamic behavior of single AGVs, this section will treat the modeling of the interconnected system consisting of an arbitrary number AGVs and a single load.

3.7.1 Equation of motion for the load

It is assumed that the load can be modelled as a planar rigid body. Therefore, the equations of motion for the load are very similar to the equations of motion for a single AGV (3.49). We fix a coordinate system Ψ_ℓ to the load. Let us denote the twist of the load with respect to the floor and expressed in Ψ_ℓ as $T_\ell^{\ell,0}$, and denote the wrench that is exerted by all the vehicles on the load and expressed in Ψ_ℓ as $W_V^{\ell,\ell} \stackrel{\text{def}}{=} W_V^\ell$. Then the equations of motion for the load are written as

$$\boxed{\dot{T}_\ell^{\ell,0} + \omega_\ell \Gamma_\ell T_\ell^{\ell,0} = M_\ell^{-1} (W_V^\ell)^T} \quad (3.99)$$

The matrices Γ_ℓ and M_ℓ are given by equations (3.43) and (3.48), respectively. The wrench W_V^ℓ that is exerted by all the AGVs on the load is the sum of the AGVs' individual wrenches on the load:

$$W_V^\ell = W_{v_1}^\ell + \dots + W_{v_N}^\ell = \sum_{k=1}^N W_{v_k}^\ell, \quad (3.100)$$

where N is the number of AGVs and $W_{v_k}^\ell$ the wrench that is exerted by AGV k on the load.

3.7.2 Interconnections

The ultimate goal of our transportation task is to move a certain object from one place to another. The motion of the object can be influenced by exerting wrenches on the object, which is also illustrated by equation (3.99). In our case the net wrench W_V^ℓ that is applied to the load is produced by the wrenches $W_{v_k}^\ell$ that are exerted by the individual AGVs on the load. If we want to be able to move the load in an arbitrary direction, then all the AGVs together must be able to generate a net wrench W_V^ℓ in any arbitrary direction.

The wrench $W_{v_k}^\ell$ that is applied by an individual AGV to the load depends on how the load is interconnected to that particular AGV. If the load is boldly fixed to the AGV, then wrenches can be transmitted in any direction. If the load is attached using a revolute joint, then forces can be transmitted at the joint, but it is not possible to transmit a torque.

Lower pairs and allowed twists

We will restrict ourselves to interconnections between the AGV and the load that are so-called *lower pairs*. As any interconnection, a lower pair restricts the relative motion $T_{v_k}^{i,\ell}$ between the AGV and the load. For a lower pair, the twist $T_{v_k}^{i,\ell}$ between AGV k and the load can be expressed as the product of a *constant* matrix $S_{i,k}$ times a reduced set of new “velocity” coordinates $\eta_k \in \mathbb{R}^{\text{d.o.f.}}$:

$$\boxed{T_{v_k}^{i,\ell} = S_{i,k} \eta_k, \quad \eta_k \in \mathbb{R}^{\text{d.o.f.}}} \quad (3.101)$$

The first subscript i denotes the coordinate system Ψ_i , which is fixed to either the load or the AGV. Without loss of generality we assume that $S_{i,k}$ has *full column rank*. Then the (column) rank of $S_{i,k}$ is equal to the *degrees of freedom* (d.o.f.) of the lower pair, or, equivalently, three minus the degrees of freedom that are fixed by the lower pair. Examples of lower pairs that are often encountered in practice include:

- **Fully rigid interconnection.** The fully rigid interconnection is also called a *rigid kinematic pair* ([114], p.41). There are zero degrees of freedom, hence $S_{i,k} = \emptyset$;
- **Prismatic joint.** This is also called slider joint. One translational motion is free. When the origin of Ψ_i is fixed to one of the two bodies, then $S_{i,k}$ is of the form $(0 \ a \ b)^T$, with $a^2 + b^2 = 1$, and $\eta_k \in \mathbb{R}$ represents the *sliding velocity* of the prismatic joint;
- **Revolute joint.** This interconnection allows rotation about one particular axis between the two bodies. $S_{i,k}$ takes a special form when Ψ_i is fixed to one of the bodies and when in addition its origin coincides with the rotation axis of the revolute joint. For that situation $S_{i,k}$ equals $(1 \ 0 \ 0)^T$, and $\eta_k \in \mathbb{R}$ represents the *rotational velocity* of the revolute joint;
- **No interconnection.** The bodies are physically separated. It is also called a *degenerate kinematic pair* ([114], p.41). There is no restriction on the motion between the two bodies, e.g. $S_{i,k} = I^{3 \times 3}$. This situation is not relevant for our cooperative transportation application.

By pre-multiplying either equation (3.101) by $Ad_{H_i^j}$, it follows that $S_{i,k}$ transforms as

$$S_{j,k} = Ad_{H_i^j} S_{i,k}. \quad (3.102)$$

Note that we did not require that Ψ_j is fixed to the load or to the AGV. Thus although here $S_{i,k}$ is constant as Ψ_i was either fixed to the load or the AGV, $S_{j,k}$ is generally not constant. Finally, we remark that the set $(T_{v_k}^{i,\ell})^{\mathcal{A}}$ of all the twists $T_{v_k}^{i,\ell}$ that are allowed by a lower pair between the AGV and the load can be expressed in terms of the image of the matrix $S_{i,k}$:

$$\boxed{(T_{v_k}^{i,\ell})^{\mathcal{A}} = \text{Im } S_{i,k}} \quad (3.103)$$

The reader is referred to e.g. pp. 46–50 of the book by Stramigioli [114] for more information on lower pairs.

Constrained wrenches

It was already argued that the wrenches $W_{v_k}^\ell$ that can be transmitted from a certain AGV to the load depend on how the AGV is interconnected to the load. In case that the interconnection between a particular AGV k and the load is a lower pair, then the set of allowed twists $(T_{v_k}^{i,\ell})^{\mathcal{A}}$ is equal to the image of a matrix $S_{i,k}$ that characterizes the interconnection. The wrenches that can be transmitted from an AGV to the load through the fixed degrees of freedom, e.g. by exploiting the kinematic constraints of the lower pair, are called the *constraint wrenches* (see [114], p.49). The set of constraint wrenches $(W_{v_k}^{i,\ell})^{\mathcal{C}}$ for the lower pair between AGV k and the load satisfies

$$\boxed{(W_{v_k}^{i,\ell})^{\mathcal{C}} = \text{ann } S_{i,k} = \{W_{v_k}^{i,\ell} \in se^*(2) \mid W_{v_k}^{i,\ell} S_{i,k} = 0\}} \quad (3.104)$$

in other words, the set $(W_{v_k}^{i,\ell})^{\mathcal{C}}$ of constraint wrenches consists of all the wrenches that *annihilate* $S_{i,k}$. From physical considerations we require that all the AGVs together can exert a net wrench W_V^ℓ on the load in any arbitrary direction. This means that the union of all the sets of constraint wrenches must be equal to the entire wrench space $se^*(2)$. For notational convenience we express all the constraint sets in a common coordinate system Ψ_ℓ that is fixed to the load. In these coordinates, it must hold that

$$(W_V^\ell)^{\mathcal{C}} = \bigcup_{k=1}^N (W_{v_k}^\ell)^{\mathcal{C}} = \bigcup_{k=1}^N \text{ann } S_{\ell,k} = se^*(2). \quad (3.105)$$

Since

$$\bigcup_{k=1}^N \text{ann } S_{\ell,k} = \text{ann} \left(\bigcap_{k=1}^N \text{Im } S_{\ell,k} \right) \quad (3.106)$$

should be equal to $se^*(2)$, it follows that condition (3.105) is equivalent to

$$\boxed{\bigcap_{k=1}^N \text{Im } S_{\ell,k} = 0} \quad (3.107)$$

We will need this condition for the observer design that is discussed in subsection 5.5 of Chapter 5.

3.7.3 Equations of motion for the interconnected system

In the previous subsections we saw that the equations of motion for the load and a single AGV k are given by (3.99) and (3.49), i.e.

$$\dot{T}_\ell^{\ell,0} + \omega_\ell \Gamma_\ell T_\ell^{\ell,0} = M_\ell^{-1} (W_V^\ell)^T \quad (3.108)$$

$$\dot{T}_{v_k}^{v_k,0} + \omega_{v_k} \Gamma_{v_k} T_{v_k}^{v_k,0} = M_{v_k}^{-1} (W_w^{v_k} - W_{v_k}^{v_k,\ell})^T. \quad (3.109)$$

Here W_V^ℓ is the net wrench that is exerted by all the AGVs on the load, $W_w^{v_k}$ is the wrench that is exerted by the wheel on AGV k , and $W_{v_k}^{v_k, \ell}$ is the wrench that is exerted by AGV k on the load. There are N AGVs and one load, so there are $3(N + 1)$ twists to describe the system (3.108)-(3.109). However, the various AGV-load interconnections reduce the number of freedoms. Since the interconnections we consider are lower pairs, it is relatively easy to describe the dynamics of the system (3.108)-(3.109) with a *reduced set of coordinates* η . For notational convenience we will illustrate the procedure using two AGVs and a load, but it is straightforward to generalize it to an arbitrary number of AGVs. As new coordinates we take the twist $T_\ell^{\ell, 0}$ of the load with respect to the floor plus the variables η_k that express the motion of AGV k with respect to the load. First we transform all the twists $T_{v_k}^{v_k, 0}$ to the load coordinate system Ψ_ℓ :

$$Ad_{H_{v_k}^\ell} T_{v_k}^{v_k, 0} = T_{v_k}^{\ell, 0} = T_\ell^{\ell, 0} + T_{v_k}^\ell = T_\ell^{\ell, 0} + S_{\ell, k} \eta_k, \quad (3.110)$$

If we stack the twists of the load and the AGVs with respect to the floor in a single vector T and express them all in the load coordinate system Ψ_ℓ , then we obtain

$$T = \begin{pmatrix} T_\ell^{\ell, 0} \\ T_{v_1}^{\ell, 0} \\ T_{v_2}^{\ell, 0} \end{pmatrix} = \underbrace{\begin{pmatrix} I & 0 & 0 \\ I & S_{\ell, 1} & 0 \\ I & 0 & S_{\ell, 2} \end{pmatrix}}_S \underbrace{\begin{pmatrix} T_\ell^{\ell, 0} \\ \eta_1 \\ \eta_2 \end{pmatrix}}_\eta = S\eta \quad (3.111)$$

We would like to express the equations of motion in terms of \dot{T} . This requires the derivatives of $T_\ell^{\ell, 0}$ and $T_{v_k}^{\ell, 0}$. The derivative of $T_\ell^{\ell, 0}$ follows straightforward from (3.108). The derivative of $T_{v_k}^{\ell, 0}$ satisfies

$$\begin{aligned} \dot{T}_{v_k}^{\ell, 0} &= \frac{d}{dt} \left(Ad_{H_{v_k}^\ell} T_{v_k}^{v_k, 0} \right) = \dot{Ad}_{H_{v_k}^\ell} T_{v_k}^{v_k, 0} + Ad_{H_{v_k}^\ell} \dot{T}_{v_k}^{v_k, 0} \\ &= Ad_{H_{v_k}^\ell} ad_{T_{v_k}^{v_k, \ell}} T_{v_k}^{v_k, 0} + Ad_{H_{v_k}^\ell} \dot{T}_{v_k}^{v_k, 0} \\ &= Ad_{H_{v_k}^\ell} ad_{T_{v_k}^{v_k, \ell}} T_{v_k}^{v_k, 0} + Ad_{H_{v_k}^\ell} \left(-\omega_{v_k} \Gamma_{v_k} T_{v_k}^{v_k, 0} + M_{v_k}^{-1} (W_w^{v_k} - W_{v_k}^{v_k, \ell})^T \right) \\ &= Ad_{H_{v_k}^\ell} (ad_{T_{v_k}^{v_k, \ell}} - \omega_{v_k} \Gamma_{v_k}) T_{v_k}^{v_k, 0} + Ad_{H_{v_k}^\ell} M_{v_k}^{-1} (W_w^{v_k} - W_{v_k}^{v_k, \ell})^T, \end{aligned} \quad (3.112)$$

where

$$ad_{T_{v_k}^{v_k, \ell}} = \begin{pmatrix} 0 & 0 & 0 \\ -v_{v_k}^{v_k, \ell} & 0 & \omega_{v_k}^{v_k, \ell} \\ u_{v_k}^{v_k, \ell} & -\omega_{v_k}^{v_k, \ell} & 0 \end{pmatrix}, \quad T_{v_k}^{v_k, \ell} = \begin{pmatrix} \omega_{v_k}^{v_k, \ell} \\ u_{v_k}^{v_k, \ell} \\ v_{v_k}^{v_k, \ell} \end{pmatrix}. \quad (3.113)$$

Since S is constant because the interconnections are lower pairs, the derivative \dot{T} is related to η by

$$\dot{T} = \dot{S}\eta + S\dot{\eta} = S\dot{\eta}. \quad (3.114)$$

Next, define the mass matrix for the interconnected system and expressed in Ψ_ℓ as

$$M = \begin{pmatrix} M_\ell & 0 & 0 \\ 0 & Ad_{H_\ell}^{T v_1} M_{v_1} Ad_{H_\ell}^{v_1} & 0 \\ 0 & 0 & Ad_{H_\ell}^{T v_2} M_{v_2} Ad_{H_\ell}^{v_2} \end{pmatrix} = \begin{pmatrix} M_\ell & 0 & 0 \\ 0 & M_{\ell, v_1} & 0 \\ 0 & 0 & M_{\ell, v_2} \end{pmatrix} \quad (3.115)$$

Here M_{ℓ, v_k} is the inertia tensor of AGV k expressed in Ψ_ℓ . If we pre-multiply $\dot{T}_\ell^{\ell, 0}$ (3.108) with M_ℓ , and $\dot{T}_{v_k}^{\ell, 0}$ (3.112) with $Ad_{H_\ell}^{T v_k} M_{v_k} Ad_{H_\ell}^{v_k}$, then we obtain

$$\begin{aligned} M\dot{T} &= \begin{pmatrix} M_\ell \dot{T}_\ell^{\ell, 0} \\ M_{\ell, v_1} \dot{T}_{v_1}^{\ell, 0} \\ M_{\ell, v_2} \dot{T}_{v_2}^{\ell, 0} \end{pmatrix} = \begin{pmatrix} -\omega_\ell M_\ell \Gamma_\ell T_\ell^{\ell, 0} + (W_V^\ell)^T \\ Ad_{H_\ell}^{T v_1} M_{v_1} (ad_{T_{v_1}}^{v_1, \ell} - \omega_{v_1} \Gamma_{v_1}) T_{v_1}^{v_1, 0} + Ad_{H_\ell}^{T v_1} (W_w^{v_1} - W_{v_1}^{v_1, \ell})^T \\ Ad_{H_\ell}^{T v_2} M_{v_2} (ad_{T_{v_2}}^{v_2, \ell} - \omega_{v_2} \Gamma_{v_2}) T_{v_2}^{v_2, 0} + Ad_{H_\ell}^{T v_2} (W_w^{v_2} - W_{v_2}^{v_2, \ell})^T \end{pmatrix} \\ &= \begin{pmatrix} -\omega_\ell M_\ell \Gamma_\ell T_\ell^{\ell, 0} + (W_V^\ell)^T + (W_{v_2}^\ell)^T \\ Ad_{H_\ell}^{T v_1} M_{v_1} (ad_{T_{v_1}}^{v_1, \ell} - \omega_{v_1} \Gamma_{v_1}) T_{v_1}^{v_1, 0} + Ad_{H_\ell}^{T v_1} (W_w^{v_1})^T - (W_{v_1}^\ell)^T \\ Ad_{H_\ell}^{T v_2} M_{v_2} (ad_{T_{v_2}}^{v_2, \ell} - \omega_{v_2} \Gamma_{v_2}) T_{v_2}^{v_2, 0} + Ad_{H_\ell}^{T v_2} (W_w^{v_2})^T - (W_{v_2}^\ell)^T \end{pmatrix} = MS\dot{\eta}. \end{aligned} \quad (3.116)$$

Subsequently, we will eliminate the constraint wrenches $W_{v_1}^\ell$ and $W_{v_2}^\ell$. The usual way to do this is by pre-multiplying (3.116) with the matrix S^T , see e.g. [29]. Since $W_{v_k}^\ell \in \text{ann}S_{\ell, k}$ implies that $S_{\ell, k}^T (W_{v_k}^\ell)^T = 0$, we find that

$$S^T \begin{pmatrix} (W_{v_1}^\ell)^T + (W_{v_2}^\ell)^T \\ -(W_{v_1}^\ell)^T \\ -(W_{v_2}^\ell)^T \end{pmatrix} = \begin{pmatrix} I & I & I \\ 0 & S_{\ell, 1}^T & 0 \\ 0 & 0 & S_{\ell, 2}^T \end{pmatrix} \begin{pmatrix} (W_{v_1}^\ell)^T + (W_{v_2}^\ell)^T \\ -(W_{v_1}^\ell)^T \\ -(W_{v_2}^\ell)^T \end{pmatrix} = \begin{pmatrix} 0 \\ 0 \\ 0 \end{pmatrix}. \quad (3.117)$$

Hence, the constraint wrenches will indeed drop out of the equation. Pre-multiplying (3.116) with S^T results in

$$S^T MS\dot{\eta} = S^T \begin{pmatrix} -\omega_\ell M_\ell \Gamma_\ell T_\ell^{\ell, 0} \\ Ad_{H_\ell}^{T v_1} M_{v_1} (ad_{T_{v_1}}^{v_1, \ell} - \omega_{v_1} \Gamma_{v_1}) T_{v_1}^{v_1, 0} \\ Ad_{H_\ell}^{T v_2} M_{v_2} (ad_{T_{v_2}}^{v_2, \ell} - \omega_{v_2} \Gamma_{v_2}) T_{v_2}^{v_2, 0} \end{pmatrix} + S^T \begin{pmatrix} 0 \\ Ad_{H_\ell}^{T v_1} (W_w^{v_1})^T \\ Ad_{H_\ell}^{T v_2} (W_w^{v_2})^T \end{pmatrix} \quad (3.118)$$

The last term on the right-hand side represents the forces that are applied by the wheels on the AGVs, and can be considered as the inputs of the interconnected system. Since S has full column rank, the ‘‘mass’’ matrix $S^T MS$ of the reduced system is invertible. Hence, an explicit expression for the derivatives $\dot{\eta}$ is easily found by pre-multiplying the above equation (3.118) by $(S^T MS)^{-1}$. The equation of motion (3.118) for an interconnected system in reduced coordinates

Tuning

4.1 Introduction

Accurate identification of effective wheel diameters and steering encoder offsets is a prerequisite for achieving accurate AGV operation. Estimation errors in the effective wheel diameters lead to incorrect estimates for the AGV's velocity and travelled distance. Inaccurate steering encoder offset settings result in crabwise or rotational motions in situations where the vehicle is expected to drive a straight line. Furthermore, the AGV solely relies on the integration of its odometric data to calculate position estimates in between absolute position measurements. Sometimes the absolute reference system consists of grid points that are indistinguishable from one another. This is for instance the case for the magnet grid in the hall of FROG Navigation Systems, which was used for the experiments that are discussed in this chapter and in Chapter 7. For such reference systems, the position estimate from the AGV's position observer is used to identify the magnets that are detected by the vehicle. When the position estimate is unreliable due to poor calibration, then this may lead to identification of the wrong magnets.

Since rough estimates are always available, we do not have to start from scratch to identify the steering angle encoder offsets and effective wheel diameters. Nominal wheel diameters are specified by the manufacturer and can also be measured by hand up to a certain accuracy. Steering encoders often have an index pulse that corresponds approximately to the zero position, and the offsets can also be estimated by merely looking at the wheels. Since the nominal wheel diameters and visually identified steering encoder offsets are used as a starting point in our estimation procedure, we refer to this procedure as *tuning*.

Apart from the effective wheel diameters and steering encoder offsets, several other parameters are required to operate an AGV at the desired accuracy. In particular, the mass of the AGV, the position of its center of gravity, its moment of inertia, and the friction forces in the wheels are important parameters. The mass properties were provided by FROG and can be measured quite easily, with exception of the moment of inertia. An elegant way to determine the complete inertia tensor for a rigid body experimentally (including the moment of inertia) is described by Previati *et al.* [100]. Furthermore, it is important to know the friction phenomena that occur in the driveline, such as the loss torques of the electromotors and the losses that occur in the reduction between the wheels and the motor. A simple Coulomb friction model with a different friction force for driving forwards and backwards is used to model the friction of the OLS vehicles. The parameters were tuned manually such that the vehicle maintains its motion when the gain of the velocity controller is set to zero.

In this chapter we will focus on the identification of steering encoder offsets and effective wheel diameters. It is assumed that the positions of the wheels and the magnet ruler are

known. We start with a brief discussion of related work. Subsequently, we present a three-step procedure to estimate the steering encoder offsets and the effective wheel diameters. The procedure has been tested in practice on both our test vehicles, which were designed to be identical in hardware. The results are presented, and the influence of different vehicle loads on the estimated parameters is investigated. Although the discussion of the tuning procedure is tailored to the OLS AGVs, it is easily generalized to other vehicles with two actuated wheels and one or more magnet rulers.

4.2 Related work

Practically all wheeled mobile robot applications use odometry as an aid to estimate the current velocity and position of the robot. Drive encoders measure the rotation of wheels when its rolling, and steering encoders measure the steering angles of the steerable wheels. Borenstein and Feng [20] list several reasons why inaccuracies occur when the encoder readings are translated to linear velocities. They classify the various error sources as ‘systematic errors’ (unequal wheel diameters, misalignment of the wheels, etc.) and ‘nonsystematic errors’ (travel of uneven floors, wheel slippage due to slippery floors, etc.). Furthermore, Borenstein and Feng point out that odometry errors on smooth indoor surfaces are mainly attributed to systematic errors, whereas nonsystematic errors are dominant on rough surfaces with significant irregularities. The aim of calibration is to minimize the systematic errors. In our case, that means finding the steering encoder offsets and wheel diameters of the two actuated wheels for the OLS vehicles.

The wheeled mobile robot (WMR) literature is dominated by differential-drive robots, which have two actuated parallel wheels and one or more passive, free rotating caster wheels. Since the actuated wheels are not steerable, there are of course no steering encoders on these wheels. Sometimes a caster wheel is equipped with a steering encoder, but this situation is rather rare. Hence, the WMR community focuses on the calibration of differential-drive robots, and, in particular, the identification of the wheel radii and the wheel base of the driven wheels. Calibration procedures for more complex vehicles such as car-like vehicles or vehicles with multiple steering wheels, e.g. the Phileas or our OLS vehicles, are hardly seen. Also, identification of steering encoders and wheel diameters is not an important topic in vehicle dynamics studies. Therefore, the literature survey below focuses on the WMR literature.

4.2.1 Wheeled mobile robots

Borenstein and Feng [20] introduced a bidirectional (i.e. clockwise and counterclockwise) square path experiment for calibrating the wheel radii and the wheel base for differential-drive mobile robots. In their procedure, the robot is driven around a 4×4 m square for several times in clockwise as well as in counterclockwise direction. The wheel base and the radii of the left and right wheels are estimated from the initial and final pose measurements together with the encoder readings. The method that was proposed by the authors has become quite popular, and is known as the UMBmark method.

Chong and Kleeman [26] describe how they used the UMBmark method to calibrate their

differential-drive “Werrimbi” robot. To overcome non-systematic odometry errors related to wheel slip, their robot is equipped with two dedicated ‘encoder wheels’ that are mounted parallel to the two driven wheels. The encoder wheels are sharp-edged to reduce the wheel base uncertainty. They are mounted on linear bearings to ensure contact with the floor. Estimated parameters are the wheel base of the encoder wheels and their radii.

The paper by McKerrow and Ratner [80] discusses the calibration of a four-wheeled car-like mobile robot that was built from an electric wheel chair. The front wheels are caster wheels equipped with steering encoders, and the rear wheels are actuated and equipped with drive encoders. Two methods for estimating the steering encoder offsets are proposed. In the first method the steering encoder offset is calibrated mechanically by turning the front wheels until they just touch a straight edge. As a second method the authors propose to drive the robot along a straight edge while simultaneously using an ultrasonic sensor to measure the distance between the robot and the edge. The steering encoder offset is estimated by considering the radius of the realized curve. The authors also discuss an extension to the UMBmark method to estimate the distance between the front and rear wheels and the relation between the drive encoder counts and the driven distance.

Caltabiano *et al.* [23] describe an Extended Kalman Filter (EKF) for estimating the wheel radii, wheel base and pose of their “Robovolc” mobile robot. Robovolc is a robot that was designed for volcano exploration. It has three driven wheels on either side that cannot steer. Changing the orientation of the robot is accomplished by means of ‘skid-steering.’ The available measurements are two optical encoder readings (from one wheel at each side) and absolute position measurements from a DGPS system. Since the proposed EKF automatically estimates the odometry parameters (wheel radii of the encoder wheels and the wheel base) during operation, the authors suggest that a dedicated, time-consuming calibration phase as with the UMBmark method is not required.

Martinelli [74] proposes a strategy for estimating four odometry-related parameters of their three-wheeled Nomad 150 robot that features a synchronous drive system. The proposed method only requires measuring the change in the pose between the initial and the final position of the robot. In another work, Martinelli *et al.* [75] adopted the Augmented Kalman Filter (AKF) by Larsen *et al.* [71] to estimate the wheel base and wheel radii of their differential-drive robot “Donald Duck.” Martinelli *et al.* use encoder readings as inputs and laser range finder as observations for the AKF. The contribution of Martinelli *et al.* is that they extended the AKF to estimate a non-systematic component of the odometry.

Antonelli *et al.* [9] describe a least-squares-based technique for odometry calibration for a unicycle-like mobile robot based on absolute position measurements before and after completing several suitably defined trajectories. Instead of identifying the usual differential-drive robot parameters (i.e. the radii of the two wheels and the wheel base), Antonelli *et al.* choose to identify the four elements of the 2×2 matrix that relates the rotational velocities of the left and right wheel to the rotational and forward velocity of the robot. This makes their method somewhat more general. Another advantage of the new parameters set is that the problem becomes linear in the parameters, which makes it relatively easy to solve using a pseudo-inverse. Furthermore, the authors point out that the condition number of the regressors provide information on the ‘optimality’ of the trajectories.

The works by Hardt *et al.* [125, 126] focus on the calibration of the odometry, magnetic compass and gyroscope of their four-wheel outdoor differential-drive mobile robot “RO-

MANE” (Robot Mobile Autonome de Navigation en Extérieur). In [126], the wheel base is estimated by a linear least squares estimator and the wheel radii by approximately driving a straight and manually measuring the distances covered by the left and right wheel. In [125], the authors propose a generalized least squares approach to identify parameters and present the estimation of the wheel base, magnetic compass and gyroscope parameters of the ROMANE robot as an example.

Roy and Thrun [103] discuss the estimation of odometry parameters in a stochastic, maximum likelihood setting. They propose to use only two parameters that respectively represent the systematic translational and rotational components of the odometry error of their four-wheel synchro-drive “RWI B21” mobile robot. The systematic odometry errors are assumed to be linearly related to the driven distance. The robot is equipped with a SICK laser range finder and 24 sonar sensors to provide absolute position measurements.

4.2.2 Positioning of our work

To the best of our knowledge, there is currently no systematic approach for estimating two or more steering encoder offsets available. The robots that are described in literature are always equipped with at least one fixed axis which is assumed to have a steering angle equal to zero. In other words, those wheels are assumed to be perfectly aligned with the vehicle. Since there is no fixed axis in our case as all wheels are steerable, we have the additional problem that inaccurate steering encoder offsets result in a crab-like motions, i.e. a motion with a nonzero side slip angle. Therefore, the procedure by McKerrow and Ratner [80] where the steering encoder offset is determined by considering the radius of the realized curve is not appropriate for our vehicles. Although their method does provide information on the difference in the steering encoder offsets, it does not yield information about their common term.

Furthermore, our vehicles are equipped with an absolute positioning system that differs from the systems generally found in mobile robotics. Our magnet measurement systems returns the position of the detected magnet in vehicle coordinates. This means that a single measurement provides very accurate information about the absolute position of one specific point on the vehicle, namely the point on the vehicle that corresponds to the position of the detected magnet. However, a single magnet measurement does not provide any information on the orientation of the vehicle. Although it is certainly possible to equip the vehicles with a SICK laser range finder and ultrasonic sensors, we prefer to use the magnet measurement system that is readily available.

Also, we prefer to work with parameters that have a direct physical interpretation rather than using lumped or artificial parameters. Besides the possibility to intuitively verify the results with physically meaningful parameters, another important reason is that the odometry parameters are used in the observer as well as for control. To translate the drive motor torques to the forces that are exerted on the floor, it is required to know the diameter of the wheels and the offsets of the steering encoders.

Finally, we decided to assume that the position of the wheels is known. Although we recognize that correct identification of the wheel base is very important for differential-drive robots with a small wheel base, we believe that the main systematic odometry errors in our test vehicles stem from the unknown steering encoder offsets.

4.3 Procedure

Goal of the tuning procedure is to estimate the offsets of the steering angle encoders and the effective wheel diameters. It is assumed that the relative positions of the wheels with respect to the vehicle are known. The effective wheel diameter is twice the effective wheel radius, and for notational convenience we will use the effective wheel radius in this section. Let us denote the effective wheel radius and the steering angle offset for wheel w_i by respectively r_{w_i} and $\delta_{w_i}^{\text{offset}}$, where $i \in \{1, \dots, n\}$ for a vehicle with n sensed wheels and $i \in \{1, 2\}$ for the OLS vehicles. The procedure that we propose to estimate r_{w_i} and $\delta_{w_i}^{\text{offset}}$ consists of three steps:

1. In the experimental part of our procedure, we fix the steering angles δ_{w_i} of the wheels and then drive a certain distance at a low, constant speed. Ideally, this should result in a perfect **circular trajectory**. An example of a realized experiment with our OLS 2 test vehicle is depicted in Figure 4.1.

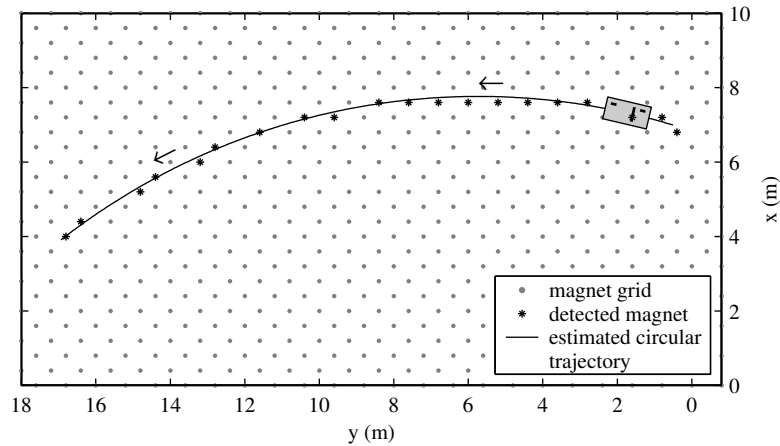


Figure 4.1: Estimated circular trajectory between the first and last detected magnets for low speed experiment 22 of the OLS 2 test vehicle (see section 4.6 for a more detailed description of this experiment). The vehicle was driving backwards.

2. The second step is to reconstruct the circular trajectory of the AGV from the sensor data that have been logged in step one. The available sensors are:
 - a **magnet ruler** that detects magnets that are buried in the floor; the number of magnets that have been detected is denoted by m ; the magnet ruler returns the relative position $M^v(k)$ of the detected magnet with respect to the AGV in the vehicle coordinate system Ψ_v , where $k \in \{1, \dots, m\}$;
 - **steering encoders** that measure the steering angles $\delta_{w_i}^{\text{encoder}}$ of the wheels; the steering angles remain (approximately) constant during the experiment;

- **drive encoders** that measure the rotations of the wheels at the time instances k that the magnet ruler detects a magnet; the encoder readings $\vartheta_{w_i}(k)$ are “unwrapped,” such that they are either monotonically increasing or monotonically decreasing;
- the **AGV’s position observer** that remained active during the calibration experiments estimated the trajectory of the AGV by integrating the (relatively poorly calibrated) odometric sensor data, and by performing corrections based on the magnet ruler’s measurements; the position observer’s estimate corresponding to the k^{th} detected magnet is denoted by $H_{v,\text{a-priori}}^0(k)$; this data is used to identify the floor position of the detected magnet and to establish an initial estimate for the circular trajectory that was performed by the vehicle;
- the **intended magnet positions** $G^0(k)$ of the detected magnets as expressed in the floor coordinate system Ψ_0 ; the magnets are placed in a regular grid, and $G^0(k)$ corresponds to the position where the magnet was intended to be placed; it is computed by using the AGV’s a-priori position estimate to transform the magnet measurement $M^v(k)$ to its approximate floor coordinates

$$M_{\text{a-priori}}^0(k) = H_{v,\text{a-priori}}^0(k)M^v(k), \quad (4.1)$$

and subsequently identifying the grid position $G^0(k)$ that is the closest to the a-priori estimate $M_{\text{a-priori}}^0(k)$.

The *shape* of the AGV’s circular trajectory is parameterized by the position (a, b) of the steering pole with respect to the floor and by the position (R_v, β_v) of the steering pole with respect to the vehicle. Here (a, b) are the (x, y) -coordinates of steering pole as expressed in the floor coordinate system Ψ_0 , and R_v and β_v are respectively the signed radius and the side slip angle corresponding to the motion of the vehicle coordinate system Ψ_v . The reader is referred to section 3.3.4 for more information on the steering pole parametrization using R_v and β_v . The AGV’s *position along the circular trajectory* is parameterized by the *path variable* S_v , see Figure 4.2. The definitions of $S_v = 0$ for a left-hand ($R_v > 0$) and a right-hand ($R_v < 0$) turn are also depicted in the figure. The situation $R_v = 0$ is not considered, because in our experiments the AGV always performs curved motions. The relation between the drive encoder measurement $\vartheta_{w_i}(k)$ of wheel w_i at the time of magnet detection k and the path variable $S_v(k)$ corresponding to that magnet measurement is modelled as

$$S_v(k) = c_{w_i}\vartheta_{w_i}(k) + o_{w_i} + \xi_{w_i}(k). \quad (4.2)$$

Here c_{w_i} (in meters/count) describes the increase in the path variable S_v per drive encoder count of wheel w_i , and o_{w_i} represents the AGV’s position when wheel w_i ’s unwrapped drive encoder reading $\vartheta_{w_i} = 0$. Furthermore, $\xi_{w_i}(k)$ is the measurement noise. We will see later that c_{w_i} is related to the effective wheel radius of wheel w_i and to the ratio of the signed radii of the motions of the vehicle coordinate system Ψ_v and the wheel center. Because the signed radius of the realized trajectory varies between experiments, c_{w_i} and o_{w_i} will also vary from experiment to experiment. The AGV’s trajectory is described in terms of the *intermediate parameters*

$\theta = (a, b, R_v, \beta_v, c_{w_i}, o_{w_i})$, and we will minimize a nonlinear least-squares criterion to estimate these parameters.

3. The third and last step of our tuning procedure is to translate the circular trajectory of the AGV, which was parameterized by $(a, b, R_v, \beta_v, c_{w_i}, o_{w_i})$, into the to-be-estimated parameters r_{w_i} and $\delta_{w_i}^{\text{offset}}$. From the intermediate parameters we can compute the so-called *kinematic steering angles* $\bar{\delta}_{w_i}$, which are the virtual wheel angles that would correspond to perfect tracking of the wheels. Because we assumed that the positions of the wheels are known, we can also compute the radius R_{w_i} of the circular trajectory of wheel w_i for the experiment. **In this step, we assume that there was no wheel slip during the experiment.** That is also the reason why the experiment was performed at a low speed. This allows us to compute the *effective wheel radius* r_{w_i} and the *steering encoder offset* $\delta_{w_i}^{\text{offset}}$ from $R_{w_i}, \bar{\delta}_{w_i}$, the intermediate parameters (β_v, R_v, c_{w_i}) , and the steering encoder reading $\delta_{w_i}^{\text{encoder}}$. The presence of lateral wheel slip would result in a bias term for the estimated steering encoder offset $\delta_{w_i}^{\text{offset}}$, and longitudinal wheel slip would result in a bias term for the estimated effective wheel radius r_{w_i} .

The first two steps of this procedure are applicable to vehicles with an arbitrary number of wheels. In the third step we had to assume that there was no wheel slip to be able to translate the identified trajectory to the steering encoder offsets and effective wheel radii. An OLS vehicle has two actuated wheels and one caster wheel. If we assume that the caster wheel does not exert horizontal forces on the floor and if we assume that the longitudinal wheel forces are very small due to the low vehicle speed, then we can safely assume that the wheel slip is negligibly small during the experiment. This still holds when the steering encoder offsets are not precisely known.

For vehicles with three or more steerable wheels, however, inaccurate steering encoder offsets will result in substantial lateral wheel slip. For these kind of vehicles, we may first tune the steering encoder offsets heuristically such that the counteracting lateral wheel forces are minimized. Subsequently, we can carry out the three-step procedure that is discussed above.

In the next section 4.4, we discuss the estimation of the realized circular trajectory by means of identifying the intermediate parameters $(a, b, R_v, \beta_v, c_{w_i}, o_{w_i})$. The computation of the estimates for the steering encoder offsets $\delta_{w_i}^{\text{offset}}$ and the effective wheel radii r_{w_i} is detailed in section 4.5. Experimental results are presented and analyzed in section 4.6.

4.4 Estimation of the circular trajectory

In this section we will present a method for estimating the trajectory that was realized by the AGV during the experimental part of our calibration procedure. Since the steering angles were kept constant during the experiment, **we assume that the realized trajectory is a pure circle segment.** Consequently, the steering pole C is assumed to remain constant with respect to the floor as well as with respect to the AGV during our experiment. As we discussed in the previous section, the available measurements are the positions $M^v(k)$ of the m detected magnets with respect to the vehicle, the rotations $\vartheta_{w_i}(k)$ of the wheels as measured

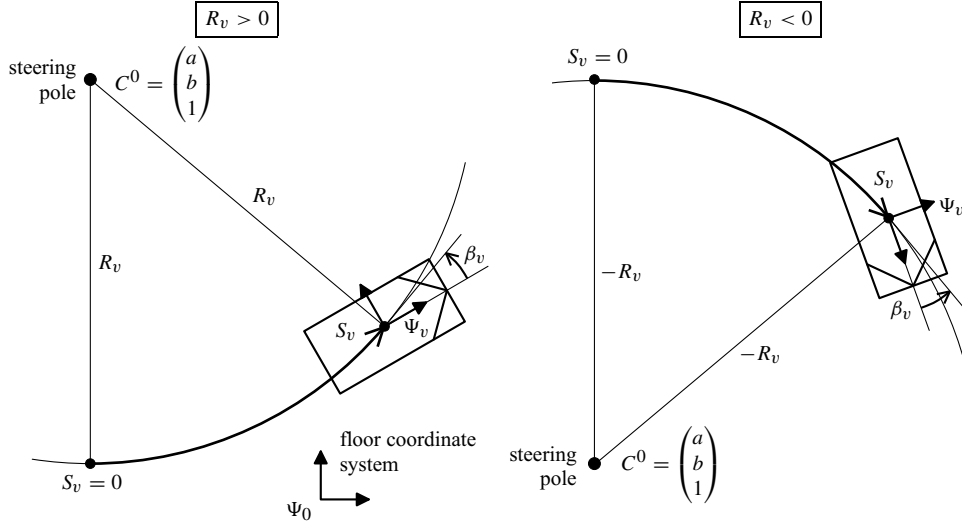


Figure 4.2: Parametrization of the vehicle's circular motion.

by the drive encoders, the position estimates $H_{v,a\text{-priori}}^0(k)$ from the AGV's position observer, and the intended floor positions $G^0(k)$ of the detected magnets. The steering angle encoder measurements $\delta_{w_i}^{\text{encoder}}$ not used for the estimation of the trajectory. For the OLS vehicles we have two sensed wheels, i.e. $i \in \{1, 2\}$.

The circular trajectory is parameterized by $(a, b, R_v, \beta_v, c_{w_i}, o_{w_i})$. Recall that (a, b) is the position of the steering pole with respect to the floor coordinate system Ψ_0 , (R_v, β_v) is the position of the steering pole with respect to the vehicle coordinate system Ψ_v , and c_{w_i} and o_{w_i} represent the relation between the path variable S_v and the drive encoder readings ϑ_{w_i} for wheel w_i . It is remarked that, as long as the wheel slip remains constant during the vehicle trajectory under consideration, *the procedure for estimating the circular trajectory will work for an arbitrary number of wheels.*

The parameter estimates for the circular trajectory will be based on the minimization of a nonlinear least-squares criterion. Before we introduce the criterion, we will first discuss the noise sources $\xi_x(k)$, $\xi_y(k)$, and $\xi_{w_i}(k)$ and introduce the definitions of the radial residuals $\xi_r(\theta, k)$ and the tangential residuals $\xi_t(\theta, k)$.

4.4.1 Radial residuals

The most important source of noise or modelling inaccuracies stems from the precision at which the magnets are placed in the floor. The grid position at which the k^{th} detected magnet was intended to be placed is denoted by $G^0(k)$. Usually the magnets are arranged according to a regular grid. The true magnet position $G_t^0(k)$ will slightly deviate from its intended grid position $G^0(k)$ due to e.g. inaccuracies in the drilling of the hole in which the magnet is placed. The relation between the *unknown* true magnet position $G_t^0(k)$ and the *known*

intended magnet position $G^0(k)$ is modelled as

$$\boxed{G_t^0(k) = G^0(k) + \begin{pmatrix} \xi_x(k) \\ \xi_y(k) \\ 0 \end{pmatrix}} \quad (4.3)$$

Here $\xi_x(k)$ and $\xi_y(k)$ represent the deviations in respectively the x - and y -directions of the true magnet position with respect to the intended magnet position. This is also illustrated in Figure 4.3. It is assumed that the deviations $\xi_x(k)$ and $\xi_y(k)$ are normally distributed with zero mean and standard deviation σ_M , i.e.

$$\begin{pmatrix} \xi_x(k) \\ \xi_y(k) \end{pmatrix} \sim \mathcal{N} \left(\begin{pmatrix} 0 \\ 0 \end{pmatrix}, \begin{pmatrix} \sigma_M^2 & 0 \\ 0 & \sigma_M^2 \end{pmatrix} \right). \quad (4.4)$$

Because there is no reason to assume that the placement of the magnets is more accurate in one direction than in another direction, $\xi_x(k)$ and $\xi_y(k)$ are assumed to have the same standard deviation and to be uncorrelated. From Figure 4.3 we see that the distance $R_G(k)$ from the

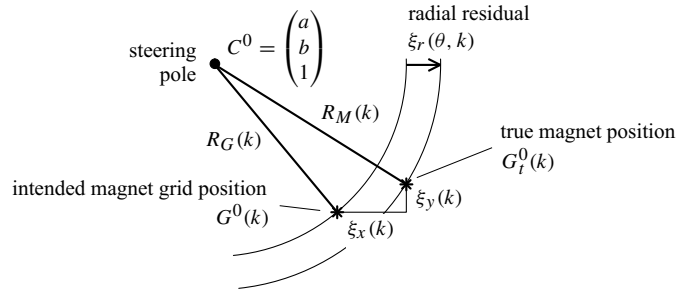


Figure 4.3: Relations between the true magnet position $G_t^0(k)$, the intended magnet position $G^0(k)$, the steering pole C , and the radial residual $\xi_r(\theta, k)$.

intended magnet position $G^0(k)$ to the steering pole C^0 equals

$$R_G(k) = \|G^0(k) - C^0\| = \sqrt{(G_x^0(k) - a)^2 + (G_y^0(k) - b)^2}. \quad (4.5)$$

Analogously, we can compute the distance $R_M(k)$ from the magnet ruler's measurement $M^v(k)$ to the steering pole C^v , as both are expressed in the vehicle coordinate system Ψ_v :

$$\begin{aligned} R_M(k) &= \|M^v(k) - C^v\|_2 = \left\| \begin{pmatrix} M_x^v(k) + R_v s \beta_v \\ M_y^v(k) - R_v c \beta_v \\ 0 \end{pmatrix} \right\|_2 \\ &= \sqrt{(M_x^v(k) + R_v s \beta_v)^2 + (M_y^v(k) - R_v c \beta_v)^2}. \end{aligned} \quad (4.6)$$

We assume that the errors in the measurements $M^v(k)$ of the magnet ruler can be neglected, as these errors are much smaller than the deviations $\xi_x(k)$ and $\xi_y(k)$. This means that the

magnet ruler's measurement $M^v(k)$ coincides exactly with the true magnet position $G_t^0(k)$. Therefore, the distance between the true magnet position and the steering pole C^0 is equal to $R_M(k)$. The *radial residuals* $\xi_r(\theta, k)$ are defined as

$$\xi_r(\theta, k) := R_M(k) - R_G(k), \quad k \in \{1, \dots, m\}, \quad (4.7)$$

see also Figure 4.3. Substitution of the expressions (4.5)-(4.6) for $R_G(k)$ and $R_M(k)$ in this definition results in

$$\xi_r(\theta, k) = \sqrt{(M_x^v(k) + R_v s \beta_v)^2 + (M_y^v(k) - R_v c \beta_v)^2} - \sqrt{(G_x^0(k) - a)^2 + (G_y^0(k) - b)^2} \quad (4.8)$$

Hence, the radial residuals $\xi_r(\theta, k)$ depend on the intermediate parameters (a, b, R_v, β_v) , on the (perfect) magnet ruler's measurements $M^v(k)$, and on the known grid positions $G^0(k)$ at which the detected magnets were intended to be placed in the floor. To relate the radial residuals $\xi_r(\theta, k)$ to the noise sources $\xi_x(k)$ and $\xi_y(k)$, with the aid of Figure 4.3 we write the distance $R_M(k)$ from the true magnet position $G_t^0(k)$ to the steering pole C^0 as

$$\begin{aligned} R_M(k) &= \sqrt{(G_{t,x}^0(k) - a)^2 + (G_{t,y}^0(k) - b)^2} \\ &= \sqrt{(G_x^0(k) + \xi_x(k) - a)^2 + (G_y^0(k) + \xi_y(k) - b)^2} \\ &= \sqrt{R_G(k)^2 + 2(G_x^0(k) - a)\xi_x(k) + 2(G_y^0(k) - b)\xi_y(k) + \xi_x(k)^2 + \xi_y(k)^2} \\ &\approx \sqrt{R_G(k)^2} + \frac{2(G_x^0(k) - a)\xi_x(k) + 2(G_y^0(k) - b)\xi_y(k) + \xi_x(k)^2 + \xi_y(k)^2}{2\sqrt{R_G(k)^2}} \\ &\approx R_G(k) + \frac{(G_x^0(k) - a)\xi_x(k) + (G_y^0(k) - b)\xi_y(k)}{\sqrt{(G_x^0(k) - a)^2 + (G_y^0(k) - b)^2}}. \end{aligned} \quad (4.9)$$

The square root was approximated using a first order Taylor expansion around $R_G(k)$. Since $R_G(k)$ is typically larger than 10 meters and $\xi_x(k)$ and $\xi_y(k)$ are smaller than 0.01 meters, this approximation is allowed. The quadratic terms $\xi_x(k)^2$ and $\xi_y(k)^2$ have been neglected because they are small when compared to the other terms. Substitution of the last expression (4.9) in (4.7) yields the relation between the radial residuals $\xi_r(\theta, k)$ and the noise sources $\xi_x(k)$ and $\xi_y(k)$ that we were looking for:

$$\xi_r(\theta, k) \approx \frac{(G_x^0(k) - a)\xi_x(k) + (G_y^0(k) - b)\xi_y(k)}{\sqrt{(G_x^0(k) - a)^2 + (G_y^0(k) - b)^2}} \sim \mathcal{N}(0, \sigma_M^2) \quad (4.10)$$

Thus we see that the radial residuals $\xi_r(\theta, i)$ are approximately normally distributed with mean zero and standard deviation σ_M , i.e. the standard deviation at which the magnets were placed in the floor.

4.4.2 Tangential residuals

To derive an expression for the tangential residuals $\xi_{t_i}(\theta, k)$, we recall from equation (4.2) that the relation between the true path variable $S_v(k)$ and the unwrapped drive encoder reading $\vartheta_{w_i}(k)$ of wheel w_i corresponding to the k^{th} detected magnet was modelled as

$$\boxed{S_v(k) = c_{w_i} \vartheta_{w_i}(k) + o_{w_i} + \xi_{w_i}(k)} \quad (4.11)$$

Here c_{w_i} is the increase in the path variable S_v per drive encoder count ϑ_{w_i} , o_{w_i} is the AGV's position when the encoder reading of wheel w_i is $\vartheta_{w_i} = 0$, and $\xi_{w_i}(k)$ is an additive noise term that represents the modeling error. Next, we consider the relation between the true vehicle position $S_v(k)$, the magnet measurement $M^v(k)$, the intended magnet grid position $G^0(k)$, the true magnet position $G_t^0(k)$, and the intermediate parameters θ that parameterize the AGV's circular trajectory. To this end, we will first define the auxiliary angles $\alpha_{v,t}(k)$ and $\alpha_v(k)$ according to Figure 4.4. From the figure we see that $\alpha_v(k)$ is the angle between the vertical axis and the line that connects the steering pole C^0 and the grid position $G^0(k)$ at which the magnet was intended to be placed in the ground. Similarly, $\alpha_{v,t}(k)$ is the angle between the vertical axis and the line that connects the steering pole C^0 and the true magnet position $G_t^0(k)$. The angles $\alpha_v(k)$ are "unwrapped" such that the difference between subsequent $\alpha_v(k)$'s is always smaller than 2π . From Figure 4.4 we find that the expressions for $\alpha_v(k)$ and $\alpha_{v,t}(k)$ are given by

$$\alpha_v(k) = \arctan2 \left(G_x^0(k) - a, \text{sign}(R_v) \left(b - G_y^0(k) \right) \right) + 2\pi k_k \quad (4.12)$$

$$\begin{aligned} \alpha_{v,t}(k) &= \arctan2 \left(G_x^0(k) + \xi_x(k) - a, \text{sign}(R_v) \left(b - G_y^0(k) - \xi_y(k) \right) \right) + 2\pi k_k \\ &\approx \alpha_v(k) + \frac{-(G_y^0(k) - b)\xi_x(k) + (G_x^0(k) - a)\xi_y(k)}{R_v \sqrt{(G_x^0(k) - a)^2 + (G_y^0(k) - b)^2}}. \end{aligned} \quad (4.13)$$

We take k_1 , i.e. the unwrap factor corresponding to the first measurement, equal to zero: $k_1 = 0$. Furthermore, we define the angle $\gamma_v(k)$ as the angle between the line that connects the magnet measurement $M^v(k)$ and the steering pole C^v and the line that connects the origin of the vehicle coordinate system Ψ_v with the steering pole C^v . This is illustrated in Figure 4.4. If we assume that $|\gamma_v(k)| < \frac{\pi}{2}$, then we see from the figure that

$$\gamma_v(k) = \text{sign}(R_v) \arctan \left(\frac{M_x^v(k)c\beta_v + M_y^v(k)s\beta_v}{R_v + M_x^v(k)s\beta_v - M_y^v(k)c\beta_v} \right). \quad (4.14)$$

As we described before, the magnet measurement $M^v(k)$ is modelled as being perfect. It therefore follows from Figure 4.4 and equation (4.13) that the true AGV position $S_v(k)$ is related to R_v , $\gamma_v(k)$, and $\alpha_v(k)$ by

$$\boxed{S_v(k) = |R_v| \alpha_v(k) - |R_v| \gamma_v(k) + \xi_s(\theta, k)} \quad (4.15)$$

with

$$\xi_s(\theta, k) = |R_v| (\alpha_{v,t}(k) - \alpha_v(k)). \quad (4.16)$$

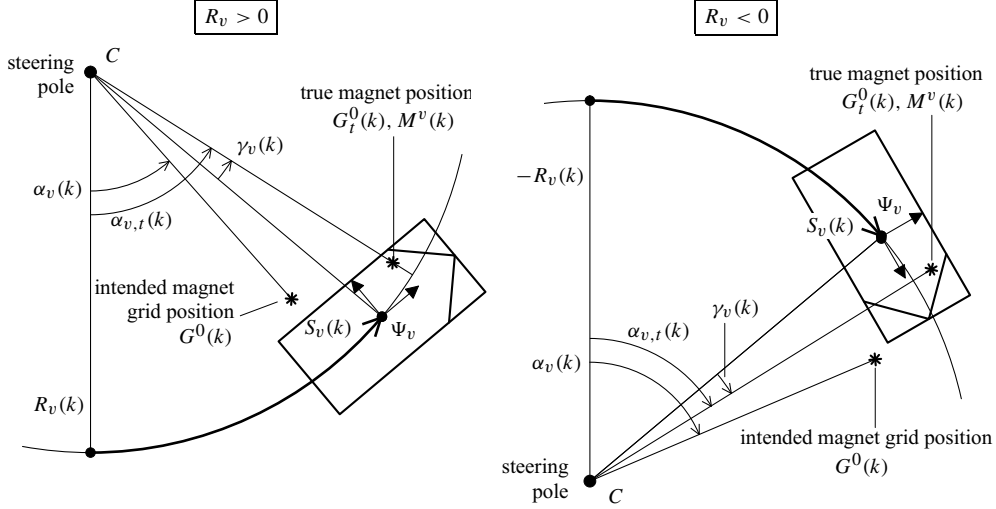


Figure 4.4: Definition of the auxiliary angles $\alpha_v(k)$, $\alpha_{v,t}(k)$, and $\gamma_v(k)$.

From (4.12)-(4.13) we see that

$$\xi_s(\theta, k) \approx \text{sign}(R_v) \frac{-(G_y^0(k) - b)\xi_x(k) + (G_x^0(k) - a)\xi_y(k)}{\sqrt{(G_x^0(k) - a)^2 + (G_y^0(k) - b)^2}} \sim \mathcal{N}(0, \sigma_M^2) \quad (4.17)$$

If we denote the number of wheels by n , then we see from equations (4.11) and (4.15) that we have $n + 1$ expressions for the unknown true AGV position $S_v(k)$ corresponding to the k^{th} magnet detection. It is possible to eliminate the unknown AGV position $S_v(k)$ from these equations by subtracting equation (4.15) from the n other equations (4.11). If we define the *tangential residual* $\xi_{t_i}(\theta, k)$ for wheel w_i as

$$\xi_{t_i}(\theta, k) = \xi_s(\theta, k) - \xi_{w_i}(k) \quad (4.18)$$

then it follows from equations (4.11) and (4.15) that

$$\xi_{t_i}(\theta, k) = c_{w_i} \vartheta_{w_i}(k) + o_{w_i} + |R_v| \gamma_v(k) - |R_v| \alpha_v(k) \quad (4.19)$$

Hence, we see that the tangential residuals $\xi_{t_i}(\theta, k)$ depend on the intermediate parameters $(a, b, R_v, \beta_v, c_{w_i}, o_{w_i})$, on the (perfect) magnet ruler measurements $M^v(k)$, and on the known grid positions $G^0(k)$ at which the detected magnets were intended to be placed in the floor. In equation (4.17) we saw that $\xi_s(\theta, k)$ was normally distributed with zero mean and standard deviation σ_M . In contrast, $\xi_{w_i}(k)$ is generally not normally distributed as it is mainly related to the unroundness of the wheels and the quantization errors that stem from the digital drive encoders. Therefore, we can not conclude that the tangential residuals $\xi_{t_i}(\theta, k)$ will follow a normal distribution. In particular, the tangential residual $\xi_{t_i}(\theta, k)$ will only be normally distributed when the errors $\xi_{w_i}(k)$ are small as compared to $\xi_s(\theta, k)$.

4.4.3 Nonlinear least-squares estimator

In the previous two subsections we saw that the radial residuals $\xi_r(\theta, k)$ and the tangential residuals $\xi_{t_i}(\theta, k)$ were defined by

$$\xi_r(\theta, k) = R_M(k) - R_G(k) \quad (4.20)$$

$$\xi_{t_i}(\theta, k) = c_{w_i} \vartheta_{w_i}(k) + o_{w_i} + |R_v| \gamma_v(k) - |R_v| \alpha_v(k), \quad (4.21)$$

with $k \in \{1, \dots, m\}$ and $i \in \{1, \dots, n\}$. Here m is the number of measurements, n is the number of wheels, and $R_M(k)$, $R_G(k)$, $\gamma_v(k)$ and $\alpha_v(k)$ all depend on θ . We will use an estimator $\hat{\theta}$ that minimizes the sum of squares of the residuals. Because relation between the residuals and the to-be-estimated parameters θ is nonlinear, this results in a *nonlinear least-squares (NLSQ) optimization problem*. In particular, we estimate our parameters $\theta = (a, b, R_v, \beta_v, c_{w_i}, o_{w_i})$ such that

$$\hat{\theta} = \arg \min_{\theta} \left(\sum_{k=1}^m \xi_r(\theta, k)^2 + \sum_{i=1}^n \sum_{k=1}^m \xi_{t_i}(\theta, k)^2 \right) \quad (4.22)$$

The first term with $\xi_r(\theta, k)$ is independent of the choice of the vehicle coordinate system Ψ_v , and represents the sum of the squared radial geometric distances between the true and the intended magnet grid positions. The second term with $\xi_{t_i}(\theta, k)$ does depend on the choice of Ψ_v . For practical situations, however, Ψ_v is somewhere fixed to the vehicle and the distance between Ψ_v and the magnet ruler's measurements $M^v(k)$ is quite small compared to the radius $|R_v|$ of the realized circular trajectory. Therefore, in practice the second term represents for each wheel the sum of the squared geometric distances between the tangential deviations of the true magnet position from their intended positions minus the encoder inaccuracies of that wheel.

There are a variety of methods available to solve the NLSQ problem (4.22). We adopted the Gauss-Newton algorithm for our experiments, because this method was successfully used by Gander *et al.* [43] to find circles and ellipses for which the sum of the squares of the geometric distances to a given set of points was minimal. The procedure that we used is detailed in Appendix A.

4.5 Calculation of steering angle encoder offset and effective wheel radius

This section discusses how the steering encoder offset $\delta_{w_i}^{\text{offset}}$ and the effective wheel radius r_{w_i} for wheel w_i can be estimated from the circular trajectory that was identified in the previous section. The circular trajectory was described by the intermediate parameters $\theta = (a, b, R_v, \beta_v, c_{w_i}, o_{w_i})$. From this set we will only use the variables (R_v, β_v, c_{w_i}) . From the parameters (R_v, β_v) and the known position H_i^v of the wheel center with respect to the vehicle, we reconstruct the kinematic steering angle $\bar{\delta}_{w_i}$ that is compatible with the performed motion and the signed radius of the circular trajectory that was performed by the wheel center. Subsequently, the steering encoder offset $\delta_{w_i}^{\text{offset}}$ and the effective wheel radius r_{w_i} are calculated.

4.5.1 Kinematic steering angle and signed radius of the wheel center

We attach a coordinate system Ψ_i to the vehicle such that its origin corresponds with the wheel center of wheel w_i and such that its x -axis indicates the neutral steering position of the wheels. This is illustrated in Figure 4.5. The steering angle δ_{w_i} is defined as the angle between the wheel plane and the x -axis of the coordinate system Ψ_i .¹ In section 3.6.2 of Chapter 3 we saw that the kinematic steering angle $\bar{\delta}_{w_i}$ corresponds to the (theoretical) situation that the wheel plane is perfectly aligned with the motion of the wheel center. This means that the angle between the wheel plane and the line that connects the wheel center with the steering pole C^v is exactly 90 deg. This is sketched in Figure 4.6. Figure 4.6 shows that the kinematic steering angle $\bar{\delta}_{w_i}$ of wheel w_i corresponds exactly to the side slip angle β_i of the motion of coordinate system Ψ_i . The position of Ψ_i with respect to Ψ_v is assumed to be known. The position of the steering pole C^v with respect to Ψ_v as parameterized by (R_v, β_v) was estimated in the previous section. Therefore, we can use the procedure that was discussed in subsection 3.3.4 to compute the side slip angle β_i . Thus to compute the kinematic steering angle $\bar{\delta}_{w_i} = \beta_i$, we first transform the expression for the steering pole from Ψ_v to Ψ_i to obtain C^i :

$$C^i = \begin{pmatrix} -R_{w_i} s \bar{\delta}_{w_i} \\ R_{w_i} c \bar{\delta}_{w_i} \\ 1 \end{pmatrix} = H_v^i C^v = H_v^i \begin{pmatrix} -R_v s \beta_v \\ R_v c \beta_v \\ 1 \end{pmatrix}, \quad (4.23)$$

with $H_v^i = (H_i^v)^{-1}$ the relative position of Ψ_v with respect to Ψ_i , and C^v is the position of the steering pole as expressed in vehicle coordinates Ψ_v . For simplicity we assume that Ψ_i and Ψ_v have the same orientation, i.e. that they are of the form

$$H_v^i = \begin{pmatrix} 1 & 0 & x_v^{w_i} \\ 0 & 1 & y_v^{w_i} \\ 0 & 0 & 1 \end{pmatrix} = \begin{pmatrix} 1 & 0 & -x_{w_i}^v \\ 0 & 1 & -y_{w_i}^v \\ 0 & 0 & 1 \end{pmatrix}, \quad (4.24)$$

with $-(x_v^{w_i}, y_v^{w_i}) = (x_{w_i}^v, y_{w_i}^v)$ the coordinates of the wheel center expressed in Ψ_v . From expressions (4.23)-(4.24) we see that

$$C^i = H_v^i \begin{pmatrix} -R_v s \beta_v \\ R_v c \beta_v \\ 1 \end{pmatrix} = \begin{pmatrix} -R_v s \beta_v - x_{w_i}^v \\ R_v c \beta_v - y_{w_i}^v \\ 1 \end{pmatrix} \quad (4.25)$$

¹Note that this definition does not hold anymore when the steering angles exceed ± 90 deg. For the OLS vehicles, however, the absolute values of the steering angles are always smaller than 90 deg.

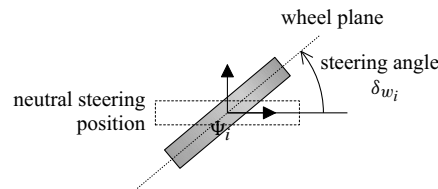


Figure 4.5: Definition of the steering angle δ_{w_i} .

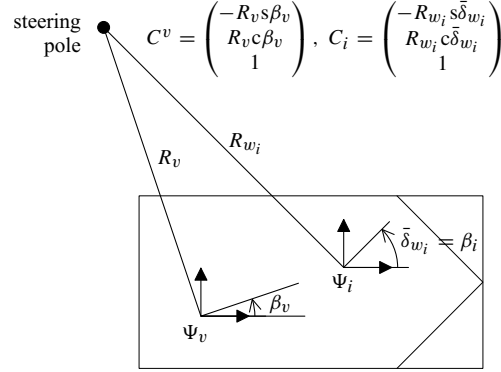


Figure 4.6: Coordinate system Ψ_i , kinematic steering angle $\bar{\delta}_{w_i}$, and the signed radius R_{w_i} of the wheel center's motion.

Finally, by equating (4.25) with (4.23) it follows that the kinematic steering angle $\bar{\delta}_{w_i}$ and the signed radius R_{w_i} of the circular motion performed by wheel w_i satisfy

$$\begin{aligned}
 \bar{\delta}_{w_i} &= -\arctan\left(\frac{C_x^i}{C_y^i}\right) = \arctan\left(\frac{R_v s\beta_v + x_{w_i}^v}{R_v c\beta_v - y_{w_i}^v}\right) \\
 R_{w_i} &= \text{sign}(C_y^i) \sqrt{(C_x^i)^2 + (C_y^i)^2} \\
 &= \text{sign}(R_v c\beta_v - y_{w_i}^v) \sqrt{R_v^2 + (x_{w_i}^v)^2 + (y_{w_i}^v)^2 + 2x_{w_i}^v R_v s\beta_v - 2y_{w_i}^v R_v c\beta_v}
 \end{aligned}
 \tag{4.26}$$

Here C_x^i and C_y^i respectively denote the first and second component of C^i as computed with (4.25). To compute estimates for $\bar{\delta}_{w_i}$ and R_{w_i} , we simply substitute the estimated parameters \hat{R}_v and $\hat{\beta}_v$ of the previous section in the expressions above.

4.5.2 Steering encoder offsets and effective wheel radius

For all the analyses that were performed previously in this chapter it was assumed that the vehicle executed a pure circular motion and that the wheel slip was constant during this maneuver. Therefore, all previous results hold for vehicles with multiple active wheels. **To compute the steering encoder offsets $\delta_{w_i}^{\text{offset}}$ and the effective wheel radius r_{w_i} we need to restrict the constant wheel slip assumption to the case that there is zero wheel slip.** In that case, the true steering angle δ_{w_i} is equal to the kinematic steering angle $\bar{\delta}_{w_i}$:

$$\delta_{w_i} = \bar{\delta}_{w_i}. \tag{4.27}$$

Then the steering angle offset $\delta_{w_i, \text{offset}}$ for wheel w_i is computed as

$$\delta_{w_i}^{\text{offset}} = \bar{\delta}_{w_i} - \delta_{w_i}^{\text{encoder}} \tag{4.28}$$

Here $\bar{\delta}_{w_i}$ is the kinematic steering angle (4.26), and $\delta_{w_i}^{\text{encoder}}$ is the steering encoder reading converted to radians. Because the wheels' steering angles are controlled by local steering controllers, the encoder data may fluctuate by some counts during the motion. Therefore, $\delta_{w_i}^{\text{encoder}}$ is taken to be the average of the encoder readings between the first and the last magnet measurement that are used to reconstruct the circular trajectory.

To compute the effective wheel radius r_{w_i} , we recall that the parameter c_{w_i} represents the number of meters travelled by the origin of Ψ_v per drive encoder count ϑ_{w_i} of wheel w_i . As can be seen from Figure 4.6, the signed radii R_v and R_{w_i} of the motions that are performed by the vehicle coordinate system Ψ_v and the center of wheel w_i are generally not identical. Consequently, the distances travelled by the center of wheel w_i differs from the distance travelled by Ψ_v . From Figure 4.6 we see that the number of meters travelled by the center of wheel w_i per drive encoder count ϑ_{w_i} of that wheel equals

$$K_{w_i}^{\text{meters/count}} = c_{w_i} \frac{R_{w_i}}{R_v} \quad (4.29)$$

Let us denote the number of encoder counts per radian wheel rotation by $K_{w_i}^{\text{counts/rad}}$. It can be computed from the encoder specifications and the known gear ratio of the reduction between the encoder shaft and the wheel shaft. Since we assumed that there is no wheel slip, the effective wheel radius r_{w_i} equals

$$r_{w_i} = K_{w_i}^{\text{meters/count}} K_{w_i}^{\text{counts/rad}} = c_{w_i} \frac{R_{w_i}}{R_v} K_{w_i}^{\text{counts/rad}} \quad (4.30)$$

This concludes the calculation of the steering encoder offset $\delta_{w_i}^{\text{offset}}$ and the effective wheel radius r_{w_i} .

4.6 Experimental results

This section discusses the experimental results for estimating the steering encoder offsets and the effective wheel diameters² of the OLS 1 and the OLS 2. For improved readability we take $i \in \{F, R\}$, where $i = F$ denotes the front wheel and $i = R$ denotes the rear wheel. First, thirty experiments were carried out without load with both vehicles at very low speeds (≈ 0.2 m/s) to minimize the influence of lateral and longitudinal wheel slip. This resulted in thirty circular trajectories for each vehicle. Subsequently, several experiments were carried out at three medium speed levels (0.6, 0.9, 1.2 m/s) and with varying loads (0, 50, 100 kg) to investigate how this would influence the parameter estimates that were obtained during the first set of experiments. Six experiments were carried out at each medium speed/load combination. This resulted in fifty-four circular trajectories per vehicle.

4.6.1 General issues and a priori parameter settings

For all experiments, the steering angles were kept constant by providing a constant planar velocity setpoint to the vehicle controller. Magnet measurement outliers occurred when the

²The effective wheel diameter is simply twice the effective wheel radius.

detected magnet was closer than 2 mm to one of the ends of the magnet ruler, when the same magnet was detected twice, or when the data association resulted in an off-magnet grid position after no magnets were detected for some time. These outliers were removed from the analyses. In addition, one measurement in low speed experiment 29 for the OLS 1 (see next subsection) was removed from the analyses because it produced a radial residual of 73 mm, which was much larger than the rest of the residuals. Inspection of the logged steer encoder data revealed that, after a short transient effect, the steering angles remained constant within a few encoder counts. When larger deviations than a few encoder counts occurred, only the part of the data was selected where the deviations remained small. A typical example of steering and unwrapped drive encoder data is displayed in Figure 4.7. For the steering angles, optical

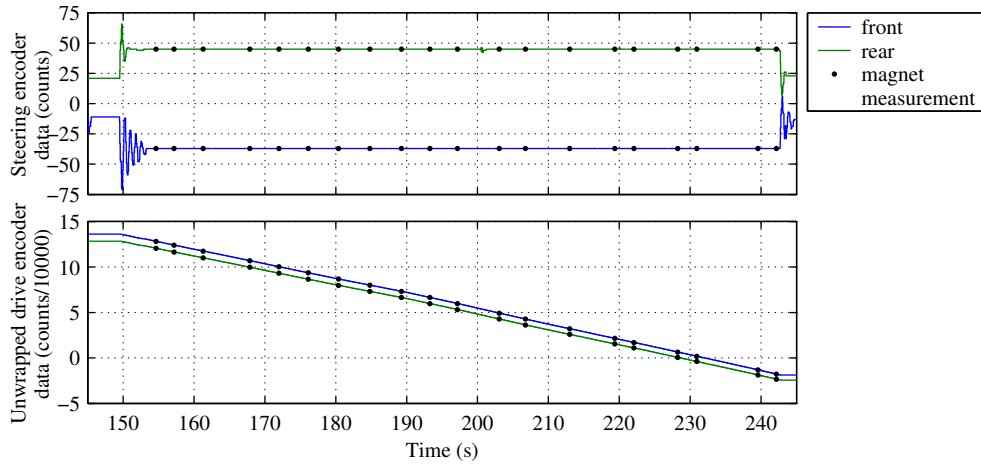


Figure 4.7: Steering encoder data (top panel) and unwrapped drive encoder data (bottom panel) for the OLS 2 for low speed experiment 22. The AGV was driving backwards during this experiment. The resolutions of the steer and drive encoders are respectively 17.4603 counts per degree steering angle and 11.0000 counts per degree wheel rotation.

encoders with a resolution of 2000 counts per revolution are connected through a reduction of 3.14286 to the steering axis, thus the number of counts per degree steering angle is

$$\frac{2000 \times 3.14286}{2\pi} = 1000.40 \text{ counts/rad steering angle} = 17.4603 \text{ counts/deg steering angle.} \quad (4.31)$$

To measure the rotation of the wheels, optical encoders with a resolution of 400 counts per revolution are connected using a reduction of 9.9 to the drive shafts, hence the number of counts per degree wheel rotation equals

$$\frac{400 \times 9.9}{2\pi} = 630.254 \text{ counts/rad wheel rotation} = 11.0000 \text{ counts/deg wheel rotation.} \quad (4.32)$$

The nominal wheel diameter of 150 mm corresponds to approximately $150/(2 \times 630.254) = 0.12 \text{ mm/count}$. In all analysis, the drive encoder data was unwrapped to obtain an affine relation between the drive encoder data and the rotation of the wheel.

In FROG's control software, the steering encoder measurements $\delta_{w_i}^{\text{encoder}}(t)$, drive encoder measurements $\vartheta_{w_i}(t)$, and magnet measurements $M^v(k)$ are stored together with their corresponding time stamps. Whereas the encoder measurements are read at a fixed sample rate, the magnet measurements take place asynchronously. Therefore, linear interpolation is used to estimate the encoder positions at the time instance k of the magnet measurement $M^v(k)$. Linear interpolation is particularly appropriate in this case, as the vehicles operate at constant speed during the experiments.

The a-priori parameters settings for the steering angle offsets and the effective wheel diameters that were used during the calibration experiments are listed in Table 4.1.

Parameter		OLS 1	OLS 2
Front steering angle offset	(mrad)	20	10
Rear steering angle offset	(mrad)	10	-20
Difference	(mrad)	10	30
Front effective wheel diameter	(mm)	151.5, 151.8	151.5, 151.8
Rear effective wheel diameter	(mm)	152.5, 152.8	152.5, 152.8

Table 4.1: A-priori steering angle offsets and wheel diameters for the OLS 1 and the OLS 2. Because the software distinguishes between a wheel diameter used in odometry computations and a wheel diameter for relating wheel torques to forces on the floor, two numbers are listed for these parameters (they should normally be equal).

4.6.2 Low speed experiments

For both the OLS 1 and the OLS 2, several tests were carried out at approximately 0.2 m/s. The constant planar velocity setpoints were selected in such a way that the vehicles performed circular motions at five different curvatures R_v^{-1} with a desired side slip angle β_v of zero degrees (see section 3.3.4 for the definitions of R_v and β_v). Each test was performed three times forwards, and three times backwards. This resulted in thirty low speed experiments for each vehicle. An overview of the low speed experiments is given in Table 4.2. As the experiments were numbered afterwards, i.e. they were not necessarily carried out in the order that is listed in the table.

Experiment	Curvature (m^{-1})	Velocity (m/s)	Load (kg)
1...6	0.08	± 0.2	0
7...12	0.06	± 0.2	0
13...18	0.00	± 0.2	0
19...24	-0.06	± 0.2	0
25...30	-0.08	± 0.2	0

Table 4.2: Overview of the low speed experiments. The vehicles drive forwards for the odd numbered experiments, and backwards for the even numbered experiments.

Estimated motion radius R_v and side slip angle β_v

The radius R_v and side slip angle β_v of the circular trajectory performed by the vehicle coordinate system Ψ_v were estimated using the procedure that was described in sections 4.3 and 4.4. Figure 4.8 displays the setpoints and the estimated values for the OLS 1 and OLS 2. The figure shows that the realized values of R_v^{-1} were lower than the setpoints for the OLS 1, whereas for the OLS 2 the realized values were higher than the setpoints. In other words, the OLS 1 had a tendency to steer to the right, whereas the OLS 2 had a tendency to steer to the left during the calibration experiments. The figure also shows that the estimated realized side slip angles β_v are close to zero. The average side slip angle β_v for the OLS 1 was slightly negative, and the average side slip angle β_v for the OLS 2 was slightly positive.

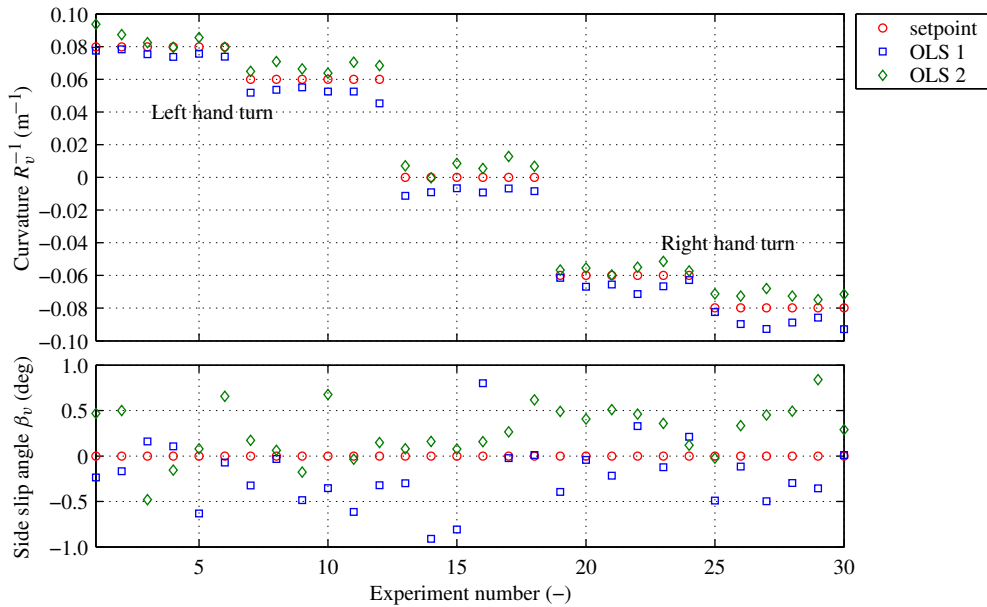


Figure 4.8: Curvature setpoint and estimated realized curvature (top panel) and side slip angle setpoint and estimated realized side slip angles (bottom panel) for the OLS 1 and OLS 2 during the low speed experiments.

Residuals

For each of the $k \in \{1, \dots, m\}$ magnet measurements and estimated intermediate parameters $\hat{\theta}$ for a given experiment, the radial residuals $\xi_r(\hat{\theta}, k)$ were computed with equation (4.8) and the tangential residuals $\xi_{tF}(\hat{\theta}, k)$ and $\xi_{tR}(\hat{\theta}, k)$ for respectively the front and rear wheel with equation (4.19). Box plots of the results are presented in Figure 4.9. The magnitude of the residuals depends, amongst others, on the number of detected magnets per experiment and the distance travelled by the origin of the vehicle coordinate system Ψ_v . These quantities are also indicated in the figure. The absolute values of almost all residuals are fairly smaller

than 10 mm. Since the parameter estimation algorithm assumed that the vehicle performs a perfect circular trajectory, deviations from this ideal trajectory will result in an increase of the residuals. Given that the residuals are very small –especially when we take into account that the vehicles also drive distances that exceed 20 meters– it can be concluded that the realized trajectories very closely resemble true circular trajectories. It is remarked that for all experiments the steering angles as measured by the steering encoders were nearly constant, because the data was selected this way. If part of an experiment had contained a step in steer encoder data of, say, five counts halfway the experiment, this will immediately lead to much larger residuals as the realized motion would not have a constant radius anymore in that case.

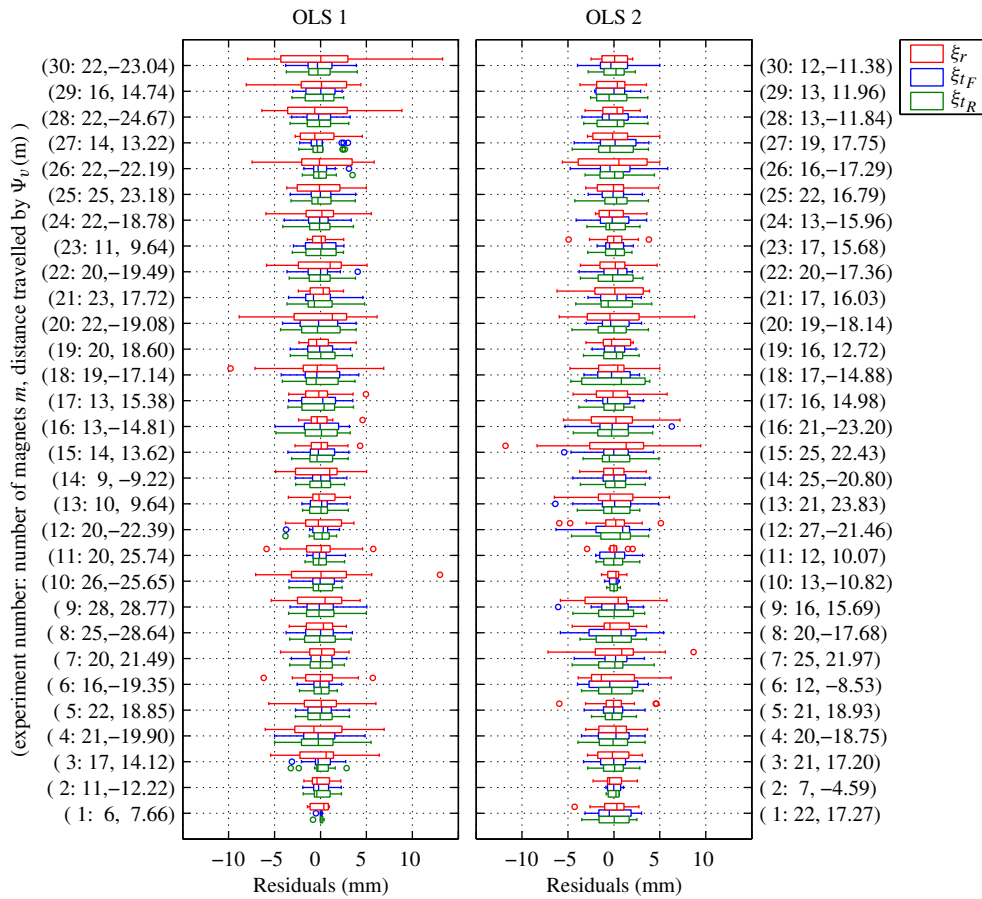


Figure 4.9: Box plots of the radial residuals $\xi_r(\hat{\theta}, k)$ and the tangential residuals $\xi_{tF}(\hat{\theta}, k)$ and $\xi_{tR}(\hat{\theta}, k)$.

Figure 4.9 also shows that the radial residuals $\xi_r(\hat{\theta}, k)$ are of the same order of magnitude

as the tangential residuals $\xi_{t_F}(\hat{\theta}, k)$ and $\xi_{t_R}(\hat{\theta}, k)$. Some preliminary experiments revealed that the residuals corresponding to a given magnet reproduced very well when the same experiment was repeated over exactly the same magnets. This led us to conclude that the largest part of the residuals is caused by the accuracy at which magnets were placed into the ground. Therefore, the low speeds experiments that are discussed here were carried out on different floor areas. A relative frequency histogram of all the radial and tangential residuals for all the low speed experiments together is plotted in Figure 4.10. The total number of low speed residuals is 3261. The mean of all the residuals is 0 mm, and the standard deviation equals 2.2374 mm. The probability density function of the normal distribution $\mathcal{N}(0, 2.2374^2)$ with these parameters is also drawn in the figure. Qualitatively the normal probability density function is very close to the empirically obtained normalized histogram of the residuals.

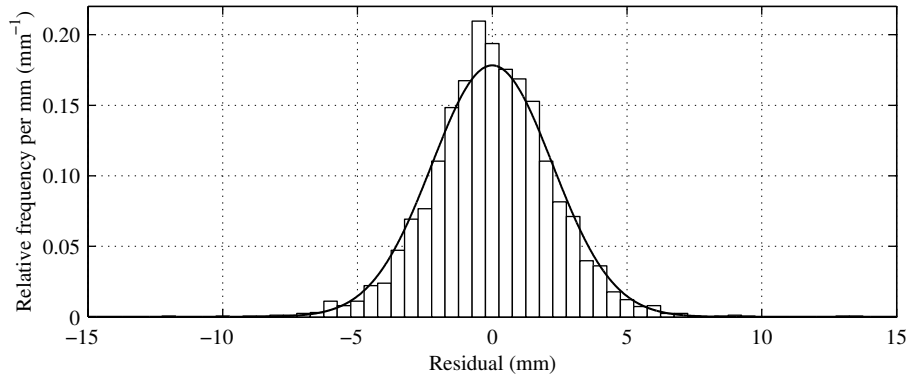


Figure 4.10: Relative frequency histogram of the 3261 longitudinal and lateral residuals for all the low speed experiments for the OLS 1 and the OLS 2 together. The thick black line is the probability density function of the normal distribution with mean 0 mm and standard deviation 2.2374 mm.

Figure 4.11 displays a typical example of the radial and tangential residuals of the OLS 1 and the OLS 2 for a single experiment. Although all the residuals together are approximately normally distributed, Figure 4.11 shows that they are not always particularly white and independent. Moreover, the tangential residuals $\xi_{t_F}(\hat{\theta}, k)$ and $\xi_{t_R}(\hat{\theta}, k)$ for the OLS 1 are as good as identical, whilst this is not the case for the OLS 2. Other experiments show the same trend, which can also be recognized from Figure 4.9. The differences between the front and rear tangential residuals for the OLS 2 are thought to be caused by unroundness of the front and rear wheel. Since the OLS 2 has been used much more frequently than the OLS 1 in the past, increased wear on the OLS 2's wheels may explain why these residuals differ more for the OLS 2 than for the OLS 1. Furthermore, in this particular example the radial residuals $\xi_r(\hat{\theta}, k)$ for the OLS 1 exhibit a sinusoidal trend.

To investigate the whiteness properties of the residuals more systematically, we can consider their autocorrelation functions $\psi_\xi(\tau)$. An estimate for the autocorrelation function

for the residuals $\xi(\hat{\theta}, k)$ can be computed with (see e.g. pp. 120–121 of [28])

$$\hat{\psi}_{\xi}(\tau) = \frac{1}{m - \tau} \sum_{k=1}^{m-\tau} \xi(\hat{\theta}, k) \xi(\hat{\theta}, k + \tau), \quad (4.33)$$

where m is the number of detected magnets. If the residuals are white, then 95% of autocorrelation function for $\tau \neq 0$ lies within $\pm 1.960 \hat{\psi}_{\xi}(0) / \sqrt{m - \tau}$. The estimated autocorrelation functions for experiment 22 that was discussed before are displayed in Figure 4.12. From equation (4.18) we see that the difference between the two tangential residuals equals

$$\xi_{t_R}(\hat{\theta}, k) - \xi_{t_F}(\hat{\theta}, k) = \xi_{w_F}(k) - \xi_{w_R}(k). \quad (4.34)$$

The autocorrelation function of the $\xi_{w_F}(k) - \xi_{w_R}(k)$ is also displayed in Figure 4.12, because this provides us information about the properties of the modeling errors ξ_{w_i} in the drive encoder model. From the figure we recognize a sinusoidal trend in the autocorrelation function of the radial residual $\xi_r(\hat{\theta}, k)$ for the OLS 1. We believe that this is due to a deviation from the pure circular trajectory. Since the absolute values of the residuals for this experiment are still small, the deviation is very modest. Furthermore, we see from Figure 4.12 that the autocorrelation function of the $\xi_{w_F}(k) - \xi_{w_R}(k)$ varies greatly between the two vehicles. The magnitude of the residuals $\xi_{w_F}(k) - \xi_{w_R}(k)$ for the OLS 1 corresponds to the size of the quantization errors in the drive encoders for that vehicle, i.e. 0.12 mm/count. The autocorrelation function for the OLS 2 for $\xi_{w_F}(k) - \xi_{w_R}(k)$ is much larger, and we believe that it is due to the unroundness of the wheels. Other experiments give similar results.

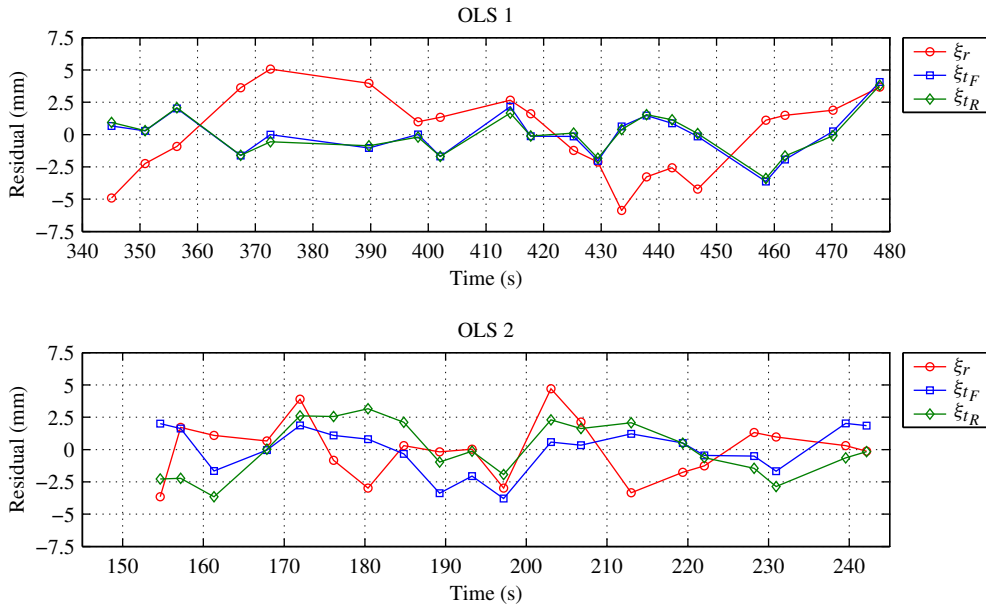


Figure 4.11: Residuals for low speed experiment 22 for the OLS 1 (top panel) and experiment 22 for the OLS 2 (bottom panel) as a function of the magnet detection number.

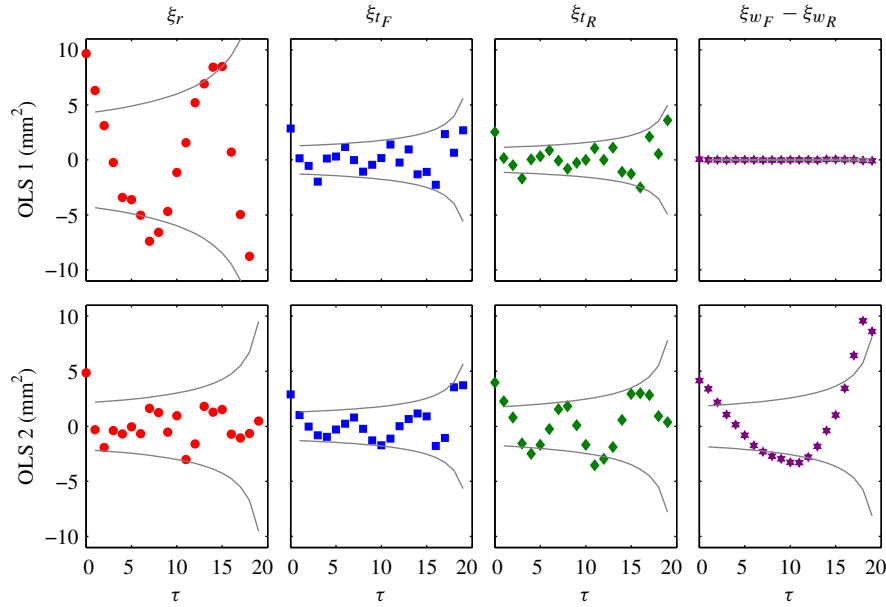


Figure 4.12: Estimated autocorrelation functions $\psi_{\xi}(\tau)$ of the residuals for the OLS 1 and the OLS 2 for low speed experiment 22, together with the 95% reliability interval that would correspond to a white noise sequence.

Estimated steering encoder offsets

The steering encoder offsets were estimated for each low speed experiment according to section 4.5. Figure 4.13 displays the estimated steering encoder offsets for the OLS 1 and OLS 2. The difference between the lowest and highest estimated steering encoder offset for a given wheel is approximately 1.5 deg. Given that the steering encoder offset should be approximately constant, this deviation is quite large. From equations (4.26) and (4.28) we see that the estimated steering encoder offset is directly related to the estimated side slip angle $\hat{\beta}_v$. In particular, β_v enters approximately additively in the estimated steering encoder offsets for small side slip angles. Because the effective length of the magnet ruler is somewhat less than 400 mm (since magnets detected near the ends produce outliers and are disregarded), it is difficult to produce an accurate side slip angle estimate $\hat{\beta}_v$. Therefore, the large spread that is seen in the estimated steering encoder offsets is mostly due to the low accuracy of the side slip angle estimate.

Since the side slip angle estimate term is present in both the front and rear steering encoder offset estimates, its effect can be eliminated by considering the difference between the front and rear steering encoder offset estimates. The differences are displayed in Figure 4.13. The figure shows that the spread for the differences is indeed smaller than the spread for the individual offset estimates. Furthermore, the spread in the differences between the front and rear steering encoder offset estimates is larger and more random for the OLS 2 than for the

OLS 1. Because the OLS 2 has been used much more frequently than the OLS 1, this might be due to increased wear and backlash of the OLS 2's steering systems. The fact that the differences of the OLS 1 slightly decrease with increasing experiment number (i.e., towards right hand turns) suggests inaccuracies in the relative positions of the wheels with respect to the magnet ruler. It is not clear why the OLS 1's differences are larger for forwards motions than for backwards motions.

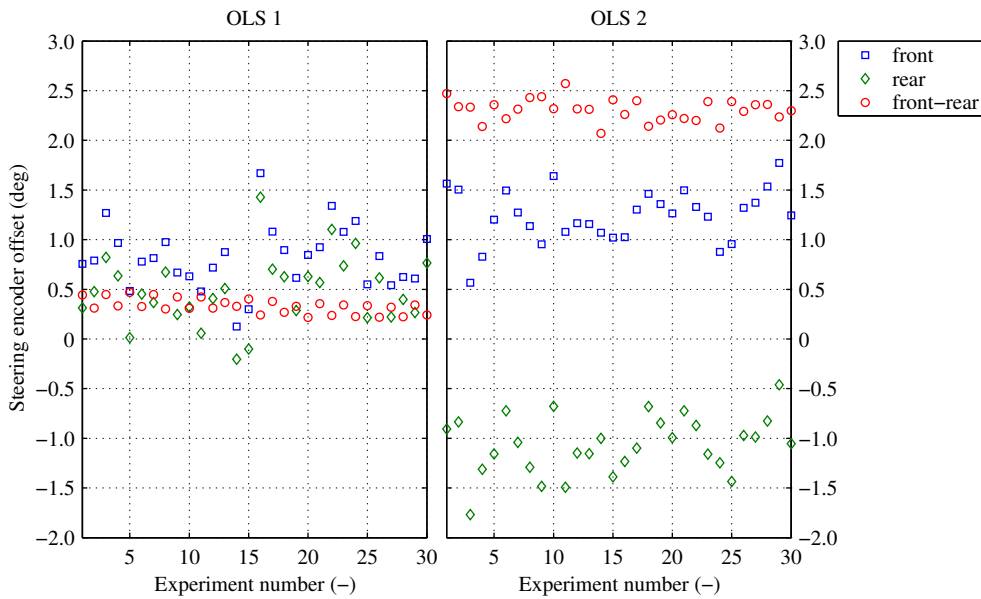


Figure 4.13: Estimated steering encoder offsets for the low speed experiments.

The posteriori steering encoder offsets that will be used in the software for the OLS 1 and the OLS 2 are simply the means of the experiments displayed in Figure 4.13. The values are listed in Table 4.3.

Parameter	OLS 1	OLS 2
Front steering encoder offset (SE) (mrad)	14.22 (1.01)	21.64 (0.84)
Rear steering encoder offset (SE) (mrad)	8.44 (1.11)	-18.60 (0.92)
Difference (SE) (mrad)	5.77 (0.24)	40.24 (0.36)
Front effective wheel diameter (mm)	151.67	151.22
Rear effective wheel diameter (mm)	151.99	153.24

Table 4.3: Estimated steering encoder offsets with standard errors (SE) and the estimated effective wheel diameters for the OLS 1 and the OLS 2 based on the low speed experiments. Because the effective wheel diameters estimates are not normally distributed, the standard deviations have been omitted for these parameters.

Estimated effective wheel diameters

The effective wheel diameters of the front and rear wheels were estimated for each low speed experiment from the estimated intermediate parameters $\hat{\theta}$ according to section 4.5. The estimated effective wheel diameters for each experiment are displayed in Figure 4.14. The most striking characteristic of the estimated effective wheel diameters is that they depend on the direction of travel. In particular, the estimated effective front wheel diameter is larger for forwards movement than for backwards movement, whereas the estimated effective rear wheel diameter is larger for backwards movement than for forwards movement. A closer examination of the vehicles revealed that the caster wheel points towards the rear when driving forwards, and towards the front when driving backwards. This results in a different distribution of the vertical wheel forces. The vertical force on the front wheel and the estimated effective front wheel diameter are both larger when driving forwards than when driving backwards. Similarly, the vertical force on the rear wheel and the estimated effective rear wheel diameter are both smaller when driving forwards than when driving backwards. Thus we see that *the effective wheel diameter increases with increasing vertical wheel load*. This relation will be studied in more detail in section 4.6.3, where the experiments with varying vehicle loads are discussed.

Figure 4.14 shows that the difference in estimated effective wheel diameters between forwards and backwards movement is larger for the OLS 1 than for the OLS 2. Because the OLS 1 was equipped with a steel roller conveyor and the OLS 2 was not, the OLS 1 was heavier than the OLS 2. This resulted in more load shift for the OLS 1, which can explain the a larger variation of the estimated effective wheel diameters between forwards and backwards movement.

From the cumulative relative frequency diagrams in Figure 4.14 we see that, although we can clearly distinguish between forwards and backwards motions, the overall range of the estimated effective wheel diameters is quite small compared to the mean estimated effective wheel diameter itself. The mean values are listed in Table 4.3. Since the estimated effective wheel diameters are within ± 0.3 mm from the means that are listed in the Table 4.3, the absolute error is only about 0.2% of the estimated value. Therefore, we will not distinguish between forwards and backwards movement in the software, but instead use the mean of the forwards and backwards experiments as the parameter setting.

4.6.3 Medium speed experiments with various loads

The previous section presented estimates for the steering encoder offsets and the effective wheel diameters that were based on very low speed experiments that were performed at ≈ 0.2 m/s. In this section we will investigate how these estimates depend on the vehicle speeds and on loads on the vehicle. To this end, experiments were carried out at three different speeds (0.6, 0.9, 1.2 m/s) and with three different loads (0, 50, 100 kg). For each load and each speed, the vehicle moved three times forwards and three times backwards. Table 4.4 presents an overview of the experiments. Because for the low speed experiments the estimated parameters were as good as independent of the radius of the circular trajectory, the planar velocity setpoints for the vehicle were chosen such that the curvature R_v^{-1} and the side slip angle β_v setpoints were both equal to zero for all medium speed experiments. This

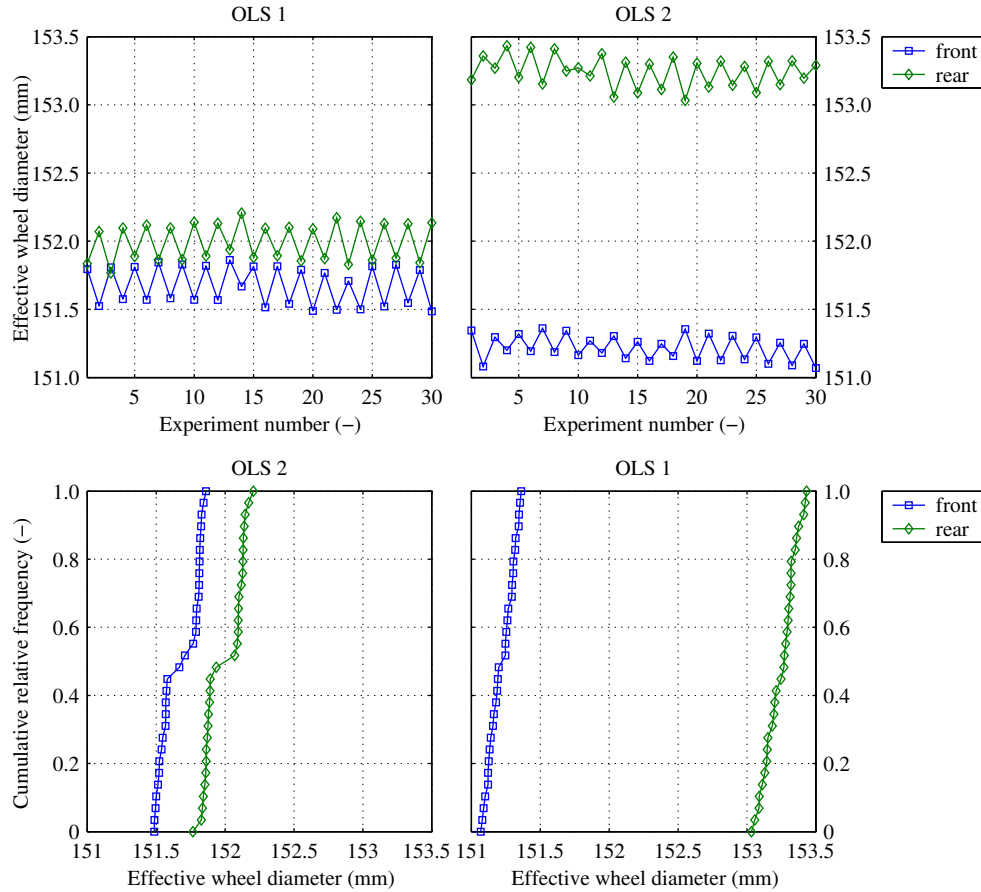


Figure 4.14: Estimated effective wheel diameters for each low speed experiment (top panels) and the cumulative relative frequency diagrams for the estimated effective wheel diameters (bottom panels). The vehicles moved forwards during the odd numbered experiments, and backwards during the even numbered experiments.

resulted in fifty-four experiments per each vehicle. Outlier removal was identical to the low speed case. However, because especially the steering angles of the OLS 1 often showed oscillatory behavior, extra care was taken to select the data such that the steering encoder data was nearly constant. The steering encoder offset estimates that were estimated in the previous section were used in the experiments (see Table 4.3 for their values).

Estimated motion radius R_v and side slip angle β_v

The estimated curvatures R_v^{-1} and the estimated side slip angles β_v of the circular trajectories of the vehicle coordinate system Ψ_v for the medium speed experiments are displayed in

Experiment	Curvature (m^{-1})	Velocity (m/s)	Load (kg)
1..6	0	± 0.6	100
7..12	0	± 0.9	100
13..18	0	± 1.2	100
1..6	0	± 0.6	50
7..12	0	± 0.9	50
13..18	0	± 1.2	50
1..6	0	± 0.6	0
7..12	0	± 0.9	0
13..18	0	± 1.2	0

Table 4.4: Overview of the medium speed experiments with varying loads. The vehicles drive forwards for the odd numbered experiments, and backwards for the even numbered experiments.

Figure B.1 of Appendix B. The estimates for the motion radii satisfied $|\hat{R}_v| \in [141, 6278]$ for the OLS 1, and $|\hat{R}_v| \in [69, 1141]$ m for the OLS 2. As Figure B.1 shows, the trajectories of the OLS 1 were indeed closer to straight lines than the trajectories of the OLS 2. The intervals for the estimated side slip angles are $\hat{\beta}_v \in [-1.83, 1.13]$ for the OLS 1, and $\hat{\beta}_v \in [-1.27, 1.85]$ for the OLS 2. They are qualitatively similar for both vehicles. Figure B.1 also suggest that the realized curvatures and side slip angles were independent of the vehicle speed and load.

Residuals

Box plots of the radial residuals $\xi_r(\hat{\theta}, k)$ and the tangential residuals $\xi_{t_F}(\hat{\theta}, k)$ and $\xi_{t_R}(\hat{\theta}, k)$ for each experiment are displayed in Figure 4.9 of Appendix B. For the OLS 2, the residuals of the medium speed experiments are similar to the residuals of the low speed experiments. For the OLS 1, on the other hand, several radial residuals of the 50 kg experiments are quite large. This is caused by oscillatory behavior of the steering system, which made it sometimes impossible to select a data slice with nearly constant steer encoder data. For the experiments where fluctuating steering angles did occur (e.g. OLS 1 50 kg experiments 10, 12, 14), the radial residuals are typically enlarged whereas the magnitude of the tangential residuals is comparable to other experiments.

Figure 4.15 shows a relative frequency histogram of all the radial and tangential residuals for all the medium speed experiments together. The total number of medium speed residuals is 4962. Compared to the low speed experiments, the relative frequency histogram of the medium speed experiments has considerably more elements in its tails. These stem from the large radial residuals of the OLS 1's 50 kg experiments that are induced by oscillatory behavior of the steering system. The probability density function of the normal distribution $\mathcal{N}(0, 2.2374^2)$ that corresponds to the residuals of the low speed experiments is also plotted in the figure. It still describes the middle section quite well, but has problems at the tails. The medium speed residuals themselves have a mean of 0 mm and a standard deviation of 2.7507 mm.

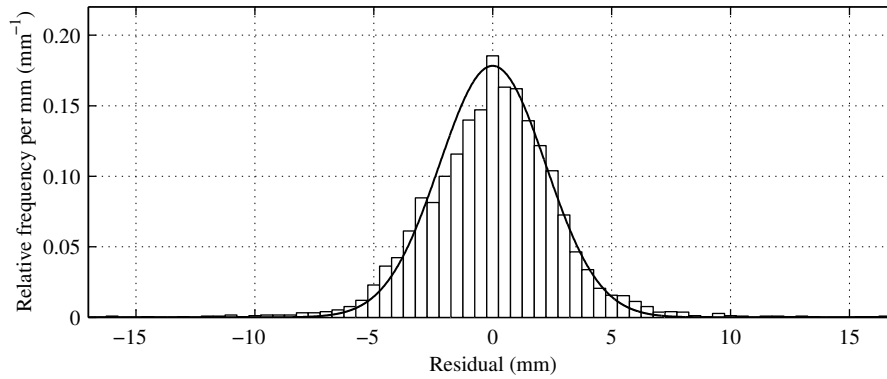


Figure 4.15: Relative frequency histogram of the 4962 longitudinal and lateral residuals for all the medium speed experiments for the OLS 1 and the OLS 2 together. The thick black line is the probability density function of the normal distribution $\mathcal{N}(0, 2.2374^2)$ as estimated from the residuals of the low speed experiments.

Estimated steering encoder offsets

The estimated steering encoder offsets are plotted in Figure 4.16. The differences between the front and rear steering encoder offset estimates are also displayed. As with the low speed experiments, here we see again that the variation in the difference between the front and rear estimates is much smaller than the variation in the estimates themselves. From Figure 4.16 we conclude that the steering encoder offset estimates do not significantly depend on the load or the vehicle speed. Therefore, estimates for these parameters were obtained by considering the medium speed experiments for all loads and all speeds together. The resulting parameter estimates are listed in Table 4.5. When comparing the steering encoder offset estimates obtained with the low speed experiments with the steering encoder offset estimates obtained with the medium speed experiments, it follows that the largest difference between the two sets of experiments occurs for the front steering encoder offset of the OLS 1. The difference between the low speed and the medium speed estimate equals $14.22 - 12.30 = 1.92$ mrad (0.110 deg). Although this is quite large in absolute value, it is of the same magnitude as the reported standard errors of approximately 1 mrad (0.057 deg). It is noted that although the difference between the front minus rear steering angle offsets between the low and medium speed experiments for the OLS 2 ($40.24 - 38.67 = 1.57$ mrad) is of the same magnitude as the other differences, in this case it is large compared to the reported standard errors of 0.36 mrad and 0.20 mrad.

Estimated effective wheel diameters

Figure 4.17 displays the estimated effective front and rear wheel diameters for each medium speed experiment for each of the three loads. It is immediate from the figure that the load has a strong influence on the estimates. In particular, we see that an increase in load results in an increase of the effective wheel diameters. This is counter-intuitive as the wheel axis will be

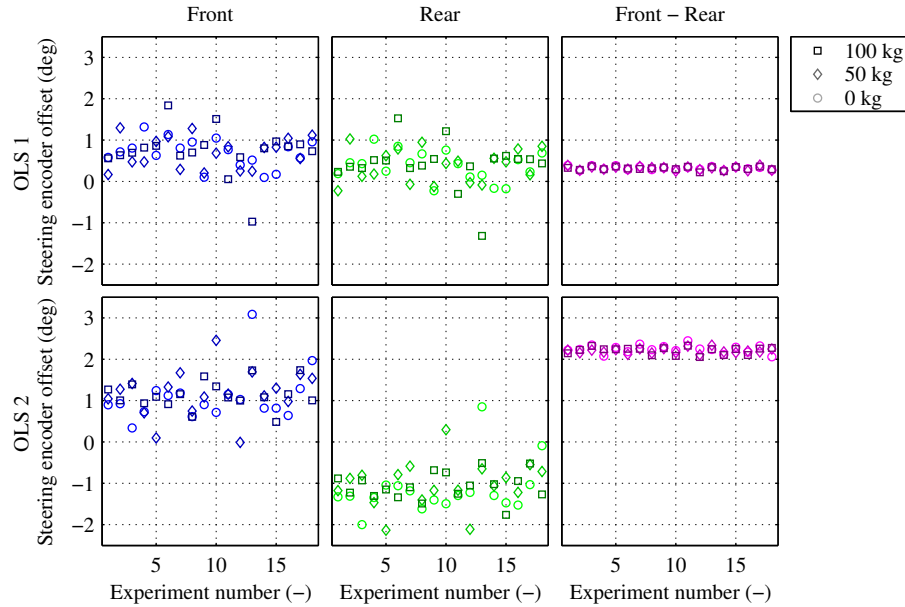


Figure 4.16: Estimated steering encoder offsets for the medium speed experiments with load.

Parameter		OLS 1	OLS 2
Front steering encoder offset (SE)	(mrad)	12.30 (1.03)	19.79 (1.22)
Rear steering encoder offset (SE)	(mrad)	6.75 (1.06)	-18.88 (1.22)
Difference (SE)	(mrad)	5.55 (0.10)	38.67 (0.20)

Table 4.5: Estimated steering encoder offsets with standard errors (SE) for the OLS 1 and the OLS 2 based on the medium speed experiments.

closer to the floor when the vertical load on a wheel is increased due to the compression of the rubber of the wheel.

Figure 4.17 also shows that the vertical load on the front wheel is larger for forward motion because then the caster wheel points towards the rear, and the vertical load on the rear wheel is larger for backwards motion because then the caster wheel points towards the front. The mean of the front and rear wheel diameter estimates $(\text{Front} + \text{Rear})/2$ are also displayed in Figure 4.17. Because the caster wheel is mounted at the middle of the vehicle and the center of gravity is also in the middle of the vehicle, the load shift is symmetrical for forwards and backwards movement. Since the front and rear wheel have similar mechanical properties, the increase in the front wheel diameter is equal to the decrease in the rear wheel diameter. Hence, their sum (divided by two) is approximately constant.

Cumulative relative frequency diagrams of the estimated front, rear and $(\text{front}+\text{rear})/2$ diameters are plotted in Figure 4.18. When comparing the medium speed 0 kg diagrams with the low speed 0 kg diagrams (Figure 4.14), it is seen that the distributions for the medium

speed experiments are wider. From Figure 4.17 we see that for increasing speeds, the differences between the forwards and backwards wheel diameters seem to become slightly bigger. This partially explains why the distributions are wider for the medium speed experiments than for the low speed experiments. Noticeably, all low speed estimates fall within the medium speed distributions.

The influence of various loads on the effective rolling radius has already been studied in 1958 by Parish within the scope of metal and rubber-covered pressure rollers [93]. Since the wheels of our AGVs also consist of an inner metal part that is covered with a small layer of solid rubber, there are many similarities with the rubber-covered pressure rollers. The experiments that are described by Parish indicate that in a roller system consisting of a metal and a rubber-covered roller rotating in contact under load, the metal roller always has the higher apparent peripheral speed whether it is driving or is driven by the rubber roller. Parish attributes this phenomenon to the extension of the rubber surface in the region of the nip, which can be ascribed to the normal loading and to the forces necessary for torque transmission through the nip. We believe that the stretching of the rubber in the tangential direction of our wheels under the influence of load results in a larger circumference of the wheel, which in turn corresponds to a larger effective wheel radius. As in our experiments, the experiments by Parish also indicated that the effective rolling radius increases for increasing loads. In addition, Parish showed that the effective rolling radius was always greater than the free (i.e. unloaded) radius, it was larger at lower speed, and it was larger for the case that the metal

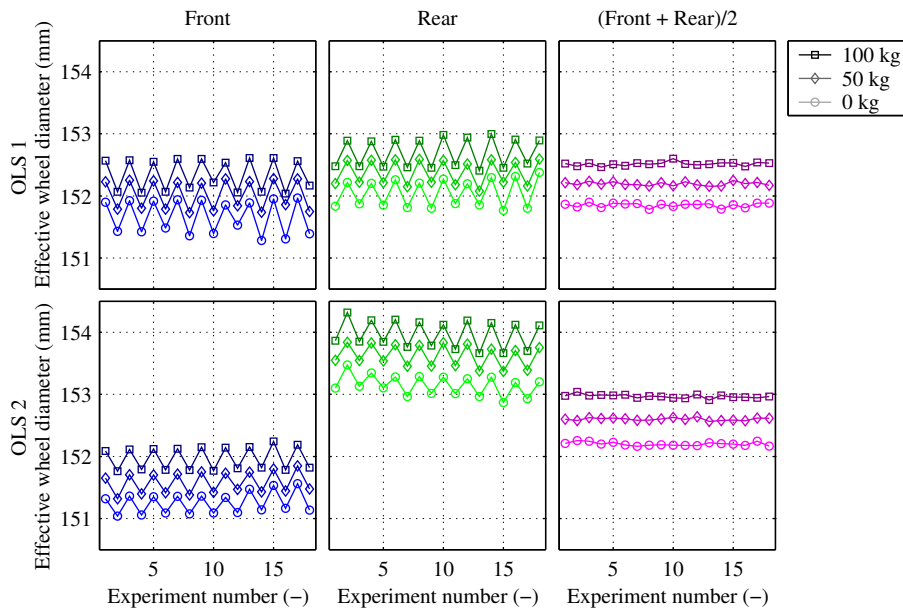


Figure 4.17: Estimated effective wheel diameters for each medium speed experiment. The vehicles moved forwards during the odd numbered experiments, and backwards during the even numbered experiments.

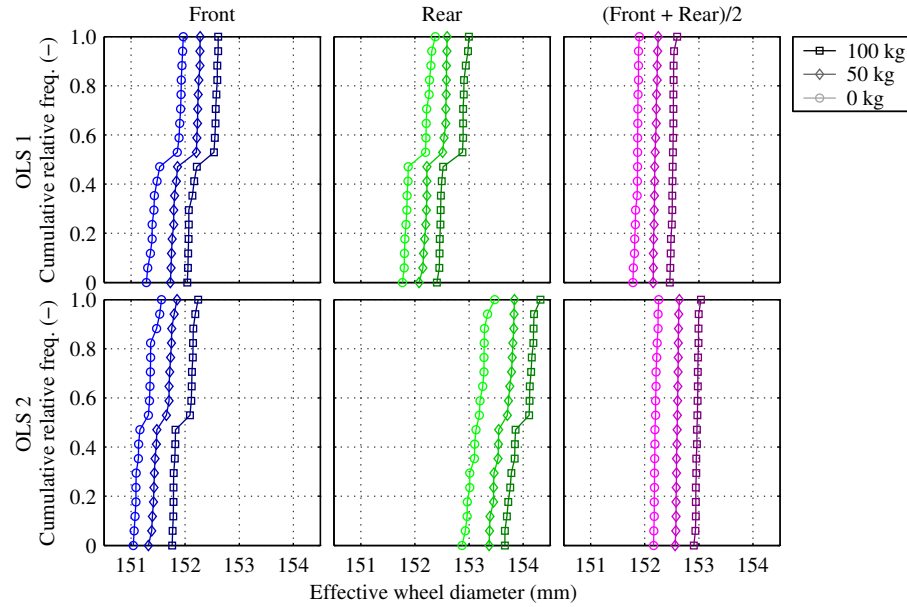


Figure 4.18: Cumulative relative frequency diagrams for the estimated effective wheel diameters for the medium speed experiments with load. The vehicles moved forwards during the odd numbered experiments, and backwards during the even numbered experiments.

was driving the rubber roller than for the rubber roller driving the metal one. Interestingly, for pneumatic tires an increase in load results in a *decrease* of the effective wheel diameter. See for example Figures 4 and 8 in the thesis by Zegelaar [130] for experimental results of the effective (rolling) radius as a function of vertical wheel load and speed for a pneumatic passenger car tire.

4.7 Concluding remarks and discussion

Cooperative transportation applications will typically require AGVs that are highly maneuverable, which means that all the wheels of an individual AGV can steer. For accurate AGV operation it is important that the offsets of the steering encoders and the effective wheel diameters are determined with high precision. Our test vehicles have two steerable wheels, which means that two steering encoder offsets and two effective wheel diameters have to be identified. It is substantially more difficult to identify the odometric parameters for omnidirectional vehicles with multiple steerable wheels than for differential drive and car-like robots and AGVs, since the latter require the identification of at most one steering encoder offset. To the best of our knowledge, there is currently no systematic procedure available to estimate the odometric parameters for vehicles with multiple steerable wheels.

We therefore developed a novel procedure for simultaneously estimating steering angle

encoder offsets and wheel diameters for a vehicle that is equipped with a magnet ruler that can detect magnets that are placed in the floor. The procedure that we propose consists of three steps.

1. The first step is the experimental part. In this step, the setpoints for the vehicle's steering systems are set to constants and the vehicle is instructed to drive a certain distance at a constant, low speed. In practice this will result in a curved trajectory with a nonzero side slip angle. Ideally, the trajectory is a pure circle segment.
2. The second step is to estimate the realized trajectory from the logged steering encoder, drive encoder, and magnet ruler data. In this step we assume that the realized trajectory was indeed a pure circle segment, possibly with a nonzero side slip angle. It is noted that the second step remains valid for nonzero wheel slip, as long as it remains constant during the motion.
3. The third and last step is to translate the realized trajectory to steering encoder offsets and effective wheel diameters. To this end, we need to strengthen the constant wheel slip assumption of the second step to a nonzero wheel slip assumption. The OLS vehicles have two actuated wheels and one caster wheel. Since the caster wheel exerts (almost) no horizontal forces on the floor, it is reasonable to assume that the wheel slip is very small during the experiment due to the low speeds.

For vehicles with three or more steerable wheels with uncalibrated steering encoder offsets, there will be substantial lateral wheel slip as the wheels are not perfectly aligned. Since there is almost no longitudinal wheel slip, we can still use the three-step procedure above to estimate the effective wheel diameters. To minimize the lateral wheel slip, we may first vary the steering encoder offsets heuristically by hand such that the counteracting lateral wheel forces are minimized. Subsequently, we can carry out the three-step procedure above, although the identified steering encoder offsets will be less accurate than for OLS-like vehicles.

The three-step procedure was tested on our two test vehicles, which were designed to be identical in hardware. The residuals were very small, and we concluded that they are mainly caused by the precision at which the magnets are placed in the floor. The accuracy of the estimated steering encoder offsets is directly related to accuracy of side slip angle estimates for the various experiments. The short magnet ruler made it rather difficult to estimate the motion's side slip angle. Consequently, the steering encoder offsets could only be estimated within 0.1 deg. The effective wheel diameters, on the other hand, can be estimated very precisely. Interestingly, the effective wheel diameter for the rubber tires of our vehicles *increase* with increasing vertical wheel loads. This is opposite to the behavior of pneumatic tires, where the effective wheel diameter decreases with increasing load. Finally, it was investigated whether experiments at higher speeds and with varying loads substantially influenced the steering encoder offsets and effective wheel diameters. This was not the case. The steering encoder offsets were also independent of the load.

Observer

5.1 Introduction

For any controlled system it is true that the accuracy at which the system can be operated depends directly on the accuracy of the sensors. Often the desired behavior of the controlled system is not directly expressed in terms of the sensor outputs, but rather in a physical quantity that is closely related to the sensor outputs. In our case, the desired behavior of the controlled system is expressed in terms of the longitudinal, lateral and rotational velocities of a coordinate system Ψ_ℓ that is attached to the load. Of secondary interest are the motions of the AGVs. Clearly, these twists of the load and vehicles with respect to the world are not measured directly. So we have to find the state by combining the odometry readings in a smart way.

In this chapter we design an observer that will be used in the control algorithm for cooperative operation that is presented in the next chapter. We start with a discussion of related work and discuss the positioning of our own study. Subsequently, we will focus on the observer for a single AGV. We answer the theoretical question if it is at all possible to reconstruct the twist from the steering and driving encoder measurements. Although this turns out to be the case, this theoretical result has limited practical meaning as it is elementary that there is no meaningful information available on the components of the vehicle speed in the direction perpendicular to the wheel planes, i.e. in the direction of the steering pole. Therefore, we subsequently focus on a more pragmatic least-squares approach to estimate the AGV's twist from the odometry measurements. Next, we will extend the single AGV case to a central least-squares based observer (in the sense that it uses the measurements of all the vehicles) for multiple AGVs that are cooperatively transporting a load. Finally, it is discussed how the central observer can be implemented in a distributed way. The necessary amount of communication is also analyzed.

5.2 Related work

In the overview of related work on modeling that was presented in section 3.2, we distinguished between the field of wheeled mobile robots (WMRs) and the field of vehicle dynamics. The most important difference was that the kinematic wheel models where slip is neglected suffice for the low speed WMR applications, whereas the prediction of wheel slip by accurate tire models is essential for the field of vehicle dynamics. Motion estimation is an important aspect of both fields, and we see that similar sensors are employed for this purpose. The majority of the applications features drive encoders to measure the travelled distance of the wheels. If the wheels are able to steer, then they are also equipped with steering angle

encoders. Although more exotic sensors such as laser range finders, radar, vision systems, magnet measurement systems, fiber optic gyroscopes, solid-snake yaw rate sensors, ultrasonic sensors, are used in both fields, they are certainly not found on every system. The motion observers in industrial AGVs are mostly based on odometric measurements, i.e. data from drive encoders and steering encoders. The techniques that are used are similar to the observers of the wheeled mobile robot and the vehicle dynamics fields. As it was already argued that the kinematics models used by the WMR community are not able to capture all the relevant behavior of our AGVs, we will only focus on the estimation techniques from the field of vehicle system dynamics. We conclude this section with a discussion of the positioning of our work.

5.2.1 Vehicle dynamics

The subfield of vehicle dynamics that is relevant for our estimation problem is the subfield that deals with the horizontal behavior of vehicles. Contrary to the WMR literature, in horizontal vehicle dynamics the main focus is on velocities rather than on absolute positions. The reason is that the behavior of a vehicle in response to the actions of a driver strongly depends on the momentary velocities and is best characterized in terms of accelerations in response to steering inputs. Although the condition of the road is a very important factor in the vehicle behavior, this can be modelled as an independent variable without considering the absolute position of the vehicle in the world. The behavior of the vehicle is usually described in terms of its longitudinal velocity, its rotational velocity, and the lateral velocity or the side slip angle at e.g. its center of gravity, depending on the preference of the authors. This triple is often referred to as the *state* of the vehicle, and the rotational velocity is also called *yaw rate*.

Nowadays we witness a vast increase of driver assistance systems that aid the driver in operating the vehicle. The interest in techniques for estimating the vehicle state, which is required by these control systems to function appropriately, has increased accordingly. The first driver assistance systems were developed to aid the driver in controlling the vehicle during extreme maneuvers to enhance the occupants' *safety*. Such systems include Anti-lock Braking Systems (ABS), Electronic Stability Programs (ESP), and Traction Control (TC). Since extreme maneuvers are characterized by high accelerations (in the order of one g), these systems typically combine acceleration and yaw rate sensors with information from digital encoders that are mounted on the wheels to estimate the current behavior of the vehicle. When the vehicle is on the verge of getting out of control, then these systems will act and try to bring the state of the vehicle back within safe limits. Besides the estimation of the vehicle state, for these systems it is also very important to have an indication about the current condition of the road. A slippery wet and icy road requires more subtle actions than dry tarmac. However, even under ideal road surface conditions the wheels will exhibit large side slip angles during these extreme maneuvers. Since large wheel slips are precisely the reason that the vehicle becomes uncontrollable and since the wheels' slip angles form the key to get the vehicle back into a safer operating region, these systems cannot adopt the wheel models from the WMR community with their ideal no-slip conditions.

Besides the driver assistance systems that help the driver during extreme maneuvers to improve safety, currently we also see an increase of systems that are also active during normal operation. The aim of these systems is to improve the driver's *comfort* or the *drivability* of

the car. One can think of the original cruise control systems and its successor Adaptive Cruise Control (ACC). Whereas the normal cruise control will keep the vehicle at a certain constant speed, in addition the ACC will automatically decelerate when the vehicle in front of the driver slows down. There are also systems that act in the lateral direction of the vehicle. At the moment experiments are carried out with systems that influence the steering angle of the front wheels. Some of these systems superimpose a small steering angle offset on top of the driver's own action to improve the handling of the car, see e.g. [63, 117]. Other systems take complete control over the lateral behavior as is the case in Automated Highway Systems (AHS) research and also in the Phileas that drives in Eindhoven city.

Most vehicle state estimators that are described in literature exploit data from wheel encoders to estimate the relevant variables. Since it is not possible to extract meaningful information about the wheel's side slip angle from the rotational velocity of the wheels, either additional measurements or vehicle models are needed to estimate the missing data. The additional measurements typically consist of inertial measurements systems, such as yaw rate sensors and accelerometers. Although the yaw rate can be measured directly, measuring the lateral velocity requires integration of a lateral accelerometer signal. These sensors are particularly interesting for estimating the vehicle state during extreme maneuvers. In those cases the signals are large compared to the sensor noise and other offsets. For normal operation, however, acceleration signals are so small that it is not possible to distinguish between banking of the road and the lateral acceleration of the vehicle with respect to the road. Likewise, the relatively cheap yaw rate sensors that are found in modern passenger cars are quite capable to detect large yaw rates. Measuring the small yaw rates that occur during normal operation, however, calls for more advanced sensors, such as fiber optic rate gyroscopes. Since the latter are too expensive for mass produced passenger cars, the observers that estimate the vehicle state during normal operation will instead incorporate vehicle models to deal with the sensor drift of the inertial systems to estimate the state during normal vehicle maneuvers.

The early driver assistance systems dealt with only one aspect of vehicle control, e.g. longitudinal velocity control (cruise control), yaw rate control, etc. Therefore, in the past these individual control systems only required a small part of the vehicle state that was relevant for their own local control task. Currently there is a trend to integrate these various control systems. More on this is found in section 6.2 of the next chapter on control. Since each system has its own sensors, there is also a trend from estimating part of the vehicle state towards estimating the complete vehicle state by fusing the measurements of the various subsystems. Often the to-be-estimated variables also include some vehicle parameters, such as inertial properties and the tire-road friction coefficient, and some external disturbances, such as the banking or the inclination of the road.

Thus there is a vast amount of literature on vehicle state observers. Several have been applied with success in the driver assistance systems of modern passenger cars. For example, Fukuda [41] describes a system to estimate the road slant, the road friction coefficient, and the vehicle side slip angle. The algorithm combines a yaw rate sensor and accelerometer with a vehicle model that incorporates a nonlinear tire model. This slip angle estimation procedure has been applied to Toyota's Vehicle Stability Control (VSC) since 1997. Also a lot of attention has been given to the problem of fusing inertial measurements with a dynamic vehicle model. For instance, Huang *et al.* [55] present a vehicle state observer that estimates the longitudinal vehicle velocity and the vehicle sideslip angle. In their strategy, measurements

from the wheel encoders, a yaw rate sensor and a longitudinal accelerometer are combined with a vehicle model. For normal driving situations, the wheel speeds and steering angle are used in combination with a linear vehicle model to determine the required states. As soon as the vehicle enters a critical driving situation with non-linear vehicle behavior, they switch to integration of vehicle accelerations. Possible offsets in the measured accelerations are estimated with Luenberger observers. Wenzel *et al.* [128] propose a different strategy for fusing data from the wheel encoders, yaw rate sensor and lateral accelerometer with a nonlinear vehicle model. Their Dual Extended Kalman Filter (DEKF) estimates three inertia parameters of the vehicle plus the vehicle state. Besides the side slip angle, yaw rate, and side slip angle, their estimator also estimates other quantities, such as accelerations, that are required by some advanced driver assistance systems. Since the vehicle inertia parameters remain constant during a journey, the authors argue that the parameter estimating part of the DEKF can be switched off once the parameters are known at the required accuracy. Some other Kalman filter solutions for vehicle dynamics estimation are for instance described by Venhovens and Naab [123]. For some more references the interested reader may consult the short literature survey in [102].

5.2.2 Positioning of our work

The observers from the wheeled mobile robot community generally assume that there is no wheel slip. From practical experience we know that for normal AGV operation the wheels' slip angles become too large to justify this assumption. This is especially the case during cornering, acceleration and braking. Therefore, for our application it is better to focus on the estimation techniques that are found in the field of vehicle dynamics. We saw that modern vehicle state observers combine vehicle and tire models for estimation during normal operation with inertial measurement systems for estimation during more extreme maneuvers. For our applications extreme maneuvers such as drifting through corners and full lock braking will not occur. So we are only interested in the parts of the vehicle state observers that deal with estimation during normal operation. From literature and also from our own experience [50] we learned that the measurements that are provided by inertial sensors, in particular accelerometers and solid-state yaw rate sensors, do not provide meaningful information for these situations. Therefore, we will restrict ourselves to state estimation that is based on odometric measurements in combination with a vehicle model. The vehicle models that are used in driver assistance systems are very similar to the dynamic AGV model with static linear tires that was presented in Chapter 3. Thus we will base our observer design on that model. Although the observer for an individual AGV has a lot in common with the vehicle state observers that are found in driver assistance systems, some important differences occur when we have to simultaneously estimate the twists of several AGVs that are cooperatively transporting a load. In addition, where vehicles will only drive forwards and backwards, AGVs are much more maneuverable and can also move sideways. The observer design and analysis for a single AGV is the topic of sections 5.3 and 5.4. Observer design for multiple physically interconnected AGVs will be addressed in section 5.5.

5.3 Observability

In this section we will investigate whether it is fundamentally possible to estimate the twist $T_v^{v,0}$ of a single AGV from the vehicle's odometric measurements (drive and steering encoder data). Recall that the twist $T_v^{v,0}$ of an AGV with respect to the floor was parameterized by the rotational velocity ω_v , the longitudinal velocity u_v and the lateral velocity v_v of a coordinate system Ψ_v that is fixed to the AGV with respect to the floor:

$$T_v^{v,0} = \begin{pmatrix} \omega_v \\ u_v \\ v_v \end{pmatrix}. \quad (5.1)$$

Each of the actuated wheel units of an OLS vehicle is equipped with a steering angle encoder and a drive encoder. This combination results in a single velocity measurement for the center of each wheel. Since an OLS vehicle has only two actuated wheel units, which corresponds to two velocity measurements, it is not possible to estimate all three components of the twist directly. Therefore, we will investigate if it is possible to estimate all three components by using the AGV model that was presented in Chapter 2. We will use the nonlinear observability concept as discussed in Chapter 3 of Nijmeijer and Van der Schaft [89]. Their discussion is based on a model of the form

$$\begin{cases} \dot{x} = f(x) + g(x)u \\ y = h(x) \end{cases} \quad (5.2)$$

Here x is the state, u is the input, and y are the measured outputs. With equation (3.49) of Chapter 3 we saw that the equation of motion for our AGVs is given by

$$\dot{T}_v^{v,0} = -\omega_v \Gamma_v T_v^{v,0} + M_v^{-1} (W^v)^T. \quad (5.3)$$

Thus we see that in our case the twist $T_v^{v,0}$ of the vehicle with respect to the floor plays the role of the state x . Since Γ_v is constant and since ω_v is simply the first component of $T_v^{v,0}$, the first term $-\omega_v \Gamma_v T_v^{v,0}$ on the right hand side depends on the state $T_v^{v,0}$ only. In the second term on the right hand side, M_v is the constant mass matrix and W^v is the wrench that is exerted on the vehicle. In case of a single vehicle this wrench is equal to the wrench that is exerted by the wheels: $W^v = W_w^v$. Although the analysis that follows is applicable to a broader class of vehicles, in the remainder of this section we will restrict ourselves to the OLS vehicles for clarity. It was already argued in section 3.6 that the original vehicle model (3.51),(3.73) was not affine in the inputs. Therefore, the model was subsequently simplified by considering the first order Taylor expansion around the momentary steering pole. This resulted in a model that is indeed of the form (5.2), where the inputs u are given by (3.95)

$$u = \begin{pmatrix} F_{w_1,u} \\ F_{w_2,u} \\ \alpha_{w_1} \\ \alpha_{w_2} \end{pmatrix} \quad (5.4)$$

Here $F_{w_i,u} \stackrel{\text{def}}{=} (W_{w_i}^{w_i,v})_u$ is the driving force and α_{w_i} is the slip angle of wheel i . It is straightforward to convert the desired slip angle α_{w_i} to the setpoint δ_{w_i} for the corresponding steering system by using equation (3.61). The advantage of using α_{w_i} over δ_{w_i} as the input, is that the equations are of a simpler form. According to the simplified model, the wrench W_w^v that is exerted by the wheels on the vehicle satisfies (3.94)

$$(W_w^v)^T = (\bar{B}_{w_1,u}^T \quad \bar{B}_{w_2,u}^T \quad -C_{\text{lat}}^{w_1} \bar{B}_{w_1,v}^T \quad -C_{\text{lat}}^{w_2} \bar{B}_{w_2,v}^T) u. \quad (5.5)$$

If we define

$$\begin{array}{l} f(x) = -\omega_v \Gamma_v T_v^{v,0} \\ g(x) = M_v^{-1} (\bar{B}_{w_1,u}^T \quad \bar{B}_{w_2,u}^T \quad -C_{\text{lat}}^{w_1} \bar{B}_{w_1,v}^T \quad -C_{\text{lat}}^{w_2} \bar{B}_{w_2,v}^T) \end{array} \quad (5.6)$$

then we see that the equation of motion (5.3)-(5.5) for the (simplified) vehicle model is indeed in the familiar form $\dot{x} = f(x) + g(x)u$. In addition to the equation of motion, the observability analysis also requires an output model $y = h(x)$. To simplify the analysis, we will now assume that the steering angle measurements are perfect. Furthermore, we will perform a continuous analysis where the driving encoders are assumed to measure the spin velocities of the wheels. From equation (3.56) it follows that the spin velocity $\dot{\theta}_{w_i}$ of wheel w_i satisfies

$$\dot{\theta}_{w_i} = \frac{u_{w_i}}{r_{w_i} (1 - K_{\text{long}}^{w_i} F_{w_i,u} \text{sign}(u_{w_i}))} \approx \frac{\bar{B}_{w_i,u} T_v^{v,0}}{r_{w_i} (1 - K_{\text{long}}^{w_i} F_{w_i,u} \text{sign}(\bar{B}_{w_i,u} T_v^{v,0}))}, \quad (5.7)$$

with $K_{\text{long}}^{w_i} \stackrel{\text{def}}{=} (C_{\text{long}}^{w_i})^{-1}$ the inverse of the longitudinal stiffness of wheel w_i . Here u_{w_i} was approximated by $\bar{B}_{w_i,u} T_v^{v,0}$ in the second step. When $\dot{\theta}_{w_i}$ is measured, an estimate for the longitudinal wheel velocity can be obtained from this equation as

$$\hat{u}_{w_i} = \hat{r}_{w_i} (1 - \hat{K}_{\text{long}}^{w_i} F_{w_i,u}^{\text{set}} \text{sign}(u_{w_i})) \dot{\theta}_{w_i} \quad (5.8)$$

By substituting (5.7) and using $u_{w_i} \approx \bar{B}_{w_i,u} T_v^{v,0}$, this can be written as

$$\hat{u}_{w_i} = \frac{\hat{r}_{w_i} (1 - \hat{K}_{\text{long}}^{w_i} F_{w_i,u}^{\text{set}} \text{sign}(u_{w_i}))}{r_{w_i} (1 - K_{\text{long}}^{w_i} F_{w_i,u} \text{sign}(u_{w_i}))} u_{w_i} \approx \frac{\hat{r}_{w_i} (1 - \hat{K}_{\text{long}}^{w_i} F_{w_i,u}^{\text{set}} \text{sign}(u_{w_i}))}{r_{w_i} (1 - K_{\text{long}}^{w_i} F_{w_i,u} \text{sign}(u_{w_i}))} \bar{B}_{w_i,u} T_v^{v,0}. \quad (5.9)$$

Next, assume that the effective wheel diameter is perfectly known, so $\hat{r}_{w_i} = r_{w_i}$. In addition, assume that $K_{\text{long}}^{w_i} F_{w_i,u}$ is small compared to 1 such that the direct feed through from the inputs $F_{w_i,u}$ to the outputs \hat{u}_{w_i} can be neglected. Under these assumptions it holds that the estimated longitudinal velocity \hat{u}_{w_i} is equal to

$$\hat{u}_{w_i} = \bar{B}_{w_i,u} T_v^{v,0}. \quad (5.10)$$

We stack the estimated longitudinal velocities \hat{u}_{w_i} of all the wheels in a single vector, and define this to be our measurements y . The i^{th} component of the measurement vector y is denoted by y_i , and satisfies

$$y_i = h_i(x) = \bar{B}_{w_i,u} T_v^{v,0} \quad (5.11)$$

One of the nice properties of the simplified model is that the measurements y_i only provide information about the velocity component that is tangent to the path of the wheel centers. In other words, for the simplified model all the information about the velocity components in the direction of the steering pole is hidden from the measurements. This is in correspondence with our intuition, which says that there is indeed no meaningful information for these velocity components available.

5.3.1 Local observability

We have seen that the equations of motion of the vehicle and the output model are of the form

$$\begin{aligned}\dot{x} &= f(x) + g(x)u \\ y &= h(x),\end{aligned}\tag{5.12}$$

where $f(x)$ and $g(x)$ are given by (5.6), and $h_i(x)$ by (5.11); $i \in \{1, 2\}$. We do not consider cases where any of the longitudinal wheel velocities are zero, hence

$$\bar{B}_{w_i,u} T_v^{v,0} \neq 0 \quad \forall i.\tag{5.13}$$

According to Corollary 3.33 of Nijmeijer and Van der Schaft [89], the system (5.12) is locally observable at x_0 if it satisfies the so-called *observability rank condition*. The observability rank condition is satisfied if the dimension of the *observability codistribution*, denoted as $d\mathcal{O}$, is equal to the dimension of the state. The observability codistribution can be computed from the *observation space* \mathcal{O} , which in turn can be determined from $f(x)$, $g(x)$ and $h_i(x)$. Due to the complicated forms of $f(x)$, $g(x)$ and $h_i(x)$, we will use Proposition 3.31 of Nijmeijer and Van der Schaft [89] to compute the observation space \mathcal{O} . This requires the so-called *accessibility algebra* \mathcal{C} . Since M_v is nonsingular and \bar{B}^T has full row rank for our vehicles, see (3.70) and (3.93), we know from (5.6) that $g(x)$ has full row rank. This means that by choosing the appropriate input u , the derivative \dot{x} of the state can be excited in every direction. Thus *accessibility distribution* $C(x)$ generated by the accessibility algebra \mathcal{C} has full rank: $\dim C(x) = 3$. This means that the accessibility distribution is equal to the tangent space for the states $T_v^{v,0}$ that we consider.

Next, we use Definition 3.29 and Proposition 3.31 of Nijmeijer and Van der Schaft [89] to characterize the observation space \mathcal{O} and to compute the observability codistribution $d\mathcal{O}$. In order to do this, we need the derivatives of the output functions $h_i(x)$ with respect to the state $x = T_v^{v,0}$. The derivative of output function h_i with respect to the state equals

$$\frac{\partial h_i}{\partial T_v^{v,0}} = \frac{\partial \bar{B}_{w_i,u} T_v^{v,0}}{\partial T_v^{v,0}} = \frac{\partial \bar{B}_{w_i,u}}{\partial \bar{\delta}_{w_i}} T_v^{v,0} \frac{\partial \bar{\delta}_{w_i}}{\partial T_v^{v,0}} + \bar{B}_{w_i,u} = \underbrace{\bar{B}_{w_i,v} T_v^{v,0}}_0 \frac{\partial \bar{\delta}_{w_i}}{\partial T_v^{v,0}} + \bar{B}_{w_i,u} = \bar{B}_{w_i,u},\tag{5.14}$$

where $\bar{\delta}_{w_i}$ is the kinematic steering angle of wheel w_i . For the third equality we used equation (3.89): $\partial \bar{B}_{w_i,u} / \partial \bar{\delta}_{w_i} = \bar{B}_{w_i,v}$. From the definition of the kinematic steering angle (3.86) we know that the lateral velocity expressed in the coordinate system $\Psi_{\bar{w}_i}$ corresponding to the kinematic steering angle is zero, hence $\bar{B}_{w_i,v} T_v^{v,0} = 0$. This was used in the last step.

Thus the co-vectorfield dh_i is given by

$$\boxed{dh_i = \frac{\partial h_i}{\partial T_v^{v,0}} = \bar{B}_{w_i,u}} \quad (5.15)$$

The OLS vehicles have one front wheel and one rear wheel: $i \in \{1, 2\}$. The dimension of the codistribution spanned by dh_1 and dh_2 is at most two. Because this is smaller than the dimension of the state, which is three, we continue to compute more co-vectorfields to span the observability distribution $d\mathcal{O}$. Corresponding to Proposition 3.31, we may use the co-vectorfields $dL_{X_j}h_i$ to this end, where X_j is any vectorfield in the accessibility distribution $C(x)$. In particular, consider a constant vector field X_j that does not depend on the state $T_v^{v,0}$. Then

$$L_{X_j}h_i = \frac{\partial h_i}{\partial T_v^{v,0}} X_j = \bar{B}_{w_i,u} X_j. \quad (5.16)$$

To find the corresponding codistribution, we need to compute $\partial L_{X_j}h_i / \partial T_v^{v,0}$. This requires the derivative of the kinematic steering angle $\bar{\delta}_{w_i}$ with respect to the state $T_v^{v,0}$:

$$\begin{aligned} \frac{\partial \bar{\delta}_{w_i}}{\partial T_v^{v,0}} &= \frac{1}{(y_{w_i}^v \omega_v - u_v)^2 + (x_{w_i}^v \omega_v + v_v)^2} \begin{pmatrix} x_{w_i}^v u_v + y_{w_i}^v v_v \\ -x_{w_i}^v \omega_v - v_v \\ -y_{w_i}^v \omega_v + u_v \end{pmatrix}^T \\ &= \frac{1}{(\bar{B}_{w_i,u} T_v^{v,0})^2} (\bar{B}_{w_i,v}^T \underbrace{\bar{B}_{w_i,u} T_v^{v,0}}_{\text{a number}})^T = \frac{\bar{B}_{w_i,u} T_v^{v,0}}{(\bar{B}_{w_i,u} T_v^{v,0})^2} \bar{B}_{w_i,v} \\ &= \frac{1}{\bar{B}_{w_i,u} T_v^{v,0}} \bar{B}_{w_i,v}. \end{aligned} \quad (5.17)$$

It follows that the codistribution $dL_{X_j}h_i$ satisfies

$$\begin{aligned} dL_{X_j}h_i &= \frac{\partial L_{X_j}h_i}{\partial T_v^{v,0}} = \frac{\partial \bar{B}_{w_i,u} X_j}{\partial T_v^{v,0}} = \bar{B}_{w_i,u} \overbrace{\frac{\partial X_j}{\partial T_v^{v,0}}}^0 + X_j^T \frac{\partial \bar{B}_{w_i,u}^T}{\partial T_v^{v,0}} = X_j^T \overbrace{\frac{\partial \bar{B}_{w_i,u}^T}{\partial \bar{\delta}_{w_i}}}^{\bar{B}_{w_i,v}^T} \frac{\partial \bar{\delta}_{w_i}}{\partial T_v^{v,0}} \\ &= \underbrace{X_j^T \bar{B}_{w_i,v}^T}_{\text{a number}} \underbrace{\frac{1}{\bar{B}_{w_i,u} T_v^{v,0}}}_{\text{a number} \neq 0} \bar{B}_{w_i,v} = \frac{\bar{B}_{w_i,v} X_j}{\bar{B}_{w_i,u} T_v^{v,0}} \bar{B}_{w_i,v}. \end{aligned} \quad (5.18)$$

For the third equality we used that $\bar{B}_{w_i,u} X_j = X_j^T \bar{B}_{w_i,u}^T$, since this is a single number. For the fourth equality it was used that the derivative of X_j with respect to the state is zero, as X_j was chosen to be constant. Since we were free to choose X_j , we can always find a constant X_j such that for a given state $T_v^{v,0}$ it holds that

$$\boxed{dL_{X_j}h_i = \frac{\partial L_{X_j}h_i}{\partial T_v^{v,0}} = \bar{B}_{w_i,v}} \quad (5.19)$$

So the observability codistribution $d\mathcal{O}$ can be written as

$$d\mathcal{O} = \text{span} \left\{ dh_1, dh_2, dL_{X_{j_1}} h_1, dL_{X_{j_2}} h_2 \right\} = \text{span} \left\{ \bar{B}_{w_1,u}, \bar{B}_{w_2,u}, \bar{B}_{w_1,v}, \bar{B}_{w_2,v} \right\} = \text{Im}(\bar{B}). \quad (5.20)$$

Since

$$\boxed{\dim(d\mathcal{O}) = \dim(\bar{B}) = \dim(T_v^{v,0}) = 3} \quad (5.21)$$

the system (5.12) satisfies the observability rank condition. Hence, the system (5.12) is locally observable for all the $T_v^{v,0}$ that satisfy $\bar{B}_{w_i,u} T_v^{v,0} \neq 0$. As we did not consider the (unrealistic) situations where $\bar{B}_{w_i,u} T_v^{v,0} = 0$, we cannot conclude that the system is observable for all $T_v^{v,0}$.

5.3.2 Practical considerations

The previous subsection illustrated that the single AGV model is locally observable for all relevant $T_v^{v,0}$. Thus in theory it is possible to reconstruct the rotational, longitudinal, and lateral velocity of the AGV with respect to the floor when the steering angles and the rotational velocities of the wheel are measured. Since an OLS vehicle has only two drive encoders and since the number of to-be-estimated variables is three, it is not possible to reconstruct all the to-be-estimated variables directly. In particular, there are no direct measurements for the velocity component in the direction of the steering pole available. Even if we had more wheels with longitudinal sensors, then it would still be practically impossible to directly translate these measurements into information about the missing velocity component.

Intuitively, we can retrieve information about this missing component by exciting the system in such a way that the position of the steering pole changes. Then the the orientation of the wheels will change, and the drive encoder will consequently measure a velocity component that lies in the direction of the old steering pole. This is the reason why we needed to compute an additional Lie bracket to show that the AGV model is locally observable. In reality we would have to change the motion of the AGV quite drastically to obtain practically meaningful information about the velocity component that is not measured directly. Since AGVs must strictly adhere to their predefined paths in industrial settings and since the design freedom of the paths is limited by the geometry of the environment, it is not a realistic option to drastically change the motion to improve the motion estimate. In addition, a change from one motion to another can only be carried out quite slowly (in the order of seconds) for AGVs and other vehicles. Thus when the wheels are finally oriented in the missing direction, then in the meantime the estimate for the velocity in another direction will have deteriorated too much. **Since it is not realistic to design an observer that uses large excursions from the nominal motion to estimate all the three velocity components $T_v^{v,0} = (\omega_v, u_v, v_v)$, we pursue a more pragmatic approach where it is assumed that the setpoints $\alpha_{w_i}^{\text{set}}$ for the wheels' slip angles are realized exactly.** As we will see in the next section, it is straightforward to obtain an estimate for the lateral wheel velocity once the wheel's slip angle α_{w_i} is known.

5.4 Least-squares observer for a single AGV

Although it was shown that the affine model (5.2) of our system is locally observable, in the previous subsection it was argued that this theoretical result is not very relevant for practice. Therefore, FROG uses a velocity observer that is based on a least-squares estimation technique. To be able to deal with situations where the steering angles are not measured directly, the true steering angles are considered to be unknowns in FROG's observer concept. This is for example the case for some of the steering systems that are encountered in passenger cars, busses and trucks. For the OLS vehicles, however, the steering angles are measured directly. Hence, for our situation the estimates of the steering angles will be identical to the encoder measurements. Therefore, we will focus on the estimation of the twist only.

5.4.1 Description of the observer

A schematic representation of the observer is depicted in Figure 5.1. The test vehicles that we consider have two drive encoders and two steering encoders. So there are four measurements available. **The measurements of the drive encoders are used to estimate the longitudinal velocities u_{w_i} of wheels.** From equation (5.8) we see that

$$\hat{u}_{w_i} = \hat{r}_{w_i} \left(1 - \hat{K}_{\text{long}}^{w_i} F_{w_i, u}^{\text{set}} \text{sign}(u_{w_i}) \right) \dot{\theta}_{w_i} \quad (5.22)$$

This requires the spin velocity $\dot{\theta}_{w_i}$ as obtained from the drive encoder measurements, the effective wheel radius \hat{r}_{w_i} that was estimated in Chapter 4, the inverse longitudinal stiffness $\hat{K}_{\text{long}}^{w_i}$, and the driving force $F_{w_i, u}^{\text{set}}$. The longitudinal cornering stiffness $\hat{K}_{\text{long}}^{w_i}$ is usually not very accurate. However, we know that the estimated longitudinal wheel velocity \hat{u}_{w_i} depends linearly on the term $(1 - \hat{K}_{\text{long}}^{w_i} F_{w_i, u}^{\text{set}})$. The product $\hat{K}_{\text{long}}^{w_i} F_{w_i, u}^{\text{set}}$ is typically small as compared to 1, especially when the driving force is small. Therefore, the estimated longitudinal velocity \hat{u}_{w_i} of wheel w_i is quite accurate. In addition, the orientation of the wheel is known from the steering encoder measurement δ_{w_i} . Thus we know both the magnitude as well as the direction of the longitudinal wheel velocity u_{w_i} .

In contrast, information about the lateral wheel velocity v_{w_i} is poor. In subsection 6.3.3 that deals with the generation of the actuator signals, we will see that the setpoints $\alpha_{w_i}^{\text{set}}$ for the wheels' slip angles are used as an intermediate step to compute the setpoints $\delta_{w_i}^{\text{set}}$ for the steering systems. In equation (6.14) of that subsection we will also see that $\delta_{w_i}^{\text{set}}$ is related to $\alpha_{w_i}^{\text{set}}$ by

$$\delta_{w_i}^{\text{set}} = \hat{\delta}_{w_i} - \alpha_{w_i}^{\text{set}} \text{sign}(\hat{u}_{w_i}), \quad (5.23)$$

where $\hat{\delta}_{w_i}$ is the steering angle of wheel w_i as measured by the steering encoder. **We obtain an estimate for the lateral wheel velocity v_{w_i} by assuming that the true wheel slip angle α_{w_i} equal to its setpoint $\alpha_{w_i}^{\text{set}}$.** From the definition (3.61) of the slip angle α_{w_i} it follows that our estimate for the lateral wheel velocity is given by

$$\hat{v}_{w_i} = \alpha_{w_i}^{\text{set}} |\hat{u}_{w_i}| \quad (5.24)$$

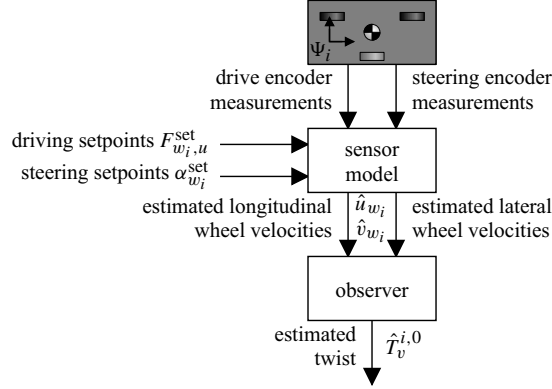


Figure 5.1: Velocity observer for a single AGV.

Let us stack the estimates \hat{u}_{w_i} and \hat{v}_{w_i} for all the wheels in a new vector z . Thus for the OLS vehicles we have

$$z = \begin{pmatrix} \hat{u}_{w_1} \\ \hat{u}_{w_2} \\ \hat{v}_{w_1} \\ \hat{v}_{w_2} \end{pmatrix} \quad (5.25)$$

We consider z , which consists of the estimates \hat{u}_{w_i} for the longitudinal wheel velocities and the estimates \hat{v}_{w_i} for the lateral wheel velocities, to be our measurements. They are directly related to the twist $T_v^{v,0}$ of the vehicle with respect to the floor. Furthermore, they are corrupted by some (additive) measurement noise. The measurement noise for the four measurements is stacked in a vector ξ . From equations (3.70)-(3.72) it follows that

$$z = B_v T_v^{v,0} + \xi. \quad (5.26)$$

This expression can be generalized to the twist of the vehicle with respect to the floor that is expressed in an arbitrary coordinate system Ψ_i . The relation between the measurements z , the twist of the vehicle with respect to the floor $T_v^{i,0}$ expressed in coordinate system Ψ_i , and the measurement noise ξ , is given by

$$z = B_i T_v^{i,0} + \xi \quad (5.27)$$

Matrix B depends on the steering angles δ_{w_i} of the wheels. **The measurements of the steering encoders are used to reconstruct the matrix B_i that describes the relation between the (pseudo-)measurements z and the AGV's twist $T_v^{i,0}$.** Since

$$z = B_i T_v^{i,0} + \xi = B_i \overbrace{Ad_{H_j}^{T_v^{i,0}}}^{T_v^{i,0}} T_v^{j,0} + \xi = \overbrace{B_i Ad_{H_j}^{T_v^{i,0}}}^{B_j} T_v^{j,0} + \xi = B_j T_v^{j,0} + \xi, \quad (5.28)$$

it follows that B_j is related to B_i by

$$\boxed{B_j = B_i Ad_{H_j^i}} \quad (5.29)$$

The elements of the 3×3 -matrix $Ad_{H_j^i}$ depend on H_j^i only, and can be found in equation (3.11). Since $Ad_{H_j^i}$ is nonsingular, the transformation (5.29) does not change the rank and size. The ‘‘tall’’ (i.e. more rows than columns) matrix B and its transformed versions $B_i = B Ad_{H_i^v}$ and B_j have full column rank in practical applications. *There are many possibilities to combine the measurements z to obtain an estimate $\hat{T}_v^{i,0}$ for the twist of the vehicle with respect to the floor. We will use an estimator that minimizes a weighted least-squares criterion that is quadratic in z .* In particular, our estimator will minimize the weighted least-squares criterion

$$\boxed{V(T_v^{i,0}) = \|z - B_i T_v^{i,0}\|_{\Sigma^{-1}}^2 = (z - B_i T_v^{i,0})^T \Sigma^{-1} (z - B_i T_v^{i,0})} \quad (5.30)$$

Here Σ^{-1} is a positive-definite weighting matrix, and $z - B_i T_v^{i,0}$ is the residual. The estimator $\hat{T}_v^{i,0}$ that minimizes the least-squares criterion (5.30) satisfies (see e.g. p. 44 of the book by Kailath [59])

$$\boxed{\hat{T}_v^{i,0} = (B_i^T \Sigma^{-1} B_i)^{-1} B_i^T \Sigma^{-1} z} \quad (5.31)$$

The symmetric matrix $B_i^T \Sigma^{-1} B_i$ is called the *information matrix*. By using relation (5.29) we see that the estimated twist but now expressed in Ψ_j can be written as

$$\begin{aligned} \hat{T}_v^{j,0} &= (B_j^T \Sigma^{-1} B_j)^{-1} B_j^T \Sigma^{-1} z \\ &= (Ad_{H_j^i}^T B_i^T \Sigma^{-1} B_i Ad_{H_j^i})^{-1} Ad_{H_j^i}^T B_i^T \Sigma^{-1} z \\ &= (Ad_{H_j^i}^T B_i^T \Sigma^{-1} B_i Ad_{H_j^i})^{-1} (Ad_{H_j^i}^T)^{-1} B_i^T \Sigma^{-1} z \\ &= (Ad_{H_j^i}^T Ad_{H_j^i}^T B_i^T \Sigma^{-1} B_i Ad_{H_j^i})^{-1} B_i^T \Sigma^{-1} z \\ &= (B_i^T \Sigma^{-1} B_i Ad_{H_j^i})^{-1} B_i^T \Sigma^{-1} z \\ &= Ad_{H_j^i}^{-1} (B_i^T \Sigma^{-1} B_i)^{-1} B_i^T \Sigma^{-1} z \\ &= Ad_{H_j^i} (B_i^T \Sigma^{-1} B_i)^{-1} B_i^T \Sigma^{-1} z \\ &= Ad_{H_j^i} \hat{T}_v^{i,0}. \end{aligned} \quad (5.32)$$

Hence, estimating the twist in Ψ_j and subsequently transforming this estimate to Ψ_i yields the same result as estimating the twist directly in Ψ_j . Thus the weighted-least-squares estimate for the twist is geometrically well-defined. From the second equality of this equation we also see that the information matrix transforms according to

$$\boxed{B_j^T \Sigma^{-1} B_j = Ad_{H_j^i}^T B_i^T \Sigma^{-1} B_i Ad_{H_j^i}} \quad (5.33)$$

Hence, the information matrix transforms in the same way as a mass matrix.

5.4.2 Stochastic interpretation

Now we will look at a stochastic interpretation of the least-squares estimator for the single AGV that was discussed in the previous subsection. Later on we will see that the theory that is derived in this section for a single AGV also applies to the case that multiple AGVs are all rigidly interconnected to the load. Furthermore, it allows us to reduce the amount of information sharing when the AGVs are semi-rigidly interconnected to the load by means of revolutes joints. Recall that the relation between the measurements z , the real twist $T_v^{i,0}$ and the additive disturbances satisfies (5.24), (5.27)

$$z = \begin{pmatrix} \hat{u}_{w_1} \\ \hat{u}_{w_2} \\ \hat{v}_{w_1} \\ \hat{v}_{w_2} \end{pmatrix} = \begin{pmatrix} \hat{u}_{w_1} \\ \hat{u}_{w_2} \\ \alpha_{w_1}^{\text{set}} |\hat{u}_{w_1}| \\ \alpha_{w_2}^{\text{set}} |\hat{u}_{w_2}| \end{pmatrix} = B_i T_v^{i,0} + \xi. \quad (5.34)$$

The covariance of the additive measurement error ξ is denoted by

$$\mathbf{E}[\xi \xi^T] = \Sigma, \quad (5.35)$$

with $\mathbf{E}[\cdot]$ the expected value operator and the square matrix Σ positive definite. Since the lateral velocity estimates $\hat{v}_{w_i} = \alpha_{w_i}^{\text{set}} |\hat{u}_{w_i}|$ are directly related to the longitudinal velocity estimates \hat{u}_{w_i} , one may expect that the matrix Σ is not diagonal. To investigate the structure of Σ , we consider the measurements of a single wheel w_i . From experience we know that in our applications most of the error in the longitudinal velocity estimate \hat{u}_{w_i} stems from inaccuracies in the parameter estimate for the effective wheel radius and from the unmodeled parts of longitudinal wheel slip. This was also reflected in equation (5.22). Thus for our applications, where the AGVs drive on smooth floors, the additive error $\xi_{u_{w_i}}$ in the longitudinal velocity estimate \hat{u}_{w_i} is approximately proportional to the longitudinal velocity. Hence,

$$\mathbf{E}[\xi_{u_{w_i}}^2] = u_{w_i}^2 \sigma_{u_{w_i}}^2, \quad (5.36)$$

where $\sigma_{u_{w_i}}$ is the standard deviation of the relative error. From Chapter 4 we know that the relative error in the parameter value for the effective wheel radius is in the order of magnitude of 1%, i.e. $\sigma_{u_{w_i}} \approx 0.01$. Uncertainties in the lateral velocity estimate are caused by uncertainties in the longitudinal velocity estimate \hat{u}_{w_i} and because the true slip angle α_{w_i} will deviate from its setpoint $\alpha_{w_i}^{\text{set}}$. We model the deviation from the setpoint by an additive noise term $\xi_{\alpha_{w_i}}$. Thus we find

$$\hat{v}_{w_i} = \alpha_{w_i}^{\text{set}} |\hat{u}_{w_i}| = (\alpha_{w_i} + \xi_{\alpha_{w_i}}) |u_{w_i} + \xi_{u_{w_i}}| = v_{w_i} + \xi_{v_{w_i}}, \quad (5.37)$$

with

$$\xi_{v_{w_i}} = \pm(u_{w_i} \xi_{\alpha_{w_i}} + \alpha_{w_i} \xi_{u_{w_i}} + \xi_{\alpha_{w_i}} \xi_{u_{w_i}}). \quad (5.38)$$

The ‘+’ of ‘ \pm ’ corresponds to the situation that $|u_{w_i} + \xi_{u_{w_i}}| > 0$, and the ‘−’ to $|u_{w_i} + \xi_{u_{w_i}}| < 0$. The variance of $\xi_{\alpha_{w_i}}$ is modelled as

$$\mathbf{E}[\xi_{\alpha_{w_i}}^2] = \sigma_{\alpha_{w_i}}^2. \quad (5.39)$$

The noise $\xi_{\alpha_{w_i}}$ represents the deviation from the known slip angle setpoint $\alpha_{w_i}^{\text{set}}$ from the unknown true slip angle α_{w_i} . The deviation is mainly caused by inaccuracies in the steering encoder offset, the non-ideal response of the wheel's steering system, and the modeling errors in the dynamics of the AGV. The inaccuracies for the OLS vehicles are in the order of one degree, i.e. $\sigma_{\alpha_{w_i}} \approx 0.02$ rad. The slip angle inaccuracy $\xi_{\alpha_{w_i}}$ and the longitudinal measurement error $\xi_{u_{w_i}}$ and their higher order moments are assumed to be uncorrelated. Hence, the variance of $\xi_{\alpha_{w_i}}$ is given by

$$\begin{aligned}
\mathbf{E}[\xi_{\alpha_{w_i}}^2] &= \mathbf{E}[(u_{w_i} \xi_{\alpha_{w_i}} + \alpha_{w_i} \xi_{u_{w_i}} + \xi_{\alpha_{w_i}} \xi_{u_{w_i}})^2] \\
&= \mathbf{E}[u_{w_i}^2 \xi_{\alpha_{w_i}}^2 + \alpha_{w_i}^2 \xi_{u_{w_i}}^2 + \xi_{\alpha_{w_i}}^2 \xi_{u_{w_i}}^2 \\
&\quad + 2u_{w_i} \alpha_{w_i} \xi_{\alpha_{w_i}} \xi_{u_{w_i}} + 2u_{w_i} \xi_{\alpha_{w_i}}^2 \xi_{u_{w_i}} + 2\alpha_{w_i} \xi_{\alpha_{w_i}} \xi_{u_{w_i}}^2] \\
&= \mathbf{E}[u_{w_i}^2 \xi_{\alpha_{w_i}}^2 + \alpha_{w_i}^2 \xi_{u_{w_i}}^2] = u_{w_i}^2 \mathbf{E}[\xi_{\alpha_{w_i}}^2] + \alpha_{w_i}^2 \mathbf{E}[\xi_{u_{w_i}}^2] = u_{w_i}^2 \sigma_{\alpha_{w_i}}^2 + \alpha_{w_i}^2 u_{w_i}^2 \sigma_{u_{w_i}}^2 \\
&= u_{w_i}^2 (\sigma_{\alpha_{w_i}}^2 + \alpha_{w_i}^2 \sigma_{u_{w_i}}^2). \tag{5.40}
\end{aligned}$$

Furthermore, the covariance of $\xi_{u_{w_i}} \xi_{\alpha_{w_i}}$ reads

$$\begin{aligned}
\mathbf{E}[\xi_{u_{w_i}} \xi_{\alpha_{w_i}}] &= \pm \mathbf{E}[\xi_{u_{w_i}} (u_{w_i} \xi_{\alpha_{w_i}} + \alpha_{w_i} \xi_{u_{w_i}} + \xi_{\alpha_{w_i}} \xi_{u_{w_i}})] \\
&= \pm \mathbf{E}[u_{w_i} \xi_{\alpha_{w_i}} \xi_{u_{w_i}} + \alpha_{w_i} \xi_{u_{w_i}}^2 + \xi_{\alpha_{w_i}} \xi_{u_{w_i}}^2] \\
&= \pm \mathbf{E}[\alpha_{w_i} \xi_{u_{w_i}}^2] \\
&= \pm u_{w_i}^2 \alpha_{w_i} \sigma_{u_{w_i}}^2. \tag{5.41}
\end{aligned}$$

Thus the covariance of the measurements errors $\xi_{w_i} = \text{stack}(\xi_{u_{w_i}}, \xi_{v_{w_i}})$ for wheel w_i is

$$\begin{aligned}
\mathbf{E}[\xi_{w_i} \xi_{w_i}^T] &= \mathbf{E} \left[\begin{pmatrix} \xi_{u_{w_i}}^2 & \xi_{v_{w_i}} \xi_{v_{w_i}} \\ \xi_{u_{w_i}} \xi_{v_{w_i}} & \xi_{v_{w_i}}^2 \end{pmatrix} \right] = u_{w_i}^2 \sigma_{u_{w_i}}^2 \begin{pmatrix} 1 & \pm \alpha_{w_i} \\ \pm \alpha_{w_i} & \alpha_{w_i}^2 + \sigma_{\alpha_{w_i}}^2 / \sigma_{u_{w_i}}^2 \end{pmatrix} \\
&\approx u_{w_i}^2 \sigma_{u_{w_i}}^2 \begin{pmatrix} 1 & 0 \\ 0 & \sigma_{\alpha_{w_i}}^2 / \sigma_{u_{w_i}}^2 \end{pmatrix} \tag{5.42}
\end{aligned}$$

As the wheel's slip angle α_{w_i} is in the order of 0.02 rad, the terms α_{w_i} and $\alpha_{w_i}^2$ can be neglected. The term $\sigma_{\alpha_{w_i}}^2 / \sigma_{u_{w_i}}^2$ is the ration between the variation $\sigma_{\alpha_{w_i}}^2$ of the additive slip angle noise and the variation $\sigma_{u_{w_i}}^2$ of the multiplicative longitudinal velocity noise. Both increase for motions that are subject to larger wheel slips. During acceleration and braking there is relatively much longitudinal wheel slip and little lateral wheel slip. Thus for those situations the ratio $\sigma_{\alpha_{w_i}}^2 / \sigma_{u_{w_i}}^2$ will be smaller as $\sigma_{u_{w_i}}^2$ is large due to the inaccurate wheel slip model (5.22). During cornering there is typically little longitudinal wheel slip and more lateral wheel slip. The slip angle estimate will deteriorate due to inaccuracies in the lateral wheel model, so the ratio $\sigma_{\alpha_{w_i}}^2 / \sigma_{u_{w_i}}^2$ becomes larger during cornering. For the OLS vehicles, the ratio $\sigma_{\alpha_{w_i}}^2 / \sigma_{u_{w_i}}^2$ varies roughly between 1 and 25. If we assume that the measurements of

one wheel are uncorrelated with the measurements from another wheel, then it follows from (5.42) that the covariance matrix Σ for two OLS AGVs equals

$$\Sigma = \begin{pmatrix} u_{w_1}^2 \sigma_{u_{w_1}}^2 & 0 & 0 & 0 \\ 0 & u_{w_2}^2 \sigma_{u_{w_2}}^2 & 0 & 0 \\ 0 & 0 & u_{w_1}^2 \sigma_{\alpha_{w_1}}^2 & 0 \\ 0 & 0 & 0 & u_{w_2}^2 \sigma_{\alpha_{w_2}}^2 \end{pmatrix}. \quad (5.43)$$

From equation (5.31) we know that the estimator that minimizes our cost criterion (5.30) satisfies

$$\hat{T}_v^{i,0} = (B_i^T \Sigma^{-1} B_i)^{-1} B_i^T \Sigma^{-1} z \quad (5.44)$$

If $\mathbf{E}[\xi] = 0$, then this estimator is interpreted as the minimum-mean-square-error unbiased linear estimator for $\hat{T}_v^{i,0}$, which is also called the *best linear unbiased estimator* (BLUE), see e.g. pp. 96–97 of the book by Rao [101]. Note that we did not require that the noise follows a Gaussian distribution.

Next, we investigate the stochastic properties of the twist estimation error. Let us denote the difference between the true twist $T_v^{i,0}$ and the estimate $\hat{T}_v^{i,0}$ by

$$\check{T}_v^{i,0} = (\hat{T}_v^{i,0} - T_v^{i,0}) \quad (5.45)$$

The mean and covariance of this estimation error $\check{T}_v^{i,0}$ are

$$\mathbf{E}[\check{T}_v^{i,0}] = (B_i^T \Sigma^{-1} B_i)^{-1} \Sigma^{-1} B_i^T \mathbf{E}[\xi] \quad (5.46)$$

$$\mathbf{E}[\check{T}_v^{i,0} \check{T}_v^{i,0T}] = \mathbf{E} \left[\begin{pmatrix} (\check{\omega}_v^{i,0})^2 & \check{\omega}_v^{i,0} \check{u}_v^{i,0} & \check{\omega}_v^{i,0} \check{v}_v^{i,0} \\ \check{\omega}_v^{i,0} \check{u}_v^{i,0} & (\check{u}_v^{i,0})^2 & \check{u}_v^{i,0} \check{v}_v^{i,0} \\ \check{\omega}_v^{i,0} \check{v}_v^{i,0} & \check{u}_v^{i,0} \check{v}_v^{i,0} & (\check{v}_v^{i,0})^2 \end{pmatrix} \right] = (B_i^T \Sigma^{-1} B_i)^{-1} \stackrel{\text{def}}{=} Q^i \quad (5.47)$$

Here $\check{\omega}_v^{i,0}$, $\check{u}_v^{i,0}$, and $\check{v}_v^{i,0}$ are respectively the estimation errors in the rotational, the longitudinal and the lateral velocity of the AGV with respect to the floor. The first component $\omega_v^{i,0}$ of the twist $T_v^{i,0}$ is invariant under coordinate transformations as we consider planar motions $T_v^{i,0} \in se(2)$ only. Therefore, we write

$$\check{\omega}_v^0 = \check{\omega}_v^{i,0} = \check{\omega}_v^{j,0}. \quad (5.48)$$

The other two coefficients $u_v^{i,0}$ and $v_v^{i,0}$ are not invariant. Therefore, the covariance matrix Q^i depend on the selected coordinate system Ψ_j . Since

$$\begin{aligned} Q^j &= (B_j^T \Sigma^{-1} B_j)^{-1} = (Ad_{H_j}^T B_i^T \Sigma^{-1} B_i Ad_{H_j})^{-1} = Ad_{H_j} (B_i^T \Sigma^{-1} B_i)^{-1} Ad_{H_j}^T \\ &= Ad_{H_j} Q^i Ad_{H_j}^T, \end{aligned} \quad (5.49)$$

we see that the covariance transforms as a 2-contravariant tensor. Stated differently, the covariance Q transforms in the same way as the inverse of the mass matrix.

5.4.3 Velocity estimate for an arbitrary point on the AGV

Now that we have an estimate $\hat{T}_v^{i,0}$ for the twist of the AGV with respect to the floor, we can use this to estimate the velocity of an arbitrary point P that is fixed to the vehicle. We use so-called homogenous coordinates P^i to express the position of a point P in a certain coordinate system Ψ_i . For the finite points that we consider, P^i is of the form

$$P^i = \begin{pmatrix} P_x^i \\ P_y^i \\ 1 \end{pmatrix}. \quad (5.50)$$

When both the point P and the coordinate system Ψ_i are fixed to the AGV, then the coordinates P^i are constant. It follows that

$$\dot{P}^i = 0. \quad (5.51)$$

If we express the coordinates of P in a coordinate system Ψ_0 that is fixed to the floor, we find that the derivatives of the coordinates satisfy

$$\dot{P}^0 = H_i^0 \tilde{T}_v^{i,0} P^i, \quad (5.52)$$

where we recall from equation (3.4) that the tilde operator is given by

$$T = \begin{pmatrix} \omega \\ u \\ v \end{pmatrix} \Leftrightarrow \tilde{T} = \begin{pmatrix} 0 & -\omega & u \\ \omega & 0 & v \\ 0 & 0 & 0 \end{pmatrix}. \quad (5.53)$$

The first two components of \dot{P}^0 are interpreted as the velocity of P with respect to the floor. The expected value of the estimate $\widehat{\dot{P}}^0$ for \dot{P}^0 is

$$\mathbf{E}[\widehat{\dot{P}}^0] = \mathbf{E}[H_i^0 \widehat{\tilde{T}}_v^{i,0} P^i] = \mathbf{E}[H_i^0 \widetilde{\widehat{T}}_v^{i,0} P^i] = H_i^0 \mathbf{E}[\widetilde{\widehat{T}}_v^{i,0}] P^i = H_i^0 \mathbf{E}[\widetilde{\widehat{T}}_v^{i,0}] P^i. \quad (5.54)$$

When the expected value of the sensor noise equals zero, i.e. $\mathbf{E}[\xi] = 0$, then $\mathbf{E}[\widehat{T}_v^{v,0}] = T_v^{v,0}$, and $\widehat{\dot{P}}^0$ will be an unbiased estimate for \dot{P}^0 . The estimation error $\check{\dot{P}}^0$ for \dot{P}^0 is related to the twist estimation error $\check{T}_v^{i,0}$ by

$$\check{\dot{P}}^0 = \widehat{\dot{P}}^0 - \dot{P}^0 = H_i^0 \widetilde{\check{T}}_v^{i,0} P^i - H_i^0 \widetilde{T}_v^{i,0} P^i = H_i^0 (\widetilde{\check{T}}_v^{i,0} - \widetilde{T}_v^{i,0}) P^i = H_i^0 \widetilde{\check{T}}_v^{i,0} P^i. \quad (5.55)$$

Using the expression above, we find that the expected mean-square-error equals

$$\begin{aligned}
\mathbf{E} \left[\check{P}^0 \check{P}^0 \right] &= \mathbf{E} \left[P^i \widetilde{T}_v^{i,0 \top} H_i^0 \widetilde{T}_v^{i,0} P^i \right] \\
&= \mathbf{E} \left[\begin{pmatrix} -p_y^i \check{\omega}_v^0 + \check{u}_v^{i,0} \\ p_x^i \check{\omega}_v^0 + \check{v}_v^{i,0} \\ 0 \end{pmatrix} \begin{pmatrix} R_i^0 \top & 0 \\ * & * & 1 \end{pmatrix} \begin{pmatrix} R_i^0 & * \\ 0 & 0 & 1 \end{pmatrix} \begin{pmatrix} -p_y^i \check{\omega}_v^0 + \check{u}_v^{i,0} \\ p_x^i \check{\omega}_v^0 + \check{v}_v^{i,0} \\ 0 \end{pmatrix} \right] \\
&= \mathbf{E} \left[\begin{pmatrix} -p_y^i \check{\omega}_v^0 + \check{u}_v^{i,0} \\ p_x^i \check{\omega}_v^0 + \check{v}_v^{i,0} \\ 0 \end{pmatrix} \begin{pmatrix} 1 & 0 & * \\ 0 & 1 & * \\ * & * & 1 \end{pmatrix} \begin{pmatrix} -p_y^i \check{\omega}_v^0 + \check{u}_v^{i,0} \\ p_x^i \check{\omega}_v^0 + \check{v}_v^{i,0} \\ 0 \end{pmatrix} \right] \\
&= \mathbf{E} \left[\begin{pmatrix} -p_y^i \check{\omega}_v^0 + \check{u}_v^{i,0} \\ p_x^i \check{\omega}_v^0 + \check{v}_v^{i,0} \\ 0 \end{pmatrix} \begin{pmatrix} -p_y^i \check{\omega}_v^0 + \check{u}_v^{i,0} \\ p_x^i \check{\omega}_v^0 + \check{v}_v^{i,0} \\ 0 \end{pmatrix} \right] \\
&= \mathbf{E} \left[P^i \widetilde{T}_v^{i,0 \top} \widetilde{T}_v^{i,0} P^i \right] \\
&= P^i \mathbf{E} \left[\widetilde{T}_v^{i,0 \top} \widetilde{T}_v^{i,0} \right] P^i, \tag{5.56}
\end{aligned}$$

where p_x^i is the x -component of P^i , p_y^i is the y -component of P^i , and

$$\mathbf{E} \left[\widetilde{T}_v^{i,0 \top} \widetilde{T}_v^{i,0} \right] = \mathbf{E} \left[\begin{pmatrix} (\check{\omega}_v^0)^2 & 0 & \check{\omega}_v^0 \check{v}_v^{i,0} \\ 0 & (\check{\omega}_v^0)^2 & -\check{\omega}_v^0 \check{u}_v^{i,0} \\ \check{\omega}_v^0 \check{v}_v^{i,0} & -\check{\omega}_v^0 \check{u}_v^{i,0} & (\check{v}_v^{i,0})^2 + (\check{u}_v^{i,0})^2 \end{pmatrix} \right]. \tag{5.57}$$

Because

$$\begin{aligned}
P^i \mathbf{E} \left[\widetilde{T}_v^{i,0 \top} \widetilde{T}_v^{i,0} \right] P^i &= P^j \mathbf{E} \left[H_j^i \widetilde{T}_v^{i,0 \top} H_i^j \widetilde{T}_v^{i,0} H_i^j \right] H_j^i P^j \\
&= P^j \mathbf{E} \left[H_j^i \widetilde{T}_v^{j,0 \top} \widetilde{T}_v^{j,0} H_i^j \right] H_j^i P^j \\
&= P^j \mathbf{E} \left[\widetilde{T}_v^{j,0 \top} \widetilde{T}_v^{j,0} \right] P^j, \tag{5.58}
\end{aligned}$$

the expected-mean-square error for the velocity of point P with respect to the world is independent of the coordinate system used to express the twist and P . If we expand expression

(5.56) above, we see that the mean-square error is related to P according to

$$\begin{aligned}
\mathbf{E} \left[\check{P}^0 \check{P}^0 \right] &= P^i \mathbf{T}^T \mathbf{E} \left[\widetilde{T}_v^{i,0} \widetilde{T}_v^{i,0} \right] P^i \\
&= (p_x^i)^2 \mathbf{E}[(\check{\omega}_v^0)^2] + 2p_x^i \mathbf{E}[\check{\omega}_v^0 \check{v}_v^{i,0}] + \mathbf{E}[(\check{v}_v^{i,0})^2] \\
&\quad + (p_y^i)^2 \mathbf{E}[(\check{\omega}_v^0)^2] - 2p_y^i \mathbf{E}[\check{\omega}_v^0 \check{u}_v^{i,0}] + \mathbf{E}[(\check{u}_v^{i,0})^2] \\
&= \mathbf{E}[(\check{\omega}_v^0)^2] \left\{ \left(p_x^i + \frac{\mathbf{E}[\check{\omega}_v^0 \check{v}_v^{i,0}]}{\mathbf{E}[\check{\omega}_v^0 \check{\omega}_v^0]} \right)^2 + \left(p_y^i - \frac{\mathbf{E}[\check{\omega}_v^0 \check{u}_v^{i,0}]}{\mathbf{E}[\check{\omega}_v^0 \check{\omega}_v^0]} \right)^2 \right\} \\
&\quad + \mathbf{E}[(\check{u}_v^{i,0})^2] + \mathbf{E}[(\check{v}_v^{i,0})^2] - \frac{(\mathbf{E}[\check{\omega}_v^0 \check{u}_v^{i,0}])^2 + (\mathbf{E}[\check{\omega}_v^0 \check{v}_v^{i,0}])^2}{\mathbf{E}[\check{\omega}_v^0 \check{\omega}_v^0]}. \quad (5.59)
\end{aligned}$$

The terms on the last expression depend on the coordinates (p_x^i, p_y^i) of the point P and on the covariance matrix Q^i . Since Q^i is fixed, this expression is quadratic in p_x^i and p_y^i . Inspection of (5.59) shows that the expected mean-square-error has a unique global minimum at the point P_m^i , where

$$P_m^i = \arg \min_{P^i} \left(P^i \mathbf{T}^T \mathbf{E} \left[\widetilde{T}_v^{i,0} \widetilde{T}_v^{i,0} \right] P^i \right) = \begin{pmatrix} -\frac{\mathbf{E}[\check{\omega}_v^0 \check{v}_v^{i,0}]}{\mathbf{E}[\check{\omega}_v^0 \check{\omega}_v^0]} \\ \frac{\mathbf{E}[\check{\omega}_v^0 \check{u}_v^{i,0}]}{\mathbf{E}[\check{\omega}_v^0 \check{\omega}_v^0]} \\ 1 \end{pmatrix} \quad (5.60)$$

The unique point P_m^i where the covariance of the velocity estimate error is minimal depends only on the covariance tensor Q^i . When we attach a new coordinate system Ψ_m with its origin to point P_m , then the covariance matrix Q^m takes a special form. If P_m is expressed in Ψ_m , we must have that $P_m^m = (0, 0, 1)^T$. Hence,

$$P_m^i = H_m^i P_m^m = H_m^i \begin{pmatrix} 0 \\ 0 \\ 1 \end{pmatrix} \Rightarrow H_m^i = \begin{pmatrix} R_m^i & p_m^i \\ 0 & 0 & 1 \end{pmatrix} = \begin{pmatrix} R_m^i & P_m^i \\ 0 & 0 & 1 \end{pmatrix}, \quad (5.61)$$

where R_m^i , i.e. the orientation of Ψ_m with respect to Ψ_i , is yet unspecified. By using $Ad_{H_m^i}$ to transform the covariance matrix from Ψ_i to Ψ_m , we obtain

$$Q^m = Ad_{H_m^i} Q^i Ad_{H_m^i}^T = \begin{pmatrix} \mathbf{E}[(\check{\omega}_v^0)^2] & 0 & 0 \\ 0 & S & 0 \\ 0 & 0 & 0 \end{pmatrix}, \quad (5.62)$$

where $S \in \mathbb{R}^{2 \times 2}$ is a symmetric, positive definite matrix. When in addition R_m^i is chosen appropriately, then Q^m reduces to

$$Q^m = Ad_{H_m^i} Q^i Ad_{H_m^i}^T = \begin{pmatrix} \mathbf{E}[(\check{\omega}_a^0)^2] & 0 & 0 \\ 0 & \mathbf{E}[(\check{u}_v^{m,0})^2] & 0 \\ 0 & 0 & \mathbf{E}[(\check{v}_v^{m,0})^2] \end{pmatrix} \quad (5.63)$$

In particular, exactly four distinct values of R_j^m will result in the form above. In subsection 5.5.2 we will exploit the special diagonal form of the covariance matrix Q^m as expressed in Ψ_m to reduce the amount of information that needs to be broadcasted by an individual AGV in a distributed observer setting. For completeness, we mention that in this coordinate system Ψ_m the expected mean-square-error (5.59) reduces to

$$\begin{aligned} \mathbf{E} \left[\check{P}^0 \check{P}^{0T} \right] &= P^m \mathbf{T} \mathbf{E} \left[\widetilde{T}_v^{m,0} \widetilde{T}_v^{m,0T} \right] P^m \\ &= \mathbf{E} \left[(\check{\omega}_v^0)^2 \right] \left\{ (p_x^m)^2 + (p_y^m)^2 \right\} + \mathbf{E} \left[(\check{u}_v^{m,0})^2 + (\check{v}_v^{m,0})^2 \right]. \end{aligned} \quad (5.64)$$

Finally, we find that the covariance of \check{P}^0 is given by

$$\begin{aligned} \mathbf{E} \left[\check{P}^0 \check{P}^{0T} \right] &= \mathbf{E} \left[H_i^0 \widetilde{T}_v^{i,0} P^i P^{iT} \widetilde{T}_v^{i,0T} H_i^{0T} \right] \\ &= H_i^0 \mathbf{E} \left[\begin{pmatrix} -p_y^i \check{\omega}_v^0 + \check{u}_v^{i,0} \\ p_x^i \check{\omega}_v^0 + \check{v}_v^{i,0} \\ 0 \end{pmatrix} \begin{pmatrix} -p_y^i \check{\omega}_v^0 + \check{u}_v^{i,0} \\ p_x^i \check{\omega}_v^0 + \check{v}_v^{i,0} \\ 0 \end{pmatrix}^T \right] H_i^{0T} \\ &= H_i^0 \mathbf{E} \left[\begin{pmatrix} (\check{u}_v^{i,0} - p_y^i \check{\omega}_v^0)^2 & (\check{u}_v^{i,0} - p_y^i \check{\omega}_v^0)(p_x^i \check{\omega}_v^0 + \check{v}_v^{i,0}) & 0 \\ (\check{u}_v^{i,0} - p_y^i \check{\omega}_v^0)(p_x^i \check{\omega}_v^0 + \check{v}_v^{i,0}) & (p_x^i \check{\omega}_v^0 + \check{v}_v^{i,0})^2 & 0 \\ 0 & 0 & 0 \end{pmatrix} \right] H_i^{0T} \\ &= H_i^0 \mathbf{E} \left[\begin{pmatrix} (p_y^i)^2 (\check{\omega}_v^0)^2 + (\check{u}_v^{i,0})^2 - 2p_y^i \check{\omega}_v^0 \check{u}_v^{i,0} & -p_x^i p_y^i (\check{\omega}_v^0)^2 + p_x^i \check{\omega}_v^0 \check{u}_v^{i,0} - p_y^i \check{\omega}_v^0 \check{v}_v^{i,0} + \check{u}_v^{i,0} \check{v}_v^{i,0} & 0 \\ \text{sym.} & (p_x^i)^2 (\check{\omega}_v^0)^2 + (\check{v}_v^{i,0})^2 + 2p_x^i \check{\omega}_v^0 \check{v}_v^{i,0} & 0 \\ 0 & 0 & 0 \end{pmatrix} \right] H_i^{0T}. \end{aligned} \quad (5.65)$$

If we use Ψ_m , this simplifies to

$$\begin{aligned} \mathbf{E} \left[\check{P}^0 \check{P}^{0T} \right] &= \mathbf{E} \left[H_m^0 \widetilde{T}_v^{m,0} P^m P^{mT} \widetilde{T}_v^{m,0T} H_m^{0T} \right] \\ &= H_m^0 \mathbf{E} \left[\begin{pmatrix} (p_y^m)^2 (\check{\omega}_v^0)^2 + (\check{u}_v^{m,0})^2 & -p_x^m p_y^m (\check{\omega}_v^0)^2 & 0 \\ -p_x^m p_y^m (\check{\omega}_v^0)^2 & (p_x^m)^2 (\check{\omega}_v^0)^2 + (\check{v}_v^{m,0})^2 & 0 \\ 0 & 0 & 0 \end{pmatrix} \right] H_m^{0T} \\ &= H_m^0 \begin{pmatrix} (p_y^m)^2 \mathbf{E}[(\check{\omega}_v^0)^2] + \mathbf{E}[(\check{u}_v^{m,0})^2] & -p_x^m p_y^m \mathbf{E}[(\check{\omega}_v^0)^2] & 0 \\ -p_x^m p_y^m \mathbf{E}[(\check{\omega}_v^0)^2] & (p_x^m)^2 \mathbf{E}[(\check{\omega}_v^0)^2] + \mathbf{E}[(\check{v}_v^{m,0})^2] & 0 \\ 0 & 0 & 0 \end{pmatrix} H_m^{0T}. \end{aligned} \quad (5.66)$$

Note that the components of the covariance matrix depend on the position of the point P .

5.4.4 Example

We illustrate the theory that was derived in the previous subsection with an example that deals with our OLS test vehicles. In our first preliminary experiments that are describe in [113], the two AGVs were rigidly interconnected using an aluminum frame as is depicted in Figure 5.2. As illustrated in the figure, we attached a coordinate frame Ψ_ℓ at the heart of the combination. Since everything is rigidly interconnected, the position of Ψ_ℓ is fixed with respect to both vehicles as well as to the load. For notational convenience, we define two additional coordinate systems Ψ_{v_1} and Ψ_{v_2} such that $\Psi_{v_1} = \Psi_{v_2} = \Psi_\ell$. This allows us to exchange the coordinate indices v_k for ℓ and vice versa, where $k \in \{1, 2\}$. The twist of the load with respect to the floor is denoted by $T_\ell^{\ell,0}$. Because all connections are completely rigid, it follows that $T_\ell^{\ell,0} = T_\ell^{\ell,0} = T_{v_k}^{v_k,0}$. We adopt the measurement model (5.27) for the measurements z_k of AGV k , i.e.

$$z_k = B_{v_k,k} T_{v_k}^{v_k,0} + \xi_k = B_{\ell,k} T_\ell^{\ell,0} + \xi_k, \quad (5.67)$$

where ξ_k is the additive measurement noise for the measurements z_k of AGV k . In equations (5.42) and (5.43) we saw that the covariance matrix Σ_k of ξ_k was diagonal. In this example, we assume that the longitudinal velocities of all the wheels are approximately the same, i.e.

$$u_{w_1,1} \approx u_{w_2,1} \approx u_{w_1,2} \approx u_{w_2,2}. \quad (5.68)$$

The second subscript refers to the AGV under consideration. This is the case when the steering pole is relatively far away. Because the AGVs were designed to be identical in hardware, we furthermore assume that the covariances of the longitudinal measurements are identical for all vehicles, and that the variances of the lateral measurements are identical:

$$\begin{aligned} \sigma_{u_{w_1,1}}^2 &\approx \sigma_{u_{w_2,1}}^2 \approx \sigma_{u_{w_1,2}}^2 \approx \sigma_{u_{w_2,2}}^2 \\ \sigma_{\alpha_{w_1,1}}^2 &\approx \sigma_{\alpha_{w_2,1}}^2 \approx \sigma_{\alpha_{w_1,2}}^2 \approx \sigma_{\alpha_{w_2,2}}^2 \end{aligned} \quad (5.69)$$

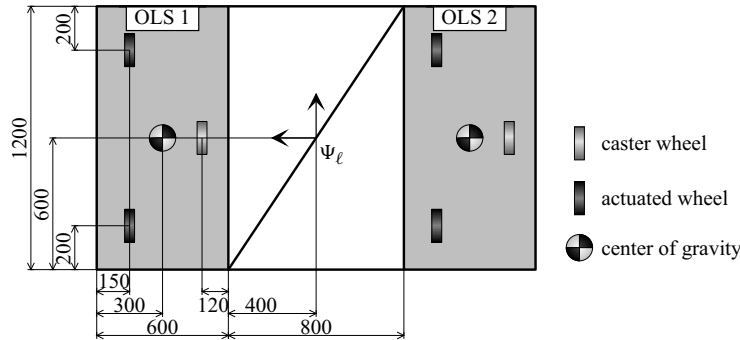


Figure 5.2: Schematic representation of the setup with two interconnected OLS AGVs used by Stouten and De Graaf [113] (dimensions in mm).

If we denote

$$\begin{aligned}\sigma^2 &= u_{w_i}^2 \sigma_{u_{w_i}}^2 \\ s &= \sigma_{\alpha_{w_i}}^2 / \sigma_{u_{w_i}}^2\end{aligned}\quad (5.70)$$

then we see from equations (5.42) and (5.43) that the covariance matrix Σ_k of ξ_k can be written as

$$\Sigma_k = \sigma^2 \begin{pmatrix} 1 & 0 & 0 & 0 \\ 0 & 1 & 0 & 0 \\ 0 & 0 & s & 0 \\ 0 & 0 & 0 & s \end{pmatrix}. \quad (5.71)$$

We indicate that the ratio s varied approximately between 1 and 25 for our OLS vehicles. We can derive an estimate for $T_\ell^{\ell,0}$ by using the measurements z_k of AGV k only, which yields (5.31)

$$\hat{T}_{\ell|z_k}^{\ell,0} = \hat{T}_{v_k|z_k}^{v_k,0} = (B_{\ell,k}^T \Sigma_k^{-1} B_{\ell,k})^{-1} B_{\ell,k}^T \Sigma_k^{-1} z_k, \quad (5.72)$$

The subscripts k indicate that we refer to AGV k . From equation (5.47) it follows that the covariance matrix Q_k^ℓ of the corresponding estimation error $\hat{T}_{\ell|z_k}^{\ell,0} - T_\ell^{\ell,0}$ reads

$$Q_k^\ell = (B_{\ell,k}^T \Sigma_k^{-1} B_{\ell,k})^{-1}. \quad (5.73)$$

Since the AGVs and the load are completely rigidly interconnected in this example, we may also consider the entire interconnected setup as one single vehicle. Then an estimate for $T_\ell^{\ell,0}$ can be obtained by considering all the measurements $z = \text{stack}(z_1, z_2)$ of the two vehicles together. This leads to

$$\hat{T}_{\ell|z}^{\ell,0} = (B_\ell^T \Sigma^{-1} B_\ell)^{-1} B_\ell^T \Sigma^{-1} z \quad (5.74)$$

$$Q^\ell = (B_\ell^T \Sigma^{-1} B_\ell)^{-1}, \quad (5.75)$$

where

$$\Sigma = \begin{pmatrix} \Sigma_1 & 0 \\ 0 & \Sigma_2 \end{pmatrix}, \quad B_\ell = \begin{pmatrix} B_{\ell,2} \\ B_{\ell,1} \end{pmatrix}, \quad z = \begin{pmatrix} z_1 \\ z_2 \end{pmatrix}. \quad (5.76)$$

Next, we will discuss two examples where we investigate the covariances of the estimation errors for various points on the vehicle. In the first example, the ratio $\sigma_{\alpha_{w_i}}^2 / \sigma_{u_{w_i}}^2$ is equal to 1, and in the second example it is equal to 25.

Example 1: ratio $\sigma_{\alpha_{w_i}}^2 / \sigma_{u_{w_i}}^2 = 1$

When the ratio $s = \sigma_{\alpha_{w_i}}^2 / \sigma_{u_{w_i}}^2 = 1$, then we see from equations (5.71) and (5.76) that the covariance matrices reduce to

$$\Sigma_1 = \Sigma_2 = \sigma^2 I, \quad \Sigma = \sigma^2. \quad (5.77)$$

From equation (3.70) of subsection 3.5.3 we know that the 4×3 -matrix $B_{v_k,k}$ for a single OLS vehicle satisfies

$$B_{v_k,k} = \begin{pmatrix} x_{w_1,k}^{v_k} s\delta_{w_1,k} - y_{w_1,k}^{v_k} c\delta_{w_1,k} & c\delta_{w_1,k} & s\delta_{w_1,k} \\ x_{w_2,k}^{v_k} s\delta_{w_2,k} - y_{w_2,k}^{v_k} c\delta_{w_2,k} & c\delta_{w_2,k} & s\delta_{w_2,k} \\ x_{w_1,k}^{v_k} c\delta_{w_1,k} + y_{w_1,k}^{v_k} s\delta_{w_1,k} & -s\delta_{w_1,k} & c\delta_{w_1,k} \\ x_{w_2,k}^{v_k} c\delta_{w_2,k} + y_{w_2,k}^{v_k} s\delta_{w_2,k} & -s\delta_{w_2,k} & c\delta_{w_2,k} \end{pmatrix}, \quad (5.78)$$

where $(x_{w_i,k}^{v_k}, y_{w_i,k}^{v_k})$ are the coordinates of the center of wheel w_i of OLS vehicle k expressed in coordinate system Ψ_{v_k} , and $\delta_{w_i,k}$ is the steering angle of that wheel. Since only the two active wheels of the OLS vehicles are equipped with sensors, we have $i \in \{1, 2\}$. Although $B_{v_k,k}$ depends on the steering angles of the wheels, it turns out that the corresponding information matrix $B_{v_k,k}^T \Sigma_k^{-1} B_{v_k,k}$ does not for the case that $\Sigma_k = \sigma^2 I$. If we write it out, then we obtain

$$B_{v_k,k}^T \Sigma_k^{-1} B_{v_k,k} = \frac{1}{\sigma^2} B_{v_k,k}^T B_{v_k,k} = \frac{1}{\sigma^2} \sum_{i=1}^2 \begin{pmatrix} (x_{w_i,k}^{v_k})^2 + (y_{w_i,k}^{v_k})^2 & -y_{w_i,k}^{v_k} & x_{w_i,k}^{v_k} \\ -y_{w_i,k}^{v_k} & 1 & 0 \\ x_{w_i,k}^{v_k} & 0 & 1 \end{pmatrix}. \quad (5.79)$$

Let us denote the front wheel of AGV k by $w_{1,k}$, and the rear wheel by $w_{2,k}$. From Figure 5.2 we see that the coordinates (m,m) of the front and rear wheel of the AGV on the left (OLS 1) are respectively (0.40, 0.85) and (-0.40, 0.85). The coordinates (m,m) of the front and rear wheel of the AGV on the right (OLS 2) are respectively (0.40, -0.55) and (-0.40, -0.55). Thus the corresponding covariance matrices Q_k^ℓ read

$$Q_1^\ell = (B_{v_1,1}^T \Sigma_1^{-1} B_{v_1,1})^{-1} = (B_{\ell,1}^T \Sigma_1^{-1} B_{\ell,1})^{-1} = \begin{pmatrix} 3.125 & 2.656 & 0.000 \\ 2.656 & 2.758 & 0.000 \\ 0.000 & 0.000 & 0.500 \end{pmatrix}, \quad (5.80)$$

$$Q_2^\ell = (B_{v_2,1}^T \Sigma_1^{-1} B_{v_2,1})^{-1} = (B_{\ell,2}^T \Sigma_2^{-1} B_{\ell,2})^{-1} = \begin{pmatrix} 3.125 & -1.719 & 0.000 \\ -1.719 & 1.445 & 0.000 \\ 0.000 & 0.000 & 0.500 \end{pmatrix}. \quad (5.81)$$

Recall that we are allowed to exchange the indices v_k and ℓ as $\Psi_{v_k} = \Psi_\ell$ in this example. The covariance matrix Q^ℓ that corresponds to the case where the measurements of both vehicles are used is given by

$$Q^\ell = (B_\ell^T \Sigma^{-1} B_\ell)^{-1} = \frac{1}{\sigma^2} (B_\ell^T B_\ell)^{-1} = \begin{pmatrix} 0.385 & 0.058 & 0.000 \\ 0.058 & 0.259 & 0.000 \\ 0.000 & 0.000 & 0.250 \end{pmatrix}. \quad (5.82)$$

Note that the variance of the estimate for the rotational velocity—the (1,1)-component of the Q -matrices above—is much smaller when the estimates are combined ($\mathbf{E}[(\hat{\omega}_{\ell|z}^0)^2] = 0.385$) than when they are not combined ($\mathbf{E}[(\hat{\omega}_{\ell|z_k}^0)^2] = 3.125$). The unique points where the covari-

ance of the error in the estimated point velocities is minimal, satisfy

$$P_{m|z_1}^\ell = \begin{pmatrix} -\frac{(Q_1^\ell)_{1,3}}{(Q_1^\ell)_{1,1}} \\ \frac{(Q_1^\ell)_{1,2}}{(Q_1^\ell)_{1,1}} \\ 1 \end{pmatrix} = \begin{pmatrix} -\frac{0.000}{3.125} \\ \frac{2.656}{3.125} \\ 1 \end{pmatrix} = \begin{pmatrix} 0.00 \\ 0.85 \\ 1 \end{pmatrix}, \quad (5.83)$$

$$P_{m|z_2}^\ell = \begin{pmatrix} -\frac{(Q_2^\ell)_{1,3}}{(Q_2^\ell)_{1,1}} \\ \frac{(Q_2^\ell)_{1,2}}{(Q_2^\ell)_{1,1}} \\ 1 \end{pmatrix} = \begin{pmatrix} -\frac{0.000}{3.125} \\ \frac{-1.719}{3.125} \\ 1 \end{pmatrix} = \begin{pmatrix} 0.00 \\ -0.55 \\ 1 \end{pmatrix}, \quad (5.84)$$

$$P_{m|z}^\ell = \begin{pmatrix} -\frac{(Q^\ell)_{1,3}}{(Q^\ell)_{1,1}} \\ \frac{(Q^\ell)_{1,2}}{(Q^\ell)_{1,1}} \\ 1 \end{pmatrix} = \begin{pmatrix} -\frac{0.000}{0.385} \\ \frac{0.058}{0.385} \\ 1 \end{pmatrix} = \begin{pmatrix} 0.00 \\ 0.15 \\ 1 \end{pmatrix}. \quad (5.85)$$

Note that σ^2 does not appear in these equations. The points $P_{m|z_1}^\ell$, $P_{m|z_2}^\ell$, and $P_{m|z}^\ell$ and the covariance of the estimation errors in the velocities of several points that are (virtually) fixed to the AGVs are displayed in Figure 5.3 for a certain value of σ^2 . We are mainly interested in the shape of the covariances.

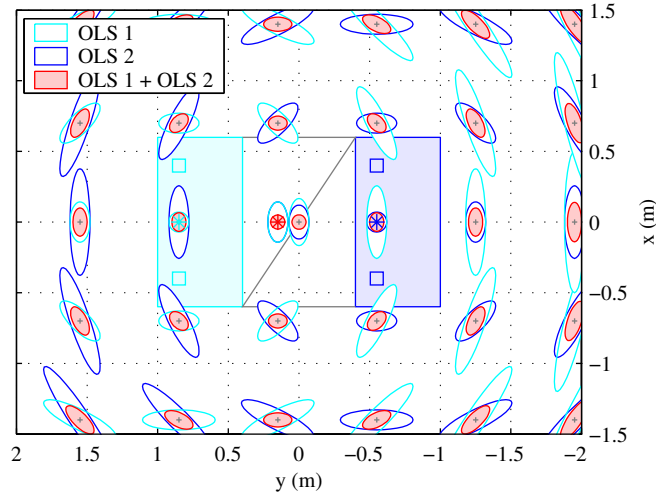


Figure 5.3: Covariances of the velocity estimation errors for various points on the vehicles. The unique points where the covariances are minimal are indicated by a '*'. The small squares '□' in the figure indicate the positions of the wheels.

As is expected from symmetry considerations, the points P_m with the minimum veloc-

ity estimate error covariance are in the center of the wheels that are used to compute the corresponding twist estimates. Hence, $P_{m|z_1}$ lies in between the two actuated wheels of the OLS 1, $P_{m|z_2}$ in between the two actuated wheels of the OLS 2, and $P_{m|z}$ in between the four actuated wheels of the interconnected system. The farther we move away from the points P_m , the larger the variance of the velocity error becomes due to the uncertainty in the rotational velocity ω_ℓ^0 . Because the variance of ω_ℓ^0 is much smaller when the measurements z of all four wheels are used to compute the twist estimate $\hat{T}_{\ell|z}^{\ell,0}$, the variance of the estimated point velocities increases much slower than for the estimate $\hat{T}_{\ell|z_k}^{\ell,0}$ that is based on the local measurements z_k of AGV k only. This example illustrates that it is beneficial to pursue a centralized observer design that uses all available measurements over local observers that use only local measurements.

Example 2: ratio $\sigma_{\alpha_{w_i}}^2 / \sigma_{u_{w_i}}^2 = 25$

In our second example, we consider the situation that the ratio $s = \sigma_{\alpha_{w_i}}^2 / \sigma_{u_{w_i}}^2$ is equal to 25. It turns out that for this case the information matrices $Q_k^\ell = (B_{\ell,1}^T \Sigma_k^{-1} B_{\ell,1})^{-1}$ and $Q^\ell = (B_\ell^T \Sigma^{-1} B_\ell)^{-1}$ are not constant anymore. Instead, they will depend on the steering angles $\delta_{w_i,k}$. As a result, the positions of the points $P_{m|z_k}$ and $P_{m|z}$ where the velocity estimate is optimal will also depend on the steering angles $\delta_{w_i,k}$.

Figure 5.4 displays the covariances of the velocity estimation errors for various points on the vehicles for four positions of the steering pole as estimated from the covariance matrix Q^ℓ , i.e. all the measurements z are used. The steering angles have been chosen such that the wheel planes are perfectly aligned with the motion of the interconnected system. We clearly see that the position of P_{m_z} as well as the shapes of the confidence intervals depends on the position of the steering pole in this example.

5.5 Least-squares observer for multiple AGVs transporting a common load

In this section we consider the situation that N possibly non-identical AGVs are semi-rigidly interconnected to the load. The example of subsection 5.4.4 showed us that an estimator that uses the measurements of all the AGVs performs better than a local estimator that uses measurements from only one AGV. In the example all the AGV-load interconnections were completely rigid. In this section we will relax this by considering interconnections that are lower pairs. This allows us to deal with revolute and prismatic joints as well. First we consider a centralized observer design, and later we will discuss how it can be implemented in a distributed fashion.

5.5.1 Centralized observer design

The goal for the central observer is to simultaneously estimate the twist of the load with respect to the floor and the twists of all the AGVs with respect to the floor. For convenience

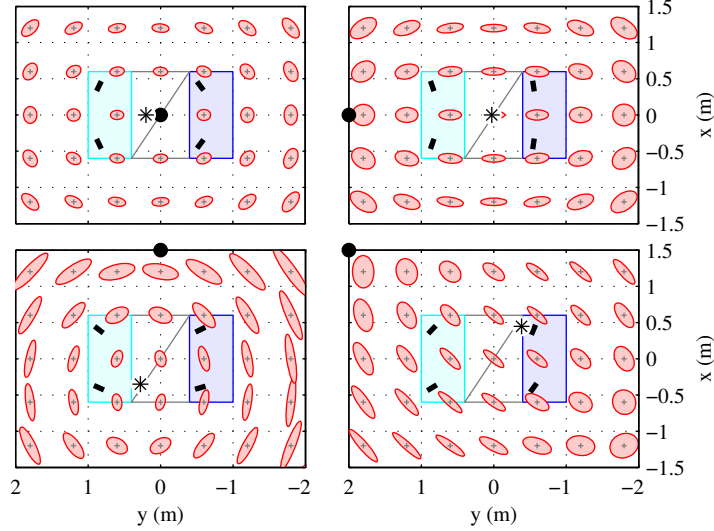


Figure 5.4: Covariances of the velocity estimation errors for various points on the vehicles for four positions of the steering pole ‘●’ when the measurements of both vehicles are used. The unique point $P_{m|z}$ where the covariance is minimal is indicated by a ‘*’.

we express all the estimates in a single coordinate system Ψ_ℓ that is fixed to the load. Thus the goal is to derive an estimator for

$$T = \begin{pmatrix} T^{\ell,0} \\ T_{v_1}^{\ell,0} \\ \vdots \\ T_{v_N}^{\ell,0} \end{pmatrix}. \quad (5.86)$$

The available measurements are the local measurements from all the N individual AGVs. Let us denote the measurements of AGV k by z_k . If we let $m_k = \text{length}(z_k)$, then we see that there are $M = \sum_{k=1}^N m_k$ measurements available.

Intuitively, each AGV can estimate its own motion from its local measurements z_k using the least-squares estimator (5.31) that was derived in subsection 5.4.1. Even when the load has no sensors to measure its relative velocity with respect to the floor, intuitively it should be possible to reconstruct the motion of the load by using the information about the kinematic constraints at the interconnections. In subsection 3.7.2 we made the assumption that all the interconnections behave as lower pairs. This means that the twist $T_{v_k}^{\ell,\ell}$ between AGV k and the load can be described as (3.101)

$$T_{v_k}^{\ell,\ell} = S_{\ell,k} \eta_k, \quad (5.87)$$

where $S_{\ell,k}$ is constant and has full column rank. Furthermore, $\eta_k \in \mathbb{R}^{\text{rank}(S_{i,k})}$ are new velocity coordinates. For a revolute joint $\eta_k \in \mathbb{R}$ represents the rotational velocity of the joint, and

for a prismatic joint it represents the sliding velocity of the joint. **We assume that the relative position $H_{v_k}^\ell$ of each AGV k with respect to the load is known, e.g. because it is measured by a sensor at the interconnection or because the interconnection is completely rigid. Furthermore, we assume that direct measurements about the relative motion of the AGVs with respect to the load are *not* available.**

In the remainder of this subsection we will focus on the situation that there are only two AGVs ($N = 2$) to ease notation. It is straightforward to generalize the results to an arbitrary number of AGVs. First, we stack all the measurements in a single vector z_k , so we have $z = \text{stack}(z_1, z_2)$. Extending our single AGV measurement model (5.27) to two AGVs yields

$$z = \begin{pmatrix} z_1 \\ z_2 \end{pmatrix} = \underbrace{\begin{pmatrix} 0 & B_{\ell,1} & 0 \\ 0 & 0 & B_{\ell,2} \end{pmatrix}}_H \underbrace{\begin{pmatrix} T_{v_1}^{\ell,0} \\ T_{v_2}^{\ell,0} \end{pmatrix}}_T + \underbrace{\begin{pmatrix} \xi_1 \\ \xi_2 \end{pmatrix}}_\xi = HT + \xi \quad (5.88)$$

This equation has the same form as the measurement model for a single AGV (5.27), in the sense that the measurements z consist of a term that is linearly related to the to-be-estimated variables T plus an additive noise term ξ . **The major difference with the single AGV case is that H in the equation above does not have full column rank, hence $H^T H$ is singular.** Therefore, it is not possible to determine a *unique* least-squares estimator \hat{T} that minimizes

$$V(T) = \|(z - HT)\|_{\Sigma^{-1}}^2 = (z - HT)^T \Sigma^{-1} (z - HT), \quad (5.89)$$

where Σ^{-1} is a positive definite matrix. To overcome this situation we use equation (5.87) to express the to-be-estimated variables T in terms of the twist $T_\ell^{\ell,0}$ of the load with respect to the floor and the velocity coordinates η_k . Since (3.110)

$$T_{v_k}^{\ell,0} = T_\ell^{\ell,0} + T_{v_k}^{\ell,\ell} = T_\ell^{\ell,0} + S_{\ell,k} \eta_k, \quad (5.90)$$

we can write T as (3.111)

$$T = \begin{pmatrix} T_\ell^{\ell,0} \\ T_{v_1}^{\ell,0} \\ T_{v_2}^{\ell,0} \end{pmatrix} = \underbrace{\begin{pmatrix} I & 0 & 0 \\ I & S_{\ell,1} & 0 \\ I & 0 & S_{\ell,2} \end{pmatrix}}_S \underbrace{\begin{pmatrix} T_\ell^{\ell,0} \\ \eta_1 \\ \eta_2 \end{pmatrix}}_\eta = S\eta \quad (5.91)$$

Subsequently, we focus on the estimation of the reduced set of coordinates η . For completely rigid interconnections η_1 and η_2 are equal to \emptyset , and we are just left with $T_\ell^{\ell,0}$. When the load is attached to the vehicles by means of revolute joints, then the dimension of η is equal to $3 + 1 + 1 = 5$. By substituting the previous equality (5.91) in our minimization criterion (5.89) we arrive at

$$V(\eta) = \|(z - HS\eta)\|_{\Sigma^{-1}}^2 = (z - HS\eta)^T \Sigma^{-1} (z - HS\eta). \quad (5.92)$$

To find a unique estimator $\hat{\eta}$ that minimizes (5.92) we need to have that HS has full column rank. The requirement of full column rank for HS is equivalent to the requirement that

$S^T H^T H S$ is nonsingular. Since $S^T H^T H S$ is symmetric, the non-singularity requirement implies that $S^T H^T H S$ should be positive definite:

$$\eta^T S^T H^T H S \eta > 0 \quad \forall \eta \neq 0. \quad (5.93)$$

Thus a necessary condition is that the kernel of S is identical to the zero element, i.e. S has full column rank. Otherwise there would exist a vector $\eta \neq 0$ such that $S\eta = 0$ and, consequently, $\eta^T S^T H^T H S \eta = 0$. Recall that all matrices $S_{\ell,k}$ have full column rank. Therefore, from the definition (5.91) of S it follows that S has full column rank. So indeed

$$\ker S = 0. \quad (5.94)$$

Furthermore, we know that H does not have full column rank. In other words, the kernel of H consists of more than the zero element. Since $B_{\ell,k}$ has full column rank for all k , it is readily seen from equation (5.88) that the kernel of H satisfies

$$\ker H = \ker \begin{pmatrix} 0 & B_{\ell,1} & 0 \\ 0 & 0 & B_{\ell,2} \end{pmatrix} = \text{Im} \begin{pmatrix} I \\ 0 \\ 0 \end{pmatrix}. \quad (5.95)$$

Condition (5.93) can only be fulfilled when $S\eta$ is not in the kernel of H for all $\eta \neq 0$. Since we already showed that $\ker S = 0$, condition (5.93) is equivalent to

$$\ker H \cap \text{Im} S = 0. \quad (5.96)$$

If we write this out using the expressions for the kernel of H and the image of S , then we get

$$S\eta = \begin{pmatrix} I & 0 & 0 \\ I & S_{\ell,1} & 0 \\ I & 0 & S_{\ell,2} \end{pmatrix} \begin{pmatrix} T_{\ell}^{\ell,0} \\ \eta_1 \\ \eta_2 \end{pmatrix} = \begin{pmatrix} T_{\ell}^{\ell,0} \\ T_{\ell}^{\ell,0} + S_{\ell,1}\eta_1 \\ T_{\ell}^{\ell,0} + S_{\ell,2}\eta_2 \end{pmatrix} = \begin{pmatrix} T_{\ell}^{\ell,0} \\ T_{v_1}^{\ell,0} \\ T_{v_2}^{\ell,0} \end{pmatrix} \neq \begin{pmatrix} * \\ 0 \\ 0 \end{pmatrix} \quad \forall \eta \neq 0. \quad (5.97)$$

This condition tells us that the AGVs should be interconnected to the load in such a way that the situation where the load is moving whilst the AGVs are standing still, i.e. $T_{\ell}^{\ell,0} \neq 0$ whilst $T_{v_1}^{\ell,0} = T_{v_2}^{\ell,0} = 0$, should never occur. Intuitively, this condition is fulfilled when there are sufficient kinematic constraints between the AGVs and the load. To show this mathematically, we investigate condition (5.97) in more detail. We start by noting that if $S\eta$ would be in the kernel of H for a certain $\eta \neq 0$, then certainly $T_{\ell}^{\ell,0}$ must be unequal to zero. But if $T_{\ell}^{\ell,0} \neq 0$, then the last two rows of (5.97) can only be both equal to zero when there exist η_1 and η_2 such that

$$-T_{\ell}^{\ell,0} = S_{\ell,1}\eta_1 = S_{\ell,2}\eta_2 \quad (5.98)$$

for some $T_{\ell}^{\ell,0} \neq 0$. In other words, condition (5.97) can only be violated when $T_{\ell}^{\ell,0}$ is in the intersection of the images of $S_{\ell,1}$ and $S_{\ell,2}$. Conversely, for condition (5.97) to hold we must have that the intersections of $S_{\ell,1}$ and $S_{\ell,2}$ is equal to the zero element. If we generalize this to N AGVs, we obtain (since we already showed that $\ker S = 0$)

$$\ker H \cap \text{Im} S \Leftrightarrow \bigcap_{k=1}^N \text{Im} S_{\ell,k} = 0. \quad (5.99)$$

We already saw in equation (3.107) of subsection 3.7.2 that this indeed is the case, as this follows from the requirement that the AGVs should collectively be able to exert a netto wrench in any arbitrary direction on the load. Hence, HS has indeed full column rank. Moreover, we have that $S^T H^T HS$ is positive definite and nonsingular. Since the weighing matrix Σ was assumed to be positive definite, then also $S^T H^T \Sigma HS$ is positive definite. This allows us to derive a standard least-squares estimator $\hat{\eta}$ that minimizes our criterion $V(\eta)$ that was given by equation (5.92). Hence, we find

$$\hat{\eta} = (S^T H^T \Sigma^{-1} HS)^{-1} S^T H^T \Sigma^{-1} z \quad (5.100)$$

To obtain an estimator for our original to-be-estimated variables T , we simply pre-multiply our estimator $\hat{\eta}$ for the reduced set of coordinates by S . This yields

$$\hat{T} = S \hat{\eta} = S (S^T H^T \Sigma^{-1} HS)^{-1} S^T H^T \Sigma^{-1} z \quad (5.101)$$

5.5.2 Distributed implementation

In the previous sections we derived a centralized observer design to estimate T . To implement it in a distributed manner, we make an additional assumption on the structure of the weighting matrix Σ . **We assume that the weighting matrix Σ that is applied to all the measurements in the interconnected system is constant and has a block diagonal form, where each (symmetric) block Σ_k is positive definite and corresponds to the measurements of AGV k .** Since the number of available measurements for AGV k is equal to $m_k = \text{length}(z_k)$, it follows that under these assumptions Σ takes the form

$$\Sigma = \text{diag}(\Sigma_1, \dots, \Sigma_N), \quad \Sigma_k^T = \Sigma_k \in \mathbb{R}^{m_k \times m_k}, \quad \Sigma_k > 0. \quad (5.102)$$

From a stochastic point of view this structure is not always justifiable. The lateral velocity measurement errors of AGV 1 are for example certainly correlated with the lateral velocity measurement errors of AGV 2 when an unmodelled external force is acting in the lateral direction of the interconnected system. Such a force can for example be caused by the banking of the floor, by a wind gust that is blowing on a load that is transported outdoors, etc. The influence of such disturbances will result in off-block-diagonal terms. Depending on the application, one may choose to slightly deteriorate the observer's performance by disregarding the off-block-diagonal terms to allow a distributed observer implementation.

If we are to implement the central design of the previous subsection in a distributed way, then we have to communicate variables that do not change over time only once at the initialization phase. Inspection of the estimator \hat{T} (5.101) shows that some terms are fortunately constant, whereas others are not. Since we restricted ourselves to lower-pair interconnections, S is constant. The two terms are not (necessarily) constant are $H^T \Sigma^{-1} H$ and $H^T \Sigma^{-1} z$. When Σ is of the form (5.102), then writing out $H^T \Sigma^{-1} H$ for $N = 2$ results in

$$H^T \Sigma^{-1} H = \begin{pmatrix} 0 & 0 & 0 \\ 0 & B_{\ell,1}^T \Sigma_1^{-1} B_{\ell,1} & 0 \\ 0 & 0 & B_{\ell,2}^T \Sigma_2^{-1} B_{\ell,2} \end{pmatrix} \quad (5.103)$$

Because direct measurements on the load's motion $T_\ell^{\ell,0}$ are not available, the first three columns are zero. When we express the least-squares estimator (5.31) that we derived for a single AGV k that is not transporting a load in Ψ_ℓ we arrive at

$$\hat{T}_{v_k|z_k}^{\ell,0} = Ad_{H_{v_k}^\ell} \hat{T}_{v_k|z_k}^{v_k,0} = (B_{\ell,k}^T \Sigma_k^{-1} B_{\ell,k})^{-1} B_{\ell,k}^T \Sigma_k^{-1} z_k. \quad (5.104)$$

Here $\hat{T}_{v_k|z_k}^{v_k,0}$ is the estimate for the twist $T_{v_k}^{v_k,0}$ of AGV k with respect to the floor expressed in vehicle coordinates Ψ_{v_k} that is based on the local measurements z_k of AGV k only. It is assumed that the relative position $H_{v_k}^\ell$ of the load with respect to the AGV is known, such that it is possible to express the local estimate in terms of the load coordinate system Ψ_ℓ . The latter estimate is denoted by $\hat{T}_{v_k|z_k}^{\ell,0}$. Pre-multiplying the previous equation by $B_{\ell,k}^T \Sigma_k^{-1} B_{\ell,k}$ leads to

$$B_{\ell,k}^T \Sigma_k^{-1} z_k = B_{\ell,k}^T \Sigma_k^{-1} B_{\ell,k} \hat{T}_{v_k|z_k}^{\ell,0}. \quad (5.105)$$

This expression can be exploited to write out the second non-constant term $H^T \Sigma^{-1} z$ of our centralized observer. For $N = 2$ this results in

$$\begin{aligned} H^T \Sigma^{-1} z &= \begin{pmatrix} 0 & 0 \\ B_{\ell,1}^T \Sigma_1^{-1} & 0 \\ 0 & B_{\ell,2}^T \Sigma_2^{-1} \end{pmatrix} \begin{pmatrix} z_1 \\ z_2 \end{pmatrix} = \begin{pmatrix} 0 \\ B_{\ell,1}^T \Sigma_1^{-1} z_1 \\ B_{\ell,2}^T \Sigma_2^{-1} z_2 \end{pmatrix} = \begin{pmatrix} 0 \\ B_{\ell,1}^T \Sigma_1^{-1} B_{\ell,1} \hat{T}_{v_1|z_1}^{\ell,0} \\ B_{\ell,2}^T \Sigma_2^{-1} B_{\ell,2} \hat{T}_{v_2|z_2}^{\ell,0} \end{pmatrix} \\ &= H^T \Sigma^{-1} H \begin{pmatrix} 0 \\ \hat{T}_{v_1|z_1}^{\ell,0} \\ \hat{T}_{v_2|z_2}^{\ell,0} \end{pmatrix}. \end{aligned} \quad (5.106)$$

Hence, our centralized observer (5.101) can equivalently be written as

$$\hat{T} = S \hat{\eta} = S \left(S^T H^T \Sigma^{-1} H S \right)^{-1} S^T H^T \Sigma^{-1} H \begin{pmatrix} 0 \\ \hat{T}_{v_1|z_1}^{\ell,0} \\ \hat{T}_{v_2|z_2}^{\ell,0} \end{pmatrix} \quad (5.107)$$

The matrix S , which was defined in (5.91), is constant. The last term, which contains the twists estimates $\hat{T}_{v_k|z_k}^{\ell,0}$ that are based on the local measurements z_k only, is certainly not constant. The twist estimate $\hat{T}_{v_k|z_k}^{\ell,0}$ of AGV k with respect to the floor can be computed locally by AGV k , see equations (5.31) and (5.104). **To decentralize the last term in the observer algorithm (5.107), AGV k should locally compute the twist estimate $\hat{T}_{v_k|z_k}^{\ell,0}$ that corresponds to its own measurements z_k , and subsequently broadcast the result to the other AGVs.** Since a twist has three components, this requires the broadcasting of three double precision numbers per AGV.

The remaining term $H^T \Sigma^{-1} H$ appears twice in our alternative formulation (5.107) above. Inspection of (5.103) shows that all the elements of $H^T \Sigma^{-1} H$ are matrices of the form $B_{\ell,k}^T \Sigma_k^{-1} B_{\ell,k}$. **Since the information matrix $B_{\ell,k}^T \Sigma_k^{-1} B_{\ell,k}$ depends on information that is**

related to AGV k only, it can be computed locally by AGV k , and subsequently broadcasted to the other vehicles. In particular, from equation (5.33) it is seen that the formula to compute $B_{\ell,k}^T \Sigma_k^{-1} B_{\ell,k}$ satisfies

$$B_{\ell,k}^T \Sigma_k^{-1} B_{\ell,k} = Ad_{H_\ell^{v_k}}^T (B_{v_k,k}^T \Sigma_k^{-1} B_{v_k,k}) Ad_{H_\ell^{v_k}}. \quad (5.108)$$

Because the information matrices $B_{\ell,k}^T \Sigma_k^{-1} B_{\ell,k}$ for each AGV are symmetric and consist of $3 \times 3 = 9$ elements, sharing an information with other vehicles requires broadcasting six double precision numbers. The interesting question is whether there exist AGV-load interconnections such that $B_{\ell,k}^T \Sigma_k^{-1} B_{\ell,k}$ remains constant during operation. The answer is yes. **In the special cases where the information matrix $B_{\ell,k}^T \Sigma_k^{-1} B_{\ell,k}$ remains constant during operation, it has to be broadcasted only once.** In the next subsection we will discuss two situations where $B_{\ell,k}^T \Sigma_k^{-1} B_{\ell,k}$ is constant.

5.5.3 Examples where the amount of information sharing can be reduced

This subsection presents two examples where the amount of information sharing between the AGVs can be reduced as $B_{\ell,k}^T \Sigma_k^{-1} B_{\ell,k}$ remains constant during operation. Before we discuss the two examples, it is convenient to express $B_{\ell,k}^T \Sigma_k^{-1} B_{\ell,k}$ in terms of the vehicle coordinate system Ψ_{v_k} . We therefore repeat equation (5.108)

$$B_{\ell,k}^T \Sigma_k^{-1} B_{\ell,k} = Ad_{H_\ell^{v_k}}^T (B_{v_k,k}^T \Sigma_k^{-1} B_{v_k,k}) Ad_{H_\ell^{v_k}}, \quad (5.109)$$

where $Ad_{H_\ell^{v_k}}$ depends on the relative position $H_\ell^{v_k}$ of the load with respect to the vehicle.

Example 1: Rigid AGV-load interconnection with $\Sigma_k = I$

In our first example, the load is boldly fixed to the AGVs. This implies that $Ad_{H_\ell^{v_k}}$ is constant. From equation (5.79) we know that $B_{v_k,k}^T \Sigma_k^{-1} B_{v_k,k}$ takes a special form for our OLS vehicles when $\Sigma_k = I$:

$$B_{v_k,k}^T \Sigma_k^{-1} B_{v_k,k} = B_{v_k,k}^T B_{v_k,k} = \sum_{i=1}^2 \begin{pmatrix} (x_{w_i,k}^{v_k})^2 + (y_{w_i,k}^{v_k})^2 & -y_{w_i,k}^{v_k} & x_{w_i,k}^{v_k} \\ -y_{w_i,k}^{v_k} & 1 & 0 \\ x_{w_i,k}^{v_k} & 0 & 1 \end{pmatrix}. \quad (5.110)$$

Because the coordinates $(x_{w_i,k}^{v_k}, y_{w_i,k}^{v_k})$ of the wheel centers of AGV k as expressed in Ψ_{v_k} are constant, so is $B_{v_k,k}^T B_{v_k,k}$. Because both $B_{v_k,k}^T \Sigma_k^{-1} B_{v_k,k}$ and $Ad_{H_\ell^{v_k}}$ are constant, it follows from (5.109) that the information matrix $B_{\ell,k}^T \Sigma_k^{-1} B_{\ell,k}$ is indeed constant for this case.

Case 2: Revolute joint with $\Sigma_k = I$

Our second example deals with the situation that the interconnection between AGV k and the load is not completely rigid. We consider an OLS vehicle with $\Sigma_k = I$ again, hence the local

information matrix $B_{v_k,k}^T \Sigma_k^{-1} B_{v_k,k} = B_{v_k,k}^T B_{v_k,k}$ is constant. Since $Ad_{H_\ell^{v_k}}$ is not constant anymore as the load can move with respect to the vehicle, expression (5.109) is generally not constant. An interconnection puts restrictions on the allowed relative positions $H_\ell^{v_k}$. Consequently, an interconnection also restricts the allowed matrices $Ad_{H_\ell^{v_k}}$. Thus we will investigate which kind of interconnections limit $Ad_{H_\ell^{v_k}}$ in such a way that the transformed information matrix $Ad_{H_\ell^{v_k}}^T B_{v_k,k}^T \Sigma_k^{-1} B_{v_k,k} Ad_{H_\ell^{v_k}}$ is constant for all relative positions $H_\ell^{v_k}$ that are allowed by the interconnection. Note that when a certain information matrix is constant, then so is its inverse. The inverse of $B_{\ell,k}^T \Sigma_k^{-1} B_{\ell,k}$ equals (5.49)

$$Q_k^\ell = (B_{\ell,k}^T \Sigma_k^{-1} B_{\ell,k})^{-1} = Ad_{H_{v_k}^\ell} (B_{v_k,k}^T \Sigma_k^{-1} B_{v_k,k})^{-1} Ad_{H_{v_k}^\ell}^T = Ad_{H_{v_k}^\ell} Q_k^{v_k} Ad_{H_{v_k}^\ell}^T, \quad (5.111)$$

where Q_k^ℓ and $Q_k^{v_k}$ represent the covariance tensor of AGV k as expressed in Ψ_ℓ and Ψ_{v_k} , respectively. Since $B_{v_k,k}^T \Sigma_k^{-1} B_{v_k,k}$ is constant, so is its inverse $Q_k^{v_k}$. We know from equation (5.63) that there exists a unique point P_{m_k} for AGV k with a corresponding coordinate system Ψ_{m_k} where the matrix representation of the covariance tensor Q_k takes a diagonal form. Since $Q_k^{v_k}$ is constant and since the position of P_{m_k} depends on Q_k only, the position of P_{m_k} is constant with respect to the vehicle. We already saw in subsection 5.4.3 that for a single OLS vehicle, the point P_{m_k} lies exactly in the middle of its two actuated wheels. If we fix Ψ_{m_k} with its origin to P_{m_k} and orient its axes appropriately, then the covariance tensor Q_k expressed in Ψ_{m_k} becomes

$$Q_k^{m_k} = \begin{pmatrix} (Q_k^{m_k})_{1,1} & 0 & 0 \\ 0 & (Q_k^{m_k})_{2,2} & 0 \\ 0 & 0 & (Q_k^{m_k})_{3,3} \end{pmatrix} = \begin{pmatrix} a & 0 & 0 \\ 0 & b & 0 \\ 0 & 0 & c \end{pmatrix}. \quad (5.112)$$

The relation between $Q_k^{m_k}$ and Q_k^ℓ (5.111) is given by

$$Q_k^\ell = Ad_{H_{v_k}^\ell} Q_k^{v_k} Ad_{H_{v_k}^\ell}^T = Ad_{H_{v_k}^\ell} Ad_{H_{m_k}^{v_k}} Q_k^{m_k} Ad_{H_{m_k}^{v_k}}^T Ad_{H_{v_k}^\ell}^T = Ad_{H_{m_k}^\ell} Q_k^{m_k} Ad_{H_{m_k}^\ell}^T, \quad (5.113)$$

where we used that $H_{m_k}^{v_k}$ is constant since Ψ_{m_k} was fixed to the vehicle. To find out when this expression is constant, we parameterize $H_{m_k}^\ell$ and $Ad_{H_{m_k}^\ell}$ as

$$H_{m_k}^\ell = \begin{pmatrix} c\varphi & -s\varphi & x \\ s\varphi & c\varphi & y \\ 0 & 0 & 1 \end{pmatrix} \Rightarrow Ad_{H_{m_k}^\ell} = \begin{pmatrix} 1 & 0 & 0 \\ y & c\varphi & -s\varphi \\ -x & s\varphi & c\varphi \end{pmatrix}, \quad (5.114)$$

where (x, y) are the coordinates of the origin of Ψ_{m_k} expressed in Ψ_ℓ , and φ is the angle between Ψ_{m_k} and Ψ_ℓ . Substitution in equation (5.113) leads to

$$Q_k^\ell = \begin{pmatrix} a & ay & -ax \\ ay & ay^2 + c + (b-c)\cos^2(\varphi) & -axy + \frac{1}{2}(b-c)\sin(2\varphi) \\ -ax & -axy + \frac{1}{2}(b-c)\sin(2\varphi) & ax^2 + b - (b-c)\cos^2(\varphi) \end{pmatrix}. \quad (5.115)$$

Since $Q_k^{m_k}$ is positive definite, a, b and c are all larger than zero. It follows that for Q_k^ℓ to be constant, we certainly must have that x and y are constant. This means that the origin of Ψ_{m_k}

is fixed with respect to the origin of Ψ_ℓ . Thus the only degree of freedom that is left for the interconnection is the rotation φ . This corresponds to a revolute joint which axis of rotation goes exactly through the special point P_{m_k} . If we leave φ free, then from the equation above we see that for Q_k^ℓ to be constant, we must in addition have that $b = c$. In other words, the last two diagonal components of $Q_k^{m_k}$ should be equal. It turns out that this is indeed the case for our OLS vehicles. This can for example be seen from equation (5.110). Since P_{m_k} lies in between the two wheels, we have $x_{w_1,k}^{m_k} = -x_{w_2,k}^{m_k} = 0.40$ and $y_{w_1,k}^{m_k} = y_{w_2,k}^{m_k} = 0$. Substituting these values in (5.110) results in

$$Q_k^{m_k} = \left(B_{m_k,k}^T B_{m_k,k} \right)^{-1} = \begin{pmatrix} 2 \times (0.40)^2 & 0 & 0 \\ 0 & 2 & 0 \\ 0 & 0 & 2 \end{pmatrix}^{-1} = \begin{pmatrix} 3.125 & 0 & 0 \\ 0 & 0.5 & 0 \\ 0 & 0 & 0.5 \end{pmatrix}. \quad (5.116)$$

The last two diagonal elements are indeed identical. **Thus when the load is interconnected to an OLS vehicle by means of a revolute joint that is attached exactly in the middle of the two actuated wheels and when in addition $\Sigma_k = I$, then the information matrix $B_{\ell,k}^T \Sigma^{-1} B_{\ell,k}$ remains constant during operation.** In that case, this vehicle only needs to communicate its local twist estimate $\hat{T}_{v_k|z_k}^{\ell,0}$ in real time.

5.6 Concluding remarks and discussion

The reconstruction of to-be-controlled variables from measurement data is a crucial aspect in all control designs. Our to-be-controlled variables are the planar motion of the load and, in case the AGV-load interconnection is not fully rigid, the motions of the AGVs with respect to the load. These variables have to be reconstructed from the odometric sensor information, which usually consists of the drive encoder and steering encoder readings. We analyzed the observability of an individual AGV and proved that it is indeed possible to reconstruct the motion from the odometric measurements.

Driven by practical considerations, we pursued a pragmatic least-squares based observer design and derived a least squares observer for a single AGV. Because there are no measurements on the velocity in the lateral directions of the wheels available, it was assumed that the wheels' side slip angles were identical to their desired values. This resulted in two additional, virtual measurements. This estimator was subsequently analyzed in a stochastic setting. The relation between the motion estimator and the estimated velocity of an arbitrary point on the vehicle was explored. We derived an expression for the covariance of the velocity of an arbitrary point on the AGV. We proved that there is one unique point for which the covariance of the estimated velocity is minimal. This was illustrated by an example where the derived theory was applied to two interconnected OLS vehicles. The example also illustrated that it would be advantageous to combine the measurements of several AGVs when all the AGV-load interconnections are completely rigid to enhance the estimate for the load's planar motion.

Therefore, in the last part of this chapter we derived a generalized observer for the case that the load is interconnected to an arbitrary number of AGVs using so-called lower pairs. Interconnections that can be described by lower pairs include fully rigid interconnections,

revolute joints, and prismatic joints. We extended the least squares observer that was derived for the single AGV case and exploited information about the kinematic constraints to infer information about the load's motion. This resulted in a centralized least squares based observer that estimates the motion of the load and the vehicles using all the available measurements. Subsequently, we discussed a distributed implementation of this observer. It is assumed that the positions of the AGVs with respect to the load are known. Measurements of the velocity of the load with respect to the AGVs are not required. For a distributed implementation of the observer we propose that each AGV estimates its own planar motion using local sensor information and subsequently broadcasts the result. This requires broadcasting of three double precision numbers per AGV. In addition, the AGVs are required to broadcast their own information matrices. Since the information matrices are symmetric, this requires broadcasting six double precision numbers per AGV. With this information, each AGV is able to compute the global estimate that corresponds to the centralized observer design.

Finally, we showed that there are some special situations where the information matrices remain constant during operation. When they are constant, they only need to be set once. This reduces the amount of information that has to be shared in real-time. We presented two such examples. Both examples are related to OLS vehicles that are collectively transporting a load. In the first example where the information matrix remains constant, the load-AGV interconnections are completely rigid. In the second example, the load is interconnected to the vehicles with revolute joints. It is shown that the information matrix remains constant when the axis of rotation of the revolute joint between vehicle k and the load coincides with the aforementioned unique point for which the variance of the estimated velocity is minimal. For an OLS vehicle this means that the revolute joint should be mounted in the middle of the two actuated wheels.

The main limitations of the distributed observer that was presented in this chapter are 1) the matrices that describe the relation between the motion of the vehicles and the measurements are assumed to be known, 2) the load is assumed to behave as a rigid body, 3) the position of the load with respect to the vehicles is assumed to be known, and 4) the observer assumes that the true side slip angles are equal to their setpoints. For a real system all these assumptions will be slightly violated. Instead of adding all the uncertainties to our model and deal with them in a theoretical framework, we prefer to follow a more pragmatic approach and just implement the designed observer on a real system to see how it performs. The experimental results for two OLS vehicles that are cooperatively transporting a load that is fully rigidly interconnected to the AGVs will be presented in Chapter 7.

6

Control

6.1 Introduction

This chapter deals with the control design for cooperatively transporting a load by multiple AGVs. We decided to restrict ourselves to control on the velocity level, as we regard this as an essential intermediate step for achieving fully automated control. The setpoint for the motions of the load and the AGVs is provided by an external host, which can be either a human operator or a computer.

In the main introduction of this thesis we formulated several requirements to increase the chance that our control design will indeed lead to practically meaningful industrial applications. The AGVs must be able to operate cooperatively as well as individually, switching between these two modes should be easy, and the algorithms must fit the industrial AGVs and the software framework that are used by FROG. We aim at a decentralized control design. Ideally, the control law for cooperative behavior is an extension of the controllers that are currently used for individual operation. We also aim at a generic control structure, such that the designed controller is capable of controlling a large class of vehicles. Furthermore, the AGVs should not counteract each other's actions. Docking and grasping procedures are not considered.

Each AGV has multiple actuated wheels. Also because the load is semi-rigidly attached to the AGVs, the interconnected system will typically have more actuators than to-be-controlled variables. Thus our system is *overactuated*, i.e. there are multiple ways of driving the actuators such that the desired motion is realized. Therefore, we need an additional requirement to resolve this ambiguity. We chose to minimize interconnection forces between the load and AGVs.

Now we continue this chapter by reviewing related work on vehicle dynamics control and cooperative transportation. Subsequently, we briefly discuss the controller that is currently used for controlling a single AGV. After that, we introduce a control strategy for cooperatively transporting a load by multiple AGVs that are semi-rigidly interconnected to the load. The chapter ends with the conclusions and a discussion.

6.2 Related work

The control of any electro-mechanical system requires the cooperation of various disciplines. Two fields are of particular importance for our cooperative transportation task, namely the field of vehicle dynamics that concerns the control of horizontal vehicle behavior, and the research field that deals with the cooperative transportation of a load by mobile robots. Before

we review these two fields and discuss the positioning of our work, we first spend some words on dedicated AGV control.

6.2.1 Automated Guided Vehicle control

The first industrial AGVs that were installed in factories followed paths that were defined by white lines on the floor or electrical wires in the ground. They transported relatively light products and operated at speeds of only a few meters per seconds. Therefore, controllers that were based on kinematic vehicle models were capable to operate these early AGVs at the required precision. A common method to control these vehicles was to translate the measured path deviation into a setpoint for the rotational and the longitudinal velocity of the AGV. The desired rotational and longitudinal velocity were subsequently realized by a lower level control loop, that drives the steering and drive actuators. These kinematic controllers are still widely used for low speed laboratory robots and low speed AGVs, see e.g. [17, 60, 90, 108, 131].

In the future, the AGV market will demand more complex vehicles and vehicles that operate at higher speeds. As a result, the study of vehicle dynamics will become increasingly important to control the more exotic future AGVs. At the European Container Terminal of Rotterdam harbour, AGVs with diesel engines and truck tires automatically transport heavy containers. The heavy load in combination with the relatively compliant truck tires require that vehicle dynamics have to be taken into account to achieve the desired behavior. Similarly, the current generation of fully automatic people movers at Rivium/Capelle aan de IJssel in Holland may already reach speeds of 30 km/h. And in autumn 2004, the double-articulated Phileas has become operational in Eindhoven. Although a driver is present for safety reasons, the Phileas is able to achieve speeds of 70 km/h in fully automatic mode. Controllers that are based on kinematic models are not suited for these high speed applications. Therefore, control designs for high speed AGVs are generally based on planar rigid body models with static, linear tire models. Such controllers are also capable of controlling AGVs at low speeds. Moreover, low speed applications will in fact benefit from wheel slip models, as this will improve velocity estimates that are derived from odometric measurements. Hence, for AGV control we see a trend from kinematic models and low speed operation towards dynamical models with wheel slip and high speed operation.

6.2.2 Vehicle dynamics control

In section 5.2 of the previous chapter, we already mentioned that nowadays we witness a steady increase in advanced driver assistance systems for passenger cars and trucks. We also indicated that the earlier systems typically dealt with one aspect of vehicle control. For example, anti-lock braking systems (ABS) help the driver to keep the vehicle under control during extreme braking maneuvers, Electronic Stability Programs (ESP) assist the driver in controlling the vehicle's yaw rate, advanced cruise control (ACC) helps the driver to keep the vehicle at a certain constant speed, etc. Currently we see a trend to integrate the various individual systems. The idea is that sensor fusion in combination with a smart distribution of the control actions will improve the vehicle's handling behavior. The interested reader may

consult the review by Shladover [106] and the articles by Abe [1] and Van Zanten *et al.* [121] for an overview of the development of advanced driver assistance systems.

Some driver assistance systems act on the vehicle by influencing the brakes (ABS,ESP), whereas others also influence the engine torque (ACC). Systems that directly influence the steering angles, such as four wheel steering (4WS), are less common, but they are available. The reader can consult the review by Furukawa *et al.* [42] for an overview of the earlier work on 4WS and a list of the first commercially available 4WS vehicles. It is expected that steer-by-wire systems, i.e. systems where there is no mechanical link between the steering wheel and the wheels, will become commercially available in the near future. Until then, car manufacturers can resort to systems that superimpose small offsets on the driver's steering angle.

Combining braking and steering commands offers new possibilities for integrated vehicle dynamics control. An early study that uses a dynamical model to optimize the braking and handling performance of a truck-semitrailer is the article by Van Zanten and Krauter [122]. It was one of the first articles where braking and the steering actions of a vehicle were optimized for certain maneuvers using the recently developed theory of optimal control.

The traditional way to design vehicle controllers is to consider the setpoint for the steering actuator and the braking torques for the wheels as inputs, see e.g. [54]. Whereas traditional cars have one steering system and four brakes, it is expected that the number of actuators will increase in the future. For example, some cars will be equipped with additional rear wheel steering systems, for some cars the front wheels will not be mechanically coupled anymore as they are steered by means of electric servos, etc. As a result, the number of actuator configurations will also increase. This has led several researchers to investigate control architectures that are more generic in nature. The generic control designs have in common that they use a layered control architecture. The idea is that the top layer is the same for all vehicles. In case of passenger cars, it is usually based on a planar rigid body model of the vehicle. The purpose of the top layer is to translate the desired rotational, longitudinal and lateral accelerations into a wrench setpoint for the vehicle. The desired wrench is subsequently distributed among the wheels. How the forces are distributed among the wheels depends on the particular vehicle configuration, and the available actuators. When a wheel is steered but not driven, this basically means that the wheel can actively generate lateral forces and a braking force. A wheel that is connected to the cars driveline by means of a fixed axis can exert braking as well as acceleration forces, but can not influence the lateral force. The lower layers have to fit the sensor and actuator configuration of the to-be-controlled vehicle.

Nowadays, generic control architectures are studied by several research groups. The Chalmers University of Technology/Royal Institute of Technology group from Sweden focuses on the control of the next generation passenger cars [7, 8, 40, 69, 70]. Besides vehicle dynamics control, their research interests also include driveline control for vehicles that are equipped with hybrid drivelines, energy management systems, and control of electric hybrid vehicles in general. The work of the Advanced Chassis and Transport Systems group of TNO Automotive in Helmond (The Netherlands) [72, 97, 98, 124] is related to their VEHIL laboratory, which includes a hall of 200 meters long with two so-called moving bases. Each moving base is in fact a high performance automated guided vehicle, which weighs 500 kg and has four steerable wheels that are equipped with racing tires. They use a generic control setup to control their mobile bases. There is also some work by Toyota Vehicle Control Lab,

see the article by Hattori [49], in which the author investigates a wheel force distribution strategy that can deal with both normal as extreme maneuvers. Finally, there are studies that do not explicitly aim to develop a generic controller, but nevertheless use similar techniques by computing the required wrench on the vehicle, and subsequently decompose this to the local tire forces (e.g. [83]).

In the future we may expect that the driver assistance systems become so advanced and integrated that the car is fully equipped with steer- and drive-by-wire systems. We will see more similarities with modern aircraft and helicopter control systems, where the pilot provides the setpoint for the motion. That setpoint is translated into a desired wrench, which is subsequently distributed among the various actuators. The autonomy of a car's control system may even increase up to a point that it is able to drive itself without any intervention of the driver. Then the car has started to look like an AGV from a functional point of view. There has already been a large amount of research on Automated Highway Systems (AHS) for quite some years. But it will take many more years before such system is reliable and accepted enough to become operational. Current state-of-the-art in autonomous car-like vehicles are the completely autonomous People Movers, which have been successfully applied for quite some years now. Hence, automated transport on dedicated, structured lanes is nowadays possible. The DARPA challenge showed that autonomous operation in unstructured and unknown environments is being actively researched, and that still a lot of work has to be done before we will see the first successful applications.

6.2.3 Cooperative transportation

An overview of relevant studies on cooperative transportation was given in subsection 1.3.3 of the main introduction of this thesis. We distinguished between behavior-based robotic studies, and research that adopted ideas of traditional industrial manipulators. Since we are interested in realizing well defined velocity setpoints in static, structured, well known environments, we concluded that our cooperative transportation application is closer related to the control of cooperating industrial mechanical manipulators than to the field of behavior-based robotics.

The first works on cooperative industrial manipulators appeared in the 1970s, see e.g. [88] for an early study. Since the cooperating industrial manipulators are relatively close to one another and fixed to the ground, there was no real need to pursue decentralized control implementations. There are many similarities between cooperating industrial manipulators and multi-fingered robotic hands, as multi-fingered robotic hands can be seen as small scale multiple cooperating manipulators. A summary of the evolution and the state of the art in the field of robot hands is given by Bicchi [15]. Important research issues in the control of cooperating manipulators as well as multi-fingered robotic hands include the modeling of the object-manipulator contacts, computation of the optimal grasp positions, and the determination of the optimal grasp forces.

From perspective of the handled object, both the multiple manipulators as well as the multi-fingered hand setups are overactuated systems. In other words, there are multiple ways to drive the actuators that all result in the same net wrench on the handled object, and consequently, the same object motion. The remaining degrees of freedom in the selection of actuator signals is usually resolved by imposing an additional constraint on the contact forces.

Possible strategies are to minimize the maximum contact force, to minimize the internal object loading, to maximize the margin to the maximum transmittable force by a finger, etc. From a conceptual perspective this is very similar to multiple AGVs transporting a load. On a higher level, the AGV platforms can be seen as the actuators, where each AGV is able to exert a certain wrench on the object. On a lower level, the wheels can be seen as the actuators that realize a certain wrench on the combine AGV-load system. There will exist sets of steering angles and wheel force setpoints that all result in the same net wrench on the combination, and consequently in the same net motion.

There are several studies on the cooperative transportation by multiple mobile robots that are closely related to our research and that adopt ideas from industrial manipulators and multi-fingered robotic hands. A recent paper dealing with a decentralized control strategy that was based on kinematic modeling ideas from traditional robotic manipulators is the work by Tang *et al.* [118]. Examples of studies that exploit dynamical models to arrive at a control law are the works by Stilwell and Bay [110], Hashimoto *et al.* [47], and Miyata *et al.* [82]. In these studies, the forces that should be exerted by each robot on the load to realize the desired motion are computed by a centralized algorithm. An example of research that uses dynamic models to design a decentralized control law are the studies of Khatib *et al.* [61, 62]. Their mobile platforms are equipped with manipulator arms and six-axis force/torque sensor in the wrist. Hirata *et al.* [51] also uses torque/force sensors to transport a plate using two mobile robots that each have two manipulator arms. Finally, there is a more recent study by Hashimoto *et al.* [46], in which the authors present a hierarchical control system to operate a loading deck with multiple wheel modules. Each wheel module consists of two differential drive wheels, and is connected to the loading deck by means of a revolute joint. Because the revolute's rotation axis does not lie in between the two drive wheels, each wheel module can exert both longitudinal as well as lateral forces on the loading deck.

The general trend in cooperative transportation by mobile robots is to use compliant mechanisms to hold the to-be-transported object, often in combination with sensors to measure the forces and torques between the object and the robots. The reason to use compliant mechanisms is that it is generally believed that the wheels impose very rigid constraints on the behavior of the vehicle, which in turn lead to unacceptably high interconnection forces. In contrast to the field of vehicle dynamics control, we see that research on cooperative transportation by multiple robots is characterized by a high heterogeneity, where robots, controller design goals, models, actuators, and sensors vary greatly between studies.

6.2.4 Positioning of our work

To be able to deal with a large variety of AGVs, we are particularly interested in the generic control designs from the field of vehicle dynamics control. FROG has used a generic control structure for several years now to control their AGVs. Their philosophy is described in the paper by De Graaf [33]. Since we are mainly interested in modest vehicle maneuvers, we will not enter the tires' nonlinear operating regions. In particular, we will not come near the maximum transmittable tire force. This means that we can use static, linear tire models and relatively simple methods to distribute the forces amongst the AGV's wheels.

In case that the load is semi-rigidly attached to multiple AGVs, e.g. by revolute joints, then we have to deal with the control of multiple physically interconnected vehicles. This

problem is not considered explicitly in vehicle dynamics control studies. However, there are some links with works that deal with the control of truck-semitrailer and car-trailer combinations. The usual solution to control the latter systems is to derive a dynamic model based on Lagrange method. The algebraic equations that represent the mechanical constraints are avoided by a smart choice of the generalized coordinates. Once the dynamical model of the articulated combination is known, it is relatively straightforward to control that system. There are two differences between our work and the control of an articulated vehicle. Firstly, AGVs used for cooperative transportation are highly maneuverable. Thus whereas articulated vehicles basically move only forwards and backwards, our interconnected system can also move sideways and perform much more complex maneuvers. Secondly, our AGVs have to be able to operate cooperatively as well as individually. We therefore aim to derive a decentralized control law. In articulated vehicle control, it is common to derive a centralized solution.

We saw that the trend in research on mobile robot cooperative transportation is to use compliant mechanisms to hold the to-be-transported object. Often sensors are used to measure the forces and torques between the object and the robots. In our research, we would like to follow a different approach. In contrast to the compliant mechanisms, we choose to attach the load to the AGVs by means of (semi-)rigid interconnections. We also aim to avoid force and torque sensors. The necessary compliance is achieved by means of wheel slip. We therefore have to consider the wheels as imperfect constraints, otherwise a minimal error in the steering encoder offset would theoretically lead to a system that cannot move. It is exactly the wheel slip that allows us to rigidly interconnect the load the AGVs. The disadvantage of wheel slip is that it makes it difficult to determine the relative velocities of the AGVs with respect to the floor.

6.3 Velocity controller for a single AGV

This section introduces the controller that is currently used to control individual AGVs. In the next section we will extend this controller to achieve cooperative behavior. The general setup of FROG's AGV controllers has been introduced in section 2.2.2 of Chapter 2. It consisted of an inner control loop to control the velocity of the AGV, and an outer control loop to control its position. In this thesis we focus on control at the velocity level, hence we restrict ourselves to the so-called *velocity layer* of the controller.

A detailed block scheme of the velocity layer is depicted in Figure 6.1. The measurements are the readings from the odometry, which consist of the steering angle and drive encoder readings. The inputs for the actuators of the AGV are the setpoints for the steering and driving systems. The odometric measurements are fed to the observer that was described in section 5.4 of Chapter 5. The observer computes an estimate $\hat{T}_v^{v,0}$ for the twist of the vehicle with respect to the floor. $\hat{T}_v^{v,0}$ is expressed in some vehicle fixed coordinate system Ψ_v . For a single AGV, Ψ_v is often chosen at the middle of the vehicle and with the x -axis pointing towards the front. Later on we will see that Ψ_v may also lie outside the vehicle, as long as it remains rigidly connected. For example, from symmetry considerations it seems logical to choose Ψ_v to lie at the geometric center of the participating vehicles for a cooperative transportation application.

The velocity controller receives the twist estimate $\hat{T}_v^{v,0}$ and an external twist setpoint $T_{v,\text{set}}^{v,0}$.

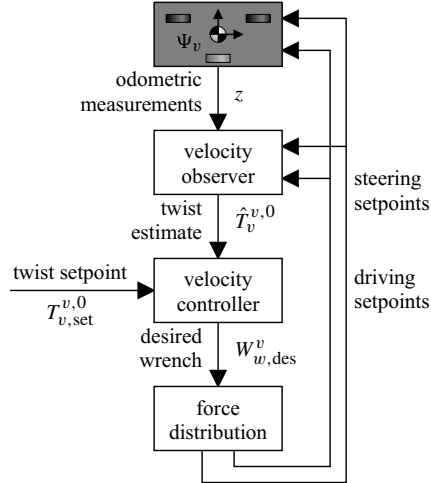


Figure 6.1: Block scheme of the single AGV controller.

The setpoint is provided by a human operator during manual operation, by the outer position control loop during automatic operation, and by an external laptop during our cooperative transportation experiments that are discussed in the next chapter. The velocity controller uses the error $T_{v,set}^{v,0} - \hat{T}_v^{v,0}$ and a planar rigid body description of the vehicle to compute the wrench $W_{w,des}^v$ that should be exerted by the wheels on the AGV. A force distribution block subsequently distributes the wrench $W_{w,des}^v$ among the wheels. Several AGVs have more than three actuators. This means that they are overactuated, i.e. several actuator inputs will result in the same behavior. To resolve this ambiguity, there is an additional criterion to minimize the squared norm of all the longitudinal and lateral tire forces. In vehicle dynamics control we encounter different norms that take nonlinearities such as saturation effects of tires during large wheel slip into account. Since we only consider gentle maneuvers, the squared norm of the tire forces is satisfactory for our applications.

In the next subsections, we will discuss the control laws of the velocity layer in more detail.

6.3.1 Desired behavior

It is desired that the rotational, longitudinal and lateral velocity components of Ψ_v with respect to the floor respond as decoupled first order linear systems to the corresponding setpoints. This is illustrated in Figure 6.2. Decoupled first order linear behavior is desired, because it prohibits infinite forces that are required to follow stepwise velocity setpoints, and it is easy to interpret for humans when they move the load in manual mode. It readily follows that the desired time derivative of $T_v^{v,0}$ satisfies

$$\dot{T}_{v,des}^{v,0} = K_v(T_{v,set}^{v,0} - T_v^{v,0}) \quad (6.1)$$

A decoupled first order linear behavior corresponds to a nonsingular, diagonal gain matrix K_v . When the desired behavior is expressed in another coordinate system Ψ_a that is fixed to the load, then the expression for the desired behavior is still equal to the above equation with v replaced by a . However, the transformed gain matrix

$$K_{a,v} = Ad_{H_v^a} K_v Ad_{H_a^v}. \quad (6.2)$$

corresponding to the new coordinates will in general not be diagonal anymore.

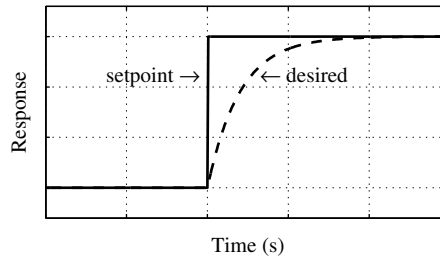


Figure 6.2: The desired behavior is a linear, first order response to (human) setpoints.

6.3.2 Velocity controller

The control law that is used in current AGV applications is obtained by substituting the desired behavior $\dot{T}_{v,\text{des}}^{v,0}$ into the equation of motion of the vehicle. This yields the net wrench $W_{w,\text{des}}^v$ that the wheels should exert on the AGV to realize the desired behavior. From equation (3.51) we recall that the equation of motion for a single AGV is given by

$$\dot{T}_v^{v,0} + \omega_v \Gamma_v T_v^{v,0} = M_v^{-1} (W_w^v)^T, \quad (6.3)$$

where Γ_v and M_v are constant matrices that encapsulate the inertial properties of the vehicle. Injecting the desired behavior (6.1) into the AGV's equation of motion (6.3) yields

$$\boxed{(W_{w,\text{des}}^v)^T = M_v K_v (T_{v,\text{set}}^{v,0} - \hat{T}_v^{v,0}) + \hat{\omega}_v M_v \Gamma_v \hat{T}_v^{v,0}} \quad (6.4)$$

Because the true twist $T_v^{v,0}$ and true rotational velocity ω_v are unknown, they were replaced by their respective estimates $\hat{T}_v^{v,0}$ and $\hat{\omega}$ in the control law (6.4) above. In fact, $\hat{\omega}$ is the first component of $\hat{T}_v^{v,0}$. The key point is that $W_{w,\text{des}}^v$ depends on the error $T_{v,\text{set}}^{v,0} - \hat{T}_v^{v,0}$, the twist estimate $\hat{T}_v^{v,0}$, and some constant matrices M_v , K_v and Γ_v .

To conclude, we would like to remark that the control law (6.4) can also be interpreted as a *feedback linearizing controller*, where the new input ν is equal to $K_v (T_{v,\text{set}}^{v,0} - \hat{T}_v^{v,0})$. Indeed, if we assume that $\hat{T}_v^{v,0} = T_v^{v,0}$ and substitute

$$(W_{w,\text{des}}^v)^T = M_v \nu + \hat{\omega}_v M_v \Gamma_v \hat{T}_v^{v,0} \quad (6.5)$$

in the equation of motion for the single AGV (6.3), then we obtain

$$\dot{T}_v^{v,0} = v. \quad (6.6)$$

Thus by applying the feedback (6.5) we have achieved that the derivative of the state depends linearly on the new input v . If we subsequently substitute the proportional controller $K_v(T_v^{v,0} - \hat{T}_v^{v,0})$ for v , then we see that the resulting behavior is equal to our desired behavior (6.1).

6.3.3 Force distribution

The net wrench $W_{w,\text{des}}^v$ that should be exerted on the AGV to achieve the desired behavior, is subsequently translated into the setpoints for the actuators. Because our test vehicles are overactuated, we choose to minimize the squared norm of the tire forces as an intermediate step. The longitudinal tire force for wheel w_i is denoted by $F_{w_i,u}$, and the lateral tire force for wheel w_i is denoted by $F_{w_i,v}$. Let us stack the tire forces in a single vector F_w . If we combine the tire model (3.63), i.e. $F_{w_i,v} = -C_{\text{lat}}^{w_i} \alpha_{w_i}$, with the definition (3.95) of u , then we see that the wheel forces F_w can also be written as

$$F_w = \begin{pmatrix} F_{w_1,u} \\ F_{w_2,u} \\ F_{w_1,v} \\ F_{w_2,v} \end{pmatrix} = \underbrace{\begin{pmatrix} 1 & 0 & 0 & 0 \\ 0 & 1 & 0 & 0 \\ 0 & 0 & -C_{\text{lat}}^{w_1} & 0 \\ 0 & 0 & 0 & -C_{\text{lat}}^{w_2} \end{pmatrix}}_C \underbrace{\begin{pmatrix} F_{w_1,u} \\ F_{w_2,u} \\ \alpha_{w_1} \\ \alpha_{w_2} \end{pmatrix}}_u = Cu. \quad (6.7)$$

Here α_{w_i} is the side slip angle of wheel w_i . From equations (3.73) and (3.94) we recall that the relation between the tire forces and the net wrench that is exerted by the wheels on the vehicle reads

$$(W_w^v)^T = B^T F_w \approx \bar{B}^T F_w, \quad (6.8)$$

where B was defined in equation (3.70) and \bar{B} in equation (3.93):

$$B = B(\delta_{w_1}, \delta_{w_2}) = \begin{pmatrix} B_{w_1,u} \\ B_{w_2,u} \\ B_{w_1,v} \\ B_{w_2,v} \end{pmatrix} = \begin{pmatrix} x_{w_1}^v s\delta_{w_1} - y_{w_1}^v c\delta_{w_1} & c\delta_{w_1} & s\delta_{w_1} \\ x_{w_2}^v s\delta_{w_2} - y_{w_2}^v c\delta_{w_2} & c\delta_{w_2} & s\delta_{w_2} \\ x_{w_1}^v c\delta_{w_1} + y_{w_1}^v s\delta_{w_1} & -s\delta_{w_1} & c\delta_{w_1} \\ x_{w_2}^v c\delta_{w_2} + y_{w_2}^v s\delta_{w_2} & -s\delta_{w_2} & c\delta_{w_2} \end{pmatrix}, \quad (6.9)$$

$$\bar{B} = B(\bar{\delta}_{w_1}, \bar{\delta}_{w_2}), \quad (6.10)$$

where $(x_{w_i}^v, y_{w_i}^v)$ are the constant coordinates of the center of wheel w_i expressed in the vehicle coordinate system Ψ_v . Matrix B depends on the steering angles δ_{w_1} and δ_{w_2} of the two actuated wheels. Matrix \bar{B} , on the other hand, was an approximation for B that was obtained by replacing the actual steering angles δ_{w_i} by the so-called kinematic steering angles $\bar{\delta}_{w_i}$. Since the kinematic steering angles only depend on the current vehicle state $T_v^{v,0}$, see equation (3.86), matrix \bar{B} does not depend on δ_{w_i} anymore. Minimizing the squared norm of the wheel forces while satisfying the constraint that their net result is equal to the desired

wrench $W_{w,\text{des}}^v$ gives us the desired wheel forces

$$F_{w,\text{des}} = \arg \min_{F_w} \left\{ \|F_w\|_2^2 \mid \bar{B}^T F_w = (W_{w,\text{des}}^v)^T \right\} \quad (6.11)$$

Note that \bar{B}^T has full row rank. From linear algebra we know that the unique solution to the convex quadratic problem (6.11) is given by

$$F_{w,\text{des}} = \bar{B}(\bar{B}^T \bar{B})^{-1} (W_{w,\text{des}}^v)^T. \quad (6.12)$$

Since $u = C^{-1} F_w$, the corresponding setpoints u_{set} for the longitudinal forces and the slip angles are

$$u_{\text{set}} = C^{-1} \bar{B}(\bar{B}^T \bar{B})^{-1} (W_{w,\text{des}}^v)^T \quad (6.13)$$

In a discrete time implementation, we may also take the matrix B that corresponds to the steering angles of the previous time instance as an alternative for \bar{B} . Because B does not change so much between two samples. Once u_{set} is available, then it is straightforward to compute the torque setpoint for the drive servo of wheel w_i by dividing the longitudinal force setpoint $F_{w_i,u}^{\text{set}}$ by the wheel radius and the gear ratio of the reduction. An additional constant term is added to the drive system setpoint to counteract the Coulomb friction. With equation (3.61), the setpoint for the steering system for wheel w_i is found by subtracting the setpoint $\alpha_{w_i}^{\text{set}}$ for the side slip angle from the kinematic steering angle. This yields

$$\delta_{w_i}^{\text{set}} = \hat{\delta}_{w_i} - \alpha_{w_i}^{\text{set}} \text{sign}(\hat{u}_{w_i}). \quad (6.14)$$

More advanced strategies for distributing wheel forces that also take the maximal transmittable tire forces into account are for example found in the works by Andreasson *et al.* [8, 7]. The modifications for cooperative transportation will be made in the higher level velocity control law (6.4). Thus this block remains unchanged.

6.4 Control for the cooperative system

We consider N AGVs that are semi-rigidly attached to a single load by means of lower pairs. The load is modelled as a planar rigid body. We aim at a decentralized implementation by extending the single AGV controllers that are already present on the individual AGVs. The general setup of the cooperative transportation controller is sketched in Figure 6.3. Each AGV has its own velocity observer, velocity controller, and a force distribution module. The decentralized velocity observers for cooperative transportation have been discussed in detail in section 5.5 of Chapter 5. In that section, we saw that the local twists estimates $\hat{T}_{v_k|z_k}^{\ell,0}$ and the corresponding information matrices $B_{\ell,k}^T \Sigma_k^{-1} B_{\ell,k}$ have to be communicated in order to compute the estimates $\hat{T}_\ell^{\ell,0}$ and $\hat{\eta}_k$ for the motion of the load and the motion of AGVs with respect to the load. We also saw that there were certain circumstances where $B_{\ell,k}^T \Sigma_k^{-1} B_{\ell,k}$ was constant, which means that we do not have to broadcast the information matrices in these

special cases. Furthermore, in that section we assumed that the relative position $H_\ell^{v_k}$ of the load with respect to AGV k is known.

The module that distributes the forces among the various actuators remains identical to the single vehicle case. See subsection 6.3.3 for a description of this module.

The remainder of this section focusses on the velocity controller for cooperative transportation. The goal of the velocity controller is to compute the net wrench $W_{w,\text{des}}^{v_k}$ that should be exerted by the wheels of a particular AGV k on that AGV. Analogously to the description of the single AGV controller, we will first introduce the desired behavior of the combined AGVs-load system. Subsequently, we derive a control law that calculates the desired net wrench that should be exerted by the wheels of a particular AGV on that AGV. Finally, we consider the special case that the AGV-load interconnections are completely rigid. We will see that the modifications for achieving cooperative behavior for that case are particularly simple.

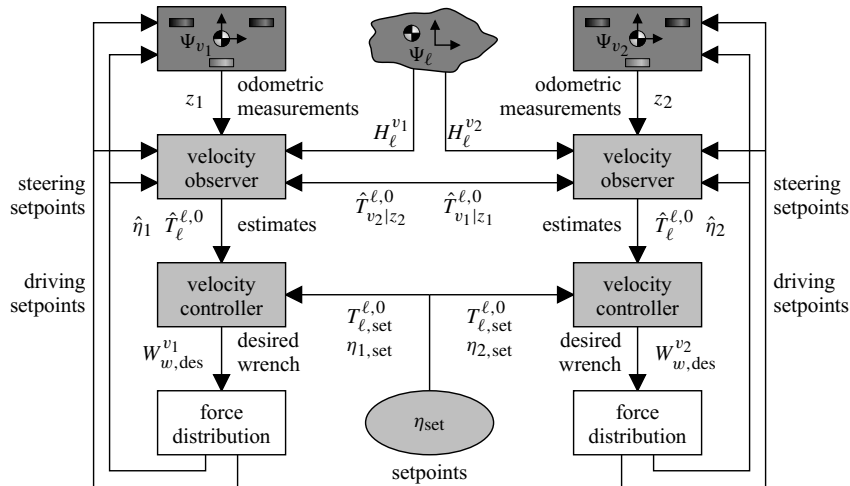


Figure 6.3: Block scheme of the cooperative transportation controller. The adjustments for achieving cooperative transportation were made in the velocity observers and the velocity controllers.

6.4.1 Desired behavior

We consider the situation that a single load is transported by N AGVs. Hence, our system consists of $N + 1$ planar rigid bodies. If we use a single twist to describe the motion for each individual body, then we have in total $N + 1$ twists for the interconnected system. Since the dimension of a twist is three, this corresponds to $3(N + 1)$ variables. However, we know that the AGVs are semi-rigidly interconnected to the load. Thus the interconnected system has less than $3(N + 1)$ degrees of freedom. Because the interconnections we consider are lower pairs, we saw with equation (3.111) of subsection 3.7.3 that the interconnected system can be

described by the reduced set of coordinates

$$\eta = \begin{pmatrix} T_\ell^{\ell,0} \\ \eta_1 \\ \vdots \\ \eta_N \end{pmatrix}. \quad (6.15)$$

Here $T_\ell^{\ell,0}$ is the twist of the load with respect to the floor, and η_k parameterizes the relative motion of AGV k with respect to the load. For a revolute joint, η_k is the rotational velocity of the AGV with respect to the load, and for a slider joint η_k is the translational velocity of the AGV with respect to the load. From equation (3.101) we recall that

$$T_{v_k}^{i,\ell} = S_{i,k} \eta_k. \quad (6.16)$$

We require that the desired behavior of the interconnected system satisfies

$$\dot{\eta}_{\text{des}} = K(\eta_{\text{set}} - \eta) \quad (6.17)$$

Furthermore, we require that the gain matrix K has the following block diagonal form:

$$K = \begin{pmatrix} K_\ell & 0 & \dots & 0 \\ 0 & K_1 & & 0 \\ \vdots & & \ddots & \\ 0 & 0 & & K_N \end{pmatrix} \quad (6.18)$$

where

$$\begin{aligned} K_\ell &\in \mathbb{R}^{3 \times 3} \\ K_k &\in \mathbb{R}^{\dim \eta_k \times \dim \eta_k} \end{aligned} \quad (6.19)$$

For the desired behavior of the interconnected system, we can distinguish between the desired behavior $\dot{T}_{\ell,\text{des}}^{\ell,0}$ of the load and the desired behavior $\dot{\eta}_{k,\text{des}}$ of AGV k with respect to the load. It follows from equations (6.17)-(6.19) that the desired time derivatives of $T_\ell^{\ell,0}$ and η_k are given by

$$\begin{aligned} \dot{T}_{\ell,\text{des}}^{\ell,0} &= K_\ell(T_{\ell,\text{set}}^{\ell,0} - T_\ell^{\ell,0}) \\ \dot{\eta}_{k,\text{des}} &= K_k(\eta_{k,\text{set}} - \eta_k) \end{aligned} \quad (6.20)$$

Note that the desired behavior of the load is very similar to the desired behavior of an AGV during individual operation (6.1). **It is assumed that the setpoints $T_{\ell,\text{set}}^{\ell,0}$ and $\eta_{k,\text{set}}$ are given.**

Now that we have the desired behavior of the interconnected AGVs as expressed in the reduced set of coordinates η , we can compute the desired time derivative of $T_{v_k}^{v_k,0}$. From equation (3.101) we know that

$$T_{v_k}^{v_k,0} = T_\ell^{v_k,0} + T_{v_k}^{v_k,\ell} = Ad_{H_\ell^{v_k}} T_\ell^{\ell,0} + S_{v_k,k} \eta_k. \quad (6.21)$$

Therefore, its derivative can be written as

$$\begin{aligned}
\dot{T}_{v_k}^{v_k,0} &= \dot{A}d_{H_\ell^{v_k}} T_\ell^{\ell,0} + Ad_{H_\ell^{v_k}} \dot{T}_\ell^{\ell,0} + \underbrace{\dot{S}_{v_k,k}}_0 \eta_k + S_{v_k,k} \dot{\eta}_k \\
&= Ad_{H_\ell^{v_k}} ad_{T_\ell^{\ell,v_k}} T_\ell^{\ell,0} + Ad_{H_\ell^{v_k}} \dot{T}_\ell^{\ell,0} + Ad_{H_\ell^{v_k}} S_{\ell,k} \dot{\eta}_k \\
&= Ad_{H_\ell^{v_k}} \dot{T}_\ell^{\ell,0} + Ad_{H_\ell^{v_k}} S_{\ell,k} \dot{\eta}_k - Ad_{H_\ell^{v_k}} ad_{T_\ell^{\ell,v_k}} T_\ell^{\ell,0}. \tag{6.22}
\end{aligned}$$

It follows that the desired time derivative of $T_{v_k}^{v_k,0}$ satisfies

$$\boxed{\dot{T}_{v_k,\text{des}}^{v_k,0} = Ad_{H_\ell^{v_k}} \left(\dot{T}_{\ell,\text{des}}^{\ell,0} + S_{\ell,k} \dot{\eta}_{k,\text{des}} - ad_{T_\ell^{\ell,v_k}} T_\ell^{\ell,0} \right)} \tag{6.23}$$

6.4.2 Velocity controller

The idea is to realize the desired twist of the load while at the same time minimizing the local forces that occur at the interconnection points where the load is attached to the AGVs. The same rationale has often been used for cooperative handling of an object by multiple robotic manipulators, and was e.g. adopted for the transportation of an object by mobile robots in the studies by Stilwell and Bay [110], Miyata *et al.* [82], and Hashimoto *et al.* [47], and Khatib *et al.* [62]. Recall that the equation of motion for the load satisfies (3.99)

$$\dot{T}_\ell^{\ell,0} + \omega_\ell \Gamma_\ell T_\ell^{\ell,0} = M_\ell^{-1} (W_V^\ell)^T. \tag{6.24}$$

The net wrench that should be exerted by the AGVs on the load to realize the desired behavior is found by substituting the desired behavior (6.20) in the equation of motion for the load. This yields

$$(W_{V,\text{des}}^\ell)^T = M_\ell K_\ell (T_{\ell,\text{set}}^{\ell,0} - T_\ell^{\ell,0}) + \omega_\ell M_\ell \Gamma_\ell T_\ell^{\ell,0}. \tag{6.25}$$

The net wrench that is exerted by the AGVs on the load is the sum of the wrenches that are exerted by each individual AGV on the load, see equation (3.100). Consequently, the sum of the desired wrenches $W_{v_k,\text{des}}^\ell$ that should be exerted by the individuals AGVs on the load should be equal to the desired net wrench $W_{V,\text{des}}^\ell$ above. When expressed in an arbitrary coordinate system Ψ_i , this condition reads

$$\sum_{k=1}^N W_{v_k,\text{des}}^{i,\ell} = W_{V,\text{des}}^{i,\ell}. \tag{6.26}$$

The forces and torques that are exerted by the AGVs on the load must be transmitted through the kinematic constraints of the interconnections. It is not possible to transmit torques and forces in the directions of the degrees of freedom that are free. With equation (3.104) of subsection 3.7.2 we saw that the constraint wrench $W_{v_k}^{i,\ell}$ is an element of the set

$$(W_{v_k}^{i,\ell})^c = \text{ann } S_{i,k} = \{W_{v_k}^{i,\ell} \in se^*(2) \mid W_{v_k}^{i,\ell} S_{i,k} = 0\}. \tag{6.27}$$

Thus the constraint wrenches $W_{v_k}^{i,\ell}$ annihilate the columns of the matrix $S_{i,k}$. For the sequel it is useful to express $(W_{v_k}^{i,\ell})^c$ in terms of the span of the rows of a certain matrix $A_{i,k}$. This allows us to write the constraint wrench $W_{v_k}^{i,\ell}$ as

$$\boxed{W_{v_k}^{i,\ell} = \lambda_k^T A_{i,k}} \quad (6.28)$$

When $A_{i,k}$ is properly scaled, **the Lagrange multipliers λ_k are interpreted as the local interconnection forces and torques that occur at the k^{th} interconnection.** Since the constraint wrenches are not producing power, we must have that

$$W_{v_k}^{i,\ell} T_{v_k}^{i,\ell} = \lambda_k^T A_{i,k} S_{i,k} \eta_k = 0 \quad \forall \lambda_k, \forall \eta_k, \quad (6.29)$$

which implies that

$$\boxed{A_{i,k} S_{i,k} = 0} \quad (6.30)$$

Thus the dual product of the rows (“unit wrenches”) of $A_{i,k}$ and the columns (“unit twists”) of $S_{i,k}$ should be zero. To span the entire constraint wrench space $(W_{v_k}^{i,\ell})^c$, we require that

$$\boxed{\text{rank } A_{i,k} + \text{rank } S_{i,k} = \dim se^*(2) = 3} \quad (6.31)$$

Thus $A_{i,k}$ and $S_{i,k}$ are closely related. Since the interconnections we consider are lower pairs, it follows that $A_{i,k}$ is constant when the coordinate system Ψ_i is fixed to either the load or to AGV k . For the sequel it is useful to stack all the local interconnection forces λ_k in a single vector λ , i.e.

$$\lambda = \begin{pmatrix} \lambda_1 \\ \vdots \\ \lambda_N \end{pmatrix}. \quad (6.32)$$

Since the constraint wrench $W_{v_k}^{i,\ell}$ was a linear combination of the local interconnection forces λ_i , this wrench can also be written as a linear combination of the vector λ with all the interconnection forces. To ease notation, we define a new matrix $G_{i,k}$ such that

$$(W_{v_k}^{i,\ell})^T = A_{i,k}^T \lambda_k = \underbrace{(0 \quad A_{i,k}^T \quad 0)}_{G_{i,k}} \lambda = G_{i,k} \lambda. \quad (6.33)$$

Consequently, we may write the net wrench that is exerted by the AGVs on the load as

$$\boxed{(W_V^{i,\ell})^T = \sum_{k=1}^N (W_{v_k}^{i,\ell})^T = \sum_{k=1}^N G_{i,k} \lambda = \underbrace{(G_{i,1} + \dots + G_{i,N})}_{G_i} \lambda = G_i \lambda} \quad (6.34)$$

Similar to the desired wrench $W_{V,\text{des}}^\ell$ that should be exerted by the vehicles on the load to realize the desired behavior, we now try to find the desired interconnection forces λ_{des} that will result in the desired behavior when they are applied to the load. The relation between the interconnection forces λ and the wrench $W_V^{i,\ell}$ is described by equation (6.34). If we substitute

the latter expression in equation (6.25), then we find that the desired wrench $W_{V,\text{des}}^\ell$ and the desired local interconnection force λ_{des} must satisfy

$$(W_{V,\text{des}}^\ell)^\text{T} = G_\ell \lambda_{\text{des}} = M_\ell K_\ell (T_{\ell,\text{set}}^{\ell,0} - T_\ell^{\ell,0}) + \omega_\ell M_\ell \Gamma_\ell T_\ell^{\ell,0}. \quad (6.35)$$

Since the AGVs and the load-vehicle interconnections have been designed such that the AGVs can move the load in any direction, G_ℓ has full row rank. Hence, there exists at least one λ_{des} such that equality (6.35) holds. Generally there are more, see e.g. [127] for all solutions. To resolve this ambiguity, we select the one such that a certain Q -norm of the interconnections forces is minimized:

$$\lambda_{\text{des}} = \arg \min_{\lambda} \left\{ \frac{1}{2} \lambda^\text{T} Q \lambda \text{ s.t. } G_\ell \lambda = (W_{V,\text{des}}^\ell)^\text{T} = M_\ell K_\ell (T_{\ell,\text{set}}^{\ell,0} - T_\ell^{\ell,0}) + \omega_\ell M_\ell \Gamma_\ell T_\ell^{\ell,0} \right\}, \quad (6.36)$$

where $Q = PP^\text{T} > 0$ is a physically meaningful, positive-definite weighting matrix. By choosing Q appropriately it is possible to indicate the importance that certain interconnection forces will be small. Although the above expression was derived to minimize the interconnection forces, it is remarked that the forces in the load can also be taken into account to some extent by choosing appropriate G_ℓ , λ , and Q . See for instance [129] for details. From linear algebra we know that the unique solution to the convex quadratic problem (6.36) is given by

$$\lambda_{\text{des}} = QG_\ell^\text{T}(G_\ell QG_\ell^\text{T})^{-1}(W_{V,\text{des}}^\ell)^\text{T} = P(QP)^+ \left(M_\ell K_\ell (T_{\ell,\text{set}}^{\ell,0} - T_\ell^{\ell,0}) + \omega_\ell M_\ell \Gamma_\ell T_\ell^{\ell,0} \right) \quad (6.37)$$

Here $(G_\ell P)^+ = P^\text{T}G_\ell^\text{T}(G_\ell P P^\text{T}G_\ell^\text{T})^{-1}$ denotes the *pseudo-inverse* of $G_\ell P$. Other criteria than (6.36) can be used to select λ_{des} . One of the reasons that we chose this one is because the corresponding pseudo-inverse solution is easy to implement and can be carried out in real-time. Now that we have the desired interconnection forces λ_{des} , we also know the desired interconnection forces $\lambda_{k,\text{des}}$ between AGV k and the load. From equations (6.34) and (6.37) it follows that the corresponding desired wrench $W_{v_k,\text{des}}^\ell$ that must be exerted by AGV k on the load equals

$$(W_{v_k,\text{des}}^\ell)^\text{T} = G_{\ell,k} \lambda_{\text{des}} = G_{\ell,k} P(QP)^+ \left(M_\ell K_\ell (T_{\ell,\text{set}}^{\ell,0} - \hat{T}_\ell^{\ell,0}) + \hat{\omega}_\ell M_\ell \Gamma_\ell \hat{T}_\ell^{\ell,0} \right) \quad (6.38)$$

We replaced the unknown, true twist $T_\ell^{\ell,0}$ and true rotational velocity ω_ℓ by their respective estimates $\hat{T}_\ell^{\ell,0}$ and $\hat{\omega}_\ell$. From equation (3.109) we recall that the equation of motion for an AGV k that is attached to a load satisfies

$$\dot{T}_{v_k}^{v_k,0} + \omega_{v_k} \Gamma_{v_k} T_{v_k}^{v_k,0} = M_{v_k}^{-1} (W_w^{v_k} - W_{v_k}^{v_k,\ell})^\text{T}, \quad (6.39)$$

where $W_{v_k}^{v_k,\ell}$ is the wrench that is exerted by the AGV on the load. Note that this wrench was not presented in the equation of motion for an individual AGV that is not interconnected to a load (6.3). If we substitute the desired behavior $\dot{T}_{v_k,\text{des}}^{v_k,0}$ (6.23) and the desired wrench $W_{v_k,\text{des}}^\ell$ (6.38) in expression (6.39), then we find that the wrench that should be exerted by the wheels on the AGV satisfies

$$(W_{w,\text{des}}^{v_k})^\text{T} = M_{v_k} \dot{T}_{v_k,\text{des}}^{v_k,0} + \hat{\omega}_{v_k} M_{v_k} \Gamma_{v_k} \hat{T}_{v_k}^{v_k,0} + G_{\ell,k} P(QP)^+ \left(M_\ell K_\ell (T_{\ell,\text{set}}^{\ell,0} - \hat{T}_\ell^{\ell,0}) + \hat{\omega}_\ell M_\ell \Gamma_\ell \hat{T}_\ell^{\ell,0} \right) \quad (6.40)$$

This wrench will be distributed among the actuators of the various wheel units by the force distribution module that was described in subsection 6.3.3. The control law (6.40) contains the term $\dot{T}_{v_k, \text{des}}^{v_k, 0}$. From equations (6.20) and (6.23) we see that $\dot{T}_{v_k, \text{des}}^{v_k, 0}$ is related to the setpoints $T_{\ell, \text{set}}^{\ell, 0}$ and $\eta_{k, \text{set}}$, and the estimates $\hat{T}_{\ell}^{\ell, 0}$ and $\hat{\eta}_k$, by

$$\dot{T}_{v_k, \text{des}}^{v_k, 0} = Ad_{H_{\ell}^{v_k}} K_{\ell} (T_{\ell, \text{set}}^{\ell, 0} - \hat{T}_{\ell}^{\ell, 0}) + S_{v_k, k} K_k (\eta_{k, \text{set}} - \hat{\eta}_k) - Ad_{H_{\ell}^{v_k}} ad_{S_{\ell, k} \hat{\eta}_k} \hat{T}_{\ell}^{\ell, 0} \quad (6.41)$$

It is remarked that the estimate $\hat{T}_{v_k}^{v_k, 0}$ is related to the estimates $\hat{T}_{\ell}^{\ell, 0}$ and $\hat{\eta}_k$ by

$$\hat{T}_{v_k}^{v_k, 0} = Ad_{H_{\ell}^{v_k}} \hat{T}_{\ell}^{\ell, 0} + S_{v_k, k} \hat{\eta}_k. \quad (6.42)$$

Equations (6.40)-(6.41) constitute the control law for cooperative transportation. To see on which terms it depends, we first note that

$$\begin{aligned} (W_{w, \text{des}}^{v_k})^T &= M_{v_k} \dot{T}_{v_k, \text{des}}^{v_k, 0} + \hat{\omega}_{v_k} M_{v_k} \Gamma_{v_k} Ad_{H_{\ell}^{v_k}} \hat{T}_{v_k}^{\ell, 0} + Ad_{H_{\ell}^{v_k}}^T (W_{v_k, \text{des}}^{\ell})^T \\ &= M_{v_k} \dot{T}_{v_k, \text{des}}^{v_k, 0} + \hat{\omega}_{v_k} M_{v_k} \Gamma_{v_k} Ad_{H_{\ell}^{v_k}} (\hat{T}_{\ell}^{\ell, 0} + S_{\ell, k} \hat{\eta}_k) + Ad_{H_{\ell}^{v_k}}^T G_{\ell, k} \lambda_{\text{des}} \\ &= M_{v_k} Ad_{H_{\ell}^{v_k}} (\dot{T}_{\ell, \text{des}}^{\ell, 0} + S_{\ell, k} \dot{\eta}_{k, \text{des}} - ad_{S_{\ell, k} \hat{\eta}_k} \hat{T}_{\ell}^{\ell, 0}) \\ &\quad + \hat{\omega}_{v_k} M_{v_k} \Gamma_{v_k} Ad_{H_{\ell}^{v_k}} (\hat{T}_{\ell}^{\ell, 0} + S_{\ell, k} \hat{\eta}_k) \\ &\quad + Ad_{H_{\ell}^{v_k}}^T G_{\ell, k} P (G_{\ell} P)^+ (M_{\ell} \dot{T}_{\ell, \text{des}}^{\ell, 0} + \hat{\omega}_{\ell} M_{\ell} \Gamma_{\ell} \hat{T}_{\ell}^{\ell, 0}). \end{aligned} \quad (6.43)$$

By rearranging the terms in the last expression and by substituting the desired behavior (6.20):

$$\begin{aligned} \dot{T}_{\ell, \text{des}}^{\ell, 0} &= K_{\ell} (T_{\ell, \text{set}}^{\ell, 0} - \hat{T}_{\ell}^{\ell, 0}) \\ \dot{\eta}_{k, \text{des}} &= K_k (\eta_{k, \text{set}} - \hat{\eta}_k) \end{aligned}, \quad (6.44)$$

we arrive at

$$\begin{aligned} (W_{w, \text{des}}^{v_k})^T &= \left(M_{v_k} Ad_{H_{\ell}^{v_k}} + G_{v_k, k} P (G_{\ell} P)^+ M_{\ell} \right) K_{\ell} (T_{\ell, \text{set}}^{\ell, 0} - \hat{T}_{\ell}^{\ell, 0}) \\ &\quad + M_{v_k} S_{v_k, k} K_k (\eta_{k, \text{set}} - \hat{\eta}_k) \\ &\quad + \left(\hat{\omega}_{v_k} M_{v_k} \Gamma_{v_k} Ad_{H_{\ell}^{v_k}} + \hat{\omega}_{\ell} G_{v_k, k} P (G_{\ell} P)^+ M_{\ell} \Gamma_{\ell} - M_{v_k} Ad_{H_{\ell}^{v_k}} ad_{S_{\ell, k} \hat{\eta}_k} \right) \hat{T}_{\ell}^{\ell, 0} \\ &\quad + \hat{\omega}_{v_k} M_{v_k} \Gamma_{v_k} S_{v_k, k} \hat{\eta}_k \end{aligned} \quad (6.45)$$

Careful inspection shows that this expression has the same structure as the control law for the single vehicle (6.4), which was given by

$$(W_{w, \text{des}}^v)^T = M_v K_v (T_{v, \text{set}}^{v, 0} - \hat{T}_v^{v, 0}) + M_v \Gamma_v \hat{\omega}_v \hat{T}_v^{v, 0}. \quad (6.46)$$

The first two lines of (6.45) correspond to the first term of the single vehicle controller, although the cooperative control law has an extended state that consists of $T_{\ell}^{\ell, 0}$ and η_k . The last two lines of (6.45) correspond to the last term of the single vehicle controller, which

represent the coriolis effects that stem from the non-inertial coordinates systems that are fixed to the AGV and load. Thus the first two lines of (6.45) correspond to a proportional control action, and the last two lines to a linearizing feedback. Furthermore, we see from (6.45) and (6.45) that the control law for cooperative transportation for AGV k depends on the

- **setpoints** $T_{\ell, \text{set}}^{\ell, 0}$ and $\eta_{k, \text{set}}$, which were assumed to be given;
- **estimates** $\hat{T}_{\ell}^{\ell, 0}$ and $\hat{\eta}_k$, which are computed by the decentralized observer that was presented in section 5.5;
- **relative position** $H_{\ell}^{v_k}$ of the load with respect to the vehicle, which was assumed to be measured directly;
- **constant inertial parameters** M_{v_k} , Γ_{v_k} , M_{ℓ} , Γ_{ℓ} of AGV k and the load, respectively;
- **constant controller gains** K_{ℓ} and K_k ;
- **constant matrices** G_{ℓ} , $G_{v_k, k}$, $S_{\ell, k}$, $S_{v_k, k}$, which represent the **lower pair interconnection** between AGV k and the load;
- **constant matrix** P , which is related to the **metric** $Q = P^T P$ that is used to minimize the interconnection forces λ .

6.4.3 Special case: completely rigid interconnections

Although most terms are constant, the velocity control law for cooperative transportation (6.45) still looks quite difficult. The expression will simplify considerably when considering the special case that the interconnection between AGV k and the load is completely rigid. In that case, all terms with $S_{i, k}$ and η_k drop out of the equation. Furthermore, the rotational velocity ω_{v_k} of AGV k will be identical to the rotational velocity ω_{ℓ} of the load, hence

$$\hat{\omega}_{v_k} = \hat{\omega}_{\ell}. \quad (6.47)$$

Injecting this in the control law (6.45) results in

$$\begin{aligned} (W_{w, \text{des}}^{v_k})^T &= \left(M_{v_k} Ad_{H_{\ell}^{v_k}} + G_{v_k, k} P (G_{\ell} P)^+ M_{\ell} \right) K_{\ell} (T_{\ell, \text{set}}^{\ell, 0} - \hat{T}_{\ell}^{\ell, 0}) \\ &\quad + \hat{\omega}_{\ell} \left(M_{v_k} \Gamma_{v_k} Ad_{H_{\ell}^{v_k}} + G_{v_k, k} P (G_{\ell} P)^+ M_{\ell} \Gamma_{\ell} \right) \hat{T}_{\ell}^{\ell, 0}. \end{aligned} \quad (6.48)$$

This expression is almost identical to the velocity controller for a single AGV (6.4). Since the AGV is rigidly interconnected to the load, we can take the vehicle coordinate system Ψ_{v_k} identical to the load coordinate system Ψ_{ℓ} , i.e.

$$H_{\ell}^{v_k} = I \quad \Leftrightarrow \quad Ad_{H_{\ell}^{v_k}} = I. \quad (6.49)$$

This will not affect the behavior of the controlled system. Moreover, when $\Psi_{v_k} = \Psi_{\ell}$ and the AGV and load are rigidly interconnected, then it is also true that

$$\hat{T}_{v_k}^{v_k, 0} = \hat{T}_{\ell}^{\ell, 0} \quad (6.50)$$

Subsequently, we define

$$\begin{cases} K_{v_k}^* &= K_\ell \\ M_{v_k}^* &= M_{v_k} + G_{v_k,k} P(G_\ell P)^+ M_\ell \\ \Gamma_{v_k}^* &= (M_{v_k}^*)^{-1} (M_{v_k} \Gamma_{v_k} + G_{v_k,k} P(G_\ell P)^+ M_\ell \Gamma_\ell) \end{cases} \quad (6.51)$$

Note that the matrices $K_{v_k}^*$, $M_{v_k}^*$ and $\Gamma_{v_k}^*$ are constant. Hence, they can be computed offline. It is assumed that $M_{v_k}^*$ is indeed invertible. By using equations (6.49)-(6.51) we can cast the control law (6.48) into the convenient form

$$(W_{w,\text{des}}^{v_k})^T = M_{v_k}^* K_{v_k}^* (T_{\ell,\text{set}}^{\ell,0} - \hat{T}_{v_k}^{v_k,0}) + \hat{\omega}_{v_k} M_{v_k}^* \Gamma_{v_k}^* \hat{T}_{v_k}^{v_k,0} \quad (6.52)$$

Thus when the load is fully rigidly interconnected to the AGVs, then the derived local controllers for cooperative operation have the same structure as the controllers that are normally used for individual operation. As a result, changing the parameter settings for K_{v_k} , M_{v_k} , and Γ_{v_k} and providing the AGVs with identical setpoints $T_{\ell,\text{set}}^{\ell,0}$ is all that is required to achieve cooperative behavior on the velocity level. We may use either the local twist estimate $\hat{T}_{v_k|z_k}^{v_k,0}$ or the load's twist estimate $\hat{T}_\ell^{\ell,0}$ in the controller law. The latter requires communication of the local twist estimates $\hat{T}_{v_k|z_k}^{v_k,0}$, whereas the former does not. In Chapter 7 we will investigate experimentally how the behavior of the interconnected system is influenced by the two estimates. Although the velocity controllers for cooperative transportation (6.52) and single operation (6.4) have identical structures, the properties of the parameters are slightly different. In particular, $M_{v_k}^*$ is not symmetrical anymore. Furthermore, $\Gamma_{v_k}^*$ may have one additional nonzero component compared to the original Γ_{v_k} . To show this, we recall from equation (3.48) of subsection 3.4.3 that Γ_{v_k} and Γ_ℓ are given by

$$\Gamma_{v_k} = \begin{pmatrix} 0 & 0 & 0 \\ -x_{v_k,c} & 0 & -1 \\ -y_{v_k,c} & 1 & 0 \end{pmatrix}, \quad \Gamma_\ell = \begin{pmatrix} 0 & 0 & 0 \\ -x_{\ell,c} & 0 & -1 \\ -y_{\ell,c} & 1 & 0 \end{pmatrix}. \quad (6.53)$$

We can use this to rewrite $\Gamma_{v_k}^*$ as

$$\begin{aligned} \Gamma_{v_k}^* &= (M_{v_k}^*)^{-1} (M_{v_k} \Gamma_{v_k} - M_{v_k} \Gamma_\ell + M_{v_k} \Gamma_\ell + G_{v_k,k} P(G_\ell P)^+ M_\ell \Gamma_\ell) \\ &= (M_{v_k}^*)^{-1} (M_{v_k} (\Gamma_{v_k} - \Gamma_\ell) + M_{v_k}^* \Gamma_\ell) = (M_{v_k}^*)^{-1} M_{v_k} (\Gamma_{v_k} - \Gamma_\ell) + \Gamma_\ell \\ &= (M_{v_k}^*)^{-1} M_{v_k} \begin{pmatrix} 0 & 0 & 0 \\ x_\ell - x_{v_k,c} & 0 & 0 \\ y_\ell - y_{v_k,c} & 0 & 0 \end{pmatrix} + \begin{pmatrix} 0 & 0 & 0 \\ -x_{\ell,c} & 0 & -1 \\ -y_{\ell,c} & 1 & 0 \end{pmatrix} = \begin{pmatrix} * & 0 & 0 \\ * & 0 & -1 \\ * & 1 & 0 \end{pmatrix}. \end{aligned} \quad (6.54)$$

Hence, we see that the upper left component of $\Gamma_{v_k}^*$ may be unequal to zero. The control law (6.52) was evaluated on a setup with two rigidly interconnected AGVs. The experimental results will be discussed in Chapter 7.

6.5 Distributed central vehicle controller

The rationale behind the controller for cooperative transportation that was presented in the previous section is to realize the desired behavior while minimizing the interconnection forces

between the load and the AGVs. Another approach to design a controller for the interconnected system is to consider the complete system as a single, overactuated vehicle. Similar to the control design for individual AGV operation that was discussed in section 6.4, the actuator redundancy can be resolved by minimizing the tire forces. In the cooperative transportation experiments that will be discussed in the next chapter, we consider the case that our two test vehicles are completely rigidly interconnected to the load, because in this situation the interaction between the AGVs and the load is the strongest. In the special case that N AGVs are attached to the load by means of fully rigid interconnections, the control law that is designed by minimizing the tire forces and considering the interconnected system as a single vehicle becomes particularly simple. Moreover, we will show that it is closely related to the control law for a single AGV (6.4) and, hence, well suited for a distributed implementation.

Since all AGVs are rigidly interconnected to the load, the desired behavior of the load characterizes the desired behavior of the complete interconnected system. Because the interconnected system behaves as a single rigid body, we can write its equations of motion as

$$\dot{T}_\ell^{\ell,0} + \omega_\ell \Gamma T_\ell^{\ell,0} = M^{-1} \sum_{k=1}^N (W_w^{vk})^\top = M^{-1} W_w^V, \quad (6.55)$$

where W_w^{vk} is the net wrench that is exerted by the wheels of AGV k on the system, and W_w^V is the net wrench that is exerted by the wheels of all N AGVs together on the system. The mass matrix M and the connection coefficients Γ for the total interconnected system read

$$\begin{aligned} M &= \begin{pmatrix} I_t + m_t(x_{t,c}^2 + y_{t,c}^2) & -m_t y_{t,c} & m_t x_{t,c} \\ -m_t y_{t,c} & m_t & 0 \\ m_t x_{t,c} & 0 & m_t \end{pmatrix} = M_\ell + \sum_{k=1}^N M_{v_k} \\ \Gamma &= \begin{pmatrix} 0 & 0 & 0 \\ -x_{t,c} & 0 & -1 \\ -y_{t,c} & 1 & 0 \end{pmatrix} = \begin{pmatrix} 0 & 0 & 0 \\ -\frac{m_t x_{t,c}}{m_t} & 0 & -1 \\ -\frac{m_t y_{t,c}}{m_t} & 1 & 0 \end{pmatrix} \end{aligned} \quad (6.56)$$

The position of the center of gravity $(x_{t,c}, y_{t,c})$ of the total interconnected system is easily computed from the components of M . The input u_{set} for the entire system consists of all inputs $u_{\text{set},k}$ of the individual AGVs $k \in \{1, \dots, N\}$ together. Because the AGVs are rigidly interconnected, we take the vehicle coordinate systems Ψ_{v_k} equal to the load coordinate system Ψ_ℓ , hence

$$T_{v_k}^{v_k,0} = T_\ell^{\ell,0}. \quad (6.57)$$

Furthermore, the C and the \bar{B}_ℓ matrix of the total system are

$$C = \begin{pmatrix} C_1 & & \\ & \ddots & \\ & & C_N \end{pmatrix}, \quad \bar{B}_\ell = \begin{pmatrix} \bar{B}_{\ell,1} \\ \vdots \\ \bar{B}_{\ell,N} \end{pmatrix}, \quad (6.58)$$

where C_k and $B_{\ell,k}$ are the matrices that correspond to AGV k . With the above characterizations of the tot interconnected system, it follows from the control law (6.4) and (6.13) for a

single AGV that the setpoints for the inputs u_{set} of the interconnected system are given by

$$\begin{aligned} u_{\text{set}} &= C^{-1} \bar{B}_\ell (\bar{B}_\ell^T \bar{B}_\ell)^{-1} (W_{w,\text{des}}^V)^T \\ &= C^{-1} \bar{B}_\ell (\bar{B}_\ell^T \bar{B}_\ell)^{-1} \left(MK_\ell (T_{\ell,\text{set}}^{\ell,0} - \hat{T}_\ell^{\ell,0}) + \hat{\omega}_\ell M \Gamma \hat{T}_\ell^{\ell,0} \right). \end{aligned} \quad (6.59)$$

If we write this out, then we see that the setpoints $u_{\text{set},k}$ for the individual AGVs equal

$$u_{\text{set}} = \begin{pmatrix} u_{\text{set},1} \\ \vdots \\ u_{\text{set},N} \end{pmatrix} = \begin{pmatrix} C_1^{-1} \bar{B}_{\ell,1} \\ \vdots \\ C_N^{-1} \bar{B}_{\ell,N} \end{pmatrix} \left(\bar{B}_\ell^T \bar{B}_\ell \right)^{-1} \left(MK_\ell (T_{\ell,\text{set}}^{\ell,0} - \hat{T}_\ell^{\ell,0}) + \hat{\omega}_\ell M \Gamma \hat{T}_\ell^{\ell,0} \right). \quad (6.60)$$

We know that $\bar{B}_\ell^T \bar{B}_\ell$ and its inverse are constant for the OLS vehicles. Let us write the local control law for AGV k as

$$\boxed{(W_{w,\text{des}}^{v_k})^T = M_{v_k}^* K_{v_k}^* (T_{\ell,\text{set}}^{\ell,0} - \hat{T}_{v_k}^{v_k,0}) + \hat{\omega}_{v_k} M_{v_k}^* \Gamma_{v_k}^* \hat{T}_{v_k}^{v_k,0}} \quad (6.61)$$

We select the parameters $K_{v_k}^*$, $M_{v_k}^*$ and $\Gamma_{v_k}^*$ in this control law according to

$$\boxed{\begin{aligned} K_{v_k}^* &= K_\ell \\ M_{v_k}^* &= (\bar{B}_{\ell,k}^T \bar{B}_{\ell,k}) (\bar{B}_\ell^T \bar{B}_\ell)^{-1} M \\ \Gamma_{v_k}^* &= \Gamma \end{aligned}} \quad (6.62)$$

Note that $M_{v_k}^*$ is not necessarily symmetric. If we substitute these parameters in (6.61) then we see that the setpoints $u_{\text{set},k}$ for the individual AGVs are indeed compatible with the centralized control law (6.60):

$$\begin{aligned} u_{\text{set},k} &= C_k^{-1} \bar{B}_{\ell,k} (\bar{B}_{\ell,k}^T \bar{B}_{\ell,k})^{-1} (W_{w,\text{des}}^{v_k})^T \\ &= C_k^{-1} \bar{B}_{\ell,k} (\bar{B}_\ell^T \bar{B}_\ell)^{-1} \left(MK_\ell (T_{\ell,\text{set}}^{\ell,0} - \hat{T}_{v_k}^{v_k,0}) + \hat{\omega}_{v_k} M \Gamma \hat{T}_{v_k}^{v_k,0} \right). \end{aligned} \quad (6.63)$$

Thus when the load is fully rigidly interconnected to the AGVs and the total system is considered as a single vehicle, then a central controller design that minimizes the tire forces can be implemented in a distributed fashion by providing the AGVs with identical setpoints and adjusting the parameter settings of the original, individual AGV controllers.

6.6 Concluding remarks and discussion

In this chapter we presented a decentralized controller for cooperatively transporting a common load by multiple AGVs. The main difference between our study and other works that have been presented in literature is that we do not use force and torque sensors to measure the interaction between the load and the AGVs. Furthermore, in our study the load is attached to the AGVs by means of (semi-)rigid interconnections instead of the compliant mechanisms

that are usually seen in literature. The necessary compliance to limit the interconnection forces is provided by the slip of the wheels.

The decentralized controller that we derived makes the AGVs track an externally provided planar motion setpoint while minimizing the interconnection forces between the load and the vehicles. Our control design is applicable to cooperative transportation by multiple AGVs with arbitrary semi-rigid AGV-load interconnections. It is noteworthy that a particularly elegant solution arises when all interconnections are completely rigid. Then the derived local controllers have the same structure as the controllers that are normally used for individual operation. As a result, changing a few parameter settings and providing the AGVs with identical setpoints is all that is required to achieve cooperative behavior on the velocity level for this case.

For the special case that all AGVs are rigidly attached to the load, we can also consider the complete interconnected system as a single vehicle and design a central controller. We showed that such a controller, which minimizes the tire forces, can be implemented in a distributed way. Again, the corresponding local controllers have the same structure as the controllers that are normally used for individual operation, and we only need to provide the AGVs with identical setpoints and change a few parameter settings to achieve cooperative behavior.

To achieve fully automatic operation, the velocity layer can be extended with an additional position control loop. As we discussed in subsection 2.2.2, the position control loop for a single AGV controller consists of a position observer and a position controller. The position observers integrates the AGV's twist estimate $\hat{T}_{v_k}^{v_k,0}$ and uses measurements from an absolute magnet measurement system to estimate the AGV's position. When the velocity estimates of the velocity observers are accurate, then we can almost directly adopt the position observer module of the single AGV controller for our cooperative transportation applications. If we know the absolute position of the AGV and the relative position of the load with respect to the AGV, then it is straightforward to compute the absolute position of the load. The position controller has to be slightly modified to achieve cooperative behavior. Whereas the single AGV position controller generates a setpoint $T_{v_k, \text{set}}^{v_k,0}$ for the AGV's twist, the position control for the cooperative transportation case will have to generate setpoints $T_{\ell, \text{set}}^{\ell,0}$ and $\eta_{k, \text{set}}$ for the relative motion of the load with respect to the floor, and the relative motion of the AGVs with respect to the load. In addition, the AGVs must receive compatible setpoints for their own paths and the desired path of the load.

Results

7.1 Introduction

In the previous two chapters we discussed the observer and controller design for cooperatively transporting a load by multiple AGVs. This chapter presents the results of several cooperative transportation experiments with the two OLS vehicles, which were introduced in Chapter 2. We decided to focus on the case that the load is fully rigidly attached to the AGVs, because in this situation the interaction between the vehicles and the load is the strongest.

In our earlier publications we presented and analyzed preliminary experiments where the two OLS vehicles were rigidly interconnected but did not transport a load [113] (see Figure 7.1), and we presented experiments where they were rigidly interconnected and transported a medium load of 150 kg [112] (see Figure 7.2). We used the decentralized controller of section 6.4 in those tests, which means that the underlying rationale was to minimize the interconnection forces between the AGVs and the load. We did exchange but not yet combine the local twist estimates of the vehicles to arrive at one global twist estimate. In other words, the vehicles used their individual twist estimates that were based on their own local odometric measurements in the control law.



Figure 7.1: Picture of the experimental setup without load that was used in [113].



Figure 7.2: Picture of the experimental setup with the 150 kg load that was used in [112].

In this chapter we present an extension of the experiments that we presented earlier in [112]. Because the load of 150 kg in our first experiments was relatively small compared to the overall vehicle weight of $2 \times 200 = 400$ kg, in the new experiments we use a load of 300 kg. We expect that a larger load has a more profound influence on the dynamics of the interconnected system. In the first experiments we only considered the decentralized controller that minimizes the interconnection forces in combination with local observers. In this chapter we compare the performance of that controller with the distributed implementation of the control design of section 6.5, which treats the interconnected system as a single vehicle

and aims to minimize the tire forces. Furthermore, we will compare the performance of the distributed centralized observer design that was proposed in section 5.5 with the approach that uses local observers only.

The outline of this chapter is as follows. First we introduce the experimental setup with the two rigidly interconnected OLS vehicles, and describe the adjustments that have been made in the hardware and the software to implement the proposed observer and controller algorithms. Subsequently, we discuss the parameter settings for the cooperative transportation experiments. We present results for the case that the two AGVs are physically interconnected but do not transport a load, and for the case that they transport a load of 300 kg paving stones. The chapter ends with the concluding remarks and discussion.

7.2 Experimental setup

7.2.1 Hardware

The two OLS vehicles that were available for testing have been described in detail in Chapter 2. They are named the OLS 1 and the OLS 2, and were designed to be identical in hardware. As we discussed in Chapter 2, each vehicle has one caster wheel and two actuated wheels. Each actuated wheel has a steering system and a drive system, and is equipped with a steering angle encoder and a drive encoder to measure respectively the steering angle and the travelled distance of that wheel. Furthermore, each vehicle is equipped with a magnet ruler to detect the magnets that are placed in the floor where the experiments are carried out. Both vehicles have their own FrogBox to run the control algorithms.¹ The operating system is Linux. A wireless local area network (WLAN) connection, serial ports, and a controller area network (CAN) interface are available for communication. The mass of a single vehicle is approximately $m_{v_k} = 200$ kg, its moment of inertia equals about $I_{v_k} = 50$ kg·m², and the center of gravity lies in the middle of the vehicle.

Adjustments have been made in the hardware and in the software for achieving cooperative behavior. Pictures of the interconnected system with load are depicted in Figures 7.3 and 7.4, and a schematic representation in Figure 7.5. The two vehicles are rigidly coupled by means of a rectangular aluminum frame (see also Figure 7.2). The frame has a width of 80 cm and a length of 120 cm. A diagonal beam provides additional stiffness for the frame. The frame is attached to each vehicle with two bolts, which makes it relatively easy to separate them if necessary. The vehicles have been oriented with their actuated wheels towards the middle, because the combination is more stable with four wheels on the inside. The load consists of a pallet of 38 concrete paving stones. Although the original intention was to put the entire load on top of the aluminium frame, in reality part of the pallet also rested on the vehicle frames. The mass of a single concrete paving stone is approximately 8.2 kg, hence the mass of the entire load is approximately $m_\ell = 300$ kg. When the set of paving stones is considered to as a homogenous mass with a length of 90 cm and a width of 60 cm, then we find that its moment of inertia equals $I_\ell = \frac{1}{12} \times 300 \times (0.6^2 + 0.9^2) = 29.25$ kg·m². The center of gravity is assumed to lie in the middle of the load. Due to the load's weight and the flexibility of the frame, the caster wheels on the outside of the setup are clear from the ground

¹The FrogBox of the OLS 1 is the fb1103, and the FrogBox of the OLS 2 is named the fb1101.

when the load is present. This is not a problem as the four actuated wheels on the inside of the setup remain in contact with the ground. Each actuated wheel can carry a load of 200 kg. The mass of the total setup is $2 \times 200 + 300 = 700$ kg, which means that the overall weight is close to the maximum capacity of $4 \times 200 = 800$ kg that the four actuated wheels can carry.



Figure 7.3: Interconnected system with load.

Figure 7.4: Close-up of the paving stones.

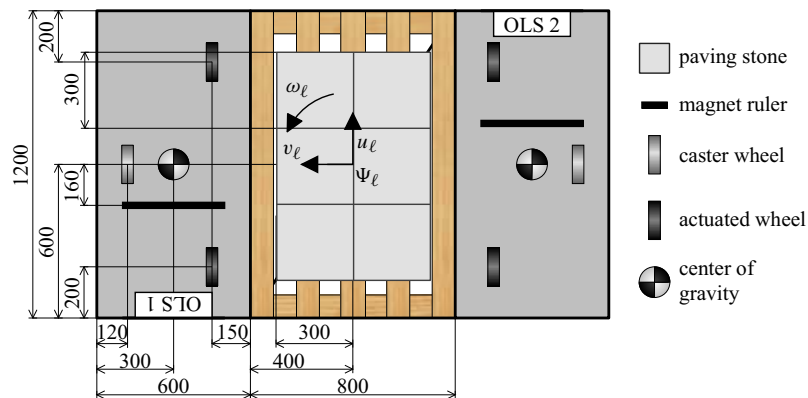


Figure 7.5: Schematic representation of the two interconnected vehicles (dimensions in mm).

7.2.2 Architecture

The architecture that is currently used for industrial AGVs that operate individually has been modified to implement the observer and control algorithms of Chapters 5 and 6. A description of the original architecture can be found in subsection 2.2.2 and section 6.3, and a block scheme of the modified architecture is depicted in Figure 7.6. The adjustments for achieving cooperative transportation were made in the velocity observers and the velocity controllers. Since the AGVs and the load are rigidly interconnected in our experiments, the adjustments

are particularly simple as we saw in the previous chapters. Because the load is rigidly attached to the AGVs, we do not need sensors to measure the position of the load with respect to the AGVs. As we discussed in Chapter 6, all vehicles should receive the same setpoint to achieve cooperative behavior. In addition, when the distributed observer design of Chapter 5 is applied, then each vehicle will also have to broadcast its local twist estimate. A brief investigation showed that the time to transmit a double precision number is shorter and much more predictable for the CAN connection than for the available WLAN connection. Some simple tests with the standard ‘ping’ command that measures the time required to send packages of 64 bytes from one of the vehicles to a desktop PC and back using the available WLAN connection showed that the loopback time ranged from 8 ms to 390 ms. The bit rate of the available CAN connection is 250 kBit/s, and the length of a single message containing one double precision number is approximately 100 bit. This means that it requires $100/250 = 0.4$ ms to send a CAN message. Comparison of the time stamps of the moments that the CAN messages are sent and received by various hosts showed that the time stamp resolution was better than 1 ms. Therefore, CAN is used for real-time communication. The sequence of setpoints are stored on a Windows 2000 laptop and broadcasted by the CANalyzer that is installed on the laptop. This allows us to repeat an experiment with the identical setpoints for various controller settings.

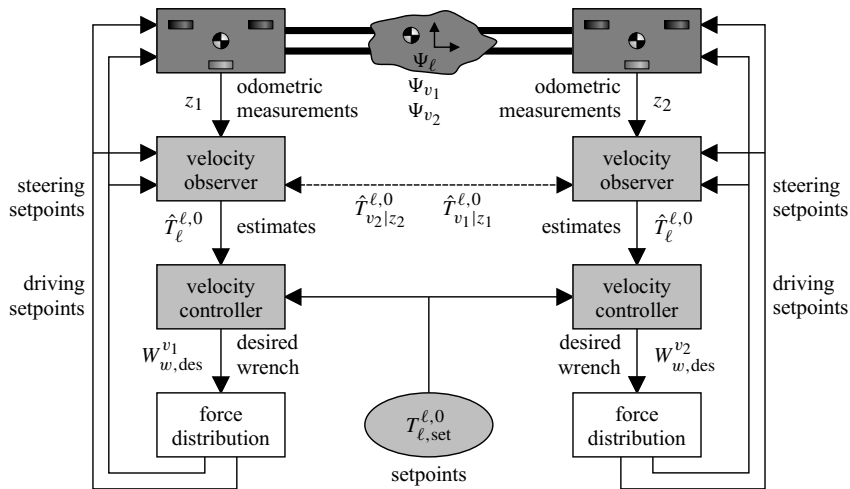


Figure 7.6: Block scheme of the cooperative transportation controller. Adjustments for achieving cooperative transportation were performed in the velocity observers and the velocity controllers.

We aim to synchronize the discrete time control cycles of the two AGVs as much as possible, because this results in the most deterministic behavior. In particular, we would like to synchronize the moments that the sensors are read and also the moments that the outputs are released. The execution of the control cycle is sketched in Figure 7.7. In the CANopen protocol that we use, a special message referred to as ‘sync’ is reserved for synchronization purposes. So it was natural to base the synchronization of the control cycles on this message

type. The sync message is broadcasted by the laptop's CANalyzer every 100 ms, which results in a sample rate of 10 Hz. As soon as AGV k receives a sync message, it starts reading its odometric sensor data z_k . After the drive encoder and steering encoder data have been retrieved, a delayed timer event that is linked to the time instance that the sync was received instructs the vehicle's local velocity observer to compute the twist estimate $\hat{T}_{v_k|z_k}^{\ell,0}$ of that AGV with respect to the floor. This local twist estimate is subsequently broadcasted on the CAN bus to the other vehicle and the laptop. Because each CAN message contains a single double precision number, three CAN messages per vehicle are needed to share the local twist estimates with the other vehicles. Sixty milliseconds after the generation of the sync message, the laptop broadcasts the setpoints on the CAN bus. Besides the setpoints for the twist, it also contains information about the position of the steering pole, a possible feed forward signal (not used in our experiments), and information to lift or activate the mechanical brakes. In total, the setpoint consists of six CAN messages. As soon as the setpoints are received, the local vehicle controller compute the desired wrench $W_{w,des}^{v_k}$ that should be exerted by the wheels on the AGV to realize the desired behavior. The control law uses either the local twist estimate $\hat{T}_{v_k|z_k}^{\ell,0}$ or a weighted version of $\hat{T}_{v_1|z_1}^{\ell,0}$ and $\hat{T}_{v_2|z_2}^{\ell,0}$, depending on the observer settings. Finally, the force distribution module of the AGV distributes the desired wrench $W_{w,des}^{v_k}$ among the vehicle's wheels by computing and releasing the setpoints for the steering and driving setpoints.

Although the absolute position measurements of the magnet rulers are not used in closed-loop in our experiments, the AGVs's position observers were operational during our experiments. They estimate the current position of the AGVs by integrating the twist estimates and performing position corrections based on the magnet measurements. Currently, the position observer of AGV k integrates that AGV's local twist estimates $\hat{T}_{v_k|z_k}^{\ell,0}$ and uses the local magnet measurements to obtain the position estimate.

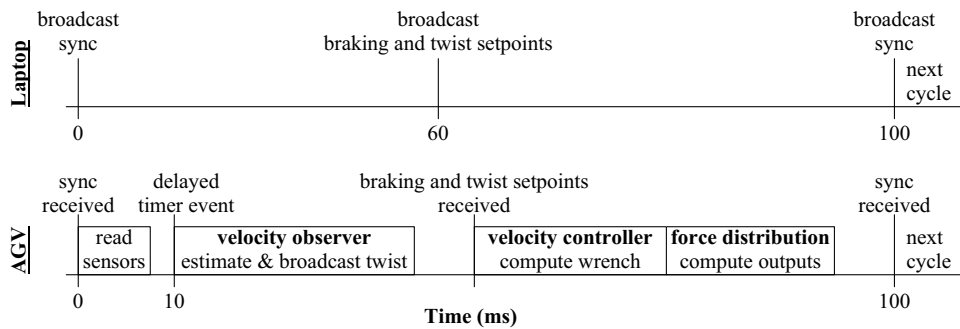


Figure 7.7: Implementation and synchronization of the control cycles.

7.3 Parameter settings

In this section we summarize the parameter settings that have been used in the cooperative transportation experiments. The dimensions of the setup are constant and illustrated in Figure 7.5. From Figure 7.6 we see that the load coordinate's system Ψ_ℓ and the vehicles' coordinate systems Ψ_{v_k} were chosen to coincide: $\Psi_\ell = \Psi_{v_1} = \Psi_{v_2}$. This is allowed as both vehicles are rigidly attached to the load. First we discuss the parameters that are related to the wheels. Subsequently, we specify the desired behavior. Finally, we summarize the parameter settings for the two observer and the two control algorithms that have been used in the experiments. The controllers have different settings for the situation without load and the situation with load.

7.3.1 Wheel parameters

The values for the wheel parameters that were used in the experiments are summarized in Table 7.1. They are based on the situation that there is no load on the vehicles. The steering encoder offsets $\delta_{w_i}^{\text{offset}}$ and wheel diameters $2r_{w_i}$ were determined in Chapter 4, see Table 4.3. The longitudinal stiffness $C_{\text{long}}^{w_i}$ and the lateral cornering stiffness $C_{\text{lat}}^{w_i}$ were not determined exactly, but rather based on experience. Furthermore, there is a Coulomb friction model for each wheel, and the corresponding friction force is compensated. The values were determined by setting the controller gain to zero and fixing the wheels in a certain position. Then the vehicle should retain a constant speed when it is pushed and the friction forces are set correctly. By pushing the vehicle during straight ahead motions as well as crab wise motions it is possible to heuristically tune the friction compensation per wheel. For the OLS 1 the friction forces turned out to be different for forwards and backwards motion.

It is reasonable to assume that the positions $(x_{w_i}^\ell, y_{w_i}^\ell)$ and the steering encoder offsets $\delta_{w_i}^{\text{offset}}$ of the wheels are identical for the experiments with and without load. For the other parameters this is less obvious. In Chapter 4 we saw that the effective wheel diameters $2r_{w_i}$ of the OLS vehicles will increase for increasing loads. It is also likely that the friction forces and the tire stiffnesses become higher. Because it is difficult to quantify the parameter values for the situation with load, the settings for the situation without load have been adopted for the experiments.

AGV	Wheel	$x_{w_i}^\ell$ (m)	$y_{w_i}^\ell$ (m)	$\delta_{w_i}^{\text{offset}}$ (mrad)	$2r_{w_i}$ (mm)	$C_{\text{long}}^{w_i}$ (kN)	$C_{\text{lat}}^{w_i}$ (kN/rad)	F_{fw}^{fric} (N)	F_{bw}^{fric} (N)
OLS 1	Front ($i=1$)	-0.40	0.55	14.22	151.67	100	100	21	-18
OLS 1	Rear ($i=2$)	0.40	0.55	8.44	151.99	100	100	24	-21
OLS 2	Front ($i=1$)	0.40	-0.55	21.64	151.22	100	100	25	-25
OLS 2	Rear ($i=2$)	-0.40	-0.55	-18.60	153.24	100	100	25	-25

Table 7.1: Wheel parameters for the cooperative transportation experiments: $(x_{w_i}^\ell, y_{w_i}^\ell)$ is the position of wheels w_i as expressed in Ψ_ℓ , $\delta_{w_i}^{\text{offset}}$ is the steering encoder offset, $2r_{w_i}$ the effective wheel diameter, $C_{\text{long}}^{w_i}$ the longitudinal stiffness, $C_{\text{lat}}^{w_i}$ the lateral cornering stiffness, F_{fw}^{fric} the forwards friction compensation, and F_{bw}^{fric} the backwards friction compensation for wheel w_i .

7.3.2 Desired behavior

The desired behavior of the controlled system is specified in terms of the twist $T_\ell^{\ell,0}$ of the setup with respect to the floor as expressed in the coordinate system Ψ_ℓ that is fixed to the middle of the experimental setup as illustrated in Figure 7.5. The desired behavior of the controlled system is that the rotational velocity ω_ℓ , the longitudinal velocity u_ℓ , and the lateral velocity v_ℓ of the coordinate system Ψ_ℓ respond as decoupled, first order systems to their corresponding setpoints. We choose identical time constants τ for the three decoupled systems. Hence, the desired time derivatives of the components of the load's twist $T_\ell^{\ell,0}$ with respect to the floor are given by

$$\dot{T}_{\ell,\text{des}}^{\ell,0} = \begin{pmatrix} \dot{\omega}_{\ell,\text{des}} \\ \dot{u}_{\ell,\text{des}} \\ \dot{v}_{\ell,\text{des}} \end{pmatrix} = \frac{1}{\tau} \begin{pmatrix} \omega_{\ell,\text{set}} - \omega_\ell \\ u_{\ell,\text{set}} - u_\ell \\ v_{\ell,\text{set}} - v_\ell \end{pmatrix} = \frac{1}{\tau} (T_{\ell,\text{set}}^{\ell,0} - T_\ell^{\ell,0}). \quad (7.1)$$

For all experiments we took a time constant of $\tau = 0.4$ s for the desired behavior, which is identical to the setting that is used for individual operation of these OLS vehicles.

7.3.3 Observer

The goal of the observer is to compute an estimate $\hat{T}_\ell^{\ell,0}$ for the twist of the setup with respect to the floor. In our experiments we consider two observer algorithms:

1. The first observer algorithm treats the two AGVs and the load as a single vehicle, and computes a global twist estimate based on the odometric measurements of all the vehicles together. From equations (5.103) and (5.107) of section 5.5 we see that the estimated twist $\hat{T}_{v_k}^{\ell,0}$ for AGV k with respect to the floor for that case can be written as

$$\hat{T}_{v_k}^{\ell,0} = E_1 \hat{T}_{v_1|z_1}^{\ell,0} + E_2 \hat{T}_{v_2|z_2}^{\ell,0}, \quad (7.2)$$

where

$$E_k = \left(B_{\ell,1}^T \Sigma_1^{-1} B_{\ell,1} + B_{\ell,2}^T \Sigma_2^{-1} B_{\ell,2} \right)^{-1} B_{\ell,k}^T \Sigma_k^{-1} B_{\ell,k}. \quad (7.3)$$

Here $\hat{T}_{v_k|z_k}^{\ell,0}$ is AGV k 's local twist estimate that is based on the own odometric measurements of that AGV only, Σ_k is a weighting matrix, and $B_{\ell,k}$ is the matrix that models the relation between the AGV's twists and the measurements. The latter depends on the steering angles of the wheels, and is given by equation (3.70). Since $\Psi_\ell = \Psi_{v_1} = \Psi_{v_2}$, we see that $\hat{T}_\ell^{\ell,0} = \hat{T}_{v_1}^{\ell,0} = \hat{T}_{v_2}^{\ell,0}$ for this observer strategy. For the distributed implementation of this algorithm, generally each AGV has to share its local twist estimate $\hat{T}_{v_k|z_k}^{\ell,0}$ and information matrix $B_{\ell,k}^T \Sigma_k^{-1} B_{\ell,k}$ with the other AGVs. In our experiments we set all weighting matrices equal to $\Sigma_k = \sigma^2 I$, as this is the setting that is commonly used for individual operation. We showed in subsection 5.5.3 that the information matrices, and consequently also E_1 and E_2 , remain constant during operation for this particular choice of Σ_k . Substituting the dimensions of Figure 7.5

into equations (3.70) and (7.3) yields

$$E_1 = \begin{pmatrix} 0.500 & -0.595 & 0 \\ -0.275 & 0.500 & 0 \\ 0 & 0 & 0.500 \end{pmatrix}, \quad E_2 = \begin{pmatrix} 0.500 & 0.595 & 0 \\ 0.275 & 0.500 & 0 \\ 0 & 0 & 0.500 \end{pmatrix}. \quad (7.4)$$

Note that $E_1 + E_2 = I$.

2. The second observer algorithm that we investigate in our experiments simply uses the AGV's local twist estimates $\hat{T}_{v_k|z_k}^{\ell,0}$. For this situation we have that E_i is equal to the identity for $i = k$, and equal to zero otherwise:

$$E_{i=k} = \begin{pmatrix} 1 & 0 & 0 \\ 0 & 1 & 0 \\ 0 & 0 & 1 \end{pmatrix}, \quad E_{i \neq k} = \begin{pmatrix} 0 & 0 & 0 \\ 0 & 0 & 0 \\ 0 & 0 & 0 \end{pmatrix}. \quad (7.5)$$

7.3.4 Controller

We consider two control strategies in our experiments. The structure of the control law is identical for both strategies and satisfies

$$(W_{w,\text{des}}^{v_k})^T = M_{v_k}^* K_{v_k}^* (T_{\ell,\text{set}}^{\ell,0} - \hat{T}_{v_k}^{v_k,0}) + \hat{\omega}_{v_k} M_{v_k}^* \Gamma_{v_k}^* \hat{T}_{v_k}^{v_k,0}. \quad (7.6)$$

Here $W_{w,\text{des}}^{v_k}$ is the wrench that should be exerted by the wheels on AGV k to realize the desired behavior (7.1), $T_{\ell,\text{set}}^{\ell,0}$ is the setpoint for the twist of the system with respect to the floor, $\hat{T}_{v_k}^{v_k,0} = \hat{T}_{v_k}^{\ell,0}$ is the estimated twist of AGV k with respect to the floor (see the previous paragraph), and $\hat{\omega}_{v_k}$ is its first component. The matrices $K_{v_k}^*$, $M_{v_k}^*$, and $\Gamma_{v_k}^*$ constitute the control settings. Because all AGV-load interconnections are completely rigid, these three matrices remain constant during our experiments. In particular, $K_{v_k}^* = I/\tau$ as we choose a single time constant τ for the desired behavior. The matrices $M_{v_k}^*$ and $\Gamma_{v_k}^*$ depend on the particular control strategy that is used and on the inertial properties of vehicles and the load that is transported. From subsection 7.2.1 we recall that the mass of a single AGV equals $m_{v_k} = 200$ kg, its moment of inertia equals $I_{v_k} = 50$ kg·m², and the center of gravity is in the middle of the vehicle. Furthermore, the mass of the load is $m_\ell = 300$ kg, its moment of inertia equals $I_\ell = 29.25$ kg·m², and its center of gravity coincides with the origin of Ψ_ℓ . The parameter settings $M_{v_k}^*$ and $\Gamma_{v_k}^*$ for the two control strategies *without load* and *with load* are described below:

1. The first strategy treats the setup of the two interconnected vehicles and the load as a single vehicle and aims to *minimize the tire forces*. The distributed implementation of this centralized control design was discussed in section 6.5. By setting $m_\ell = 0$ kg and $I_\ell = 0$ kg·m² and plugging the inertial properties of the vehicles into equations (6.56) and (6.62), we find that the parameters $M_{v_k}^*$ for the situation *without load* read

$$M_{v_1}^* = \begin{pmatrix} 148 & -110 & 0 \\ -176 & 200 & 0 \\ 0 & 0 & 200 \end{pmatrix}, \quad M_{v_2}^* = \begin{pmatrix} 148 & 110 & 0 \\ 176 & 200 & 0 \\ 0 & 0 & 200 \end{pmatrix}. \quad (7.7)$$

Analogously, for the situation *with load* we have

$$M_{v_1}^* = \begin{pmatrix} 163 & -192 & 0 \\ -193 & 350 & 0 \\ 0 & 0 & 350 \end{pmatrix}, \quad M_{v_2}^* = \begin{pmatrix} 163 & 192 & 0 \\ 193 & 350 & 0 \\ 0 & 0 & 350 \end{pmatrix}. \quad (7.8)$$

For this control strategy, the matrix $\Gamma_{v_k}^*$ is always equal to

$$\Gamma_{v_1}^* = \Gamma_{v_2}^* = \begin{pmatrix} 0 & 0 & 0 \\ 0 & 0 & -1 \\ 0 & 1 & 0 \end{pmatrix}. \quad (7.9)$$

for our experiments.

2. The second strategy is to *minimize the interconnection forces* between the AGVs and the load. This strategy was discussed in section 6.4 for a general setup with semi-rigid interconnections. Subsection 6.4.3 dealt with the special case that the interconnections were completely rigid. The computation of the parameters for this control strategy require a model for the relation between the local interconnection forces λ_k and the wrench $W_{v_k}^\ell$ that is exerted by AGV k on the load, see equations (6.28) and (6.33) of subsection 6.4.2. To this end we take

$$W_{v_1}^\ell = \lambda_1^T A_{\ell,1} = \lambda_1^T \begin{pmatrix} -0.4 & 1 & 0 \\ 0.4 & 0 & 1 \\ -0.4 & 1 & 0 \\ -0.4 & 0 & 1 \end{pmatrix}, \quad W_{v_2}^\ell = \lambda_2^T A_{\ell,2} = \lambda_2^T \begin{pmatrix} 0.4 & 1 & 0 \\ 0.4 & 0 & 1 \\ 0.4 & 1 & 0 \\ -0.4 & 0 & 1 \end{pmatrix}. \quad (7.10)$$

This corresponds to pure longitudinal and lateral forces in the bolts that connect the rectangular aluminum frame to the AGVs. If all interconnection forces are weighted equally, then the corresponding parameter settings for the situation *without load* are

$$M_{v_1}^* = \begin{pmatrix} 148 & -140 & 0 \\ -140 & 200 & 0 \\ 0 & 0 & 200 \end{pmatrix}, \quad M_{v_2}^* = \begin{pmatrix} 148 & 140 & 0 \\ 140 & 200 & 0 \\ 0 & 0 & 200 \end{pmatrix}, \quad (7.11)$$

$$\Gamma_{v_1}^* = \begin{pmatrix} 0 & 0 & 0 \\ 0 & 0 & -1 \\ -0.7 & 1 & 0 \end{pmatrix}, \quad \Gamma_{v_2}^* = \begin{pmatrix} 0 & 0 & 0 \\ 0 & 0 & -1 \\ 0.7 & 1 & 0 \end{pmatrix}. \quad (7.12)$$

This corresponds to the settings for a single vehicle controller with its coordinate shifted to the position that is indicated in Figure 7.5. The parameters for the situation *with load* are

$$M_{v_1}^* = \begin{pmatrix} 163 & -200 & 0 \\ -158 & 350 & 0 \\ 0 & 0 & 350 \end{pmatrix}, \quad M_{v_2}^* = \begin{pmatrix} 163 & 200 & 0 \\ 158 & 350 & 0 \\ 0 & 0 & 350 \end{pmatrix}, \quad (7.13)$$

$$\Gamma_{v_1}^* = \begin{pmatrix} 0 & 0 & 0 \\ 0 & 0 & -1 \\ -0.4 & 1 & 0 \end{pmatrix}, \quad \Gamma_{v_2}^* = \begin{pmatrix} 0 & 0 & 0 \\ 0 & 0 & -1 \\ 0.4 & 1 & 0 \end{pmatrix}. \quad (7.14)$$

Since part of the pallet rests on the vehicles themselves, it is noted that the above model (7.10) for the interconnection force is not very accurate. Although the interconnection force will therefore not be minimized, the settings above do theoretically result in the desired behavior (7.1).

7.4 Experimental results

The experiments were carried out in the hall of FROG Navigation Systems (Utrecht, The Netherlands) on March 16 and 17, 2005. Goal of the experiments was to investigate the performance of the two observer and the two controller algorithms that were introduced in Chapters 5 and 6. Observer algorithm 1 treats the setup as a single vehicle and computes a global twist estimate, and observer algorithm 2 uses only local measurements to determine a local twist estimate. Furthermore, control algorithm 1 regards the setup as a single vehicle and aims to minimize the tire forces, whereas control algorithm 2 aims to minimize the interconnection forces between the AGVs and the load. Thus there are four observer-controller combinations. For each combination, two test runs without a load and two test runs with a load were performed with identical setpoints. This resulted in the following sixteen experiments:

- global twist estimate, distributed central controller (2× no load, 2× with load);
- global twist estimate, interconnection force controller(2× no load, 2× with load);
- local twist estimates, distributed central controller (2× no load, 2× with load);
- local twist estimates, interconnection force controller (2× no load, 2× with load).

The parameter settings were discussed in the previous section. Before the start of each experiment, the vehicles were manoeuvred manually to the initial position on the floor that was designated as $(x, y, \varphi) = (0, 0, 0)$, and the position observers were initialized accordingly. Synchronization of the various log files was achieved by defining the time stamp of the sync pulse just before the first lift braking setpoint as $t = 0$.

7.4.1 Setpoints

The laptop broadcasted the same twist and braking setpoints during all experiments, which allows us to compare the results. The twist setpoints, the desired twists and their differences are displayed in Figure 7.8. They are identical to the setpoints that we used in [112], with the exception of a minor change around $t = 67$ s (the position of the steering pole position now changes instantaneously instead of smoothly at the end of the pirouette-like motion). The desired twists differ from the twist setpoints, because the desired behavior is to respond to the twist setpoints as a first order system (7.1) and not to follow them as close as possible.

The twist setpoints were designed such that the vehicles approximately followed the trajectory that is sketched in Figure 7.9. First, they drive forward for about nine meters. After a left-hand turn, a straight of about five meters and a second left hand turn, the vehicles start

performing a crab wise motion, where they move sideways to the left and subsequently sideways to the right while keeping their original orientation. Then they come to a stop, and subsequently perform a counter-clockwise pirouette. Next, there is a section that combines crab wise and rotational movements. Finally, the vehicles move backwards and crab slightly to the left to return approximately to the positions where they have started from.

Because the controllers in our experiments operate at the velocity level, the vehicles' real positions will soon deviate from the positions that are found by integrating the twist setpoints and the desired twists. Therefore, the twist setpoint was designed experimentally by modifying the curvatures of the first two left hand turns, the duration of the pirouette, and the length of the reverse section, until the vehicles returned to their initial positions. The integrated versions of the twist setpoints and desired twists of Figure 7.8 are displayed in Figure 7.10. They were computed by the algorithm that was discussed in subsection 3.3.5, which assumes that the position of the steering pole remains constant during the sample interval. They clearly deviate from the desired trajectory sketched in Figure 7.9.

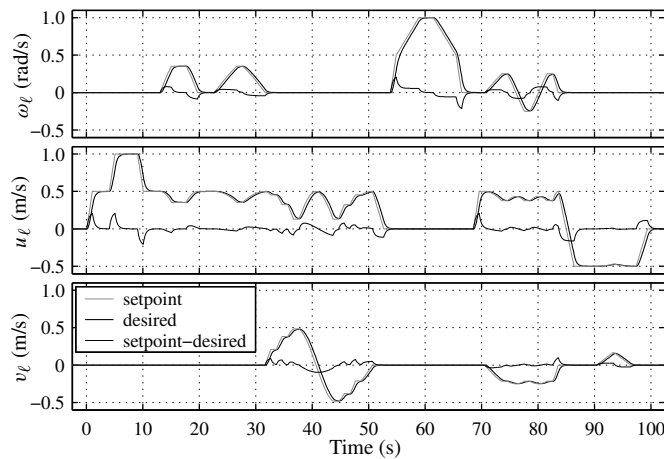


Figure 7.8: Twist setpoints and desired twists.

7.4.2 Realized trajectories

The realized trajectories of the vehicles as estimated by the AGVs' local position observers are displayed in Figure 7.11 for the tests without load and in Figure 7.12 for the tests with the 300 kg load. It is difficult for the magnet ruler to detect magnets during the crab wise motion, which results in the jumps in the estimated position at the end of the crab section. From the figures we see that the trajectories for the experiments without load clearly differ from the trajectories of the experiments with load. This is mainly due to a different behavior during cornering, i.e. the change in orientation during a corner is smaller for the setup with load than for the setup without load. Except for the difference in the trajectories between the tests without and with load, the trajectories reproduce very well and are almost independent of

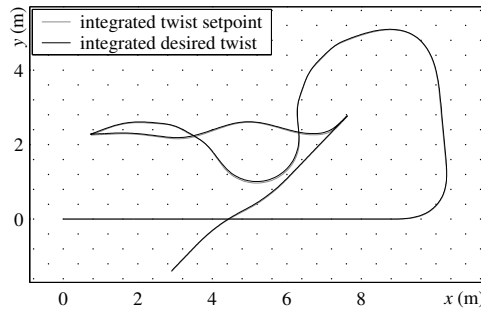
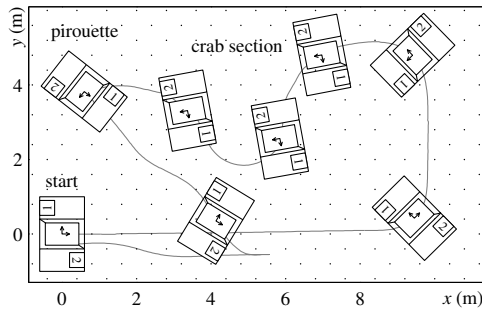


Figure 7.9: Sketch of the desired trajectory Figure 7.10: Integrated twist setpoint and integrated desired twist. (the black dots indicate magnets in the floor).

the type of observer (global versus local estimates) and the type of controller (central design versus minimization of the interconnection forces) that is used.

The fact that the vehicles were maneuvered manually to their initial positions at the start of each experiment accounts for some of the variations within the 'without load' and the 'with load' cases, and is similar to what we have seen in our earlier experiments [112]. Again we see that the position estimate of the OLS 1 is consistently 5 cm to the left and 1 cm to the front with respect to the position estimate of the OLS 2, which is most easily seen at the end of the experiments. The most likely explanation is that this offset reflects the inaccuracies of the positions of the magnet rulers with respect to the vehicles and each other.

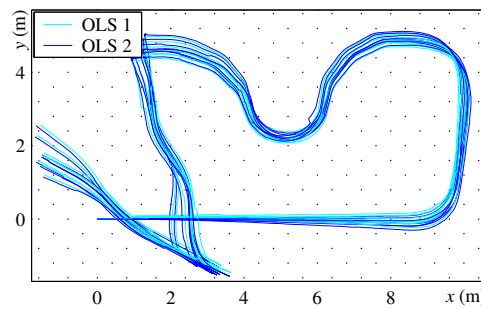
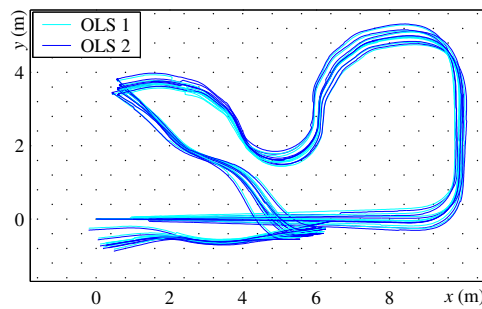


Figure 7.11: Realized trajectories for the eight experiments without load as estimated by the AGVs' local position observers.

Figure 7.12: Realized trajectories for the eight experiments with load as estimated by the AGVs' local position observers.

7.4.3 Integrated twist estimates

Comparing the integrated twist estimates to the data from the AGVs' position observers provides information on the accuracy of the twist estimates and the calibration of the odometry. Three twist estimates are available for the experiments with the centralized observer algo-

rithm, viz. one local twist estimate for each of the two AGVs and one global twist estimate that is derived from the two local estimates. Figure 7.13 shows the three estimated twists and the data from the AGV's position observers for an experiment without load, and Figure 7.14 displays the same variables for an experiment with load. Both experiments used the controller strategy that aims to minimize the interconnection forces between the AGVs and the load. The integrated twist estimates and the data from the position observers match quite well for these two experiments. Sometimes the integrated local twist estimate of the OLS 1 is closer to the real position, and sometimes this is true for the local twist estimate of the OLS 2. There is no apparent difference in the accuracy of the integrated twists between the experiment without load and the experiment with load. This means that we have introduced only a small error by adopting the single vehicle odometric parameters for the situation with the 300 kg load. Interestingly, there is no direct evidence that the global twist estimate is much more accurate than the local twist estimates. The other control strategy, which aims to minimize the tire forces, yields very similar results for the integrated local and global twist estimates. For example, the integrated local twist of the OLS 2 will always have the largest y-coordinate at the end of the crab section just before the pirouette.

For the experiments where the local observers' twist estimates are used in the control law, the global twist estimate is not available. The behavior of the integrated local twist estimates was independent of observer strategy that was used in the control law. Just like for the experiments with the central observer strategy, the integrated local twist of the OLS 2 always had the largest y-coordinate at the end of the crab section. Thus we conclude that the performance of the integrated (local) twist estimates is relatively independent of the observer and control strategy that is being used.

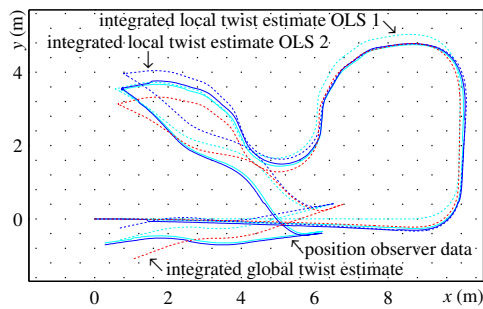


Figure 7.13: Position observer data and integrated twist estimates for the global observer and interconnection controller without load.

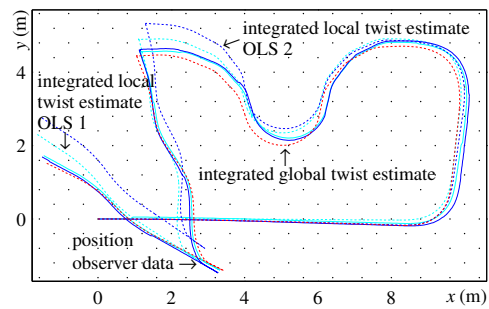


Figure 7.14: Position observer data and integrated twist estimates for the global observer and interconnection controller with load.

7.4.4 Twist tracking errors

The performance of the two observer and the two controller algorithms is studied by examining the twist tracking errors $T_{\ell,des}^{\ell,0} - \hat{T}_{\ell}^{\ell,0}$. Note that we took the desired twist $T_{\ell,des}^{\ell,0}$, because our aim was that the AGV responds to setpoints as a first order system and not to minimize

the quantity $T_{\ell,\text{set}}^{\ell,0} - T_{\ell}^{\ell,0}$. For the twist estimate $\hat{T}_{\ell}^{\ell,0}$ we took the global twist estimate for the experiments with the centralized observer design, and the local twist estimates for the experiments with the local observers. Thus for the first observer algorithm we have a single twist tracking error, and for the second observer strategy we have two twist tracking errors. In the previous subsections we showed that the realized trajectories and the integrated versions of the twist estimates reproduced very well when an experiment was repeated with identical observer and controller settings. This is also true for the twist tracking error(s). Moreover, for an experiment with an identical load, identical observer settings, but a different control strategy, the errors were also very similar. Therefore, we restrict ourselves to the study of the tracking errors for the control strategy that aims to minimize the interconnection forces.

The differences between the desired twists and the twist estimates for the central observer and the local observer strategies are depicted in Figure 7.15 for one experiment without load and one experiment with load. Although there are two tracking errors (one for each AGV) when local controllers are used, at each time instant we plotted only the one with the largest absolute error to limit the number of signals in the plots. The spike that was present at 70 s in our earlier experiments [112] was no longer present because we corrected a minor error in the setpoint as we discussed in subsection 7.4.1.

We see that the tracking errors for the individual twist components for the experiments with load are roughly a factor two larger than for the experiments without load. Although the errors for the local observer approach are somewhat noisier than for the centralized observer approach, the figure shows that they are relatively independent of the chosen observer algorithm. This is confirmed by the cumulative relative frequency polygons of the twist tracking errors that are displayed in Figure 7.16. Noticeably, Figure 7.15 shows that the tracking errors do not substantially diminish during the sections where the interconnected system travels at a constant speed. Therefore, we conclude that the inertial properties of the load were determined quite well, and that the error is largely due to another physical phenomenon. One explanation is that the (Coulomb) friction in the wheels and the drive system has increased for the experiments with load due to the increased weight. For a straight ahead motion the controller gain for each AGV is $\frac{m}{2 \times \tau} = \frac{200}{2 \times 0.4} = 250 \text{ N} \cdot (\text{m/s})^{-1}$ per wheel for the cases without load, and $\frac{m}{2 \times \tau} = \frac{350}{2 \times 0.4} = 438 \text{ N} \cdot (\text{m/s})^{-1}$ per wheel for the cases with load. The tracking errors in the longitudinal velocity u_{ℓ} during straight ahead motion are approximately 0.02 m/s for the cases without load, and 0.05 m/s for the cases with load. This would correspond to unmodeled friction forces of respectively $250 \times 0.02 = 5 \text{ N}$ and $438 \times 0.05 = 22 \text{ N}$ per wheel for the ‘without load’ and the ‘with load’ situations. Because the Coulomb friction forces for the individual wheels ranged from 18 to 25 N, see Table 7.1, these values seem realistic.

Another reason for additional forces could be that the wheels are counteracting each others actions. The longitudinal tire force component that is related to the lateral wheel slip equals approximately $C_{\text{lat}}^{w_i} \alpha_{w_i}^2$. Therefore, we find that a force of 5 N corresponds to a slip angle α_{w_i} of approximately $\sqrt{F_{w_i}^{\text{fric}} / C_{\text{lat}}^{w_i}} = \sqrt{\frac{5}{100,000}} \times \frac{180}{\pi} = 0.4 \text{ deg}$. However, during the calibration experiments we encountered errors of the same magnitude as for the tests with the interconnected setup without load. We know that the wheels did not counteract each other’s lateral control actions in calibration experiments, as an individual OLS vehicle has only two actuated wheels. Because the magnitude of the longitudinal velocity errors for the experiments with the interconnected system matches that of the calibration tests with the individual

vehicles, this suggests that the additional wheel forces do not stem from counter steering wheels.

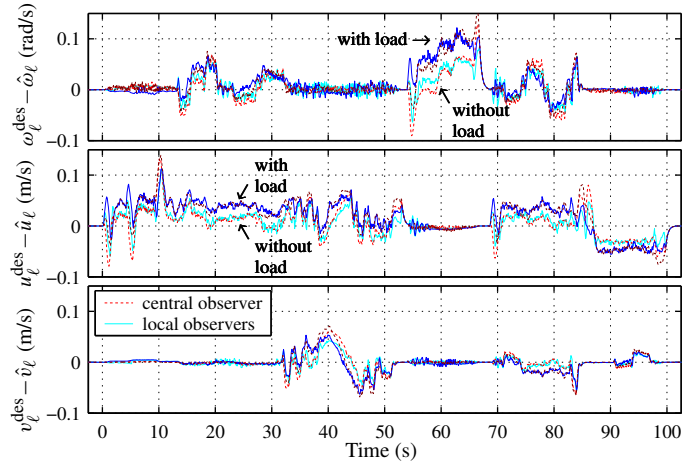


Figure 7.15: Twist tracking errors for the controller that aims to minimize the interconnection forces.

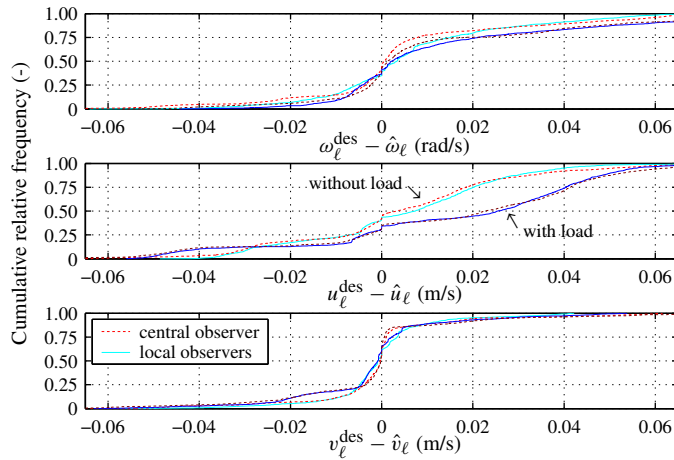


Figure 7.16: Cumulative relative frequency polygons of the twist tracking errors for the controller that aims to minimize the interconnection forces.

7.5 Concluding remarks and discussion

In this chapter we presented experimental results for transporting a load of 300 kg paving stones by two AGVs using distributed observer and controller implementations. We tested

two observer algorithms in combination with two controller algorithms, and compared the results with the situation that the AGVs were rigidly interconnected but did not transport a load.

The realized trajectories were very reproducible and relatively independent of the types of observers and controllers that were used. There was a clear difference between the trajectories of the experiments where the load was present and where it was not. We believe that this difference is caused by the increased friction forces in the wheels under influence of the heavy load. We also studied the integrated versions of the local and global twist estimates. They corresponded well to the estimates of the AGVs' local position observers, which were based on integration of the local twist estimates in combination with updates from the magnet ruler that detects the magnets in the floor. There was no substantial difference between the approach where each vehicle uses only local odometric data to estimate its twist with respect to the floor, and the approach where the local estimates were exchanged to arrive at one global estimate that exploits the odometric measurements of all the vehicles.

The tracking errors for the test with load were roughly a factor two larger than for the experiments without load. Because the errors are also present during constant velocity maneuvers and when the vehicles are physically separated, we believe that they are caused by inaccurate modeling of the friction phenomena. The most logical step to improve the performance with load is therefore to increase the coefficients for the Coulomb friction compensation. The twist tracking errors were a little bit noisier for the local observer strategy than for the centralized observer strategy, but the order of magnitude was comparable. Although the performance of the setup with load can be improved by optimizing the controller settings, it still was within acceptable limits.

The aim of the second control strategy was to minimize the interconnection forces between the AGVs and the load. A shortcoming of this study is that we have not measured these forces, which means that we do not know whether this goal was achieved. Because the load was partially carried by the vehicles, the model of the interconnection forces was inaccurate and somewhat artificial. In addition, the model takes not into account the vertical forces at the interconnections, which will be typically an order of magnitude higher than the horizontal forces due to gravity. Since the part of the strategy that computes the net wrench that should be exerted on the complete setup is independent of the model of the interconnection forces, the setup is still able to achieve the desired behavior on the velocity level. Therefore, the model of the interconnection forces should be merely seen as a method for distributing the net wrench among the individual wheels.

From the experiments we conclude that both control strategies perform satisfactory, and that there were no substantial drawbacks when the centralized observer algorithm was replaced by local observers that are based on local odometric measurements. The most logical step to improve the performance for the setup with load is to apply different settings for the Coulomb friction compensation.

To achieve fully automatic operation, the algorithms that have been evaluated in this chapter have to be extended with an additional feedback loop that estimates and controls the positions of the AGVs and the load such that they can follow a pre-defined path. A brief inspection of the AGV's position observers showed that the state corrections at the magnet measurements were quite small, which again confirms that the integrated local twist estimates are quite accurate. We can therefore start by directly adopting the AGV's original position

observers, which uses only the AGV's own magnet ruler, for our test setup. It is worth to see how the setup performs when the AGV's local position controllers are activated. If we use a proportional controller in combination with a relatively low gain to prevent force fighting, then it should be possible to achieve control on the position level by providing the AGVs with identical path setpoints .

Finally, we remark that the AGVs were relatively close to one another in our experimental setup. When the vehicles are further apart, then it becomes more difficult to accurately estimate the motion of the coordinate system Ψ_ℓ as the distance to the sensed wheels will become larger. In those situations it may be more advantageous to use the central observer approach than the local observers. Furthermore, the AGVs were very rigidly coupled, both in hardware by the rectangular aluminum frame as well as in software by the synchronization of the control cycles that was based on the sync message. For future research it is interesting to investigate how the performance is affected when a more flexible load is used and when the controller cycles are not synchronized anymore.

Conclusion and recommendations

8.1 Concluding remarks

For several practical control engineering applications it is desirable that multiple systems can operate independently as well as in cooperation with each other. Especially when the transition between individual and cooperative behavior and vice versa can be carried out easily, this results in flexible and scalable systems. In this thesis we considered one particular application of multiple systems that can operate independently as well as in concert with each other, namely the cooperative transportation of a large object by multiple Automated Guided Vehicles (AGVs). Recently there has been an increasing demand from industry to transport very large objects such as sewer pipes, rotor blades of wind turbines and pieces of scenery for theaters, which may reach lengths of over thirty meters. A realistic option is to let several AGVs operate together to handle these types of loads.

In this thesis we investigated how single AGV controllers can be extended such that multiple AGVs can transport a common load in cooperation with each other. We focused on the situation that the load is rigidly or semi-rigidly attached to the vehicles, e.g. by means of completely rigid interconnections, revolute joints, or slider joints. Furthermore, attention was restricted to control on the velocity level, which we regard as an intermediate step for achieving fully automatic operation. In our setup the motion setpoint is provided by an external host. The load is assumed to be already present on the vehicles. Docking and grasping procedures are not considered. The project is a collaboration between FROG Navigation Systems (Utrecht, The Netherlands) and the Control Systems group of the Technische Universiteit Eindhoven. Two omni-directional AGVs and facilities for testing were provided by FROG.

Industrial AGVs are custom made for the transportation tasks at hand and come in a variety of forms. To reduce development times it is desirable to follow a model-based control design approach as this allows generalization to a broad class of vehicles. We have adopted rigid body modeling techniques from the field of robotic manipulators to derive the equations of motion for the AGVs, the load, and the interconnected system in a systematic way. These models are based on physical considerations such as Newton's second law and the positions and dimensions of the wheels, sensors and actuators. Special emphasis was put on the modeling of the wheel-floor interaction, for which we adopted tire models that stem from the field of vehicle dynamics. The resulting models have a clear physical interpretation and are capable to describe a large class of vehicles with arbitrary wheel configurations. This ensures us that the controllers, which are based on these models, are also applicable to broad class of vehicles.

An important prerequisite for achieving smooth cooperative behavior it that the individual AGVs operate at the required accuracy. The performance of an individual AGV is directly

related to the precision of the estimates for the odometric parameters, i.e. the effective wheel diameters and the offsets of the encoders that measure the steering angles of the wheels. Cooperative transportation applications will typically require AGVs that are highly maneuverable, which means that all the wheels of an individual AGV should be able to steer. Since there will be more than one steering angle encoder, the identification of the odometric parameters is substantially more difficult for these omni-directional AGVs than for the mobile wheeled robots that are commonly seen in literature and laboratory settings. We presented a novel three-steps procedure for simultaneously estimating effective wheel diameters and steering angle encoder offsets for a vehicle that is equipped with a measurement system that can detect magnets that are placed in the floor. The first step is the experimental part. In this step, the setpoints for the vehicle's steering systems are set to constants and the vehicle is instructed to drive a certain distance at a constant, low speed. Ideally, this results in a pure circular motion. In the second step, we assume that the realized motion was indeed a pure circle segment, and we subsequently use a nonlinear least-squares estimator to estimate the realized circular trajectory. In the third and last step, it is assumed that there was no wheel slip during the experiment, which allows us to translate the identified trajectory to the steering encoder offsets and the effective wheel diameters. The validity of the tuning procedure was confirmed by experiments with the two omni-directional test vehicles with varying loads. A surprising result was that the effective wheel diameters of the rubber wheels of our AGVs increase with increasing load.

A crucial aspect in all control designs is the reconstruction of the to-be-controlled variables from measurement data. Our to-be-controlled variables are the planar motion of the load and the degrees of freedom between the AGVs on the load. These have to be reconstructed from the odometric sensor information, which consists of the drive encoder and steering encoder readings. We analyzed the observability of an individual AGV and proved that it is theoretically possible to reconstruct its complete motion from the odometric measurements. Due to practical considerations, we pursued a more pragmatic least-squares based observer design. We show that the least-squares based motion estimate is independent of the coordinate system that is being used. The motion estimator was subsequently analyzed in a stochastic setting. The relation between the motion estimator and the estimated velocity of an arbitrary point on the vehicle was explored. We derived how the covariance of the velocity estimate of an arbitrary point on the vehicle is related to the covariance of the motion estimate. We proved that there is one unique point on the vehicle for which the covariance of the estimated velocity is minimal. Next, we investigated how the local motion estimates of the individual AGVs can be combined to yield one global estimate for the load's motion. We assumed that the position of the load with respect to the AGVs was known, but we did not require velocity measurements of the load with respect to the vehicle. We propose that each AGV estimates its own planar motion using local sensor information and subsequently broadcasts the result and their corresponding information matrices. With this information, each AGV is able to compute the global estimate that corresponds to the centralized observer design. Finally, we showed that there are some special situations where the information matrices remain constant during operation. For our test vehicles, this is the case when the load is either completely rigidly attached to the vehicles, or by means of a revolute joint that is mounted in the middle of the two actuated wheel units.

The key issue in the control design for cooperative transportation tasks is that the various

AGVs must not counteract each others' actions. The decentralized controller that we derived makes the AGVs track an externally provided planar motion setpoint while minimizing the interconnection forces between the load and the vehicles. Although the control design is applicable to cooperative transportation by multiple AGVs with arbitrary semi-rigid AGV-load interconnections, it is noteworthy that a particularly elegant solution arises when all interconnections are completely rigid. Then the derived local controllers have the same structure as the controllers that are normally used for individual operation. As a result, changing a few parameter settings and providing the AGVs with identical setpoints is all that is required to achieve cooperative behavior on the velocity level. The decentralized control design for the rigid situation was successfully implemented on the two test vehicles. The experimental results were reproducible and illustrated the practical validity of the designed observers and controller. Interestingly, for our setup there was no noticeable difference in performance when the AGVs used only local sensor information to estimate the twist the interconnected system.

8.2 Recommendations

The wheel-floor contact is currently modelled by means of a linear, static tire model. Although there is a lot of knowledge and data available on the pneumatic tires that are seen in passenger cars and busses, there is almost no literature that deals with the cornering properties of the solid rubber wheels that are commonly used in AGV applications. In particular, the cornering stiffnesses that were used in the experiments of Chapter 7 are only very rough estimates, and it could well be that they are a factor ten too large. It would be interesting to investigate the relation between the side slip angle of a solid rubber wheel and the corresponding lateral force, and how this relation is affected by varying vertical wheel loads. Since omni-directional AGVs will often perform tight turns with a small turning radius, there will be a difference in speed between the inside and the outside of the wheel's contact patch. This so-called turn-slip will result in an additional moment that is exerted by the floor on the wheel, and it would be interesting to investigate the magnitude of this phenomenon.

A shortcoming of the three-step tuning procedure that we proposed is that we had to assume that there was no wheel slip during the experiment to reconstruct the steering encoder offsets and effective wheel diameters from the realized circular trajectory. For vehicles with at most two actuated wheels, such as our test vehicles, this is not a limitation since there will be almost no lateral wheel slip when the experiments are carried out at low speeds. For vehicles with multiple steerable wheels, however, conflicting lateral forces will occur when the steering encoder offsets are not properly calibrated. We therefore may first minimize the conflicting forces heuristically by experimentally varying the steering encoder offsets. For a vehicle with three steerable wheels, this means that we have to adjust one steering encoder offset. When the encoder offset is changed in the right direction, then the conflicting forces will diminish, and the vehicle speed will increase. Subsequently, we can use the proposed three-steps tuning procedure, although the identified steering encoder offsets will be less accurate than for vehicles with two steerable wheels such as our test vehicles.

In the distributed cooperative transportation observer and controller that we presented in this thesis, we focused on the velocity level. To achieve fully automatic operation, the pre-

sented algorithms have to be extended with an additional feedback loop that estimates and controls the positions of the AGVs and the load such that they can follow a pre-defined path. When absolute position measurements are not available, e.g. in between magnet detections for a magnet measurement system, the position observer has to rely on integration of the estimated planar velocities. Therefore, the accuracy of the position estimates is directly related to the performance of the velocity observer that we proposed. In the cooperative transportation experiments that were presented in Chapter 7, the position observer of the individual AGVs remained operational. The experiments showed that the position updates at the magnet detections were quite small, which means that the designed velocity observer performed quite well as integration of the velocity estimates led to only small errors. We can therefore directly adopt the AGV's original position observers for the test setup with our two rigidly interconnected vehicles. In case that the vehicles are semi-rigidly attached to the load, e.g. by means of revolute joints, then we have to make some adjustments to estimate the degrees of freedom between the AGVs and the load.

Because the estimates from the position observers were reasonably accurate during our experiments, we expect that the original, local position controllers will already perform quite well when we provide identical path setpoints to both vehicles. Since the local vehicle clocks are not perfectly synchronized, special measures have to be taken to guarantee that the path is executed at the same times for both vehicles. One interesting result of our experiments was that the position estimates of the two vehicles were consistently five centimeters apart. This is likely caused by inaccuracies in the positions of the magnet rulers of the two vehicles. There will always be a difference in the estimated positions when using local position observers that are based on the measurements from the local magnet ruler only. This means that it is physically not possible to make the position tracking errors for both vehicles identical to zero. Force-fighting of the multiple local controllers can be prevented by avoiding integral actions in the control algorithms. A first logical step is to see how the setup performs when using proportional position controllers with relatively low gains.

The two vehicles were relatively close together in the cooperative transportation experiments that we presented. Moreover, they were both attached to the load by means of fully rigid interconnections, and the load was very rigid. More experiments are needed to see how the designed observers and controllers will perform when longer objects are transported, when the load exhibits more flexibility, and when semi-rigid interconnections such as revolute joints are considered. It would also be interesting to evaluate the forces between the load and the AGVs. Furthermore, in our experiments the control cycles of the two vehicles were synchronized very tightly by means of communication over the CAN bus. It would be interesting to evaluate the performance of the controller under less synchronized conditions, for example when the communication over the CAN bus is replaced by communication using wireless LAN.

Although a commercial application requires several additional modifications such as installing safety measures, emergency stops, automatic load handling devices, etc., the experiments in this thesis show that the proposed tuning, observer and control algorithms certainly have the potential to evolve into meaningful, industrial cooperative transportation applications.

A

Minimization of the nonlinear least-squares tuning criterion

A.1 Introduction

In section 4.4 we introduced a nonlinear least-squares estimator for the intermediate parameters $\theta = (a, b, R_v, \beta_v, c_{w_i}, o_{w_i})$ that describe the circular trajectory of an AGV during the experimental part of our tuning procedure. Here (a, b) is the position of the steering pole with respect to the floor coordinate system Ψ_0 , (R_v, β_v) is the position of the steering pole with respect to the vehicle coordinate system Ψ_v as parameterized by the signed motion radius R_v and the side slip angle β_v , and c_{w_i} and o_{w_i} represent the relation between the path variable S_v and the drive encoder reading ϑ_{w_i} for wheel w_i .

From equation (4.22) of subsection 4.4.3 we recall that the nonlinear least-squares estimator $\hat{\theta}$ was given by

$$\hat{\theta} = \arg \min_{\theta} \left(\sum_{k=1}^m \xi_r(\theta, k)^2 + \sum_{i=1}^n \sum_{k=1}^m \xi_{t_i}(\theta, k)^2 \right), \quad (\text{A.1})$$

where m is the number of detected magnets, n is the number of wheels, $\xi_r(\theta, k)$ are the radial residuals, and $\xi_{t_i}(\theta, k)$ are the tangential residuals for wheel w_i . In equations (4.20)-(4.21) we saw that the residuals satisfy

$$\xi_r(\theta, k) = R_M(k) - R_G(k) \quad (\text{A.2})$$

$$\xi_{t_i}(\theta, k) = c_{w_i} \vartheta_{w_i}(k) + o_{w_i} + |R_v| \gamma_v(k) - |R_v| \alpha_v(k), \quad i \in \{1, \dots, n\}, \quad (\text{A.3})$$

where $R_M(k)$, $R_G(k)$, $\gamma_v(k)$ and $\alpha_v(k)$ are auxiliary variables that are defined in section 4.4. They all depend on θ . A closer inspection shows that the radial residual depends on the four variables (a, b, R_v, β_v) only, i.e. $\xi_r(\theta, k) = \xi_r(a, b, R_v, \beta_v, k)$. Moreover, in our experiments we have selected the planar velocity setpoints such that the side slip angle β_v is small and the motion radius $|R_v|$ is large. In particular, β_v was typically smaller than 1.5 deg and $|R_v|$ was larger than 10 m. For these parameter values, the radial residuals $\xi_r(\theta, k)$ are almost independent of β_v . Furthermore, the influence of (a, b, R_v) on the tangential residuals $\xi_{t_i}(\theta, k)$ is very small for large motion radii $|R_v|$. Hence, for large motion radii the

nonlinear-least squares estimator (A.1) can be approximated by

$$\hat{\theta}_r = \arg \min_{\theta_r} \sum_{k=1}^m \xi_r(\theta_r, \beta_v, k)^2 \quad (\text{A.4})$$

$$\hat{\theta}_t = \arg \min_{\theta_t} \sum_{i=1}^n \sum_{k=1}^m \xi_{t_i}(\theta_r, \theta_t, k)^2, \quad (\text{A.5})$$

where

$$\theta_r = (a, b, R_v) \quad (\text{A.6})$$

$$\theta_t = (\beta_v, c_{w_1}, o_{w_1}, \dots, c_{w_n}, o_{w_n}). \quad (\text{A.7})$$

A.2 Iterative procedure

We will use an iterative procedure that is based on two alternating Gauss-Newton algorithms to solve (A:V1)-(A.5), because this method was successfully used by Gander *et al.* [43] to find circles and ellipses for which the sum of the squares of the geometric distances to a given set of points was minimal. The procedure consists of the following steps

1. Establish initial estimates for θ_r and β_v ;
2. Iterative algorithm for estimating θ_r and θ_t :
 - (a) Gauss-Newton method to estimate θ_r for given β_v ;
 - (b) Establish initial estimates for θ_t ;
 - (c) Gauss-Newton method to estimate θ_t for given θ_r ;
 - (d) Repeat steps (a)-(c) until θ_r and θ_t have converged.

The next sections discuss these steps in more detail. In practice, there is a very fast convergence rate, and steps (a)-(c) only have to be executed one or two times. In our experiments we set the number of repetitions equal to ten.

A.2.1 Establish initial estimates for θ_r and β_v

We take the side slip angle β_v that corresponds to the planar velocity setpoint for the vehicle during the tuning experiment as an initial estimate for β_v . For our experiments this means that the initial estimate for β_v equals zero. We establish initial estimates for $\theta_r = (a, b, R_v)$ by fitting a circle through the $k = 1, \dots, m$ a-priori estimated floor coordinates $M_{\text{a-priori}}^0(k)$ that were defined in equation (4.1). Several well documented procedures are available for fitting a circle through a given set of data points. These procedures typically return the radius $r > 0$ and the coordinates of the center (a, b) of the circle. We will use Gander *et al.*'s Matlab routine 'algcircle.' The underlying method plus the source code of this routine are described in detail in [43].

Although the a and b from the ‘algcircle’ routine can be used directly as initial estimates for the center of orientation, we still have to determine the sign of R_v since ‘algcircle’ always returns a positive radius $r = |R_v|$. The sign of R_v depends on whether Ψ_v is moving ‘forwards’ or ‘backwards,’ and whether the circle is travelled in clockwise or in counterclockwise direction. Ψ_v is said to move forwards when $u_v > 0$, and to move backwards when $u_v < 0$. The velocity observer that is running on the AGV already estimates u_v , so it is natural to use this estimate to find Ψ_v ’s direction of travel. Whether the motion is clockwise or counterclockwise can be determined by examining the angles ψ_i between the horizontal floor axis and the lines from the steering pole C^0 to the a-priori magnet positions $M_{\text{a-priori}}^0(k)$, $k = 1, \dots, m$. Figure A.1 shows that the angle ψ_i satisfies

$$\psi_k = \arctan2\left(M_{\text{a-priori},y}^0(k) - b, M_{\text{a-priori},x}^0(k) - a\right). \quad (\text{A.8})$$

The sequence of angles ψ_1, \dots, ψ_m is ‘unwrapped’ by changing absolute jumps greater than π to their 2π complement, for example with the Matlab routine ‘unwrap.’ If $\psi_{m,\text{unwrapped}} < \psi_1$, then the circle is travelled in clockwise direction. Conversely, $\psi_{m,\text{unwrapped}} > \psi_1$ means that the circle is travelled in counterclockwise direction. The relation between $\text{sign}(R_v)$, the forwards/backwards motion of Ψ_v , and the clockwise/counterclockwise direction of the motion of Ψ_v is summarized in Table A.1.

	forwards	backwards
clockwise direction	–	+
counterclockwise direction	+	–

Table A.1: $\text{sign}(R_v)$ as a function of the forwards/backwards and clockwise/counterclockwise motion of Ψ_v . $R_v > 0$ corresponds to a left hand turn, and $R_v < 0$ corresponds to a right hand turn.

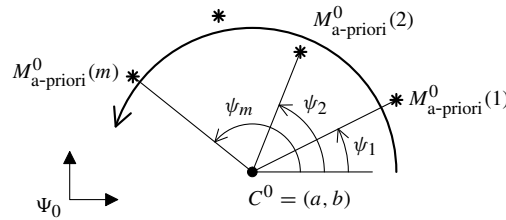


Figure A.1: Definition of ψ_k .

A.2.2 Gauss-Newton method to estimate θ_r for given β_v

The objective of this step is to determine

$$\hat{\theta}_r = \arg \min_{\theta_r} \sum_{k=1}^m \xi_r(\theta_r, \beta_v, k)^2. \quad (\text{A.9})$$

We use a Gauss-Newton method to solve this nonlinear least-squares minimization problem. This requires the partial derivatives of $\xi_r(\theta_r, \beta_v, k)$ with respect to the parameters $\theta_r = (a, b, R_v)$. These are given by

$$\frac{\partial \xi_r(\theta_r, \beta_v, k)}{\partial a} = -\frac{\partial R_G(k)}{\partial a} = \frac{-1}{2\sqrt{(G_x^0(k)-a)^2 + (G_y^0(k)-b)^2}} \frac{\partial (G_x^0(k)-a)^2}{\partial a} = \frac{G_x^0(k)-a}{R_G(k)} \quad (\text{A.10})$$

$$\frac{\partial \xi_r(\theta_r, \beta_v, k)}{\partial b} = -\frac{\partial R_G(k)}{\partial b} = \frac{-1}{2\sqrt{(G_x^0(k)-a)^2 + (G_y^0(k)-b)^2}} \frac{\partial (G_y^0(k)-b)^2}{\partial b} = \frac{G_y^0(k)-b}{R_G(k)} \quad (\text{A.11})$$

$$\begin{aligned} \frac{\partial \xi_r(\theta_r, \beta_v, k)}{\partial R_v} &= \frac{\partial R_M(k)}{\partial R_v} = \frac{1}{2\sqrt{(M_x^v(k)+R_v s\beta_v)^2 + (M_y^v(k)-R_v c\beta_v)^2}} \frac{\partial (M_x^v(k)+R_v s\beta_v)^2 + (M_y^v(k)-R_v c\beta_v)^2}{\partial R_v} \\ &= \frac{1}{2R_M(k)} (2s\beta_v(M_x^v(k)+R_v s\beta_v) - 2c\beta_v(M_y^v(k)-R_v c\beta_v)) \\ &= \frac{R_v + M_x^v(k)s\beta_v - M_y^v(k)c\beta_v}{R_M(k)}. \end{aligned} \quad (\text{A.12})$$

The updated parameters are

$$\hat{\theta}_r^{j+1} = \hat{\theta}_r^j - \left(J_r^{jT} J_r^j \right)^{-1} J_r^{jT} \xi_r(\hat{\theta}_r^j, \beta_v) = \hat{\theta}_r^j - h_r^j, \quad (\text{A.13})$$

with

$$\xi_r(\theta_r^j, \beta_v) = \begin{pmatrix} \xi_r(\theta_r^j, \beta_v, 1) \\ \vdots \\ \xi_r(\theta_r^j, \beta_v, m) \end{pmatrix}, \quad J_r^j = \begin{pmatrix} \frac{\partial \xi_r(\theta_r, \beta_v, 1)}{\partial a} & \frac{\partial \xi_r(\theta_r, \beta_v, 1)}{\partial b} & \frac{\partial \xi_r(\theta_r, \beta_v, 1)}{\partial R_v} \\ \vdots & \vdots & \vdots \\ \frac{\partial \xi_r(\theta_r, \beta_v, m)}{\partial a} & \frac{\partial \xi_r(\theta_r, \beta_v, m)}{\partial b} & \frac{\partial \xi_r(\theta_r, \beta_v, m)}{\partial R_v} \end{pmatrix} \Bigg|_{\hat{\theta}_r^j}. \quad (\text{A.14})$$

J_r^j is the Jacobian corresponding to the j^{th} iteration step. In the current implementation, the update step is performed until $\|h_r^j\|_2 \leq 10^{-8} \|\hat{\theta}_r^j\|_2$. This usually only required two or three iterations for our experiments.

A.2.3 Establish initial estimates for θ_t

The Gauss-Newton algorithm for estimating θ_t that will be discussed in the next subsection requires an initial estimate $\hat{\theta}_t^1$ for the first iteration step. We choose to approximate the term $|R_v|\gamma_v(k)$ in the tangential residual (4.19)

$$\xi_{t_i}(\theta_r, \theta_t, k) = c_{w_i} \vartheta_{w_i}(k) + o_{w_i} + |R_v|\gamma_v(R_v, \theta_t, k) - |R_v|\alpha_v(\theta_r, k) \quad (\text{A.15})$$

by assuming that $|R_v|$ is large and that β_v is small. This yields

$$|R_v|\gamma_v(R_v, \theta_t, k) = R_v \arctan \left(\frac{M_x^v(k)c\beta_v + M_y^v(k)s\beta_v}{R_v + M_x^v(k)s\beta_v - M_y^v(k)c\beta_v} \right) \approx M_x^v(k) + M_y^v(k)\beta_v. \quad (\text{A.16})$$

If we substitute this approximation in equation (A.15), then we obtain an affine relation between the residuals $\xi_{t_i}(\theta_r, \theta_t, k)$ and θ_t . In particular, for a vehicle with $n = 2$ two wheels we obtain

$$\begin{pmatrix} \xi_{t_1}(\theta_r, \theta_t) \\ \xi_{t_2}(\theta_r, \theta_t) \end{pmatrix} \approx \begin{pmatrix} M_y^v & \vartheta_{w_1} & 0 & I & 0 \\ M_y^v & 0 & \vartheta_{w_2} & 0 & I \end{pmatrix} \theta_t + (M_x^v - |R_v|\alpha_v(\theta_r)) = A_t \theta_t - b_t, \quad (\text{A.17})$$

where the tangential residuals $\xi_{t_i}(\theta_r, \theta_t, k)$, the measurements $M_x^v(k)$ and $M_y^v(k)$ of the magnet ruler, the drive encoder readings $\vartheta_{w_i}(k)$, and the auxiliary angles $\alpha_v(\theta_r, k)$ have been stacked in the respective vectors $\xi_{t_i}(\theta_r, \theta_t)$, M_x^v , M_y^v , ϑ_{w_i} , and $\alpha_v(\theta_r)$. As initial estimate for θ_t we take the least-squares solution to the above system of equations:

$$\hat{\theta}_t^1 = (A_t^T A_t)^{-1} A_t^T b_t. \quad (\text{A.18})$$

A.2.4 Gauss-Newton method to estimate θ_t for given θ_r

The objective of this step is to determine

$$\hat{\theta}_t = \arg \min_{\theta_t} \sum_{i=1}^n \sum_{k=1}^m \xi_{t_i}(\theta_r, \theta_t, k)^2. \quad (\text{A.19})$$

We use a Gauss-Newton method to solve this nonlinear least-squares minimization problem. This requires the partial derivatives of $\xi_r \xi_{t_i}(\theta_r, \theta_t, k)$ with respect to the parameters $\theta_t = (\beta_v, c_{w_1}, o_{w_1}, \dots, c_{w_n}, o_{w_n})$. The nonzero partial derivatives satisfy

$$\frac{\partial \xi_{t_i}(\theta_r, \theta_t, k)}{\partial \beta_v} = -R_v \frac{M_x^v(k)^2 + M_y^v(k)^2 + M_x^v(k)R_v s \beta_v - M_y^v(k)R_v c \beta_v}{R_v^2 + M_x^v(k)^2 + M_y^v(k)^2 + 2M_x^v(k)R_v s \beta_v - 2M_y^v(k)R_v c \beta_v} \quad (\text{A.20})$$

$$\frac{\partial \xi_{t_i}(\theta_r, \theta_t, k)}{\partial c_{w_i}} = \vartheta_{w_i}(k) \quad (\text{A.21})$$

$$\frac{\partial \xi_{t_i}(\theta_r, \theta_t, k)}{\partial o_{w_i}} = 1. \quad (\text{A.22})$$

The parameters are updated according to

$$\hat{\theta}_t^{j+1} = \hat{\theta}_t^j - \left(J_t^{jT} J_t^j \right)^{-1} J_t^{jT} \xi_t(\theta_r, \hat{\theta}_t^j) = \hat{\theta}_t^j - h_t^j, \quad (\text{A.23})$$

with

$$\xi_t(\theta_r, \hat{\theta}_t^j) = \begin{pmatrix} \xi_{t_1}(\theta_r, \hat{\theta}_t^j) \\ \xi_{t_2}(\theta_r, \hat{\theta}_t^j) \end{pmatrix}, \quad J_t^j = \begin{pmatrix} \frac{\partial \xi_{t_1}(\theta_r, \theta_t)}{\partial \theta_t} \\ \vdots \\ \frac{\partial \xi_{t_n}(\theta_r, \theta_t)}{\partial \theta_t} \end{pmatrix} \bigg|_{\hat{\theta}_t^j}. \quad (\text{A.24})$$

Here J_t^j is the Jacobian corresponding to the j^{th} iteration step. For a vehicle with $n = 2$ wheels we have for example

$$J_t^j = \begin{pmatrix} -R_v \frac{M_x^v + M_y^v + M_x^v R_v s \beta_v - M_y^v R_v c \beta_v}{R_v^2 + M_x^v + M_y^v + 2M_x^v R_v s \beta_v - 2M_y^v R_v c \beta_v} & \vartheta_{w_1} & 0 & I & 0 \\ -R_v \frac{M_x^v + M_y^v + M_x^v R_v s \beta_v - M_y^v R_v c \beta_v}{R_v^2 + M_x^v + M_y^v + 2M_x^v R_v s \beta_v - 2M_y^v R_v c \beta_v} & 0 & \vartheta_{w_2} & 0 & I \end{pmatrix}. \quad (\text{A.25})$$

In the current implementation, the update step is performed until $\|h_t^j\|_2 \leq 10^{-8} \|\hat{\theta}_t^j\|_2$. This usually only required two or three iterations for our experiments.

B

Additional figures for the medium speed tuning experiments with various loads

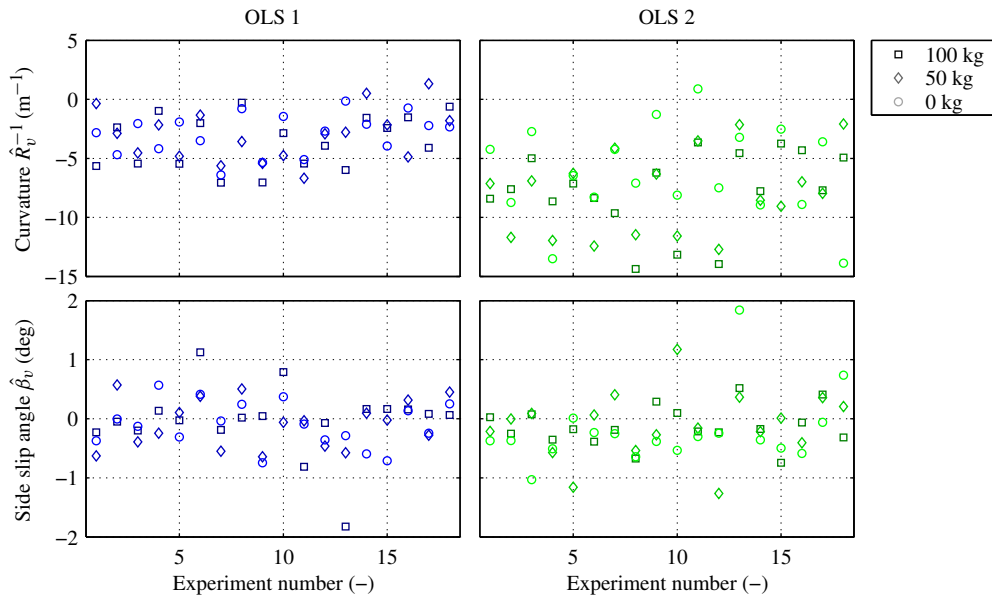


Figure B.1: Estimated curvature \hat{R}_v^{-1} (top panels) and estimated side slip angles $\hat{\beta}_v$ (bottom panels) for the OLS 1 (left panels) and the OLS 2 (right panels) during the medium speed experiments with varying loads. The setpoints for the curvature and the side slip angle were zero for all medium speed experiments.

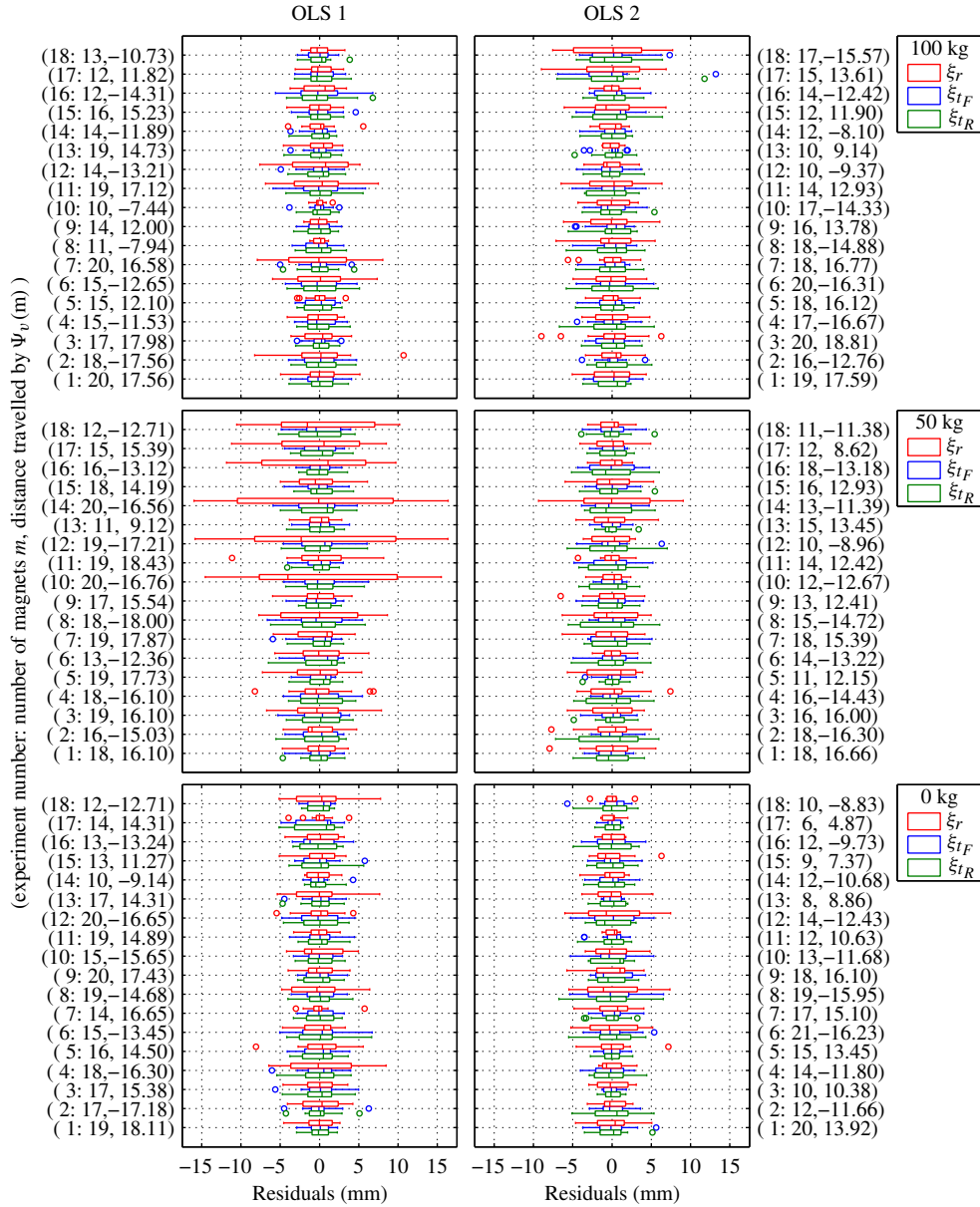


Figure B.2: Box plots of the radial residuals $\xi_r(\hat{\theta}, k)$ and the tangential residuals $\xi_{tF}(\hat{\theta}, k)$ and $\xi_{tR}(\hat{\theta}, k)$ for the medium speed experiments with varying loads.

C

Nomenclature

C.1 Abbreviations

$$c\varphi = \cos(\varphi), \quad s\varphi = \sin(\varphi), \quad M_v = M_{v,v}, \quad T_i^j = T_i^{j,j}, \quad W_i^j = W_i^{j,j}.$$

C.2 Greek symbols

<i>Symbol</i>	<i>Description</i>	<i>Page</i>
α_v	Auxiliary angle used in the tuning procedure of Chapter 4	81
$\alpha_{v,t}$	Auxiliary angle used in the tuning procedure of Chapter 4	81
α_{w_i}	Side slip angle of wheel w_i	57
β_v	Side slip angle of the motion of Ψ_v with respect to the floor	44
Γ_{ij}^k	Connection coefficients	50
Γ_ℓ	Matrix representation of the load's connection coefficients in body fixed coordinates	65
Γ_v	Matrix representation of the vehicle's connection coefficients in body fixed coordinates	54
$\Gamma_{v_k}^*$	Controller setting for the connection coefficient matrix of vehicle k	154
γ_v	Auxiliary angle used in the tuning procedure of Chapter 4	81
δ_{w_i}	Steering angle of wheel w_i	55
$\bar{\delta}_{w_i}$	Kinematic steering angle for wheel w_i	61
$\delta_{w_i}^{\text{encoder}}$	Steering angle encoder measurement for wheel w_i	75
$\delta_{w_i}^{\text{offset}}$	Steering angle encoder offset for wheel w_i	75
$\delta_{w_i,k}$	Steering angle of wheel w_i of vehicle k	124
η	Reduced set of coordinates to describe the interconnected system	67
$\hat{\eta}$	Estimated motion of the interconnected system, expressed in the reduced set of coordinates η	130
η_k	Velocity coordinates for the lower pair interconnection between vehicle k and the load	66
θ	Intermediate parameters used to characterize the realized circular trajectory in the tuning procedure	77
$\dot{\theta}_{w_i}$	Spin velocity of wheel w_i	56
ϑ_{w_i}	Drive encoder reading (unwrapped) for wheel w_i	75

Symbol	Description	Page
κ_{w_i}	Longitudinal slip of wheel w_i	57
λ	Vector with the local interconnection forces λ_k for all the vehicle-load interconnections	150
λ_k	Local interconnection forces that occur at the interconnection between vehicle k and the load	150
ξ	Measurement errors corresponding to z	113
$\xi_{\alpha_{w_i}}$	Deviation from the wheel's side slip angle setpoint $\alpha_{w_i}^{\text{set}}$ from its true side slip angle α_{w_i}	115
ξ_k	Measurement errors corresponding to z_k	122
$\xi_r(\theta, k)$	Radial residual corresponding to magnet measurement k	78
$\xi_s(\theta, k)$	Auxiliary residual	82
$\xi_{t_i}(\theta, k)$	Tangential residual corresponding to magnet measurement k for wheel w_i	81
$\xi_{u_{w_i}}$	Additive error in the longitudinal velocity estimate \hat{u}_{w_i}	115
$\xi_{v_{w_i}}$	Additive error in the lateral velocity estimate \hat{v}_{w_i}	115
ξ_{w_i}	Measurement noise for drive encoder of wheel w_i (Chapter 4)	76
ξ_{w_i}	Measurement errors for wheel w_i (Chapter 5)	116
(ξ_x, ξ_y)	Deviation of the true magnet position with respect to the intended magnet position	79
ρ_v	Signed curvature of the motion of Ψ_v with respect to the floor	45
Σ	Covariance matrix of the additive measurement errors ξ	115
Σ^{-1}	Positive-definite weighting matrix	114
Σ_k	Covariance matrix of the additive measurement errors ξ_k for vehicle k	123
$\sigma_{\alpha_{w_i}}$	Standard deviation of the side slip angle deviation $\xi_{\alpha_{w_i}}$	115
σ_M	Standard deviation of the precision at which the magnets are placed in the floor	79
$\sigma_{u_{w_i}}$	Standard deviation of the relative longitudinal velocity error $\xi_{u_{w_i}}$	115
τ	Time constant for the desired behavior of the controlled system	165
φ_v	Orientation of Ψ_v with respect to Ψ_0	38
Ψ_0	Floor-fixed coordinate system	38
Ψ_ℓ	Load-fixed coordinate system	65
Ψ_v	Vehicle-fixed coordinate system	38
Ψ_{w_i}	Wheel coordinate system (the x_{w_i} -axis coincides with the wheel plane)	55
$\Psi_{\tilde{w}_i}$	Wheel coordinate system for the simplified model (x_{w_i} -axis coincides with the wheel's velocity vector)	62
ω_ℓ	Rotational velocity of Ψ_ℓ with respect to the floor	
ω_v	Rotational velocity of Ψ_v with respect to the floor	41

C.3 Latin symbols

<i>Symbol</i>	<i>Description</i>	<i>Page</i>
$A_{i,k}$	Matrix that relates the local interconnection forces λ_k , which occur at the interconnection between vehicle k and the load, to the wrench $W_{v_k}^{i,\ell}$ that is exerted by that vehicle on the load	150
$Ad_{H_k^l}$	Adjoint matrix corresponding to H_k^l	43
(a, b)	Position of the steering pole expressed in Ψ_0	76
$ad_{T_i^{k,j}}$	Matrix used to compute the time derivative of $Ad_{H_i^j}$	68
B	Matrix that describes the relation between the twist $T_v^{v,0}$ of the vehicle with respect to the floor and the longitudinal and lateral velocities of the wheels (identical to B_v)	59
\bar{B}	Approximation of B based on the kinematic steering angles	64
$B_{i,k}$	Matrix that describes the relation between the twist $T_{v_k}^{i,0}$ of vehicle k with respect to the floor and the longitudinal and lateral velocities of the wheels	122
$B_{w_i,u}$	Row of B that relates the twist $T_v^{v,0}$ of the vehicle with respect to the floor to the longitudinal velocity of wheel w_i	59
$\bar{B}_{w_i,u}$	Approximation of $B_{w_i,u}$	64
$B_{w_i,v}$	Row of B that relates the twist $T_v^{v,0}$ of the vehicle with respect to the floor to the lateral velocity of wheel w_i	59
$\bar{B}_{w_i,v}$	Approximation of $B_{w_i,v}$	64
C	Matrix that relates the inputs u to the wheel forces F_w	145
C^0	Steering pole expressed in Ψ_0	79
C^v	Steering pole expressed in Ψ_v	44
C_k	Matrix that relates the inputs u of vehicle k to the wheel forces F_w of vehicle k	155
$C_{w_i}^{w_i}$	Lateral cornering stiffness of wheel w_i	56
$C_{w_i}^{\text{lat}}$	Longitudinal cornering stiffness of wheel w_i	56
$C_{w_i}^{\text{long}}$	Increase in S_v per drive encoder count ϑ_{w_i} of wheel w_i	76
c_{w_i}	Weighting factor that is used in the observer for the twist of vehicle k	165
E_k	Backward Coulomb friction compensation for wheel w_i	164
F_{bw}^{fric}	Forward Coulomb friction compensation for wheel w_i	164
F_{fw}^{fric}	Vector with the longitudinal and lateral wheel forces	145
F_w	Longitudinal tire force (identical to $(W_{w_i}^{w_i,v})_u$)	59
$F_{w_i,u}$	Lateral tire force (identical to $(W_{w_i}^{w_i,v})_v$)	59
$F_{w_i,v}$	Grid position at which the magnet was intended to be placed expressed in Ψ_0	76
G^0	Matrix that relates the vector of interconnection forces λ to the net wrench $W_V^{i,\ell}$ that is exerted by all the vehicles on the load	150

Symbol	Description	Page
$G_{i,k}$	Matrix that relates the vector of interconnection forces λ to the wrench $W_{v_k}^{i,\ell}$ that is exerted by vehicle k on the load	150
G_t^0	True magnet position expressed in Ψ_0	78
g	Gravitational acceleration	51
H	Matrix that relates the measurements z of the interconnected system to the motion T of the interconnected system	128
H_v^0	Relative position of Ψ_v with respect to Ψ_0	38
I_ℓ	Load's moment of inertia corresponding to center of gravity	
I_t	Moment of inertia of the rigidly interconnected systems corresponding to its center of gravity	53
I_v	Vehicle's moment of inertia corresponding to center of gravity	155
K	Gain matrix that specifies the first order desired behavior of the interconnected system	148
K_k	Gain matrix that specifies the first order desired behavior of the interconnection between the k^{th} vehicle and the load	148
K_ℓ	Gain matrix that specifies the first order desired behavior of the load	148
$K_{\text{long}}^{w_i}$	Inverse of the longitudinal stiffness for wheel w_i (identical to $(C_{\text{long}}^{w_i})^{-1}$)	108
K_v	Gain matrix that specifies the first order desired behavior of a controlled single vehicle	143
$K_{v_k}^*$	Controller setting for the gain matrix of vehicle k	154
M	Inertia tensor of the interconnected system expressed in Ψ_ℓ	69
M^v	Relative position of a magnet measurement with respect to Ψ_v	75
M_ℓ	Load's inertia tensor expressed in body fixed coordinates	65
M_v	Vehicle's inertia tensor expressed in body fixed coordinates	54
$M_{v_k}^*$	Controller setting for the mass matrix of vehicle k	154
m	Number of detected magnets	75
m_ℓ	Load mass	
m_t	Mass of the rigidly interconnected system	155
m_v	Vehicle mass	53
N	Number of vehicles in the interconnected system	
n	Number of (actuated) wheels	
o_v	Origin of Ψ_v	44
o_{w_i}	Path variable S_v corresponding to $\vartheta_{w_i} = 0$	76
P	Decomposition of the interconnection forces weighting matrix Q such that $PP^T = Q$	151
P^v	Coordinates of the point P expressed in Ψ_v	48
P_m^i	Unique point on the vehicle, expressed in Ψ_i , where the covariance of the velocity estimate error is minimal	120
$P_{m z_k}^i$	Unique point on the vehicle, expressed in Ψ_i , where the covariance of the velocity estimate error is minimal when only the measurements z_k are used for the velocity estimate	125

Symbol	Description	Page
Q	Weighting matrix used to define a norm on the interconnection forces λ	151
Q^i	Covariance tensor expressed in Ψ_i	117
Q_k^i	Covariance tensor for vehicle k expressed in Ψ_i	123
q_v	Relative position of Ψ_v with respect to Ψ_0 ; $q_v = (\varphi_v, x_v, y_v)$	39
R_G	Distance from the intended magnet grid position G^0 to the steering pole C^0	79
R_M	Distance from the magnet measurement M^v to the steering pole C^v	79
R_v	Signed radius of the motion of Ψ_v with respect to the floor	44
R_{w_i}	Signed radius of the motion of wheel w_i	85
r_{w_i}	Effective rolling radius of wheel w_i	56
S	Matrix that relates η to T	68
$S_{i,k}$	Full column rank matrix that relates η_k to $T_{v_k}^{i,\ell}$	66
S_v	Path variable/position of Ψ_v along the circular trajectory	76
T	Vector containing the twists of the load and the vehicles of the interconnected system with respect to the floor expressed in Ψ_ℓ	68
\hat{T}	Estimate for the the twists of the load and the vehicles of the interconnected system with respect to the floor expressed in Ψ_ℓ	130
$T_i^{k,j}$	Twist of body i with respect to body j expressed in Ψ_k	40
$\hat{T}_i^{k,j}$	Estimated twist of body i with respect to body j expressed in Ψ_k	114
$\hat{T}_{i z}^{k,j}$	Estimated twist of body i with respect to body j expressed in Ψ_k that is based on the measurements z only	123
$(T_{v_k}^{i,\ell})^{\mathcal{A}}$	Set of allowed twists between vehicle k and the load expressed in Ψ_i	66
t	Time	
u	Inputs	64
u_ℓ	Longitudinal velocity of Ψ_ℓ with respect to the floor	
u_v	Longitudinal velocity of Ψ_v with respect to the floor	41
u_{w_i}	Longitudinal velocity of wheel w_i (identical to $(T_{w_i}^{w_i,0})_v$)	59
V_v	Tangential velocity of the motion of Ψ_v with respect to the floor	44
v_ℓ	Lateral velocity of Ψ_ℓ with respect to the floor	
v_v	Lateral velocity of Ψ_v with respect to the floor	41
v_{w_i}	Lateral velocity of wheel w_i (identical to $(T_{w_i}^{w_i,0})_v$)	59
W^v	Net wrench that is exerted on the vehicle expressed in Ψ_v	54
$W_i^{k,j}$	Wrench exerted by body i on body j expressed in Ψ_k	
W_V^ℓ	Net wrench that is exerted by all the vehicles on the load	65
W_w^v	Wrench that is exerted by the wheels on the vehicle expressed in Ψ_v	55
$(W_{v_k}^{i,\ell})^{\mathcal{C}}$	Set of wrenches that can be transmitted from vehicle k to the load expressed in Ψ_i	67
$W_{v_k}^\ell$	Wrench that is exerted by vehicle k on the load expressed in Ψ_ℓ	65

<i>Symbol</i>	<i>Description</i>	<i>Page</i>
$(x_{\ell,c}, y_{\ell,c})$	Coordinates of the load's center of gravity expressed in Ψ_{ℓ}	
$(x_{t,c}, y_{t,c})$	Coordinates of the rigidly interconnected system's center of gravity expressed in Ψ_{ℓ}	155
(x_v, y_v)	Coordinates of the origin of Ψ_v expressed in Ψ_0	39
$(x_{v,c}, y_{v,c})$	Coordinates of the vehicle's center of gravity expressed in Ψ_v	53
$(x_{w_i}^v, y_{w_i}^v)$	Coordinates of the center of wheel w_i expressed in Ψ_v	59
z	Measurements	113
z_k	Measurements corresponding to vehicle k	122

Bibliography

- [1] M. Abe. On advanced chassis control technology for vehicle handling and active safety. In *3th Int. Symp. on Advanced Vehicle Control*, pp. 1–12, Aachen, Germany, 24–28 June 1996.
- [2] M.N. Ahmadabadi and E. Nakano. A “Constrain and Move” approach to distributed object manipulation. *IEEE Transactions on Robotics and Automation*, 17(2):157–172, April 2001.
- [3] R.W. Allen, J.P. Christos, and T.J. Rosenthal. A tire model for use with vehicle dynamics simulations on pavement and off-road surfaces. In F. Böhm and H.-P. Willumeit, editors, *Proc. 2nd Int. Colloquium on Tyre Models for Vehicle Dynamics Analysis*, Berlin, Germany, 20–21 February 1997.
- [4] R.W. Allen, R.E. Magdaleno, T.J. Rosenthal, D.H. Klyde, and J.R. Hogue. Tire modeling requirements for vehicle dynamics simulation. *SAE Technical Paper*, (950312), 1995.
- [5] C. Altafini and A. Speranzon. Backward line tracking control of a radio-controlled truck and trailer. In *Proc. IEEE Int. Conf. Robotics and Automation*, volume 1, pp. 169–174, Seoul, Korea, 21–26 May 2001.
- [6] C. Altafini, A. Speranzon, and B. Wahlberg. A feedback control scheme for revising a truck and trailer vehicle. *IEEE Transactions on Robotics and Automation*, 17(6):915–922, December 2001.
- [7] J. Andreasson and L. Laine. Driving dynamics for hybrid electric vehicles considering handling and control architecture. In *18th Int. Symp. IAVSD, Dynamics of Vehicles on Roads and Tracks*, Kanagawa, Japan, 25–29 August 2003.
- [8] J. Andreasson, L. Laine, and J. Fredriksson. Evaluation of a generic vehicle motion control architecture. In *FISITA*, Barcelona, Spain, 23–27 May 2004.
- [9] G. Antonelli, S. Chiaverini, and G. Fusco. An odometry calibration method for mobile robots based on the least-squares technique. In *Proc. American Control Conference*, pp. 3429–3434, Denver, Colorado, USA, 4–6 June 2003.
- [10] R.C. Arkin. *Behavior-based robotics*. MIT Press, London, 1998.
- [11] R.C. Arkin. Multi-robot control and formation control. In *Lecture notes from European Summer School on Cooperative Robotics*, Instituto Superior Técnico (IST), Lisboa, 2–7 September 2002.
- [12] Y. Asahiro, H. Asama, I. Suzuki, and M. Yamashita. Improvement of distributed control algorithms for robots carrying an object. In *IEEE Int. Conf. Systems, Man, and Cybernetics*, volume 6, pp. 608–613, 12–15 October 1999.
- [13] Y. Asahiro, E.C.H. Chang, A. Mali, I. Suzuki, and M. Yamashita. A distributed ladder transportation algorithm for two robots in a corridor. In *Proc. IEEE Conf. Robotics and Automation*, volume 3, pp. 3016–3021, Seoul, Korea, 21–26 May 2001.
- [14] E. Bakker, L. Nyborg, and H.B. Pacejka. Tire modelling for use in vehicle dynamic studies. *SAE Technical Paper*, (870421), 1987.
- [15] A. Bicchi. Hands for dexterous manipulation and robust grasping: a difficult road towards simplicity. *IEEE Transactions on Robotics and Automation*, 16(6):652–662, December 2000.
- [16] A. Bicchi and D. Prattichizzo. Manipulability of cooperating robots with unactuated joints and closed-chain mechanisms. *IEEE Transactions on Robotics and Automation*, 16(4):336–345, August 2000.
- [17] E. Bicho. *Dynamic Approach to Behavior-Based Robotics: Design, Specification, Analysis, Simulation and Implementation*. PhD thesis, University of Minho, Guimarães, Portugal, 1999.
- [18] E. Bicho, L. Louro, and W. Erlhagen. Coordinated transportation with minimal explicit communication between robots. In *5th IFAC/EURON Symp. Intelligent Autonomous Vehicles*, Instituto Superior Técnico, Lisboa, Portugal, 5–7 July 2004.
- [19] J. Borenstein. Experimental results from internal odometry error correction with the OmniMate mobile robot. *IEEE Transactions on Robotics and Automation*, 14(6):963–969, December 1998.

- [20] J. Borenstein and L. Feng. Measurement and correction of systematic odometry errors in mobile robots. *IEEE Transactions on Robotics and Automation*, 12(6):869–880, December 1996.
- [21] R.W. Brockett, R.S. Millman, and H.J. Sussman, editors. *Differential Geometric Control Theory*, Chapter: Asymptotic stability and feedback stabilization, pp. 181–191. Birkhäuser, Boston (MA), USA, 1983.
- [22] R.A. Brooks. A robust layered control system for a mobile robot. *IEEE Journal of Robotics and Automation*, 2(1):14–23, March 1986.
- [23] D. Caltabiano, G. Muscato, and F. Russo. Localization and self calibration of a robot for volcano exploration. In *Proc. IEEE Int. Conf. Robotics and Automation*, pp. 586–591, New Orleans, LA, USA, April 2004.
- [24] Y.U. Cao, A.S. Fukunaga, and A.B. Kahng. Cooperative mobile robotics: Antecedents and directions. *Autonomous Robots*, 4:1–23, 1997.
- [25] K.S. Chang, R. Holmberg, and O. Khatib. The augmented object model: cooperative manipulation and parallel mechanism dynamics. In *Proc. IEEE Int. Conf. Robotics and Automation*, pp. 470–475, San Francisco, USA, April 2000.
- [26] K.S. Chong and L. Kleeman. Accurate odometry and error modelling for a mobile robot. In *Proc. IEEE Int. Conf. Robotics and Automation*, pp. 2783–2788, Albuquerque, New Mexico, USA, April 1997.
- [27] E. Dahlberg and N.-G. Vågstedt. The advantages of a simple approach modelling heavy vehicle handling. *SAE Technical Paper*, (973264), 1997.
- [28] A.A.H. Damen. Physiological processes and parameter estimation. Lecture notes for course 5Q240, Technische Universiteit Eindhoven, Eindhoven, The Netherlands, November 2003.
- [29] B. D’Andréa-Novel, G. Campion, and G. Bastin. Control of wheeled mobile robots not satisfying ideal velocity constraints: a singular perturbation approach. *Int. Journal of Robust and Nonlinear Control*, 5:243–267, 1995.
- [30] D. de Bruin. *Lateral guidance of all-wheel steered multiple-articulated vehicles*. PhD thesis, Technische Universiteit Eindhoven, Eindhoven, The Netherlands, 2001.
- [31] D. de Bruin, A.A.H. Damen, A. Prohromsky, and P.P.J. van den Bosch. Backstepping control for lateral guidance of all-wheel steered multiple articulated vehicles. In *Proc. IEEE Intelligent Transportation Conf.*, pp. 95–100, Dearborn (MI), USA, 1–3 October 2000.
- [32] A.J. de Graaf. *On-line measuring systems for a mobile vehicle and a manipulator gripper: a model based approach*. PhD thesis, Universiteit Twente, Enschede, 1994.
- [33] A.J. de Graaf. Architecture of a generic vehicle controller. In *Proc. IEEE Intelligent Vehicle Symposium*, pp. 77–80, Versailles, France, June 2002.
- [34] G. Dudek, M.R.M. Jenkin, E. Miliotis, and D. Wilkes. A taxonomy for multi-agent robotics. *Autonomous Robots*, 3(4):375–397, December 1996.
- [35] M. El-Gindy and J.Y. Wong. A comparison of various computer simulation models for predicting the directional response of articulated vehicles. *Vehicle System Dynamics*, 16:249–268, 1987.
- [36] E. Esmailzadeh. Directional performance and yaw stability of articulated combination trucks. *SAE Technical Paper*, (962154), 1996.
- [37] E. Esmailzadeh and B. Tabarrok. Handling performance and lateral stability of articulated logging trucks. *SAE Technical Paper*, (982786), 1998.
- [38] P. Fancher, J. Bernard, C. Clover, and C. Winkler. Representing truck tire characteristics in simulations of braking and braking-in-a-turn maneuvers. In F. Böhm and H.-P. Willumeit, editors, *Proc. 2nd Int. Colloquium on Tyre Models for Vehicle Dynamics Analysis*, Berlin, Germany, 20–21 February 1997.
- [39] T. Frankel. *The geometry of physics: an introduction*. Cambridge University Press, Cambridge, 1997.
- [40] J. Fredriksson, J. Andreasson, and L. Laine. Wheel force distribution for improved handling in a hybrid electric vehicle using nonlinear control. In *43rd IEEE Conf. on Decision and Control*, pp. 4081–4086, Atlantis, Paradise Island, Bahamas, 14–17 December 2004.
- [41] Y. Fukuda. Estimation of vehicle slip-angle with combination method of model observer and direct integration. In *4th Int. Symp. on Advanced Vehicle Control*, pp. 201–206, Nagoya, Japan, 14–18 September 1998.

- [42] Y. Furukawa, N. Yuhara, S. Sano, H. Takeda, and Y. Matsushita. A review of four-wheel steering studies from the viewpoint of vehicle dynamics and control. *Vehicle System Dynamics*, 18:151–186, 1989.
- [43] W. Gander, G.H. Golub, and R. Strebel. Fitting of circles and ellipses, least squares solution. Technical report 1994TR-217, Institut für Wissenschaftliches Rechnen, ETH Zürich, 1994.
- [44] J.J. Graig. *Introduction to robotics: mechanics and control*. Addison-Wesley, Reading (Massachusetts), 2 edition, 1989.
- [45] G. Hammond. *AGVS at work: automated guided vehicle systems*. Springer, Berlin, 1986.
- [46] M. Hashimoto, T. Eguchi, and F. Oba. Control and odometry of an omnidirectional vehicle with multiple modular steerable drive wheels. In *4th Int. Symp. on Advanced Vehicle Control*, pp. 761–766, Nagoya, Japan, 14–18 September 1998.
- [47] M. Hashimoto, F. Oba, H. Nakahara, K. Imamaki, and T. Eguchi. Trajectory generation and tracking control methods for a multiple transfer robots system. In *Proc. IEEE/RSJ Int. Workshop Intelligent Robots and Systems*, pp. 799–804, Osaka, Japan, 1991.
- [48] M. Hashimoto, F. Oba, and S. Zenitani. Coordinative object-transportation by multiple industrial mobile robots using coupler with mechanical compliance. In *Proc. Int. Conf. Industrial Electronics, Control, and Instrumentation*, volume 3, pp. 1577–1582, 15–19 November 1993.
- [49] Y. Hattori. Optimum vehicle dynamics control based on tire driving and braking forces. *R&D Review of Toyota CRDL*, 38(4):23–29, 2003.
- [50] W. Hendrix and B. Stouten. Implementing and testing a state observer for a guided vehicle. *Journal A*, 42(1):38–43, 2001.
- [51] Y. Hirata, Y. Kume, T. Sawada, Z.-D. Wang, and K. Kosuge. Handling of an object by multiple mobile manipulators in coordination based on caster-like dynamics. In *Proc. IEEE Int. Conf. Robotics and Automation*, volume 1, pp. 807–812, New Orleans, USA, 26 April – 1 May 2004.
- [52] R.H. Hollier, editor. *Automated Guided Vehicle Systems*, Chapter: Evolutionary AGVS - From concept to present reality, pp. 3–9. IFS Publications, Bedford, UK, 1987.
- [53] R.H. Hollier, editor. *Automated Guided Vehicle Systems*. IFS Publications, Bedford, UK, 1987.
- [54] S. Horiuchi, K. Okada, and S. Nohtomi. Integrated control of four wheel steering and wheel torques using nonlinear predictive controller. *4th Int. Symp. on Advanced Vehicle Control*, pp. 111–116, 14–18 September 1998.
- [55] P. Huang, H. Smakman, and J. Guldner. Design of a vehicle state observer for vehicle dynamics control systems. In *5th Int. Symp. on Advanced Vehicle Control*, pp. 201–206, Ann Arbor, Michigan, USA, August 22–24 2000.
- [56] T. Huntsberger, P. Pirjanian, A. Trebi-Ollenu, H. Das Nayar, H. Aghazarian, A.J. Ganino, M. Garrett, S.S. Joshi, and P.S. Schenker. CAMPOUT: A control architecture for tightly coupled coordination of multirobot systems for planetary surface exploration. *IEEE Transactions on Systems, Man, and cybernetics*, 33(5):550–559, September 2003.
- [57] International Standardization Organization. Road vehicles - Interchange of digital information - Controller area network (CAN) for high speed communication. Technical Report ISO 11898, 1998.
- [58] L. Iocchi, D. Nardi, and M. Salerno. Reactivity and deliberation: a survey on multi-robot systems. In *Lecture notes from European Summer School on Cooperative Robotics*, Instituto Superior Técnico (IST), Lisboa, 2–7 September 2002.
- [59] T. Kailath, A.H. Sayed, and B. Hassibi. *Linear Estimation*. Prentice Hall, Upper Saddle River, New Jersey, USA, 2000.
- [60] J.J.A.M. Keij. Obstacle avoidance for wheeled mobile robotic systems. Master’s thesis, Technische Universiteit Eindhoven, Eindhoven, The Netherlands, 2003.
- [61] O. Khatib, K. Yokoi, K. Chang, D. Ruspini, R. Holmberg, and A. Casal. Decentralized cooperation between multiple manipulators. In *5th IEEE Int. Workshop on Robot and communication*, pp. 183–188, Tsukuba, 11–14 November 1996.

- [62] O. Khatib, K. Yokoi, K. Chang, D. Ruspini, R. Holmberg, and A. Casal. Vehicle/arm coordination and multiple mobile manipulator decentralized cooperation. In *Proc. IEEE/RSJ Int. Conf. Intelligent Robots and Systems*, pp. 546–553, Osaka, Japan, 1996.
- [63] S. Kim, J. Jin, and S. Chung. Development of active front steering. In *7th Int. Symp. on Advanced Vehicle Control*, pp. 755–760, Arnhem, The Netherlands, 23–27 August 2004.
- [64] W.-J. Kok. Internal communication, December 2000.
- [65] D. Kortenkamp, R.P. Bonasso, and R. Murphy. *Artificial intelligence and mobile robots : case studies of successful robot systems*. AAAI Press, London, 1998.
- [66] K. Kosuge, T. Oosumi, M. Satou, K. Chiba, and K. Takeo. Transportation of a single object by two decentralized-controlled nonholonomic mobile robots. In *Proc. IEEE Int. Conf. Robotics and Automation*, volume 4, pp. 2989–2994, Leuven, Belgium, 16–20 May 1998.
- [67] J. Kumagai. Sand trap: DARPA's 320-kilometer robotic race across the Mojave desert yields no winners, but plenty of new ideas. *IEEE Spectrum*, pp. 34–40, June 2004.
- [68] P. Lacroix, V. Polotski, J.-Y. Hervé, and P. Cohe. Decentralized control of two cooperative car-like robots performing a transportation task. In *Proc. 3rd IFAC Symp. Intelligent Autonomous Vehicles*, volume 1, pp. 101–106, Madrid, Spain, 25–27 March 1998.
- [69] L. Laine and J. Andreasson. Generic control architecture applied to a hybrid electric sports utility vehicle. In *Proc. 20th Int. Electric Vehicle Symp. (EVS)*, Long Beach, California, USA, November 15–19 2003.
- [70] L. Laine and J. Andreasson. Modelling of generic hybrid electric vehicles. In *Proc. 3th Int. Modelica Conf.*, pp. 87–94, Linköping, November 3–4 2003.
- [71] T.D. Larsen, M. Bak, N.A. Andersen, and O. Ravn. Location estimation for Autonomously Guided Vehicles using an augmented Kalman filter to autocalibrate the odometry. In *FUSION98 Spie Conference*, Las Vegas, USA, July 1998.
- [72] R. Leenen, J. Ploeg, L. Moreau, and H. Nijmeijer. Motion control design for an overactuated automatic guided vehicle. In *7th Int. Symp. on Advanced Vehicle Control*, pp. 309–314, Arnhem, The Netherlands, 23–27 August 2004.
- [73] J. Liu and J. Wu. *Multi-agent robotic systems*. CRC, London, 2001.
- [74] A. Martinelli. The odometry error of a mobile robot with a synchronous drive system. *IEEE Transactions on Robotics and Automation*, 18(3):399–405, June 2002.
- [75] A. Martinelli, N. Tomatis, A. Tapus, and R. Siegwart. Simultaneous localization and odometry calibration for mobile robot. In *Proc. IEEE/RSJ Int. Conf. Intelligent Robots and Systems*, volume 2, pp. 1499–1504, 27–31 October 2003.
- [76] M.J. Mataric, M. Nilsson, and K.T. Simsarian. Cooperative multi-robot box-pushing. In *Proc. IEEE/RSJ Int. Conf. Intelligent Robots and Systems*, volume 3, pp. 556–561, 5–9 August 1995.
- [77] D. Mathijssen. Woestijnrace for robots. *Kijk*, (2):6–11, Februari 2004.
- [78] J.P. Maurice. *Short wavelength and dynamic tyre behavior under lateral and combined slip conditions*. PhD thesis, Technische Universiteit Delft, Delft, The Netherlands, 1999.
- [79] P.J. McKerrow. *Introduction to robotics*. Electronic Systems Engineering Series. Addison-Wesley, Amsterdam, reprint with corrections edition, 1993.
- [80] P.J. McKerrow and D. Ratner. Calibrating a 4-wheel mobile robot. In *Proc. IEEE/RSJ Int. Conf. Intelligent Robots and Systems*, volume 1, pp. 859–864, 30 September – 5 October 2002.
- [81] N. Miyata, J. Ota, Y. Aiyama, J. Sasaki, and T. Arai. Cooperative transport system with regrasping car-like mobile robots. In *Proc. IEEE/RSJ Int. Conf. Intelligent Robots and Systems*, volume 3, pp. 1754–1761, 7–11 September 1997.
- [82] N. Miyata, J. Ota, T. Arai, E. Yoshida, D. Kurabayashi, J. Sasaki, and Y. Aiyama. Cooperative transport with regrasping of torque-limited mobile robots. In *Proc. IEEE/RSJ Int. Conf. Intelligent Robots and Systems*, pp. 304–309, Osaka, Japan, 1996.
- [83] O. Mokhiamar and M. Abe. How the four wheels should share forces in an optimum cooperative chassis control. In *IFAC Symp. on Advances in Automotive Control*, Salerno, Italy, 19–23 April 2004.

- [84] C. Moler and C. van Loan. Nineteen dubious ways to compute the exponential of a matrix, twenty-five years later. *SIAM Review*, 45(1):3–49, 2003.
- [85] I. Motte. *Contribution to modeling and control design for wheeled mobile robots*. PhD thesis, Université Catholique de Louvain, Louvain-la-Neuve, Belgium, September 2002.
- [86] T. Müller. *Automated guided vehicles*. Springer, Berlin, 1983.
- [87] R.M. Murray, Z. Li, and S.S. Sastry. *A Mathematical Introduction to Robotic Manipulation*. CRC Press, London, UK, 1994.
- [88] E. Nakano, S. Ozaki, T. Ishida, and I. Kato. Cooperational control of the anthropomorphic manipulator “MELARM”. In *Proc. 4th Int. Symp. Industrial Robots*, pp. 251–260, Tokyo, 1974.
- [89] H. Nijmeijer and A. van der Schaft. *Nonlinear Dynamical Control Systems*. Springer-Verlag, New York, USA, 1990.
- [90] W. Oelen and J. van Amerongen. Robust tracking control of two-degrees-of-freedom mobile robots. *Control Engineering Practice*, 2(2):333–340, 1994.
- [91] H.B. Pacejka and E. Bakker. The magic formula tyre model. In Hans B. Pacejka, editor, *Proc. 1st Int. Colloquium on Tyre Models for Vehicle Dynamics Analysis*, Delft, The Netherlands, 21–22 October 1991.
- [92] H.B. Pacejka and I.J.M. Besselink. Magic formula tyre model with transient properties. In F. Böhm and H.-P. Willumeit, editors, *Proc. 2nd Int. Colloquium on Tyre Models for Vehicle Dynamics Analysis*, Berlin, Germany, 20–21 February 1997.
- [93] G.J. Parish. Apparent slip between metal and rubber-covered pressure rollers. *British Journal of Applied Physics*, 9:428–433, 1958.
- [94] L.E. Parker. ALLIANCE: An architecture for fault tolerant, cooperative control of heterogeneous mobile robots. In *Proc. IEEE/RSJ/CI Int. Conf. Intelligent Robots and Systems*, volume 2, pp. 776–783, 12–16 September 1994.
- [95] L.E. Parker, G. Bekey, and J. Barhen, editors. *Distributed autonomous robotic systems 4*, Chapter: Current State of the Art in Distributed Autonomous Mobile Robotics, pp. 3–12. Springer, Tokyo, 2000.
- [96] W.R. Pasterkamp. *The tyre as sensor to estimate friction*. PhD thesis, Technische Universiteit Delft, Delft, The Netherlands, 1997.
- [97] J. Ploeg, Z. Papp, R.C. van de Pijpekamp en S.E. Skolnik, and E.A.C. van den Eijnden. ControlCIT – a control design and implementation toolbox for automatic guided vehicles. In *7th Int. Symp. on Advanced Vehicle Control*, pp. 315–320, Arnhem, The Netherlands, 23–27 August 2004.
- [98] J. Ploeg, A.C.M. van der Knaap, and D.J. Verburg. ATS/AGV design: Implementation and evaluation of a high performance AGV. In *Proc. IEEE Intelligent Vehicle Symp. (IV)*, pp. 127–134, Versailles, France, 2002.
- [99] L. Polak. *Racen. Kijk*, (6):72, June 2004.
- [100] G. Previati, M. Gobbi, M. Pennati, and G. Mastinu. Accurate measurement of mass properties of ground vehicles and their subsystems. In *7th Int. Symp. on Advanced Vehicle Control*, pp. 375–380, Arnhem, The Netherlands, 23–27 August 2004.
- [101] C.R. Rao and H. Toutenburg. *Linear Models: Least Squares and Alternatives*. Springer, Berlin, Germany, 1995.
- [102] J. Rijnbout. *Vehicle modelling by using tensors and a modular structure*. Master thesis, Technische Universiteit Eindhoven, Eindhoven, The Netherlands, 2001.
- [103] N. Roy and S. Thrun. Online self-calibration for mobile robots. In *Proc. IEEE Int. Conf. Robotics and Automation*, pp. 2292–2297, Detroit, Michigan, USA, May 1999.
- [104] D. Rus, B. Donald, and J. Jennings. Moving furniture with teams of autonomous robots. In *Proc. IEEE/RSJ Int. Conf. Intelligent Robots and Systems*, volume 1, pp. 235–242, 5–9 August 1995.
- [105] A.J.C. Schmeitz. *A semi-empirical three-dimensional model of the pneumatic tyre rolling over arbitrarily uneven road surfaces*. PhD thesis, Technische Universiteit Delft, Delft, The Netherlands, 2004.
- [106] S.E. Shladover. Review of the state of development of advanced vehicle control systems (AVCS). *Vehicle System Dynamics*, 24:551–595, 1995.

- [107] R. Soares and E. Bicho. Using attractor dynamics to generate decentralized motion control of two mobile robots transporting a long object in coordination. In *Proc. workshop on "Cooperative Robotics", IEEE/RSJ Int. Conf. Intelligent Robots and Systems*, Lausanne, Switzerland, 2002.
- [108] J.G. Starrenburg, W.T.C. van Luenen, W. Oelen, and J. van Amerongen. Learning feedforward controller for a mobile robot vehicle. *Control Engineering Practice*, 4(9):1221–1230, 1996.
- [109] D.J. Stilwell and J.S. Bay. Toward the development of a material transport system using swarms of ant-like robots. In *Proc. IEEE Int. Conf. Robotics and Automation*, volume 1, pp. 766–771, 2–6 May 1993.
- [110] D.J. Stilwell and J.S. Bay. Optimal control for cooperating mobile robots bearing a common load. In *Proc. IEEE Int. Conf. Robotics and Automation*, pp. 58–63, San Diego, CA, USA, 1994.
- [111] P. Stone and M. Veloso. Multiagent systems: A survey from a machine learning perspective. *Autonomous Robotics*, 8(3):345–383, June 2000.
- [112] B. Stouten and A.J. de Graaf. Cooperative transportation by multiple AGVs. In *7th Int. Symp. on Advanced Vehicle Control*, pp. 613–618, Arnhem, The Netherlands, 23–27 August 2004.
- [113] B. Stouten and A.J. de Graaf. Cooperative transportation of a large object – Development of an industrial application. In *Proc. IEEE Int. Conf. Robotics and Automation*, pp. 2450–2455, New Orleans, USA, 26 April – 1 May 2004.
- [114] S. Stramigioli. *Modeling and IPC control of interactive mechanical systems: a coordinate free approach*. Number 266 in Lecture Notes in Control and Information Sciences. Springer-Verlag, London, 2001.
- [115] S. Stramigioli and H. Bruyninckx. Modeling and control of rigid mechanical systems [Lecture Notes]. Dutch Institute of Systems and Control, The Netherlands, Fall 2001.
- [116] T. Sugar and V. Kumar. Decentralized control of cooperating mobile manipulators. In *Proc. IEEE Int. Conf. Robotics and Automation*, volume 4, pp. 2916–2921, Leuven, Belgium, 16–20 May 1998.
- [117] M. Suzumura, T. Kojo, Y. Tsuchiya, K. Asano, Y. Hatori, and K. Fukui. Development of the active front steering control system. In *7th Int. Symp. on Advanced Vehicle Control*, pp. 53–58, Arnhem, The Netherlands, 23–27 August 2004.
- [118] C.P. Tang, R. Bhatt, and V. Krovu. Decentralized kinematic control of payload transport by a system of mobile manipulators. In *Proc. IEEE Int. Conf. Robotics and Automation*, volume 3, pp. 2462–2467, New Orleans, USA, 26 April – 1 May 2004.
- [119] A. Trebi-Ollennu, H. Das Nayar, H. Aghazarian, A. Ganino, P. Pirjanian, B. Kennedy, T. Huntsberger, and P. Schenker. Mars rover pair cooperatively transporting a long payload. In *Proc. IEEE Int. Conf. Robotics and Automation*, volume 3, pp. 3136–3141, Washington DC, USA, 11–15 May 2002.
- [120] H. van Brussel, C.C. van Helsdingen, and K. Machiels. FROG - free ranging on grid: new perspectives in automated transport. In *Proc. 6th Int. Conf. Automated Guided Vehicle Systems*, pp. 223–232, Brussels, Belgium, 25–26 October 1988.
- [121] A.T. van Zanten, R. Erhardt, K. Landesfeind, and G. Pfaff. VDC systems development and perspective. *SAE Technical Paper*, (980235), 1998.
- [122] A.Th. van Zanten and A.I. Krauter. Optimal control of the tractor-semitrailer truck. *Vehicle System Dynamics*, 7:203–231, 1978.
- [123] P.J.Th. Venhovens and K. Naab. Vehicle dynamics estimation using Kalman filters. *Vehicle System Dynamics*, 32:171–184, 1999.
- [124] D.J. Verburg, A.C.M. van der Knaap, and J. Ploeg. VEHIL: Developing and testing intelligent vehicles. In *Proc. IEEE Intelligent Vehicle Symp. IV*, pp. 537–544, Versailles, France, 2002.
- [125] H.-J. von der Hardt, R. Husson, and D. Wolf. An automatic calibration method for a multisensor system: application to a mobile robot localization system. In *Proc. IEEE Int. Conf. Robotics and Automation*, pp. 3141–3146, Leuven, Belgium, May 1998.
- [126] H.-J. von der Hardt, D. Wolf, and R. Husson. The dead reckoning localization system of the wheeled mobile robot ROMANE. In *IEEE/SICE/RSJ Proc. Int. Conf. Multisensor fusion and Integration for Intelligent Systems*, pp. 603–610, Washington DC, USA, December 1996.

-
- [127] I.D. Walker, R.A. Freeman, and S.I. Marcus. Internal object loading for multiple cooperating robot manipulators. In *Proc. IEEE Conf. Robotics and Automation*, pp. 606–611, Scottsdale, AZ, USA, 1989.
- [128] T.A. Wenzel, K.J. Burnham, M.V. Blundell, and R.A. Williams. Approach to vehicle state and parameter estimation using extended Kalman filtering. In *7th Int. Symp. on Advanced Vehicle Control*, pp. 725–730, Arnhem, The Netherlands, August 23–27 2004.
- [129] D. Williams and O. Khatib. The Virtual Linkage: A model for internal forces in multi-grasp manipulation. In *Proc. IEEE Int. Conf. Robotics and Automation*, pp. 1025–1030, Atlanta, GA, USA, 1993.
- [130] P.W.A. Zegelaar. *The dynamic response of tyres to brake torque variations and road unevennesses*. PhD thesis, Technische Universiteit Delft, Delft, The Netherlands, 1998.
- [131] Y. Zhou, R. Wang, X. An, and S. Zhou. A control strategy for AGVS to stop at the specified location. In *3th Int. Symp. on Advanced Vehicle Control*, pp. 1343–1350, Aachen, Germany, 24–28 June 1996.

Acknowledgments

This thesis could have never been realized without the help and experience of many people. First of all I would like to thank Aart-Jan de Graaf for setting out the main lines of my Ph.D. research, for sharing his experience and ideas with me, for implementing the observer and control strategies that are presented in this thesis, and for all the help with performing the experiments and understanding FROG's control architecture. I would like to thank Ad Damen for carefully reading my thesis, for our discussions and his delicious tea, and for his useful suggestions for improving the readability of my work.

I would also like to thank FROG Navigation Systems for providing testing facilities and for giving me the opportunity to perform the experiments that are presented in this thesis. In particular, thanks to Roel van de Kraats and Ralf Siebert for helping me with using FROG's software, data logging, and writing tcl-scripts, Sjoerd Schreurs and Henk van Os for their technical assistance and repairing the vehicles, Jean-Luc Valk for our discussions on parameter estimation, Jaap Duiser for providing me room to do the experiments, Dirk Boom, Harry Spierenburg, and Marieke van Hilten for helping me with Linux and teaching me how to use the VI editor during my stay at FROG, and Paul Peteri for our discussions and for towing the vehicles when the processor card was broken.

Also thanks to my colleagues at the Control Systems group. Dik de Bruin, thank you for introducing me to vehicle and tire modeling. Will Hendrix for helping with the first experiments and for lending me the necessary equipment for the later experiments. Maarten Nauta for having fun and keeping me company during the last phase of my research. Mark "Storm" Musters, Aleksandar Juloski and Michiel Koot for entering our room over and over again. Andrej Jokic for helping me with the equations for the observer. Willem-Jan Kok for his insights on tire modeling, and Jasper Rijnbout for his ideas on vehicle modeling. Barbara Cornelissen for answering all my questions, and Paul van den Bosch for extending my contract. Thanks and greetings to my colleagues Victor van Acht, Hardy Siahaan, Patricia Astrid, Leo Huisman, John Kessels, Nelis van Lierop, Heiko Sandee, Mircea Lazar, and my former room mates Maurice Heemels and Mario Balenović.

Thanks to Udo Bartzke and the rest of the ICT team for repairing my laptop several times, to Frans Veldpauw for lending me his AVEC proceedings, and to Luc Moreau for our discussions on differential geometry. To the library staff for providing the literature that I requested. Thanks to Paul Verspaget for designing the cover and to Luud Breuking and the Printservice TU/e for printing this thesis.

Finally, I would like to thank my parents Ed and Marijke, and Famke and Tim for their support during the last five years.

Samenvatting

Voor verscheidene praktische regeltechniek toepassingen is het wenselijk dat meerdere systemen onafhankelijk evenals in samenwerking met elkaar kunnen werken. Vooral wanneer de omschakeling van individueel naar coöperatief gedrag en vice versa eenvoudig te realiseren is, resulteert dit in flexibele en eenvoudig uit te breiden systemen. Een subklasse wordt gevormd door systemen die fysiek gescheiden zijn tijdens individueel bedrijf, en zeer sterk gekoppeld gedurende handelingen die gezamenlijk worden verricht.

Eén van de vele toepassingen van meervoudige systemen die onafhankelijk en ook in samenwerking met elkaar kunnen opereren is het transporteren van een grote last met behulp van meerdere Automatisch Geleide Voertuigen (AGV's). AGV's worden in de industrie ingezet om allerlei goederen te vervoeren, variërend van kleine bakjes met CD's en DVD's tot houten pallets en rollen plaatstaal die meer dan veertig ton kunnen wegen. Huidige toepassingen bestaan typisch uit een kleine vloot AGV's, waarbij de voertuigen de producten op een individuele basis vervoeren. Op het moment is er een toenemende vraag naar het transport van zeer grote objecten, zoals rioolpijpen, wieken van windturbines, en decorstukken voor in het theater. Deze objecten kunnen meer dan dertig meter lang zijn. Een realistische optie is om meerdere kleinere AGV's te laten samenwerken om dit soort objecten te vervoeren.

Dit proefschrift beschrijft de ontwikkeling, implementatie, en het testen van gedistribueerde regelstrategieën om met meerdere AGV's een last in een industriële omgeving te vervoeren. Wij hebben ons gericht op de situatie dat de last met behulp van (semi-)rigide interconnecties aan de AGV's is bevestigd. Verder beperkten we ons tot een beschouwing op snelheidsniveau, omdat dit in onze visie een belangrijke tussenstap voor het realiseren volledig geautomatiseerde gedrag is. In onze toepassing levert een externe host het bewegingssetpoint aan. We veronderstellen dat de last reeds op de voertuigen aanwezig is. Procedures voor het plaatsen van de last op de voertuigen vallen buiten het kader van dit onderzoek. Dit project is een samenwerking tussen het bedrijf FROG Navigation Systems B.V. (Utrecht, Nederland), en de Control Systems groep van de Technische Universiteit Eindhoven. FROG stelde de test faciliteiten en twee omni-directionele AGV's om experimenten mee uit te voeren beschikbaar.

Er is een grote verscheidenheid aan industriële AGV's, en ze worden op maat gemaakt voor de desbetreffende toepassingen. Om ontwikkeltijden te verkorten is het wenselijk om een modelgebaseerd regelaarontwerp na te streven. Dit maakt generalisatie tot een brede klasse van voertuigen mogelijk. Modellingstechnieken voor starre lichamen uit het vakgebied van de robot manipulators zijn gebruikt om de bewegingsvergelijkingen voor de AGV's en de last op een systematische wijze op te stellen. Deze modellen zijn gebaseerd op fysische overwegingen zoals de tweede wet van Newton en de posities en de afmetingen van de wielen, sensoren, en actuators. Er is speciale aandacht geschonken aan de modellering van de wiel-vloer interactie, waarvoor wij de bandmodellen uit het vakgebied van de voertuigdynamica hebben gebruikt. De resulterende modellen hebben een duidelijke fysische interpretatie en omvatten een grote klasse van voertuigen met vele wielconfiguraties. Dit verzekert ons dat de ontworpen regelstrategieën, die op deze modellen gebaseerd zijn, eveneens toepasbaar zijn op een brede klasse van voertuigen.

Een belangrijke vereiste voor het realiseren van soepel coöperatief gedrag is dat de individuele AGV's met de vereiste nauwkeurigheid kunnen opereren. De prestaties van een individuele AGV zijn direct gekoppeld aan de precisie van de schattingen van de odometrische parameters, d.w.z. de effectieve wieldiameters en de offsets van de encoders die de stuurhoeken van de wielen meten. Toepassingen die het gezamenlijk transporteren van een grote last betreffen zullen typisch AGV's vereisen die een hoge graad van manoeuvreerbaarheid bezitten. Dit betekent dat alle wielen van de individuele AGV's stuurbaar zullen zijn. Aangezien een individuele AGV hierdoor meer dan één stuurhoek-encoder zal bezitten, is de identificatie van de odometrische parameters wezenlijk moeilijker voor deze omni-directionele AGV's dan voor de meeste mobiele robots die in de literatuur en in laboratoria worden aangetroffen. Dit proefschrift beschrijft een nieuw ontwikkelde procedure om gelijktijdig de effectieve wieldiameters en de offsets van de stuurhoek-encoders te schatten door verscheidene zuivere cirkelsegmenten te rijden. De toepasbaarheid van deze procedure is bevestigd aan de hand van experimenten met de twee omni-directionele testvoertuigen onder invloed van verschillende verticale belastingen. Een verrassend resultaat is dat de effectieve wieldiameters van de rubberwielen van onze AGV's toe blijken te nemen bij een toenemende verticale belasting.

Een essentieel aspect in elk regelaarontwerp is het reconstrueren van de te regelen grootheden uit de meetgegevens. Onze te regelen grootheden zijn de planaire beweging van de last en de bewegingen van de AGV's ten opzichte van de last. Deze dienen gereconstrueerd te worden uit de odometrische meetgegevens, welke bestaan uit de metingen van de wielencoders en de stuurhoek-encoders. Wij hebben de observeerbaarheid van een individuele AGV geanalyseerd, en bewezen dat het theoretisch mogelijk is om de volledige planaire beweging uit de odometrische meetgegevens te reconstrueren. Uit praktische overwegingen hebben wij een observer ontwerp op basis van de meer pragmatische kleinste-kwadraten methode uitgevoerd. We toonden aan dat de afgeleide kleinste-kwadraten bewegingsschatter onafhankelijk is van het gebruikte coördinaatsysteem. De bewegingsschatter is vervolgens geanalyseerd in een stochastisch kader. De relatie tussen de bewegingsschatter voor de planaire voertuigbeweging en de schatting van de snelheid van een willekeurige punt op het voertuig werd onderzocht. We leidden af hoe de covariantie van de snelheidsschatting van een willekeurig punt op het voertuig gerelateerd is aan de covariantie van de kleinste-kwadraten bewegingsschatting. We bewezen dat er één uniek punt is op het voertuig waarvoor de covariantie van de geschatte snelheid minimaal is. Vervolgens onderzochten we hoe de lokale bewegingsschattingen van individuele AGV's gecombineerd kunnen worden om één globale schatter te bepalen. Wanneer de last volledig star aan de AGV's is bevestigd, dan is het voldoende dat iedere AGV zijn lokale bewegingsschatting uitzendt en de schattingen van de andere AGV's ontvangt. Wanneer de last op semi-rigide wijze aan de AGV's bevestigd is, bijvoorbeeld door middel van een rotatiescharnier of een schuifscharnier, dan dient iedere AGV bovendien zijn corresponderende informatiematrix uit te zenden. We toonden aan dat de informatiematrix constant blijft als de last aan de AGV wordt bevestigd met een rotatiescharnier indien de rotatie-as samenvalt met het eerder genoemde unieke punt waar de covariantie van de snelheidsschatting minimaal is. Dit betekent dat de desbetreffende AGV zijn informatiematrix voor deze speciale situatie niet hoeft uit te zenden.

Het belangrijkste punt in het regelaarontwerp voor coöperatief vervoer van een last is dat de verscheidene AGV's elkaars acties niet mogen tegenwerken. Het gedecentraliseerde regelalgoritme dat wij afleidden zorgt ervoor dat de AGV's het extern verstrekte planai-

re bewegingssetpoint volgen, terwijl gelijktijdig de interconnectiekrachten tussen de last en de voertuigen worden geminimaliseerd. Hoewel het regelaarontwerp van toepassing is op coöperatief transport met meerdere AGV's en willekeurige semi-rigide AGV-last interconnecties, vonden we op dat de oplossing voor het geval dat alle interconnecties volkomen rigide zijn bijzonder eenvoudig is. In dat geval hebben de lokale regelalgoritmen dezelfde structuur als het regelalgoritme dat normaal wordt gebruikt voor individueel AGV bedrijf. Voor deze speciale situatie volstaat het om een aantal parameterinstellingen te wijzigen en om de AGV's van identieke setpoints te voorzien om coöperatief gedrag op snelheidsniveau te realiseren.

De observer- en regelstrategieën voor een last die volledig star aan de AGV's is verbonden zijn met succes geïmplementeerd op de twee testvoertuigen. Er zijn experimenten uitgevoerd zonder en met last, waarbij de last uit een pallet met 300 kg stoeptegels bestond. De resultaten waren reproduceerbaar en illustreerden de praktische geldigheid van de ontworpen observers en regelaars. Er traden geen noemenswaardige nadelen op toen de lokale observers slechts hun lokale sensor informatie gebruikten, wat betekent dat onze opstelling ook bevredigend presteert wanneer de lokale snelheidsschattingen niet worden uitgewisseld met de andere AGV's.

Curriculum vitae

Bart Stouten was born in Uden, the Netherlands, on the first of October in 1975. He attended the elementary school De Vlonder in Uden from 1980 to 1988, and subsequently went to the Kruisheren Kollege high school, also in Uden.

He graduated from the Atheneum in June 1994, and started studying mechanical engineering at the Technische Universiteit Eindhoven in autumn 1994. His traineeship at the System and Control Group of the departments of Applied Physics and Chemical Technology comprised the “Development of a Heating-Cooling System with two solenoid valves.” His graduation project took place at the Section of Systems and Control of the department of Mechanical Engineering within the scope of the EcoDrive project, and concerned the “Modeling and Control of a Continuously Variable Transmission.” He received his M.Sc.-degree in Mechanical Engineering in April 2000, and was awarded the Mignot price for the second best master thesis of the Technische Universiteit Eindhoven of that year. He stayed at the department of Mechanical Engineering as a research assistant for two months.

In June 2000, he started working towards his Ph.D. thesis at the Control Systems group of the department of Electrical Engineering at the Technische Universiteit Eindhoven. The topic of his Ph.D. research was “Parameter Tuning and Cooperative Control for Automated Guided Vehicles.” The project was carried out in close cooperation with the company FROG Navigation Systems, which develops and markets Automated Guided Vehicle Systems and navigation hard- and software.

As part of his Ph.D. research, he successfully completed the EUROMOTOR Vehicle Dynamics in Simulation and Testing course, which was held in Nunspeet, The Netherlands, from 17 to 19 September 2001. He attended the Engineering Mechanics/DISC Summer School on Modeling and Control of Mechanical Systems that took place in Zeist, The Netherlands, from 1 to 4 July 2002. Later that year he joined the Euron Robotics European Summer School on Cooperative Robotics, which was held at the Instituto Superior Técnico in Lisbon, Portugal, from 2 to 7 September. In 2003 he attended the Euron/Geoplex Summer School on Modeling and Control of Complex Dynamical Systems -from Ports to Robotics- at the University of Bologna Residential Centre of Bertinoro, Italy, from 6 to 12 July. In 2003 he received the course certificate of the Dutch Institute of Systems and Control DISC for completing a required number of postgraduate courses.

